Applied microfluidic stripline NMR spectroscopy

Proefschrift

ter verkrijging van de graad van doctor
aan de Radboud Universiteit Nijmegen
op gezag van de Rector Magnificus prof. dr. J. H. J. M. van Krieken,
volgens besluit van het college van decanen
in het openbaar te verdedigen op

donderdag 13 juni 2019
om 12.30 uur precies

door

Anna Jo de Vries

geboren op 8 september 1980

te Scheemda

Promotor:	Prof. dr.	A. P. M. Kentgens
Manuscriptcommissie:	Prof. dr.	W. T. S. Huck
	Prof. dr.	J. Roithova
	Prof. dr.	M. Utz (University of Southampton, UK)

A.J. Oosthoek - de Vries, Applied Microfluidic Stripline NMR spectroscopy.
PhD thesis, Radboud Universiteit Nijmegen, the Netherlands
ISBN 978-94-6332-506-6

Printed by: GVO drukkers en vormgevers B.V., Ede

An electronic version of this dissertation is available at http://repository.ru.nl/.

This research was financially supported by the ACTS - Process on a Chip Programme of The Netherlands Organization for Scientific Research (NWO).

Contents

List of Abbreviations

B_0 ..... static magnetic field

BIRB796 ..... p38α mitogen-activated protein kinase inhibitor

COSY ..... correlation spectroscopy

CSF ..... cerebrospinal fluid

DIPEA ..... N,N-diisopropylethylamine

DNP ..... dynamic nuclear polarisation

EC ..... electrochemical conversion

emf ..... electromotive force

FID ..... free inducation decay

f_{fill} ..... filling factor

f_{obs} ..... observe factor

FS ..... fused-silica

FWHH/FWHM . full width at half height/maximum (peak height)

HMBC ..... heteronuclear multiple bond correlation

HMQC ..... heteronuclear multiple quantum correlation

HSQC ..... heteronuclear single quantum correlation

LOD ..... limit of detection

MAS ..... Magic angle spinning

NMR ..... Nuclear Magnetic Resonance

ω_0 ..... Larmor frequency

PDE . . . . . Partial differential equation

rf . . . . . radio frequency

r.m.s. . . . . . root-mean-square

SNR . . . . . signal-to-noise ratio

SPE . . . . . solid phase extraction

$\mathbf{T}_1$ . . . . . longitudinal relaxation time constant

$\mathbf{T}_2$ . . . . . transverse relaxation time constant

TEA . . . . . triethylamine

TMS . . . . . tetramethylsilane

TOCSY . . . . . total correlation spectroscopy

$\mathbf{V}_{coil}$ . . . . . active volume of a coil

$\mathbf{V}_{obs}$ . . . . . detection sample volume effectively observed in measurement

$\mathbf{V}_s$ . . . . . sample volume

$\mathbf{V}_{total}$ . . . . . total volume of sample needed for measurement

Preface

The foundations of quantum mechanics were laid in the beginning of the 20th century. Quantisation of angular momentum in a magnetic field was first shown in the Stern-Gerlach experiment in 1922, where beams of silver atoms were deflected by an inhomogeneous magnetic field according to their intrinsic angular momentum. In 1926, Goudsmit and Uhlenbeck proposed the concept of electron spin, an essential element for the theory of NMR. In 1938, Rabi et al [1] modified the Stern-Gerlach experiment, using rf irradiation at the Larmor frequency of the nuclei in a beam in order to measure the nuclear magnetic moment, which can be regarded as the first NMR experiment. Rabi received a Nobel prize for this work in 1944.

Thereafter, attempts to observe the NMR phenomenon in bulk were done, most notably by Gorter, who was not successful because of the intrinsic low sensitivity of NMR and the long relaxation times of his samples. Until 1946, when two independent groups measured the first bulk NMR spectra. Bloch, Hansen and Packard [2], applying rf irradiation to a sample of water in a magnetic field measuring the induced current in a coil. Purcell, Torrey and Pound [3] used a sample of paraffin, measuring the absorption of rf energy by the proton magnetic moments. Bloch and Purcell were awarded with a Nobel prize in 1952.

Following this discovery, NMR was used for magnetic moment determination of different nuclei. However, when sensitivity and resolution increased it was observed that deviations occurred depending on the surroundings of the nuclei. This marks the discovery of the chemical shift: the resonance frequency determined by the shielding of the nuclei, depending on density and configuration of surrounding electrons. The first spectrum of ethanol is a renowned example [4].

When sensitivity and resolution further improved, by increasingly powerful magnets and developments in electromagnetics, multiplet structures within peaks became ap-

parent: resulting from spin-spin coupling of nearest neighbours within molecules. Also chemical exchange was found to be visible in the NMR spectrum. This opened up possibilities in molecular structure determination, causing NMR spectroscopy to emerge as an impressive analytical tool for chemistry.

From then on, as a result of continuously increasing sensitivity and resolution, the usefulness of NMR spectroscopy has made an enormous growth. On the one hand substantial improvements were made in hardware by developing higher and more homogeneous magnetic fields, and stabler and cooler probes. On the other hand, milestones such as Fourier transform NMR spectroscopy, magic angle spinning, developments of pulse sequences contributed to efficiency, resolution and functionality. As a result, high resolution NMR has become an important well-established spectroscopic technique, in chemistry as well as in physics, and also NMR imaging (MRI). Although an intrinsic low sensitivity remains problematic for some applications with low concentrated or mass-limited samples, since the measurement time increases quadratically with a decrease in the amount of spins in the sample.

NMR spectroscopy nowadays plays an vital role in characterisation of molecules, analysing the composition of samples and monitoring of reactions, in the fields of chemistry, biology, medicine, physics and pharmacy.

More recently, realising the importance of sustainability, many researchers in these fields focus on finding ways to minimise impact on the environment. In chemical industry, continuous flow microstructured reactors can be an important strategy in developing green chemistry[5]. Performing chemical reactions at microscale in continuous flow instead of using stirred tank reactors enhances process control. For that reason, microreactor chemistry is less dangerous, produces less waste as less solvents can be used, in addition to processing advantages that improve efficiency and enable fast reactions. In continuous flow microtechnology, the reaction is monitored online, so small-scale analyte samples are used for fast and effective analysis.

In biochemistry, sample availability can be very limited in amount or in low concentrations, especially when mimimum impact on animal/plant subjects is desired. Furthermore, if lab animals are used for research, ethics requires us to use as few and little of a lab animal as possible. Additionally, when researching specificity, a single animal is monitored, in contrast to pooling. But a single animal can provide a limited amount of sample. The method for analysis should therefore be tuned to the sample size.

Summarising, there are several use cases for using small amounts of sample and

spectroscopic detection and analysis in situ or in flow. Both in biomedical and organic chemistry there are examples of analysis preferably done on the microscale. The spectroscopic techniques should match the size of the samples to be analysed, but in conventional NMR this is sometimes impossible, because of its sensitivity issues.
The typical NMR detection volume is 500 μl, when the sample is smaller, dilution may affect the sample, but also increases measurement time. Only offline measurements on relatively stable samples are possible in this setup, which is time- and solvent consuming. Several developments have improved resolution and sensitivity: a higher and more homogeneous field, lower temperature or non-Boltzmann methods. However, all of these have their practical drawbacks, are expensive, or not generally suitable. Despite numerous improvements, one is still unable to measure small or in situ samples as such in a conventional NMR spectrometer.
An alternative way to increase sensitivity is to adapt the probe. In 1976, Hoult and Richards[6] showed that mass sensitivity could be improved by miniaturisation of the rf coil. Since then, many designs have been proposed to miniaturise the rf coil: a wound microcoil solenoid and a planar helical coil are much explored designs. However, the solenoid is difficult to miniaturise beyond 100 μm, and also not a lithography compatible technique. The planar helical coil is a printable 2D structure, but not as good as other coils in terms of resolution and sensitivity.
A stripline NMR chip is a planar 2D structured rf coil, in which the rf field is homogeneous and strong, combining high resolution with high sensitivity. In 2004 the rf stripline coil was introduced, and in 2007 a prototype was presented[7, 8] and used. The results were promising and led to improvements in the design. After several iterations, the stripline NMR chips have both high resolution and sensitivity. The detection volumes that were used are 150-250 nl, but is scalable. Furthermore, the stripline chip can be coupled to microfluidics for continuous flow measurements. In this thesis, stripline NMR chips were used for measuring static plugs of small volume biological samples, and also coupling to a microfluidic environment to achieve both in situ and continuous flow measurements of microvolume samples.

Scope of this thesis

This thesis explores some possible, relevant applications of the stripline NMR chip, in organic and pharmaceutical chemistry. **Chapter 1** gives a theoretical background of the NMR experiment, focussing on sensitivity enhancement. An explanation is given of

how miniaturisation of the rf coil improves mass sensitivity. Different microcoil designs are discussed. Several designs of the stripline NMR chip are used in this research, an overview of the stripline NMR chips will be presented. One of the possible applications for which microcoil NMR is interesting is mass-limited samples. In **Chapter 2** static measurements are performed using a stripline NMR chip with a replaceable capillary as a sample holder. Two examples are individual mouse CSF (cerebro spinal fluid) and strigolactone (plant hormone), both very limited in amount, analysed as a plug. The strigolactones were also measured in solid state NMR. The spectra are analysed to show structural information and concentration. In **Chapter 3**, three types of NMR chips are coupled to a microfluidic setup. Standard ^{1}H, and ^{13}C experiments were performed, but also two dimensional ^{1}H-^{1}H and ^{1}H-^{13}C experiments in continuous flow. It is shown that this setup decreases measurement time and/or reduces the volume of analyte needed. Our stripline NMR setup is coupled to a microreactor platform in **Chapter 4**, so that reaction monitoring of fast chemical reactions is possible: we performed an in-depth study of the acetylation of benzyl alcohol. Measuring in continuous flow while the reaction proceeds enables NMR spectra to be taken during the first 10 minutes of the reaction. In combination with conventional NMR spectra, a reaction mechanism for this fast reaction is proposed. Using a similar microfluidic NMR setup, an even faster reaction, the Paal Knorr pyrrole synthesis, is studied in **Chapter 5**. The reaction is finished in a few minutes, without leaving intermediate products. In conventional NMR the progress of the reaction cannot be followed, nor the intermediate products. A series of 1D spectra and two dimensional experiments in continuous flow were performed during the progress of the reaction giving kinetic information. **Chapter 6** explores the hyphenation of electrochemistry with microfluidic stripline NMR spectroscopy for metabolomic studies. An unstable compound produced in an electrochemical cell, was collected in an SPE (solid phase extraction) and subsequently measured in stopped-flow in the stripline NMR chip.

References

[1] I. I. Rabi, J. R. Zacharias, S. Millman, and P. Kusch, "A new method of measuring nuclear magnetic moment," *Phys. Rev.*, vol. 53, p. 318, 1938.

[2] F. Bloch, W. W. Hansen, and M. Packard, "Nuclear induction," *Phys. Rev.*, vol. 69, p. 127, 1946.

[3] E. M. Purcell, H. C. Torrey, and R. V. Pound, "Resonance absorption by nuclear magnetic moments in a solid," *Phys. Rev.*, vol. 69, p. 37, 1946.

[4] J. T. Arnold, S. S. Dharmatti, and M. E. Packard, "Chemical effects on nuclear induction signals from organic compounds," *J. Chem. Phys.*, vol. 19, p. 507, 1951.

[5] C. Wiles and P. Watts, "Continuous flow reactors: a perspective," *Green Chem.*, vol. 14, p. 38, 2012.

[6] D. Hoult and R. Richards, "The signal-to-noise ratio of the nuclear magnetic resonance experiment," *J. Magn. Reson.*, vol. 24, p. 71, 1976.

[7] P. J. M. van Bentum, J. W. G. Janssen, and A. P. M. Kentgens, "Towards nuclear magnetic resonance m-spectroscopy and μ-imaging," *Analyst*, vol. 129, p. 793, 2004.

[8] P. J. M. van Bentum, J. W. G. Janssen, A. P. M. Kentgens, J. Bart, and J. G. E. Gardeniers, "Stripline probes for nuclear magnetic resonance," *J. Magn. Reson.*, vol. 189, p. 104, 2007.

Chapter 1

Introduction

1.1 The NMR experiment

(a) Spectrometer

(b) Probe

(c) Stripline RF coil

Figure 1.1

In this section we present a basic general introduction to NMR with a focus on the aspects relevant to this thesis. The reader may want to refer to NMR textbooks [1, 2, 3, 4] for a broader introduction to NMR spectroscopy.

Nuclear magnetic resonance (NMR) spectroscopy probes the resonance frequencies of nuclear spins in a sample, which are influenced by their chemical and physical properties. Nuclear spin is a characteristic of atomic nuclei, a microscopic magnetic moment, with a specific angular momentum. In an external magnetic field, the spin energy levels are quantised, i.e. aligned in a limited number of orientations relative to the magnetic field. The splitting of energy levels is known as Zeeman splitting, see Figure 1.3. In a static magnetic field the nuclear spins are aligned and precess (rotating like the wobbling of a spinning top) with a frequency that is called the Larmor frequency ω_0, which related to the energy difference between spin energy levels: $\Delta E = \hbar\omega_0$. When a quantum of electromagnetic energy, matching the energy difference between the spin states, is applied to a spin, a transition to a higher energy level results.

A sample in a static magnetic field at thermal equilibrium contains an ensemble of spins. The population of the spin system over the energy levels is described by a Boltzmann distribution, with the lower energy levels more populated depending on the temperature. The population difference between the energy levels forms a macroscopic

net magnetisation. This net magnetisation vector is initially aligned with the magnetic field, but, in an NMR experiment, is tipped 90 degrees, accomplished by applying an electromagnetic pulse to the sample, i.e. rf (radiofrequency) irradiation generated by an rf coil. After this rf pulse, the net magnetisation vector relaxes back to thermal equilibrium and the Boltzmann distribution is re-established. The rotating magnetic dipoles representated by the magnetisation vector induce an electromotive force (emf), which can be detected by the rf coil. From the rf signal, the resonance frequencies of the nuclei in the sample are obtained by Fourier transformation, giving a spectrum from which information about the chemical properties of the nuclei can be deduced.

1.1.1 Experimental setup

NMR experiments are typically performed in a strong, stable and homogeneous magnet, such as the spectrometer shown in Figure 1.1a. In a higher magnetic field, the magnetistion is stronger, which increases the signal-to-noise ratio (SNR) (section 1.3.2). Moreover, the chemical shift resolution of the spectrum increases. The magnet used in our experiments is 14.1 T (600 MHz). Stronger magnetic field strengths are continuously being developed, the strongest magnets currently available are around 23.5 T (1 GHz), and 28.2 T (1.2 GHz) is under development (due next year). To achieve such high magnetic fields strengths, superconducting magnets are used which are cooled with liquid nitrogen (77K) and helium (< 4K) baths. Not only field strength, but also homogeneity of the magnetic field is an important aspect. In order to ensure a high resolution, small shimming magnets are used to fine-tune the magnetic field at the heart of the magnet, in order to produce the most homogeneous field at the position of the sample. The sample is placed there using a probe (height around 50 cm). One of the probes used in our experiments is shown in Figure 1.1b. The design of the probe and coil is optimised so that it minimally affects the homogeneity of the magnetic field. Besides functioning as a sample holder, the probe also contains an rf coil for rf pulsing and detection, and electronics for tuning and matching of the rf field.

1.1.2 1D ^{1}H and ^{13}C NMR spectrum

The resonance frequency is a characteristic for a certain nucleus, for example the ^{1}H nucleus has a typical resonance frequency of 600 MHz for a 14.1 T magnet, whereas the ^{13}C nucleus has a resonance frequency of 150 MHz at that field. In the remainder of this text only these two nuclei are taken into consideration.

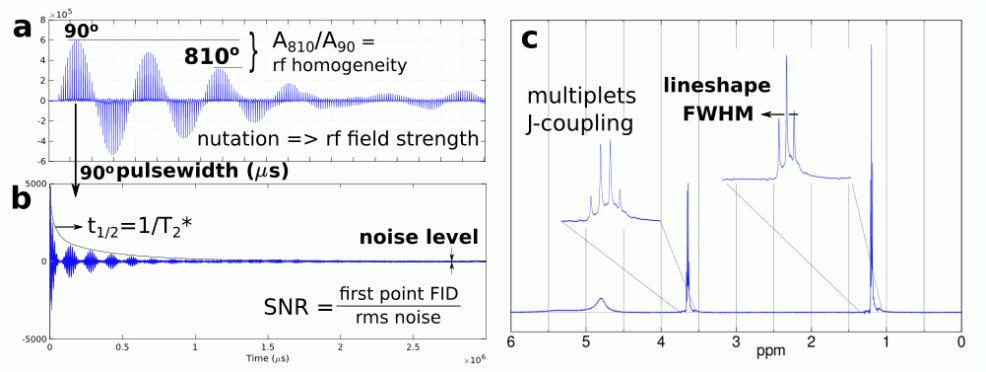

Figure 1.2: Ethanol (70%) in chip-in-a-box stripline NMR, a) nutation of ethanol triplet b) FID c) single scan spectrum. The nutation is a series of measurements with increasing pulsewidth. The 90 degree pulsewidth can be determined from this. Also, a nutation gives information about rf strength and rf homogeneity. By applying the exact 90 degree pulsewidth that was found, a FID can then be obtained. The SNR can be calculated by dividing the intensity of the first point of the FID by the rms (root mean square) of the noise. Also, the observed relaxation time constant T_2^* can be found. Fourier transformation of the FID results in the NMR spectrum. Here we find the chemical shift values for each resonance peak. Multiplets give additional information about the molecular structure. The FWHM value (full width at half maximum) is typically obtained from the ethanol triplet.

NMR was at first used for determining the magnetic moment of elements, when in 1951 chemical shift was discovered[5]. A nucleus experiences an effective magnetic field depending on the local electron distribution which contributes to shielding the nucleus from the external magnetic field. The magnetic field strength experienced by the nucleus therefore differs from the applied magnetic field, this is called chemical shift. A chemical shift value δ can be assigned to the resonance frequency relative to a reference value, for ^{1}H and ^{13}C the resonance frequency of tetramethylsilane (TMS). The ppm-scale is used, to be magnetic field strength independent: $\delta_{ppm} = \frac{2\pi\delta\nu}{\gamma B_0}$ and the resonance frequency of TMS is fixed at 0 ppm.

The chemical environment, i.e. surrounding electrons and other atoms in the molecule, influences the shielding and thereby the measured chemical shift. Nuclei that experience a higher electron density are shielded from the external field, which results in a lower chemical shift. Equivalent nuclei are in the same chemical environment, so have the same chemical shift. Structural features (eg. the type of bond and substituents) determine the electron distribution, which affects shielding of a nucleus, so the chemical shift contribute to molecular structure information.

When resolution increases, one finds that resonance peaks often are split into multiplets. These multiplets arise from J-coupling or spin-spin coupling, resulting when spins are coupled to neighbouring equivalent spins by one or more chemical bonds. Each of the neighbouring spins-1/2 can be in a spin state up (aligned with B_0) or down (opposed to B_0), an ensemble of n spins can have $(2nI + 1)$ configurations. The spin states are almost equally populated, two spin-1/2 nuclei can be both up, both down or one up and one down. The aligned spins experience a slightly higher field and so a slightly higher frequency, therefore are present at a shifted position. In the ^{1}H spectrum of ethanol in Figure 1.2c, a triplet formed by these interactions can be observed, as well as a quartet for the two protons.
Since J-coupling is a through-bond interaction, arising from neighbouring protons via hyperfine interactions of the bonding electrons, J-coupling indicates direct connectivity within the molecule. The multiplet pattern can give insight into the amount of protons attached to the neighbouring nuclei. Therefore, the multiplicity of the signal gives information of the molecular structure. Furthermore, J-coupling can be used in correlation experiments to examine connectivity within the molecule. It is desirable to have a high-resolution spectra, in order to be able to use this information, which can be critical in applications determining molecular structure.

Relaxation In absence of an external magnetic field, the spin states are degenerate. When the spins in a sample are immersed in a magnetic field, polarisation increases until thermal equilibrium is reached with a Boltzmann distribution over the spin states. Also, when the equilibrium has been disturbed, eg. by applying an rf pulse, the nuclei relax to their equilibrium populations. This recovery process is called longitudinal relaxation, or spin-lattice relaxation, and characterised by relaxation time constant T_1. The magnetisation along the z-axis M_z at time t depends exponentially on T_1, where M_0 is the magnetisation at thermal equilibrium, and an rf pulse is given at $t = 0$:

$$M_z = M_0(1 - e^{-t/T_1}) \tag{1.1}$$

To obtain a qualitative spectrum by signal averaging over multiple scans, only after the nuclei are back in thermal equilibrium and magnetisation is fully build-up, the sample is in the same starting conditions and a new pulse can be applied. In practice, 3-5 times T_1 is used as an acquisition delay between multiple pulses to obtain a quantitative spectrum. Unfortunately, in some cases this delay time can become very long, for

example for quartenary carbon nuclei, which increases the experiment time when signal averaging is needed for obtaining sufficient signal. For continuous flow NMR, this is of importance because it is possible to shorten the observed value of the relaxation time T_1^*, by refreshing the sample and flowing spins that are prepolarised in the field into the detection volume, rather than waiting for the spins to recover to thermal equilibrium between scans.

Transverse relaxation is the loss of coherence between the spins, which has the effect that the magnetisation vector in the xy-plane after an rf pulse dephases, resulting in zero net transverse magnetisation. Local magnetic field disturbances originating from intermolecular and intramolecular interactions cause this decoherence, characterised by spin-spin relaxation time constant T_2, which is typically smaller than or equal to T_1. The transverse relaxation process follows a similar exponential behaviour. In addition to microscopic field disturbances, macroscopic inhomogeneities in the B_0 field, due to experimental imperfections or susceptibility effects, also cause dephasing of magnetisation, expressed by the time constant T_2'. Transverse relaxation is observed in the spectrum, since the dephasing of the magnetisation vector introduces an uncertainty in resonance frequency, which broadens the resonance peak. The experimentally observed relaxation rate contains both microscopic and macroscopic effects: $1/T_2^* = 1/T_2 + 1/T_2'$. The observed relaxation time T_2^* can be determined by the linewidth of a peak (FWHH, full width at half height): FWHH $= 1/\pi T_2^*$. T_2^* can also be observed from the decaying FID, see Figure 1.2b, by:

$$T_2^* = \frac{t_{(1/2)}}{ln2} \tag{1.2}$$

The significance of T_2 in continuous flow NMR is that when the sample flows out of the detection area during acquisition faster than T_2, the FID is artificially shortened, giving rise to a smaller observed T_2^*, which may broaden the signals. The effect of continuous flow NMR on the observed relaxation times is discussed in Chapter 3. On the other hand, chemical processes can influence the linewidth as well when the dynamics is on the same timescale as the chemical shift difference, which will be encountered in Chapter 4.

^{13}C NMR experiment

The ^{13}C NMR experiment can in principle be acquired similarly as the ^{1}H NMR spectrum, but an important difference between ^{1}H and ^{13}C involves the strength of the

signal. First of all, the natural abundance (naturally occurring amount of an isotope) of ^{1}H is almost 99.98 %, but unfortunately ^{12}C, the naturally dominant isotope, has no spin, and the natural abundance of ^{13}C, having spin 1/2, is only 1.11 %. Furthermore, the gyromagnetic ratio γ influences the strength of the signal, as nuclei with a higher γ have a higher resonance frequency, a higher magnetic moment and a higher precession rate. The sensitivity of the experiment scales with the gyromagnetic ratio γ of the nucleus to the power 5/2 as will be shown below, in (1.22). A ^{1}H nucleus has both a high abundance and a high γ, which gives comparable to ^{13}C a much better signal ($1 : 1.76 \cdot 10^{-4}$). In some cases, it may be possible to use labelled ^{13}C nuclei for the NMR experiments, but often in order to obtain sufficient signal it is necessary to acquire many scans, in which the T_1 relaxation time has to be taken into account as an acquisition delay between scans. Signal averaging over N scans improves the SNR of the spectra only with: $SNR \propto N^{1/2}$, so that it may be necessary to take many scans for sufficient improvement of the signal. As a conclusion, acquiring a ^{13}C spectrum can take a very long time. Here, continuous flow NMR can be useful as explained above, as the waiting for T_1 relaxation time may not be necessary and the acquisition time can be significantly increased, as will be shown in Chapter 3.

1.1.3 Two dimensional correlation spectroscopy

Two dimensional correlation spectroscopy shows nuclear shift correlations, correlations within the molecules. Since evidence of connectivity between nuclei gives a lot of structural insight, these are very interesting techniques and used throughout this thesis.

^{1}H-^{1}H: COSY (correlation spectroscopy) and TOCSY (total correlation spectroscopy) In general, a two dimensional pulse sequence is formed by several blocks: preparation, evolution (t_1), mixing and detection (t_2). The 2D spectrum is acquired as a function of t_1 and t_2, and Fourier transformed over both time scales, to get a 2D spectrum with two frequency axes, the direct and indirect dimension. In a COSY experiment, the preparation and mixing are both a 90 degree pulse. By incrementally increasing t_1, the precession frequency of the nucleus is obtained. When nuclei are coupled, coherence transfer is introduced, magnetisation transfer from one spin to neighbouring coupled spins occurs through J-coupling. The precession frequency of one spin therefore transfers to the coupled spins. In the 2D spectrum, this is found as a cross peak.

In the TOCSY or HOHAHA (Hartmann-Hahn homonuclear cross polarisation) pulse sequence, instead of a single pulse for mixing a spin lock is used, resulting in isotropic mixing. A spin lock sequence consists of a series of 180 pulses with infinitely small time in between. During the spin lock the chemical shift is continually refocused, whereas the spin-spin coupling stays active, this allows the magnetisation eventually to propagate across the complete molecule to all coupled spins. The TOCSY spectrum therefore shows cross peaks through the whole molecule.

^{1}H-^{13}C: HSQC, HMQC, HMBC Besides homonuclear 2D correlation spectroscopy, also correlations between different nuclei can be obtained. Three experiments are used here: HSQC (heteronuclear single quantum correlation), HMQC (heteronuclear multiple quantum correlation), HMBC (heteronuclear multiple bond correlation). Heteronuclear ^{1}H - ^{13}C correlation spectroscopy correlates carbon nuclei to the attached protons. Furthermore, this technique makes it easier to distinguish crowded ^{1}H multiplets to different ^{13}C nuclei. To increase sensitivity, polarisation transfer is induced from the sensitive ^{1}H to the insensitive ^{13}C, and then back to the observed ^{1}H nuclei. A cross peak in the 2D spectrum reveals connectivity between ^{1}H to the ^{13}C nucleus. In the case of heteronuclear single and multiple quantum correlation (HSQC and HMQC) this shows correlations over a single bond, i.e. directly coupled spins, whereas the HMBC experiment shows multiple bond correlations. The details of the spin dynamics of these pulse sequences are beyond the scope of this thesis, and can be found in references[6, 7, 8] or NMR textbooks. It will be shown in Chapter 3 that HSQC and HMQC experiments can be performed in the microfluidic stripline NMR setup during continuous flow, which diminishes the experimental time. Furthermore, to aid in solving reaction mechanisms HSQC and HMBC will be used in Chapter 4.

1.2 Magnetisation

In this section we will go into more detail regarding spins in a magnetic field and deriving an expression for the magnetisation of the sample, as this will be used in the expression for sensitivity in the next section.

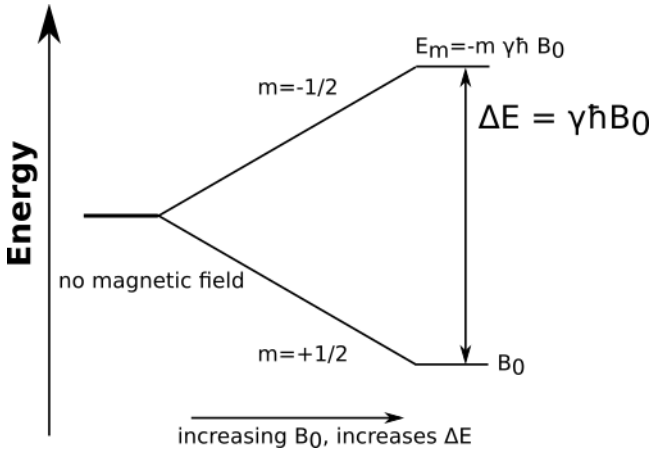

Figure 1.3: Zeeman effect, for spin-1/2 nuclei with γ is negative.

1.2.1 Interactions of matter with a magnetic field

Atomic nuclei have intrinsic properties: mass, electric charge, magnetism and spin. Nuclear spin is a type of quantum mechanical angular momentum. The other type is orbital angular momentum. Both types are quantised, but whereas orbital angular momentum arises from rotation, nuclear spin angular momentum is an intrinsic nuclear property. Nuclear spins $\boldsymbol{J}$ are labelled by a nuclear spin quantum number I, which is a positive multiple of 1/2, depending on the type of particle. Nuclei with $I = 0$ do not have nuclear spin, and are not amendable to NMR experiments.

In the absence of a magnetic field the spin states are degenerate, i.e. the spin states have the exact same energy. In a magnetic field this degeneracy is lifted, giving rise to different energy levels, so the energy and orientation of spins is quantised. This separation of energy levels is called the Zeeman effect, see Figure 1.3. The nuclear spin states in a magnetic field are labelled with nuclear spin quantum number m, ranging from $-I$ to $+I$ in steps of 1, where the largest nuclear spin quantum number m corresponds to the lowest energy spin state. For a particle with spin quantum number I, the multiplicity of possible spin states is given by $2I + 1$. For a nuclear spin with $I = 1/2$, two Zeeman levels exist $-I$ and $+I$. The spins states are populated according to Boltzmann's distribution law of statistical mechanics.

The spin angular momentum $\boldsymbol{J}$ gives rise to a magnetic moment $\boldsymbol{\mu}$, proportional to $\boldsymbol{J}$:

$$\mu = \gamma * J \tag{1.3}$$

where γ is the magnetogyric/gyromagnetic ratio, defined by $\gamma = \frac{-eg}{2m}$, with e the charge of the nucleus, m the mass, and g is the g factor, which is a specific value for a given nucleus. The sign of γ determines the direction of the precession. Nuclei with negative γ, such as ^1H and ^{13}C, exhibit clockwise rotation and spin 'up', aligned with B_0, is the lower energy state and most stable, spin 'down', orientated against B_0, is the higher energy state.
The angular momentum vector $\boldsymbol{J}$ precesses around the axis of the applied external field, with strength B_0, with an angular frequency known as the Larmor frequency:

$$\omega = -\gamma B_0 = \frac{egB_0}{2m}(rad/s) \tag{1.4}$$

or in frequency (Hz):

$$\nu = \frac{-\gamma}{2\pi}B_0 \tag{1.5}$$

By applying radiofrequency radiation, an rf pulse, with oscillating frequency matching the energy difference between the nuclear orientations, excitation occurs. The condition applies that the frequency of the electromagnetic radiation matches the Larmor precession frequency $h\nu_{precesession} = h\nu_{photon} = \Delta E$.
The magnetic Zeeman energy E of a nucleus with magnetic moment μ in the presence of a magnetic field $\boldsymbol{B}$ is:

$$E = -\mu \cdot \boldsymbol{B} = -\mu \cdot \gamma * J \tag{1.6}$$

The z- component of the magnetic moment is:

$$\mu_z = \gamma \hbar m_i \tag{1.7}$$

with m_i is -I .... +I
And so the Zeeman energy is:

$$E_{m_i} = -\gamma \hbar m_i B_0 \tag{1.8}$$

For $I = 1/2$, the energy difference ΔE between the two spin states is:

$$\Delta E = ((-1/2) - (1/2))\frac{\gamma h B_0}{2\pi} = \gamma \hbar B_0 = \hbar \omega_0 \tag{1.9}$$

1.2.2 Macroscopic magnetisation

The sum of the microscopic magnetic moments $\boldsymbol{\mu_m}$ in an external magnetic field B_0 gives rise to a macroscopic magnetisation $\boldsymbol{M}$ per unit volume:

$$\boldsymbol{M} = \frac{1}{V}\sum_{m=1}^{n}\boldsymbol{\mu_m} \tag{1.10}$$

The total magnetisation is M_0:

$$M_0 = \sum_{m} < \mu_z > \rho_m \tag{1.11}$$

where $< \mu_z >$ is the expectation value of the microscopic moment which equals $\gamma\hbar m_z$, (1.7). ρ_m is the population of spins in energy level N_m. At thermal equilibrium, the spins distribute over the Zeeman energy states with Boltzmann's law. So ρ_m can be written accordingly as:

$$\rho_m = \frac{N_m}{N} = \frac{exp\frac{-E_m}{k_BT}}{\sum_{m=-l}^{l}(exp\frac{-E_m}{k_BT})} \tag{1.12}$$

In this expression N is the total spin population, T is the temperature and k_B is Boltzmann's constant, with $E_m = -m_m\gamma\hbar B_0$. Substituting into M_0:

$$M_0 = N\gamma\hbar\frac{\sum_{m=-l}^{l} m_m exp\frac{E_m}{k_BT}}{\sum_{m=-l}^{l} exp\frac{E_m}{k_BT}} \tag{1.13}$$

At room temperature, $h\gamma B_0 << k_BT$, the 'high field approximation' is valid ($\exp^{-x} \approx 1 - x$).

$$M_0 \approx N\gamma\hbar\frac{\sum_{m=-l}^{l} m_z(1 - \frac{-m_m\gamma\hbar B_0}{k_BT})}{\sum_{m=-l}^{l}(1 - \frac{-m_m\gamma\hbar B_0}{k_BT})} \tag{1.14}$$

Using polynomial expressions (square pyramidal number: $\sum_{m=-l}^{l} m_z^2 = 1/3(2I + 1)(I + 1)$ and $\sum_{i=m}^{n} = n - m + 1$), this gives Curie's law:

$$M_0 = \frac{N\gamma^2\hbar^2 B_0 I(I+1)}{3k_B T} \tag{1.15}$$

The magnetisation of the sample depends on the spin population difference, following Boltzmann's distribution law. Because of the very small population differences, sensitivity in NMR experiments can be a serious problem, especially for lowly concentrated samples or very small volume samples. As we will discuss in the next section, several approaches to enhance sensitivity can be explored. In the stripline approach, we address sensitivity enhancement by miniaturisation of the NMR coil.

1.3 SNR enhancement of the NMR experiment

The sensitivity of NMR spectroscopy is relatively low, compared to other spectroscopic techniques. The limit of detection (LOD) is a value representing the amount of sample needed for a certain SNR. In NMR, the LOD can be defined as the amount of spins that are required to give a SNR of 1 in a bandwith of 1 Hz[9]. The LOD of NMR is orders of magnitude less than for example infrared (IR), UV-vis, fluorescence or mass spectroscopy[10, 11]. As shown above, this is a result of the Boltzmann distribution of the nuclei and the small energy differences between energy levels. In the following sections, from an expression for the SNR, the factors that can increase NMR sensitivity can be deduced. Miniaturisation of the rf coil is one of the approaches that is discussed.

1.3.1 The signal-to-noise ratio (SNR)

After applying an rf pulse ($90°$ or $\pi/2$ pulse) to the polarised spin system in the sample, precession of the magnetisation $\boldsymbol{M}$ occurs while the magnetisation returns back to its equilibrium aligned with the $\boldsymbol{B}_0$ magnetic field. The rotating magnetic dipoles in the sample induce an electromotive force (emf ξ), which is the signal that can be detected in the rf coil. The value of the SNR is the maximum intensity of this NMR signal divided by the root-mean-square value (r.m.s.) of the noise.
The induced emf ξ is described by Faraday's law as the change in magnetic flux Φ,

which is the integral of the magnetic field over surface area A of the loop:

$$\xi(t) = -\frac{d\Phi}{dt} = -\frac{d}{dt}\int_A \boldsymbol{B}(\boldsymbol{r},t)\cdot d\boldsymbol{a} \tag{1.16}$$

Hoult and Richards[12, 13] applied the principle of reciprocity to the NMR experiment to derive an expression for the emf ξ in an NMR experiment. The reaction of the receiving coil to the magnetic field produced by the nuclear magnetic moments in the sample is difficult to calculate, but as the reciprocity principle states it is the same as passing unit current through the coil and measure the magnetic field produced at a given point in the sample. The precessing magnetisation of a single magnetic dipole is $\boldsymbol{m}$, which is a infinitesemal loop with cross-sectional area A, and the magnetic moment $\boldsymbol{m} = iA$. The magnetic field induced in the coil by unit current is B_1/i.

$$\xi(t) = -\frac{d}{dt}(\frac{\boldsymbol{B}_1}{i}\cdot\boldsymbol{m}(\boldsymbol{r},t)) \tag{1.17}$$

For a sample of volume V_s, the emf ξ can be calculated by integration over the whole sample:

$$\xi(t) = -\int_{sample}\frac{d}{dt}\frac{\boldsymbol{B}_1}{i}\cdot\boldsymbol{M}(\boldsymbol{r},t)dV_s \tag{1.18}$$

A scaling factor k_0 is introduced to include the inhomogeneity of the B_1 field produced by the probe, so that B_1 can be considered constant over the sample volume. The integration then gives:

$$\xi(t) = -k_0\omega_0\frac{B_1}{i}\,M_0V_s\cos\omega_0 t \tag{1.19}$$

where the Larmor frequency is ω_0. The time dependence of the signal is $\exp(i\omega t)$, but only the real part is used for the expression of the emf ξ. For the maximum signal intensity, at $t = 0$, this factor is 1.
Then, substituting Curie's law (1.15) for the magnetisation M_0, the maximum signal S induced in the receiving coil directly following excitation of a sample is given by

$$S = \frac{k_0\frac{B_1}{i}V_sN\gamma\hbar^2I(I+1)\omega_0^2}{3k_BT_{sample}} \tag{1.20}$$

In an NMR experiment random noise is present, which generally falls in three cat-

egories: thermal noise, shot noise, flicker noise. The thermal noise due to random motion of charge carriers from the coil and the sample at a certain temperature T is the dominant source of noise [14, 15].
Thermal noise is defined by the Nyquist formula as:

$$N_R = \sqrt{4k_B T_{coil} R \Delta f} \tag{1.21}$$

where, R is the resistance of the conductor and Δf is the band width of the NMR experiment.
Combining (1.20) and (1.21), the SNR is:

$$SNR = \frac{S}{N_R} = \frac{k_0 \frac{B_1}{i} V_s N \gamma \hbar^2 I(I+1)\omega_0^2}{(k_B T_{sample} 3\sqrt{2})\sqrt{4k_B T_{coil} R \Delta f}} \tag{1.22}$$

1.3.2 Approaches for SNR enhancement

The expression for the SNR of the NMR experiment Eq.(1.22) shows some factors which can be influenced to achieve a higher sensitivity. In general, approaches to increase the NMR signal can be found in hardware design and hyperpolarisation NMR, some recent reviews [16, 17, 18] cover this topic in detail focussing on microcoil NMR.
Many developments that aim at increasing the SNR are involved with the hardware, i.e. probe and magnet. Stronger magnets, which increases the B_0 field, are continuously being developed, since a higher field contributes to a higher SNR: $SNR \propto \omega^2$. Another strategy is minimising the noise, which can be achieved by lowering the temperature of the preamplifiers and the rf coil ($SNR \propto 1/\sqrt{T_{coil}}$) [19, 20]. In conventional NMR, cryoprobes are commonly used operating at around 20K, which increases the SNR by a factor 2-4 up to 20 [17, 21].
An alternative approach is the development of hyperpolarisation techniques. In dynamic nuclear polarisation (DNP), polarisation transfer is induced from unpaired electrons, with a higher magnetic moment, to other nuclei. Microwave irradiation of the (cooled) sample combined with radicals is required, which can give a enhancement of 660 for protons [22, 23, 24]. In the recent years DNP has become a commercially available technique, however much research is still devoted to improving the technique and a drawback is the need of special chemicals and microwave setup, and also the cooling, melting and shuttling of the sample is challenging. Several related techniques that use polarisation transfer to increase sensitivity are (photo) chemically induced DNP

(CIDNP), spin-exchange optical pumping (e.g. SPINOE) and parahydrogen induced polarisation (PHIP, e.g. SABRE)[25]. In these techniques the high polarisation that comes from radicals produced by (photo)chemical reactions, Rb excited by polarised light or parahydrogen is transferred to NMR nuclei in the sample by chemical reaction, via spin exchange with a nobel gas (^{3}He or ^{129}Xe), hydrogenation of the sample or temporarily complex formation with metal centre, respectively. Although these technique are in development, promising signal enhancements are obtained.

Furthermore, the coil should be designed such as to fit the highest amount of sample, and maximise N in Eq.(1.22). The observe volume of the probe is the effective detection volume from which the signal is observed V_{obs}. The observe factor can then be defined as the ratio between V_{obs} and the total volume of sample $f_{obs} = V_{obs}/V_{total}$. The filling factor is the fraction of coil volume occupied by the observed sample $f_{fill} = V_{obs}/V_{coil}$. Both f_{fill} and f_{obs} should be maximised for highest efficiency of the coil[26]. In microcoil NMR, often the coil is designed so that f_{fill} is optimised, and can be larger than in conventional NMR where an airgap between the sample and saddle coil is present. In the case of mass-limited sample, also f_{obs} can be optimised, when the coil matches the sample f_{obs} can be up to 1, without needing to dilute the sample. In a microfluidic setup a large part of the sample is outside of V_{obs}, namely in the pumping system capillaries, therefore f_{obs} is much less than 1. However, a microcoil in a microfluidic setup serves a different purpose, such as matching the size of the chemical setup (microreactor) or analysing unstable samples.

In remote detection NMR[27, 28, 29], a microfluidic setup is used with two separate coils, the encoding coil and detection coil. A large sample volume is polarised and encoded by gradients, whereas the observe factor can be high when acquiring the data in a smaller microcoil volume.

When a limited amount of sample is available, compared to the conventional volume of 500 μl, it is beneficial to sensitivity to match the coil to the sample. The coil geometry influences the SNR via the factor B_1/i, the magnitude of the magnetic field B_1, produced in the sensitive area of the coil by unit current i. B_1/i reflects the sensitivity of the probe and depends on the coil geometry by 1/d, as we will see in the next section. Therefore, miniaturisation is another option to increase sensitivity, when all other factors remain the same.

1.4 Increased mass sensitivity by microcoil NMR

The mass m of a sample may be limited in cases such as natural or expensive products. Sample concentrations C may be limited if solubility is low or, for example, in biological fluids. For both limitations, gaining sufficient sensitivity requires a different approach. The sensitivity of the NMR probe can be defined in terms of mass sensitivity S_m or concentration sensitivity S_C[26, 30], which are normalised by the acquisition time t_a

$$S_m = \frac{SNR}{m \times \sqrt{t_a}} \tag{1.23}$$

and

$$S_C = \frac{SNR}{C \times \sqrt{t_a}} \tag{1.24}$$

S_C and S_m are related by the observed sample volume V_{obs}:

$$S_C = V_{obs} S_m \tag{1.25}$$

For a certain sample of mass m_{obs} in V_{obs}, $m_{obs} = CV_{obs}$. Increasing the observe volume in a probe for a sample of fixed concentration, increases its concentration sensitivity S_C, as the amount of spins N in V_{obs} increases and the SNR is related to number of spins N and volume V_{obs} in Eq. (1.22).
However, for fixed mass, N and V_{obs} cannot be increased if the available sample volume is similar or smaller than the observed volume V_{obs}. As decreasing the coil increases the transverse magnetic field strength per unit volume and thereby the SNR per unit mass, matching the coil to fit the size of the sample increases the SNR. Therefore, for a small mass-limited sample miniaturisation of the coil is a way to increase sensitivity S_m.

1.4.1 RF microcoils

A saddle coil, typically used in conventional liquid-state NMR, gives a very homogeneous B_1 field, but this design is difficult to miniaturise. For microcoil NMR, other designs have been developed: a solenoid, flat helical or stripline is a common design, shown in Figure 1.4. Several reviews discuss the principles and designs of NMR mi-

crodetectors[9, 16, 18, 21, 31, 32]. In the design of a microcoil, the size of the coil matching the sample, and the observe and filling factor have to be considered. Furthermore, the SNR is influenced by the geometry of the coil: by factor B_1/i and the resistance R (see Eq.(1.22)). The sensitivity of a coil, expressed as B_1/i, can be calculated for different coil types using Biot-Savart's law. In general, the SNR scales roughly with 1/d, the inverse diameter of the coil, as a smaller diameter gives a relative higher transverse magnetic field strength in the coil. Some examples of the possible NMR microcoil designs are discussed next.

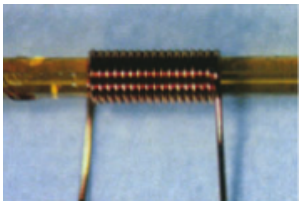

(a) Hand-wound Solenoid, from Ref. 33

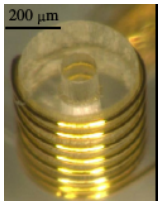

(b) Microfabricated Solenoid, from Ref. 34

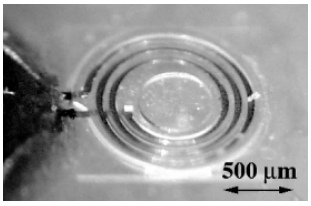

(c) Helical planar coil, from Ref. 35

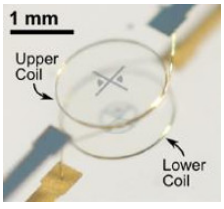

(d) Helmholtz coil, from Ref. 36

(e) Stripline coil

(f) Needle coil, from Ref. 37

Figure 1.4: NMR microcoil designs

Solenoids

The first solenoidal microcoils were being used for in-vivo NMR spectroscopy in 1966[38]. In 1994, the first high-resolution solenoidal microcoils were developed by Sweedler et al[33, 39, 40]. A simple solenoid microcoil consists of a copper wire hand-wound around a capillary containing the sample. In this arrangement the solenoid coil can be very efficiently used so that the filling factor is large. Also, the solenoid generates a high B_1 field per unit current. However, when the sample is very close to the copper coil, line broadening may occur due to magnetic susceptibility mismatch between

coil, sample and medium. When the coil is immersed in susceptibility matching fluid (eg. FC-43) a uniform medium surrounds the sample and a good resolution can be obtained[41]. Alternatively, zero-susceptibility wire solenoids have been developed[42], which also improves sensitivity and resolution.
Peck et al.[15] analysed the SNR and the resistance R of a microsolenoid coil.The sensitivity B_1/i of a coil can be calculated for different coil types using Biot-Savart's law. At the center of a solenoid, a simple expression can be found:

$$\frac{B_1}{i} = \frac{\mu_0 n}{d\sqrt{1+[h/d]^2}} \tag{1.26}$$

where μ_0 is the permeability of free space, n is the number of turns of the solenoid, h is the coil length and d is the coil diameter. When the ratio h/d is fixed, the factor B_1/i is therefore relative to $1/d$, showing that the sensitivity of a coil is proportional to the inverse diameter.
The current density of an alternating high frequency current is concentrated at the surface of the material, decreasing exponentially with increasing distance from the surface, which is known as the skin effect. For copper at 600 MHz, the skin depth δ is 2.7 μm, which is the value where the current density is at 1/e of its maximum value at the surface. Peck[15] shows that when the diameter of the wire is much larger than the skin depth δ, the resistance of the coil is determined by the proximity effect and skin effect. The proximity effect is the increased resistance arising from interactions between the windings of the coil. For the regime where the coil diameter larger than the skin depth, the SNR for constant coil length to coil diameter ratio:

$$SNR \approx \frac{\omega^{7/4}}{d_{coil}} \tag{1.27}$$

When the diameter of the coil is smaller than the skin depth, the current is uniform and can be approximated by an AC current. The SNR in this case:

$$SNR \approx \frac{\omega^2}{\sqrt{n d_{coil}}} \tag{1.28}$$

Furthermore, Hoult and Richards[12] showed a comparison of a solenoid and saddle coil under similar conditions, concluding that a solenoid has a three times higher performance. This is explained by the fact that the magnetic energy is not as efficiently stored in the saddle coil, due to its open structure, and therefore the flux in the sample

is not as high as in a solenoid.
Although the microsolenoid gives good results, downscaling of the coil is difficult and results in fragile structures, hand-winding of the coil limits the miniaturisation. Recently, attempts to deal with this limitation involves the development of microfabricated solenoids, which make use of an automated microwirebonder[43, 44]. A solenoid microcoil is fabricated by a wirebonder, wrapping the wire around a SU-8 cylinder, which is also the sample holder. The filling factor is not as high as in the hand-wound coil and the coil is rather large (1mm outer diameter). Meier et al[34] used an automated wirebonding technique in combination with a microfabricated microfluidic channel for the sample to flow through. A relatively large linewidth was observed, probably due to susceptibility broadening. Wirebonding around a support decreases the filling factor, but Kamberger et al[45] showed that it is also possible to use a sacrificial inner support, which is dissolved after a pmma support is applied at the outside of the coil. The detection volume can be used up to 100%. Although the reported sensitivity was comparable to other designs, the linewidth is relatively large.
A variation of the microfabricated solenoid is a Helmholtz coil, constructed as a double solenoid coil where the sample is placed between the coils. Spengler et al. [36, 46] developed a Helmholtz microcoil, consisting of two 1.5 winding solenoid coils, made by an automated wirebonder and microfabrication techniques. The sample is loaded via a disposable insert. This design aims to combine the possibilities by microfabrication with the sensitivity and resolution of a solenoid.

Planar coils

Adjusting the microcoil design towards a 2D structure, a planar helical coil can be regarded, see Figure 1.4c. Peck et al.[47] showed the results for the first planar microcoils. Since the planar coil can be fabricated by photolithographic techniques, these microcoils can be more easily fabricated in batch and scaled down in size. The sample can be put in a capillary on top of the coil or in a microfluidic setup beneath the coil. Unfortunately, the planar helix usually shows a disappointing sensitivity and resolution. The sensitive area close to the coil experiences a very inhomogeneous B_1 field, and further from the coil the field is more homogeneous but becomes very weak. Also, susceptibility mismatch plays a role in linebroadening when the sample is close to the coil. Stocker[48] shows that enclosing the coil and sample in a susceptibility matching fluid (FC-43) improves resolution. The sensitivity and resistance of a flat helical coil

are more difficult to calculate than for a solenoid, but as it was shown analytically by Eroglu[49], increasing the number of turns increases the center field strength, although every added winding contributes less. However, more windings increases the resistance, and the proximity effect becomes more dominating. Simulations of the induced field[9] show that inhomogeneities arise from Eddy currents in the center windings due to outer windings. In conclusion, sensitivity remains lower than a solenoid[32].

Nevertheless, the planar coil is often used, most importantly because the planar coil is compatible to microfabrication techniques and can be coupled to microfluidics [50]. Wensink et al[51] used a planar coil integrated with a microfluidic chip for analysis of reaction kinetics of imine formation from benzaldehyde and aniline. More recently, Gomez[52] used planar coils integrated with microreactor setup to efficiently study reaction kinetics, in a single on-flow experiment. The use of microtechnology decreases the amount of time and compounds necessary for analysing the reaction. Fratila[53] used a non-resonant planar spiral coil which can be used to detect nuclei in a broad frequency range, enabling heteronuclear 2D experiments on a micofluidic sample.

In order to improve homogeneity Ryan et al[54] developed a contactless, inductively coupled planar coil. Bridging connections that disturb the homogeneity can be left out. A microfluidic channel for the sample is below the coil, and has a detection volume of 1.2 μl. This microcoil setup has a resolution of 4.5 Hz and a sensitivity comparable to the stripline used in Ref. 55, 56.

Also, Helmholtz coils can improve homogeneity of the magnetic field and can be constructed from planar coils. Linewidth and sensitivity can be much increased comparing planar coils to planar Helmholtz coils[57]. An example is a planar Helmholtz coil patterned on both sides of a sample chamber made of two bonded substrates[58]. Another rectangular planar coil in Helmholtz arrangement, patterned on two substrates separated by spacer beads was demonstrated by Syms et al[59].

Leidich et al[60] went one step further by also rotating the sample to increase resolution, a rotating 5-40 nl sample in a capillary in a Helmholtz coil improved resolution up to less than 3 Hz.

Furthermore, the planar microprintable coil opens up possibilities in medicine, several implantable planar microcoils have been developed[61, 62, 63]. Similar to the planar coil is a needle coil, a one-turn planar coil printed on a substrate (silicon or plastic) which is used as a shaft and has applications in real-time NMR spectroscopy and imaging in cancer surgery[37, 64]. For all these type of coils it remains a challenge to have a good resolution, minimise susceptibility effects, and increase sensitivity.

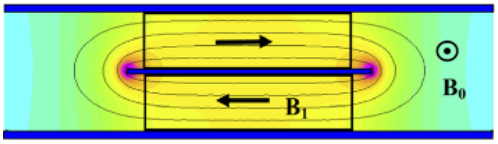

Figure 1.5: Schematic cross-section of the stripline design, from Ref. 66. The strength of the $\boldsymbol{B_1}$ rf field is highest (magenta) at the edges of the strip and lowest (blue) at the outer regions. In the middle part, indicated by the rectangles, an intermediate $\boldsymbol{B_1}$ (yellow) is present, which is homogeneous within 10%. In that region, the field lines run almost parallel to the surface, forced between strip and boundary planes.

Striplines

The previously discussed microcoil designs, typically involved a wound or spiral coil. For NMR spectroscopy, a magnetic rf field $\boldsymbol{B_1}$ perpendicular to $\boldsymbol{B_0}$ is required. In the simplest case, this can be accomplished by using a long metal wire parallel to the $\boldsymbol{B_0}$ field. A current flowing in the surface layer (skin depth δ) of this wire induces a cylindrical $\boldsymbol{B_1}$ field around the wire, which diminishes with the radial distance from the wire r. When the length of the wire relative to its diameter can be considered infinitely long, a very homogeneous magnetic field is present. This arrangement gives a poor sensitivity, since the field strength diminishes with r. In a coaxial arrangement (such as toroid or coaxial probe[65]), the field lines are confined within an outer boundary hollow wire. This increases the sensitivity of the coil, but inhomogeneity of the field increases as well, therefore a low resolution results. However, when the wire is replaced by a flat strip, the field lines are arranged parallel to the strip on both sides, and a very homogeneous field is achieved. The $\boldsymbol{B_1}$ field is enclosed between boundary planes, so that a high $\boldsymbol{B_1}$ rf field is confined to a small volume where one puts the sample, therefore high sensitivity is achieved. Figure 1.5 shows a schematic of the $\boldsymbol{B_1}$ field in cross-section of the stripline, the detection volume is within the region of 10 % field homogeneity.

A microstrip transmission line resonator for MRI was introduced in 2001 by Zhang et al[67]. The stripline NMR configuration makes use of a constriction to select the detection area, was introduced in 2004[31]. In 2007, a prototype stripline NMR chip was established[66], and subsequent stripline NMR chips will be discussed in the next section.

For a stripline configuration, the B_1/i factor and resistance R can be calculated[66].

From Ampere's law:

$$\frac{B_1}{i} = \frac{\mu_0}{2w + 2d} \tag{1.29}$$

with w is the width of the strip and d is the distance beween the ground planes.
The resistance R of the stripline coil is determined by the length L and width w of the constriction, with the skin depth δ:

$$R = \rho_{copper} \frac{L}{2 * w * \delta} \tag{1.30}$$

Comparing these figures with the solenoid geometry a $\sqrt{2}$ larger SNR is expected, so it can be concluded that the stripline is a more sensitive design for the same experiment. In microcoil design, the sample is close to the rf coil and so local variations of the B_0 field arising from susceptiblity mismatch can have a detrimental effect on the attainable resolution. The relatively long copper stripline structure parallel to the B_0 field, facilitates a high resolution, since an infinitely long homogeneous structure parallel to the B_0 field does not influence homogeneity of the field[66]. In practice, the stripline copper structure has some effect on the resolution, but optimisation of stripline geometry and susceptibility matching of the gap between the copper structures on the substrate minimises susceptibility broadening, which further increases resolution. In Chapter 3 it is shown that the resolution is very sensitive to irregularities of the substrate.
Badilita et al[32] give an overview, which compares experimental results of sensitivity and resolution for selected microcoils as reported in literature, showing very wide ranging values for resolution from 2600 to 1.8 ppb (parts per billion). The stripline NMR chip mentioned in this overview has a 80 ppb (50 Hz) linewidth[66]. However, the resolution of stripline chips has improved since, by optimisation of the design, reaching a linewidth of 0.7 Hz (1.2 ppb)[56]. The current stripline chips, demonstrate typical linewidths of around 2 Hz (3 ppb), and when using a plug of ethanol even 0.5 Hz (8.0 ppb) can be obtained, as shown in Chapter 2. These values are among the highest resolutions reported in the overview.
Besides the stripline NMR chips used in this thesis, recently also a similar double-stripline has been developed by Utz et al[68, 69]. This chip has a larger detection volume 2 μl, the design focuses on an integrated microfluidic setup, and the geometry was optimised on sensitivity and rf homogeneity. A good resolution (1.7 Hz) and excellent

sensitivity is obtained. The microslot probe is a variation on the planar waveguide design, where a hole in the strip is used as a detection area, however, it does not use ground planes to homogenise the B_1 field. A 25 nl volume microslot coil was developed by Maguire et al.[70], and a 10 nl detection volume design by Krojanski et al.[71]. Furthermore, a double microstripline consisting of two parallel stripline structures with the sample in between, was succesfully used for MRI microscopy[72].

Characterisation

The ideal NMR rf coil combines high resolution with high sensitivity. High resolution ensures that the resonance frequency of the nuclei is precisely determined, and results in a small linewidth, standardized by the full width of the peak at half maximum (FWHM in Hz). The efficiency of the probe is characterised by the $\boldsymbol{B_1}$ rf field in the detection volume, specifically the rf field strength which is determined by the B_1/i factor, and the rf homogeneity (A_{810}/A_{90}), which is of importance for complex pulse sequences. Rf field strength and rf homogeneity are obtained from a nutation experiment, see Figure 1.2. The sensitivity is measured by the SNR of a spectrum or the FID, or the limit of detection (LOD), which is related to the single-scan SNR in the time domain:

$$LOD = \frac{N_S}{SNR_{t_{SS}} * \sqrt{\Delta SW}} \tag{1.31}$$

taking into account the amount of spins in the detection volume (N_S) and the bandwidth of the experiment ΔSW.
Badilita et al.[32] give an overview of resolution and normalised LOD for 20 microcoil NMR detectors. Finch et al.[68] compare the concentration LOD calculated from the same results. Both comparisons confirm that roughly the smaller the detector diameter, the lower the LOD.

1.4.2 Overview of stripline NMR chips

As shown above a miniaturised detection coil gives a better mass sensitivity. The stripline NMR microcoil aims for a high resolution with high sensitivity for limited detection volume. In this work, three generations of stripline NMR chips were used, shown in Figure 1.6. For clarity here an overview is given. Fabrication details of the chips can be found in Ref. 73 and Appendices B.1 and B.2. In this section, some

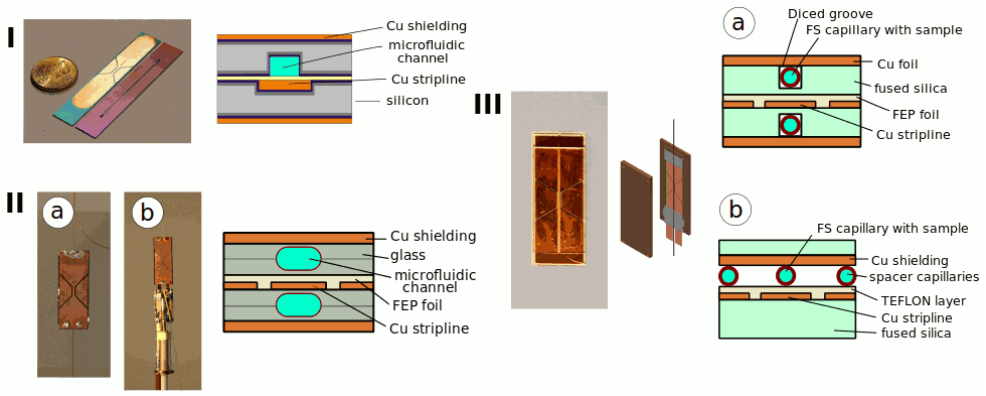

Figure 1.6: Three generations of stripline NMR chips

practical aspects are discussed.

In general, the stripline coil is a copper structure electroplated on a silicon, glass or fused silica (FS) substrate. The choice of a substrate depends on processing aspects (as bonding, etching, dicing may be needed), electronic properties of the material (dielectric permittivity ϵ_r, and $\tan\delta$ representing losses at the substrate) and moreover, the material should be proton-free so that the substrate does not contribute to the spectrum.

After the first prototype stripline NMR chip gave promising results[66], the chip (I) in Figure 1.6 was developed by Bart et al.[56, 73] The chip (I) is made of two FEP bonded silicon layers with amorphous silicon (α-Si) deposition for surface passivation to prevent losses at the substrate. One layer contains a stripline structure with the detection volume defined by the constriction (1x5mm) in the middle, where the B_1 field is high. The other silicon layer contains an etched microfluidic channel (300 μm deep) with inlet and outlet through this substrate layer, and a deposited copper shielding plane at the outer side. The sample volume is 1.125 μl. The chip was used for preliminary acetylation reaction kinetics experiments and small volume sample analysis[55]. Unfortunately, the sensitivity of the chip was lower than expected, which was attributed to losses in the substrate. Moreover, as the analyte came directly in contact with the copper structure on the chip, and the microfluidic inlet and outlet components were screwed onto the backside of the chip, over time the chip's performance deteriorated due to fracture and damage.

Bart's thesis[73] describes the development of a new generation glass chips (II). Here, borosilicate glass was used as a substrate, which is easier to process and the sensitivity

was expected to be less affected by losses at the surface of the material. On both sides of the stripline structure a isotropically etched microfluidic channel was present, so that the two microfluidic channels can be used simultaneously, for example for doubling the detection volume or deuterium locking. Standard FS capillaries are glued into the holes on top and bottom of the chip to serve as an inlet and outlet, which subsequently could straightforwardly be connected to a standard microfluidic setup. Two versions of this design have been produced. Figure 1.6 IIa shows the first chip with a thickness of 630 μm and the detection volume 245 nl per channel. This chip is used in Chapter 3. The thickness of the second chip IIb is 460 μm, the detection volume for one channel is 165 nl. This chip is used in Chapters 3 to 6. Unfortunately, the sensitivity was not as high as aimed for as ionic species in borosilicate glass lead to dielectric losses. Furthermore, to optimise the filling factor very thin substrates were used in the chips, which made the chips very fragile. Leakages occurred in the substrates and microfluidic connections, after which the chips could not be operated anymore.

Both previous designs were affected by the microfluidic contact with analyte, therefore it was concluded that for durability a more robust design is needed in which contact with the sample is prevented. At the same time, to ensure high sensitivity the use of a low loss substrate is crucial, which led to the choice of fused silica (FS) as a substrate in chips (III). A disadvantage of FS, however, is that the material is more difficult to process. Therefore, a different design is used in which processing steps such as ething are unnecessary. The sample is contained in replacable FS capillaries, which are placed into the chip so that the fluidic sample does not come into contact with the material of the chip. This does not only prevent leakages in the microfluidic connections, but also enables experiments on small samples in a static plug. A replacable capillary as a sample holder gives many advantages in flexibility of the experiment, purity of the sample and durability of the chip, but as a disadvantage, the filling factor is decreased in comparison to the previous designs.

Two versions of this chip were made, see Figure 1.6 III. Version a) consists of two FEP bonded FS layers, on one of the layers a copper stripline structure has been deposited. Both halves have a diced microfluidic channel through which a FS capillary can be placed, containing the sample in a plug or connected to microfluidics. Copper shielding is applied surrounding the chip by using a copper foil. This chip with diced channels is used in Chapter 3, fabrication details can be found in Appendix B.2. Although good sensitivity was obtained, the diced channel appears to be too rough, resulting in

irregularities and disturbances in the homogeneity of the field, affecting the resolution. Therefore, a second design was developed, version b) which has the same substrate but an alternative sample holder. Here, FS capillaries function as spacers between stripline and shielding replacing the FS substrate with the diced channel. Copper shields are deposited on FS substrate to add more stability. For support and electronics, a copper box contains the chip and sample. This chip gave both high sensitivity and good resolution and is used in Chapter 2 on small volume samples.

1.5 Conclusion

NMR spectroscopy is a powerful analytical tool, based on the precise measurement of the resonance frequencies of nuclear spins. As these NMR frequencies are influenced by structural properties of the molecule, a wealth of information is contained in the NMR spectrum. In order to measure an NMR spectrum, the sample is placed in a static magnetic field, which polarises the nuclear spins. After applying an rf pulse, the collective magnetisation vector precesses with Larmor frequency ω_0 in the magnetic field, which induces a signal containing frequency information. Since the energy difference between energy levels is very small, and the population differences are governed by the Boltzmann distribution, the sensitivity of the NMR spectroscopy experiment is relatively low. For several applications, such as analysis of natural products, high throughput screening or reaction kinetics, it can be a problem to acquire sufficient signal in a given amount of time. Sensitivity enhancement is therefore a much investigated topic for these kind of applications. The sensitivity of an NMR experiment can be influenced by different factors, including hardware, non-Boltzmann distribution and miniaturisation. As the SNR relates to B_1/i which is proportional to the inverse diameter of the coil, the smaller the coil the higher the sensitivity per unit mass. So for mass-limited samples, matching the size of the NMR coil to the sample increases sensitivity, which is realised in microcoil NMR. Furthermore, coupling of a microNMR coil to a microfluidic device enables continuous flow measurements. One of the possible microcoil designs is the stripline NMR chip. In this thesis, the stripline NMR chip is applied for measurement of mass-limited samples (Chapter 2), continuous flow NMR (Chapter 3), *in situ* reaction kinetics (Chapter 4 and 5) and hyphenation of electrochemistry to microNMR (Chapter 6).

References

[1] T. D. W. Claridge, *High-resolution NMR techniques in organic chemistry*, vol. 27 of *Tetrahedron Organic Chemistry*. Elsevier, 2009.

[2] R. S. Macomber, *A Complete Introduction to Modern NMR Spectroscopy*. Wiley-Interscience, 1997.

[3] M. H. Levitt, *Spin Dynamics: Basics of Nuclear Magnetic Resonance*. Wiley, 2001.

[4] O. Zerbe and S. Jurt, *Applied NMR Spectroscopy for chemists and life scientists*. Wiley-VCH, 2014.

[5] J. T. Arnold, S. S. Dharmatti, and M. E. Packard, "Chemical effects on nuclear induction signals from organic compounds," *J. Chem. Phys.*, vol. 19, p. 507, 1951.

[6] G. Bodenhausen and D. Ruben, "Natural abundance nitrogen-15 NMR by enhanced heteronuclear spectroscopy," *Chem. Phys. Lett.*, vol. 69, p. 185, 1980.

[7] A. Bax and S. Subramanian, "Sensitivity-enhanced two-dimensional heteronuclear shift correlation NMR spectroscopy," *J. Magn. Reson.*, vol. 67, p. 565, 1986.

[8] A. Bax and M. Summers, "^{1}H and ^{13}C assignments from selectivity-enhanced detection of heteronuclear multiple-bond connectivity by 2D multiple quantum NMR," *J. Am. Chem. Soc.*, vol. 108, p. 2093, 1986.

[9] A. P. M. Kentgens, J. Bart, P. J. M. van Bentum, A. Brinkmann, E. R. H. van Eck, J. G. E. Gardeniers, J. W. G. Janssen, P. Knijn, S. Vasa, and M. H. W. Verkuijlen, "High-resolution liquid- and solid-state nuclear magnetic resonance of nanoliter sample volumes using microcoil detectors," *J. Chem. Phys.*, vol. 128, p. 052202, 2008.

[10] A. Webb, "Radiofrequency coils in magnetic resonance," *Prog. Nucl. Magn. Reson. Spectrosc.*, vol. 31, p. 1, 1997.

[11] M. E. Lacey, R. Subramanian, D. L. Olson, A. G. Webb, and J. V. Sweedler, "High-Resolution NMR spectroscopy of sample volumes from 1 nl to 10 μL," *Chem. Rev.*, vol. 99, no. 10, p. 3133, 1999.

[12] D. Hoult and R. Richards, "The signal-to-noise ratio of the nuclear magnetic resonance experiment," *J. Magn. Reson.*, vol. 24, p. 71, 1976.

[13] D. Hoult, "The principle of reciprocity in signal strength calculations - a mathematical guide," *Concepts Magn. Reson.*, vol. 12, p. 173, 2000.

[14] T. L. Peck, *Sensitivity and noise analysis of solenoidal coils for nuclear magnetic resonance microscopy*. PhD thesis, University of Illinois at Urbana Champaign, USA, 1992.

[15] T. Peck, R. Magin, and P. Lauterbur, "Design and analysis of microcoils for NMR microscopy," *J. Magn. Reson., Ser. B*, vol. 108, p. 114, 1995.

[16] R. M. Fratila and A. H. Velders, "Small-volume nuclear magnetic resonance spectroscopy," *Annu. Rev. Anal. Chem.*, vol. 4, p. 227, 2011.

[17] A. Webb, "Radiofrequency microcoils for magnetic resonance imaging and spectroscopy," *J. Magn. Reson.*, vol. 229, p. 55, 2013.

[18] S. S. Zalesskiy, E. Danieli, B. Blűmich, and V. P. Ananikov, "Miniaturization of NMR systems: Desktop spectrometers, microcoil spectroscopy, and *NMR on a Chip* for chemistry, biochemistry, and industry," *Chem. Rev.*, vol. 114, p. 5641, 2014.

[19] M. Spraul, A. S. Freund, R. E. Nast, R. S. Withers, W. E. Maas, and O. Corcoran, "Advancing NMR sensitivity for LC-NMR-MS using a cryoflow probe: application to the analysis of acetaminophen metabolites in urine," *Anal. Chem.*, vol. 75, p. 1536, 2003.

[20] W. W. Brey, A. S. Edison, R. E. Nast, J. R. Rocca, S. Saha, and R. S. Withers, "Design, construction, and validation of a 1-mm triple-resonance high-temperature-superconducting probe for NMR," *J. Magn. Reson.*, vol. 179, p. 290, 2006.

[21] C. J. Jones and C. K. Larive, "Could smaller really be better? Current and future trends in high-resolution microcoil NMR spectroscopy," *Anal. Bioanal. Chem.*, vol. 402, p. 61, 2012.

[22] A. Abragam and M. Goldman, "Principles of dynamic nuclear polarisation," *Rep. Prog. Phys.*, vol. 41, p. 395, 1978.

[23] T. Maly, G. T. Debelouchina, V. S. Bajaj, K.-N. Hu, C.-G. Joo, M. L. Mak-Jurkauskas, J. R. Sirigiri, P. C. A. van der Wel, J. Herzfeld, R. J. Temkin, and R. G. Griffin, "Dynamic nuclear polarization at high magnetic fields," *J. Chem. Phys.*, vol. 128, p. 052211, 2008.

[24] Q. Zhe Ni, E. Daviso, T. V. Can, E. Markhasin, S. K. Jawla, T. M. Swager, R. J. Temkin, J. Herzfeld, and R. G. Griffin, "High frequency dynamic nuclear polarization," *Acc. Chem. Res.*, vol. 46, no. 9, p. 1933, 2013.

[25] J. H. Lee, Y. Okuno, and S. Cavagnero, "Sensitivity enhancement in solution NMR: Emerging ideas and new frontiers," *J. Magn. Reson.*, vol. 241, p. 18, 2014.

[26] D. L. Olson, J. A. Norcross, M. O'Neil-Johnson, P. F. Molitor, D. J. Detlefsen, A. G. Wilson, and T. L. Peck, "Microflow NMR: Concepts and capabilities," *Anal. Chem.*, vol. 76, p. 2966, 2004.

[27] E. E. McDonnell, S. Han, C. Hilty, K. L. Pierce, and A. Pines, "Nmr analysis on microfluidic devices by remote detection," *Anal. Chem.*, vol. 77, p. 8109, 2005.

[28] T. Z. Teisseyre, J. Urban, N. W. Halpern-Manners, S. D. Chambers, V. S. Bajaj, F. Svec, and A. Pines, "Remotely detected NMR for the characterization of flow and fast chromatographic separations using organic polymer monoliths," *Anal. Chem.*, vol. 83, p. 6004, 2011.

[29] E. Harel, C. Hilty, K. Koen, E. E. McDonnell, and A. Pines, "Time-of-flight flow imaging of two-component flow inside a microfluidic chip," *Phys. Rev. Lett.*, vol. 98, p. 017601, 2007.

[30] A. Webb, "Microcoil nuclear magnetic resonance spectroscopy," *J. Pharm. Biomed. Anal.*, vol. 38, p. 892, 2005.

[31] P. J. M. van Bentum, J. W. G. Janssen, and A. P. M. Kentgens, "Towards nuclear magnetic resonance m-spectroscopy and μ-imaging," *Analyst*, vol. 129, p. 793, 2004.

[32] V. Badilita, R. C. Meier, N. Spengler, U. Wallrabe, M. Utz, and J. G. Korvink, "Microscale nuclear magnetic resonance: a tool for soft matter research," *Soft Matter*, vol. 8, p. 10583, 2012.

[33] D. L. Olson, T. L. Peck, A. G. Webb, R. L. Magin, and J. V. Sweedler, "High resolution microcoil 1H-NMR for mass-limited, nanoliter-volume samples," *Science*, vol. 270, p. 1967, 1995.

[34] R. C. Meier, J. Höfflin, V. Badilita, U. Wallrabe, and J. G. Korvink, "Microfluidic integration of wirebonded microcoils for on-chip applications in nuclear magnetic resonance," *J. Micromech. Microeng.*, vol. 24, p. 045021, 2014.

[35] C. Massin, G. Boero, F. Vincent, J. Abenhaim, P. Besse, and R. Popovic, "High-Q factor rf planar microcoils for micro-scale NMR spectroscopy," *Sens. Actuators, A*, vol. 97-98, p. 280, 2002.

[36] N. Spengler, A. Moazenzadeh, R. C. Meier, J. G. Korvink, and U. Wallrabe, "Microfabricated Helmholtz coil featuring disposable microfluidic sample inserts for applications in nuclear magnetic resonance," *J. Micromech. Microeng.*, vol. 24, p. 034004, 2014.

[37] R. R. A. Syms, M. M. Ahmad, I. R. Young, D. Gilderdale, and D. J. Collins, "Micro-engineered needle micro-coils for magnetic resonance spectroscopy," *J. Micromech. Microeng.*, vol. 16, p. 2755, 2006.

[38] E. Odeblad, "Micro-NMR in high permanent magnetic fields," *Acta Obstet. Gynecol. Scand.*, vol. 45, p. Suppl. 2, 1966.

[39] N. Wu, T. L. Peck, A. G. Webb, R. L. Magin, and J. V. Sweedler, "^{1}H-NMR spectroscopy on the nanoliter scale for static and on-line measurements," *Anal. Chem.*, vol. 66, p. 3849, 1994.

[40] N. Wu, T. L. Peck, A. G. Webb, R. L. Magin, and J. V. Sweedler, "Nanoliter volume sample cells for ^{1}H-NMR: Application to on-line detection in capillary electrophoresis," *J. Am. Chem. Soc.*, vol. 116, p. 7929, 1994.

[41] B. Behnia and A. G. Webb, "Limited-sample NMR using solenoidal microcoils, perfluorocarbon plugs, and capillary spinning," *Anal. Chem.*, vol. 70, p. 5326, 1998.

[42] R. Kc, I. D. Henry, G. H. J. Park, A. Aghdasi, and D. Raftery, "New solenoidal microcoil NMR probe using zero-susceptibility wire," *Concepts Magn. Reson., Part B*, vol. 37B, p. 13, 2010.

[43] K. Kratt, V. Badilita, T. Burger, J. Korvink, and U. Wallrabe, "A fully MEMS-compatible process for 3D high aspect ratio micro coils obtained with an automatic wire bonder," *J. Micromech. Microeng.*, vol. 20, p. 015021, 2010.

[44] M. Mohmmadzadeh, N. Baxan, V. Badilita, K. Kratt, H. Weber, J. Korvink, U. Wallrabe, J. Hennig, and D. von Elverfeldt, "Characterization of a 3D MEMS fabricated microsolenoid at 9.4 T," *J. Magn. Reson.*, vol. 208, p. 20, 2011.

[45] R. Kamberge, A. Moazenzadeh, J. G. Korvink, and O. G. Gruschke, "Hollow microcoils made possible with external support structures manufactured with a two-solvent process," *J. Micromech. Microeng.*, vol. 26, p. 065002, 2016.

[46] N. Spengler, J. Höfflin, A. Moazenzadeh, D. Mager, N. MacKinnon, V. Badilita, U. Wallrabe, and J. G. Korvink, "Heteronuclear micro-helmholtz coil facilitates μm-range spatial and sub-Hz spectral resolution NMR of nL-volume samples on customisable microfluidic chips," *PLoS ONE*, vol. 11, no. 1, p. e0146384, 2016.

[47] T. Peck, R. Magin, J. Kruse, and M. Feng, "NMR microspectroscopy using 100 μm planar RF coils fabricated on gallium arsenide substrates," *IEEE Trans. Biomed. Eng.*, vol. 41, no. 7, p. 706, 1994.

[48] J. E. Stocker, T. L. Peck, A. G. Webb, M. Feng, and R. L. Magin, "Nanoliter volume, high-resolution NMR microspectroscopy using a 60- μm planar microcoil," *IEEE Trans. Biomed. Eng.*, vol. 44, p. 1122, 1997.

[49] S. Eroglu, G. Friedman, and R. L. Magin, "Estimate of losses and signal-to-noise ratio in planar inductive micro-coil detectors used for NMR," *IEEE Trans. Magn.*, vol. 37, p. 2787, 2001.

[50] J. D. Trumbull, I. K. Glasgow, D. J. Beebe, and R. L. Magin, "Integrating microfabricated fluidic systems and NMR spectroscopy," *IEEE Trans. Biomed. Eng.*, vol. 47, p. 3, 2000.

[51] H. Wensink, F. Benito-Lopez, D. C. Hermes, W. Verboom, J. G. E. Gardeniers, D. N. Reinhoudt, and A. van den Berg, "Measuring reaction kinetics in a lab-on-a-chip by microcoil NMR," *Lab Chip*, vol. 5, p. 280, 2005.

[52] M. V. Gomez, A. M. Rodriguez, A. de la Hoz, F. Jimenez-Marquez, R. M. Fratila, P. A. Barneveld, and A. H. Velders, "Determination of kinetic parameters within a single nonisothermal on-flow experiment by nanoliter NMR spectroscopy," *Anal. Chem.*, vol. 87, p. 10547, 2015.

[53] R. M. Fratila, V. Gomez, S. Sýkora, and A. H. Velders, "Multinuclear nanoliter one-dimensional and two-dimensional NMR spectroscopy with a single non-resonant micro-coil," *Nat. Commun.*, vol. 5, p. 3025, 2014.

[54] H. Ryan, S.-H. Song, A. Zaß, J. Korvink, and M. Utz, "Contactless NMR spectroscopy on a chip," *Anal. Chem.*, vol. 84, p. 3696, 2012.

[55] J. Bart, A. J. Kolkman, A. J. Oosthoek-de Vries, K. Koch, P. J. Nieuwland, J. W. G. Janssen, P. J. M. van Bentum, K. A. M. Ampt, F. P. J. T. Rutjes, S. S. Wijmenga, J. G. E. Gardeniers, and A. P. M. Kentgens, "A microfluidic high-resolution NMR flow probe," *J. Am. Chem. Soc.*, vol. 131, p. 5014, 2009.

[56] J. Bart, J. W. G. Janssen, P. J. M. van Bentum, A. P. M. Kentgens, and J. G. E. Gardeniers, "Optimization of stripline-based microfluidic chips for high-resolution NMR," *J. Magn. Reson.*, vol. 201, p. 175, 2009.

[57] K. Ehrmann, N. Saillen, F. Vincent, M. Stettler, M. Jordan, F. M. Wurm, P. Besse, and R. Popovic, "Microfabricated solenoids and Helmholtz coils for NMR spectroscopy of mammalian cells," *Lab Chip*, vol. 7, p. 373, 2007.

[58] J. H. Walton, J. S. de Ropp, M. V. Shutov, A. G. Goloshevsky, M. J. McCarthy, R. L. Smith, and S. D. Collins, "A micromachined double-tuned NMR microprobe," *Anal. Chem.*, vol. 75, p. 5030, 2003.

[59] R. R. A. Syms, M. M. Ahmad, I. R. Young, Y. Li, J. Hand, and D. Gilderdale, "MEMS Helmholtz coils for magnetic resonance imaging," *J. Micromech. Microeng.*, vol. 15, p. S1, 2005.

[60] S. Leidich, M. Braun, T. Gessner, and T. Riemer, "Silicon cylinder spiral coil for nuclear magnetic resonance spectroscopy of nanoliter samples," *Concepts Magn. Reson., Part B*, vol. 35B, no. 1, p. 11, 2009.

[61] L. Renaud, M. Armenean, L. Berry, P. Kleimann, P. Morin, M. Pitaval, J. OḂrien, M. Brunet, and H. Saint-Jalmes, "Implantable planar rf microcoils for NMR microspectroscopy," *Sens. Actuators, A*, vol. 99, p. 244, 2002.

[62] N. Baxan, A. Rengle, J. Châteaux, A. Briguet1, G. Pasquet, P. Morin, and L. Fakri-Bouchet, "NMR planar micro coils for micro spectroscopy: Design and characterisation," *Proc. - IEEE EMBS Annu. Int. Conf., 28th*, p. 4314, 2006.

[63] A. Kadjo, N. Baxan, R. Cespuglio, A. Briguet, C. Rousset, M. Hoang, D. Graveron-Demilly, and L. Fakri-Bouchet, "In vivo animal nmr studies using implantable micro-coil," *Proc. Intl. Soc. Mag. Reson. Med.*, vol. 17, p. 4275, 2009.

[64] F. A. Howe, R. R. Syms, M. M. Ahmad, L. M. Rodrigues, J. R. Griffiths, and I. R. Young, "In vivo ^{31}P magnetic resonance spectroscopy using a needle microcoil," *Magn. Reson. Med.*, vol. 61, p. 1238, 2009.

[65] Y. Tang, M. Hurlimann, S. Mandal, J. Paulsen, and Y. Song, "Coaxial probe for nuclear magnetic resonance diffusion and relaxation correlation experiments," *J. Appl. Phys.*, vol. 115, p. 073903, 2014.

[66] P. J. M. van Bentum, J. W. G. Janssen, A. P. M. Kentgens, J. Bart, and J. G. E. Gardeniers, "Stripline probes for nuclear magnetic resonance," *J. Magn. Reson.*, vol. 189, p. 104, 2007.

[67] X. Zhang, K. Ugurbil, and W. Chen, "Microstrip RF surface coil design for extremely high-field MRI and spectroscopy," *Magn. Reson. Med.*, vol. 46, p. 443, 2001.

[68] G. Finch, A. Yilmaz, and M. Utz, "An optimised detector for in-situ high-resolution NMR in microfluidic devices," *J. Magn. Reson.*, vol. 262, p. 73, 2016.

[69] A. Yilmaz and M. Utz, "Characterisation of oxygen permeation into a microfluidic device for cell culture by in situ NMR spectroscopy," *Lab Chip*, vol. 16, p. 2079, 2016.

[70] Y. Maguire, I. L. Chuang, S. Zhang, and N. Gershenfeld, "Ultra-small-sample molecular structure detection using microslot waveguide nuclear spin resonance," *Proc. Natl. Acad. Sci. U. S. A.*, vol. 104, no. 22, p. 9198, 2007.

[71] H. G. Krojanski, J. Lambert, Y. Gerikalan, D. Suter, and R. Hergenroder, "Microslot NMR probe for metabolomics studies," *Anal. Chem.*, vol. 80, p. 8668, 2008.

[72] K. Jasinski, A. Mlynarczyk, P. Latta, V. Volotovskyy, W. Weglarz, and B. Tomanek, "A volume microstrip RF coil for MRI microscopy," *Magn. Reson. Imaging*, vol. 30, p. 70, 2012.

[73] J. Bart, *Stripline-based microfluidic devices for high-resolution NMR spectroscopy*. PhD thesis, University of Twente, Enschede, the Netherlands, 2009. ISBN 978-90-365-2898-6.

Chapter 2

Stripline high-resolution NMR experiments of submicroliter volume samples

Abstract

Nuclear magnetic resonance (NMR) spectroscopy is of significant use for the analysis of biological samples, for example. However, since the sensitivity of this technique is relatively low and the amount of available sample may be low in some cases, it can become a problem to achieve a sufficient signal-to-noise ratio. Therefore, much research is focused on the development of a high resolution and high sensitivity of the spectroscopic NMR tool. One of the approaches to increase sensitivity is miniaturisation of the NMR coil. The stripline NMR setup presented here consists of an NMR microcoil equipped with a lock coil and is evaluated for NMR experiments performed on sample plugs of 150 nl. We succesfully measured low concentrated plugs, mouse cerebrospinal fluid (CSF) and plant hormones (strigolactones).

2.1 Introduction

NMR spectroscopy can provide very detailed information about molecular structures, by probing not only the molecules, but also the surrounding of the nuclei. Therefore, it is an invaluable tool for analysing biological samples.
The NMR signal results from the Boltzmann distributed population difference between the high and low energy state, which occurs when the nuclei interact with a magnetic field. As both the energy difference between the high and low energy states and the population difference is very small, the sensitivity is much lower in NMR spectroscopy than in other spectroscopic techniques [1, 2, 3].
The sensitivity of the NMR experiment is related to the obtained signal-to-noise ratio (SNR). Repeating Eq. (1.22), Hoult and Richards' [4] definition of the SNR:

$$SNR = \frac{k_0 \frac{B_1}{i} V_s N \gamma \hbar^2 I(I+1)\omega_0^2}{(k_B T_{sample} 3\sqrt{2})\sqrt{4 k_B T_{coil} R \Delta f}} \tag{2.1}$$

or rewritten and collecting all constants in C:

$$SNR = C \frac{(B_1/i)N}{\sqrt{TR\Delta f}} \tag{2.2}$$

B_1/i is the transverse magnetic field generated by a current i, N is the number of spins in the effective detection volume (V_{obs}), Δf is the spectral width of the experiment, R is the resistance of the coil and sample.

Approaches to enhance sensitivity can be derived from this formula and explain the focus on increasing the magnetic field B_0, lowering the temperature T_{coil} (cryo-probes), optimising the filling factor and thereby the number of spins N in V_{obs}, increasing the population differences (eg. hyperpolarisation, DNP, parahydrogen) and miniaturisation[2, 3].

From the principle of reciprocity[4, 5, 6] it is derived that the factor B_1/i increases for a smaller coil, and therefore miniaturisation of the coil improves the sensitivity of the NMR experiment for mass-limited samples. Several microcoil designs are known from literature[2]: the wound solenoid, planar microcoils and stripline/microslot. The latter is used here and has the advantages that the rf field is homogeneous, the filling factor is high and the design is scalable[7, 8].

For mass limited samples it is interesting to consider the filling factor f_{fill} and observe factor f_{obs}[9]. The coil volume V_{coil} is defined as the total active volume from which an NMR signal can be obtained, i.e. the volume within or near the coil where magnetic energy is sufficiently concentrated and within a certain range of homogeneity. The coil volume depends not only on the design parameters, but also on coil geometry. A shown theoretically by Hoult and Richards[4] for a homogeneous B_1 field in the solenoid's sample volume, the energy stored in the sample volume is:

$$\frac{1}{2\mu_0}\int_{sample} B_1^2 dV \sim \frac{1}{4\mu_0}\int_{allspace} B_1^2 dV \tag{2.3}$$

Thus, for a solenoid half of the magnetic energy is stored outside of the coil. In this respect, in a stripline "coil" the magnetic energy is more efficiently used, as the magnetic energy is concentrated in the coil volume, since it is confined by the boundary planes. For a planar coil where the magnetic energy rapidly diminishes out from the surface, the magnetic energy in the sample is much lower.[7]. In practice, the homogeneity of the field is important for NMR measurements and can be accounted for by defining the volume where the B_1 field does not deviate more than (for example) 10% from its value at the centre of the coil. Van Bentum et al. evaluated the rf field for a solenoid, a planar coil and a stripline, respectively, which showed that 15%, 4% and 50% of the magnetic energy is concentrated in the effective sample volume with less than 10% deviation from central field. The detection (observe) volume V_{obs} is the active volume of a coil that can be occupied by the analyte, which can be limited by the wall thickness of the sample volume or capillary. The filling factor is the fraction of coil volume occupied by the sample $f_{fill} = V_{obs}/V_{coil}$. When the filling factor is

high, the coil's magnetic energy is efficiently used. In contrast, the observe factor f_{obs} reflects the efficiency of sample observation. f_{obs} is the fraction of total volume of the sample required for the NMR measurement V_{total} that is actually inside the detection volume at a measurement: $f_{obs} = V_{obs}/V_{total}$.
In the design of the stripline NMR chip some progress has been made in optimising f_{obs} while the high resolution is maintained. A homogeneous field is obtained by sandwiching the stripline coil structure between parallel copper shielding plates. In this chip, this is achieved by separating the stripline chip and the shielding plates with minimal distance using spacer capillaries the same diameter as the sample capillary. A lock channel has been incorporated, which is important for long measurements of low concentrated samples, to prevent line broadening due to drifting of the external magnetic field. A plug of sample is prepared in a replaceable fused-silica (FS) capillary to optimise f_{obs}, enclosed between fluorinert to prevent susceptibility mismatch[10]. The sample plug is positioned at the sensitive region of the stripline. If the sample plug is the same length as the stripline's constriction length (i.e. 3 mm), all of the sample is in the coil's active volume during measurement so that $f_{obs} \sim 1$.
In this Chapter, first the setup is characterised by standard samples (ethanol and 17-α estradiol). To test the usability of the setup for mass limited samples, compounds are analysed that are inherently mass-limited: cerebrospinal fluid (CSF) of mice and strigolactones (plant hormones).

2.2 Experimental setup

2.2.1 Stripline chip

Figure 2.1 shows the stripline NMR chip used for the experiments. The detection volume of the NMR chip is approximately 150 nl, the sample is contained in a fused silica (FS) capillary. The copper stripline rf coil is deposited by sputtering and electroplating on a fused silica (FS) substrate (500 μm thick), such as described in more detail in Appendix B.2. The constriction in width in the middle of the stripline defines the area where the radio frequency (rf) field is highest and therefore this is also the sensitive region of the strip[7, 8]. A FS capillary (360 μm outer diameter, 250 μm inner diameter) containing the sample, is placed into the chip. A copper mirror plane is similarly deposited on a FS substrate and used as shielding. On the left and right edges of the chip, FS capillaries (360 μm outer diameter) are placed as spacers, ensuring

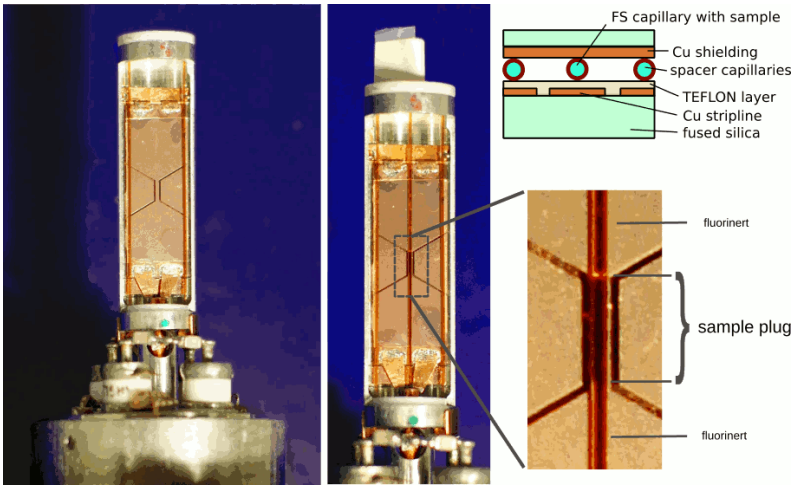

Figure 2.1: Showing the top part of the probe with mirror plane removed, the stripline chip without sample, a 150 nl sample plug covering the detection area and a schematic of the chip.

stability of the stack. The capillaries are guided through the casing on top and bottom of the chips stack, which holds the stack into place.

2.2.2 Lock channel

For lowly concentrated samples, acquisition times can be long as accumulation of many scans is needed to obtain sufficient SNR. The magnetic field strength may then drift to some extent during the experiment, giving rise to broadening of the peaks in the spectrum. The lock, specifically the field frequency lock, used in conventional NMR experiments, controls the magnetic field in the sample in such a way that the resonance frequencies do not drift. Typically, the measured resonance frequency of deuterium in the sample's deuterated solvent is used to correct for any drift.
To prevent line broadening when measuring low concentrated samples, a lock channel is installed on the home-built probe. Figure 2.2 shows pictures and schematic of the lock channel. The 600 MHz Varian console has a lock input that is tuned to the resonance frequency for deuterium. The X-channel of the probe can be disconnected from the probehead X-rf input at point A and be used as a lock channel for deuterium. A compensating current is added to the Z0 coil room temperature shim of the magnet so that the original value of the ^{1}H frequency is restored. All other frequencies used in the experiment are coupled to the frequency of the lock channel.
A strong deuterium lock signal is needed as a reference. The solvent in the sample,

however, does not give a strong enough signal. Also, adding the second microfluidic channel at the other side of the stripline (see Figure 2.1), does not result in sufficient strong lock signal. Therefore, a separate coil is attached to the probe for this purpose. A small coil made from 26AWG isolated wire, 9 turns, and an inner diameter of 1.5 mm is horizontally mounted at one side of the aluminium cylinder which holds the stripline chip. The axis of the lock coil is aligned with the center of the stripline chip. Inside this coil, a capillary with a length of about 8 mm containing the deuterium sample, is placed. A clamp around the aluminium cylinder is holding the small lock coil in position and connects it to ground. The other end of the coil is soldered to point A instead of the probehead X-rf input. The tune- and match capacitors are the same as used for the original X-channel but are tuned and matched to the resonance frequency of deuterium.

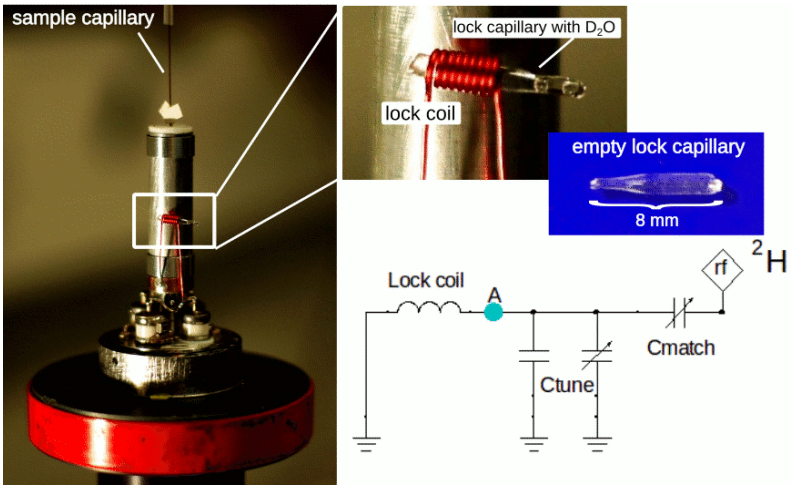

Figure 2.2: Showing the top of the probe with the lock coil, lock sample, and a schematic of the circuit

2.3 Measuring a plug of low-concentrated sample

The proximity of the sample to the microcoil makes it sensitive to magnetic field distortions. Volume magnetic susceptibility (ξ_v) mismatch may arise from discontinuities from the interfaces of sample volume with air in the capillary, which should be prevented in order to optimise the resolution [10, 11, 12]. One way to prevent line broadening due to susceptibility mismatch is to have the sample plug significantly longer than the

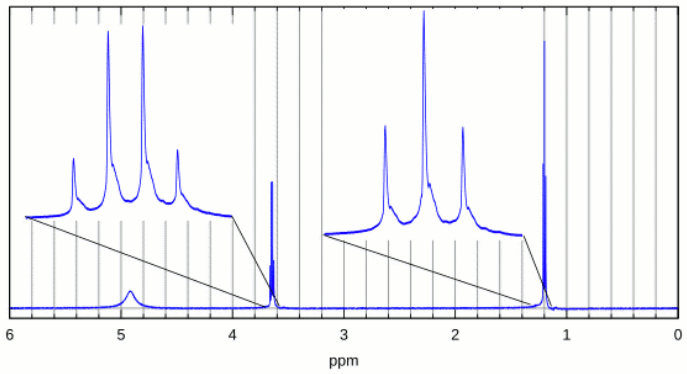

Figure 2.3: Proton spectrum of a plug of 150 nl ethanol (70%)

coil length. In our case we take the plug as long as the stripline plus the wings, since the field strength drastically decreases outside of the constriction. Alternatively, to optimise the efficient use of the sample, i.e. to optimise f_{obs}, the sample can be concentrated in a plug and enclosed between fluorinert (FC43), a perfluorocarbon liquid which has the same magnetic susceptibility as copper and therefore also increases the resolution.

To prepare a capillary containing a plug of sample, the FS capillary is first filled with about 2-3 cm fluorinert. Then the desired amount of sample is drawn in, taking care to prevent air bubbles. The fluorinert gives a clear interface with the sample and does not mix. Finally, the rest of the capillary is filled with fluorinert.

For characterisation of the chip a 150 nl plug of 70% ethanol in water, enclosed between fluorinert, is used. From a single scan measurement, shown in Figure 2.3, the resolution and limit of detection (LOD) are obtained. A resolution of 0.5 Hz (full width at half maximum) is estimated from the triplet. The lineshape suffers from a broad "foot", arising from shimming difficulties.

The signal-to-noise ratio (SNR) of the triplet is 1593 for the applied experimental conditions, which corresponds to a LOD of around $8 \cdot 10^{13}$ spins/$\sqrt{Hz}$, which is only a factor 3.5 more than the calculated theoretical minimum value of $2.43 \cdot 10^{13}$ spins/$\sqrt{Hz}$. For a sample capillary over the full length of the chip filled with ethanol, the resolution broadens to more than 2 Hz. The SNR for the entirely filled cappilary is 1661, from which a LOD of around $7.5 \cdot 10^{13}$ spins/$\sqrt{Hz}$ is obtained.

A plug containing 150 nl 10 mM 17α-estradiol solution in methanol-d_4 was prepared. The amount of 17α-estradiol in the plug is 1.5 nmol or 400 ng. A 1024 scans spectrum

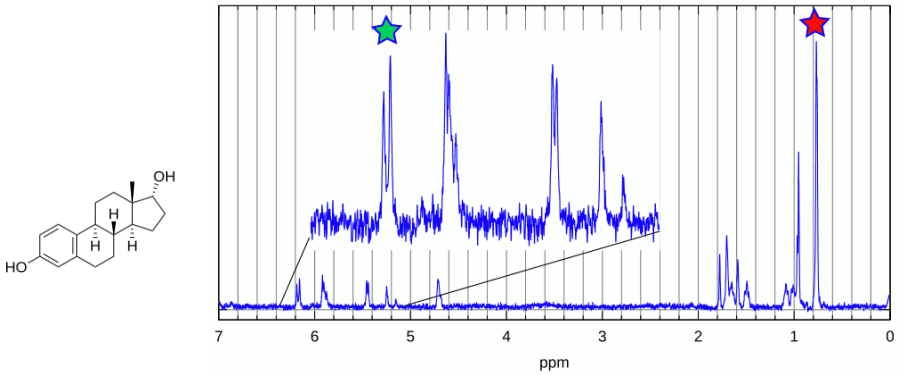

(a) 17α-estradiol (b) Proton spectrum of 150 nl plug of 10 mM 17α-estradiol, 1024 scans. For processing, 0.5 Hz Lorentzian line broadening, zero-filling up to 64000 points and baseline correction were applied. Insert: zooming into the aromatic region. The peaks with green and red star give an SNR of 23 and 205, respectively.

Figure 2.4: Molecular structure and spectrum of 17α-estradiol

is acquired while using the lock-function, as is shown in Figure 2.4b. From the multiplets in the aromatic region we can estimate a SNR of 23 (doublet with green star) and for the highest peak 205 (peak with red star).

The resolution obtained from the doublet is approximately 6 Hz (FWHH), which is not as good as on the ethanol sample in Figure 2.3. A drawback of this setup with low concentrated samples, is that the sample is not concentrated enough to give sufficient single scan intensity for optimal shimming. The lock sample, in conventional NMR a very useful tool for shimming, can also not be used because it is not at the same position as the measurement sample. Changing the sample to a reference sample for shimming is not an option in this setup, since this would involve taking out the probe and opening the chip for replacing the FS capillary. Shimming may be possible in most cases on water or another solvent peak, but this gives not as accurate a result as shimming on an ethanol plug. Using a microfluidic stopped flow setup might solve this problem, since low concentrated sample plugs for analysis can follow sample plugs containing ethanol for shimming without altering the setup. However, the conventional shim coils are not very well suited for shimming on microcoils, since the sample and coil are relatively small, lead to large field gradients and are difficult to position in the exact centre of the magnet. Recently, a Shim-on-Chip system has been developed which solves this shimming problem, by attaching a flat ribbon cable with 40 wires to the chip, through

which locally applied shim currents improve the lineshape significantly[13].
The effect of measuring with a lock can be observed from Figure 2.5, in which 8 blocks of 128 accumulated scans and the summation of the 8 blocks are shown. Without using the lock function (Figure 2.5a), a drift can be observed over approximately 10 Hz in a experiment time of 2 hours. When the blocks are summed the lines in the spectrum are visibly broadened. When using the lock function (Figure 2.5b), the magnetic field drift is corrected for and the variation between the blocks is diminished. An overall improvement of the resolution in the accumulated spectrum results. Since it is rather time-consuming to manually correct for magnetic field drift, especially for measurements of large amounts of samples or very long measurements (eg. 2D spectra) the ability to use a lock function is a great benefit.

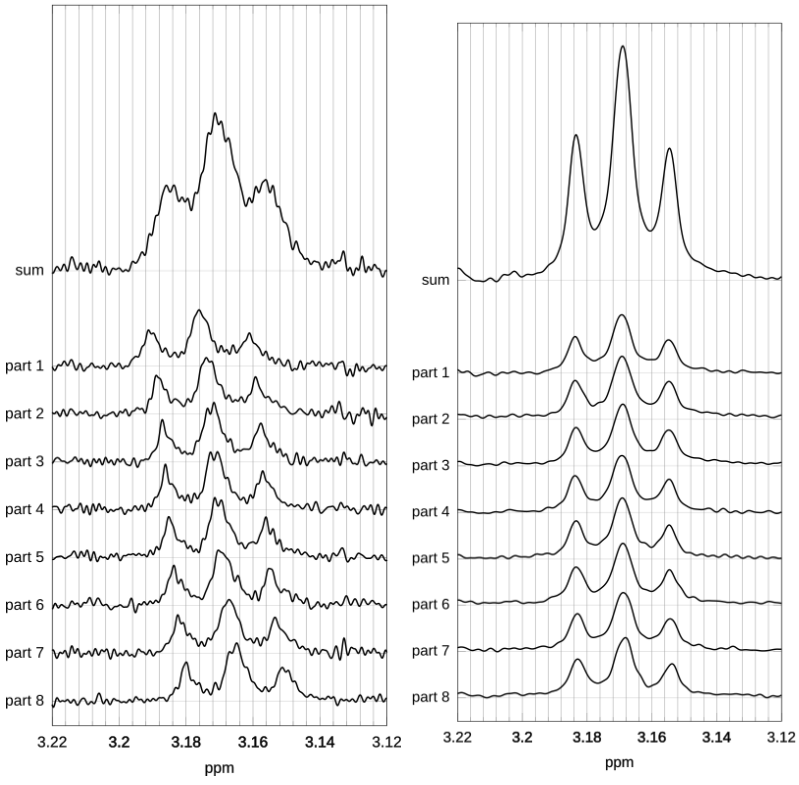

(a) Without lock (b) With lock

Figure 2.5: CSF spectra of same sample, a) without lock, b) with lock: both accumulating 8 blocks of 128 scans.

2.4 Metabolites in mouse CSF

Metabolites are small molecules, the intermediate and end products of metabolism which are present in microbial, animal or plant biofluids, such as urine, saliva, serum, blood plasma, cerebrospinal fluid (CSF) or plant sap. Metabolomic processes give insight into the functioning of the biological system and changes in metabolite concentrations reflect the reaction of the system to stimuli (environment, medicine, disease)[14, 15].

The analytical tools routinely used in metabolomics are mass-spectroscopy (MS with separation in liquid or gas chromatography (LC-MS or GC-MS)) or NMR. Advantages of NMR are that the experiments can be done quantitatively and non-destructively, identification of novel compounds is possible, and sample preparation steps are usually not as laborious[16]. The wealth of information of a metabolomic spectrum can be viewed as an advantage as well as a challenge. A disadvantage of NMR in this field, however, is the low sensitivity compared to MS[15].

If only very limited amounts of sample is available, due to limited availability of the sample[17, 18] or because of a limited amount of sample per individual[19, 20], it can become difficult to measure the sample in conventional NMR. Special procedures or pooling may be required. An example of limited volume NMR is the absolute quantification of metabolites in larvea of the fruitfly *Drosophila melanogaster*[21]. The volume of the hemolymph of the larvae ranges between 700 and 250 nl, and the obtained metabolite concentrations 70 mM to 50 μM. To enable quantification of these concentrations, it is necessary to precisely determine the sample volume. For this purpose Ragan et al[21] developed a procedure using two internal standards (VDTS). In another example, metabonomics study is used for enabling the early detection of epithelial ovarian cancer[17]. Detection in an early stage greatly improves chances of survival and might be possible via serum. The availability if serum is, however, very limited, and therefore a minimum amount of sample (20 μl) was used in a microflow probe to efficiently analyse the samples in order to find biomarkers for this disease[17]. CSF is used for study and detection of neurological diseases, such as meningitis, schizophrenia, Huntington's disease, Alzheimer's disease or multiple sclerosis[16]. Human CSF has been succesfully measured previously in a stripline NMR setup[22]. Some advancements in the current setup include the replaceable capillary, so that the sample volume can be efficiently used (for a plug smaller than the length of the stripline $f_{obs} = 1$) and the lock channel to minimise line broadening in long measurements.

The amount of human CSF is usually sufficient to be measured in conventional NMR, however for a mouse study only a limited amount is available per mouse (5-7 μl ante mortem, serial sampling[18, 23, 24]).
The objective of our experiments is twofold, first we make a comparison of the mouse CSF measured in the stripline NMR chip with part of the same sample measured in conventional NMR, and second, we analyse the samples measured under the original condition, to evaluate the setup for analysing these type of unprocessed samples.

2.4.1 Experiments

Sample preparation

The first sample was measured in stripline NMR as well as in conventional NMR (sample 1 in Figure 2.6). Approximately 10 μl CSF sample from a single mouse was freeze-dried and subsequently dissolved in 2 μl D_2O. From this solution, 150 nl was taken for the stripline NMR measurement, while the remainder was used for the conventional NMR measurement. For the stripline NMR measurement a FS capillary was prepared as described above containing a 150 nl sample plug (3 mm length) enclosed between fluorinert. For the conventional NMR measurement the remaining 1850 nl of CSF solution was diluted with buffer solution (D_2O with PBS pH buffer and 100 μM trimethylsilyl propanoic acid (TSP) as an internal standard) to a total volume of 200 μl, measured in a Shigemi tube. The resulting stripline plug contains 7.5% of the sample, which is 5 x concentrated relative to the original CSF. The conventional NMR sample is approximately 100 x diluted.
The other sample capillaries (sample 2-4 in Figure 2.6) are prepared without any processing of the CSF. Sample 2 contains a 3 mm plug enclosed between fluorinert, sample 3 contains a 5.5 mm plug enclosed between fluorinert and sample 4 is a entirely filled capillary, covering more than the stripline and wings. Sample 1 has been prepared immediately after thawing the frozen samples, whereas samples 2-4 have been prepared after 2 years, this long storage period can affect the concentrations in the sample.

NMR measurements

The conventional NMR spectrum has been acquired using a Bruker 600 MHz spectrometer, accumulating 1024 scans, with an acquisition delay of 3 seconds. The total measurement time was 1 hour and 4 minutes. The stripline NMR spectra were mea-

sured in the setup as described above. All spectra are a accumulation of 1024 scans, with an acquisition delay of 3 seconds. The total measurement time was about 1 hour and 10 minutes per spectrum.
For processing, the FIDs were zero-filled up to 64000 points, 0.5 Hz line broadening was applied, and Asymmetric Least Squares[25] baseline correction for the stripline spectrum.

2.4.2 Results and Discussion

The stripline NMR and conventional NMR spectra of sample 1 are shown on top in Figure 2.6. The resolution of the stripline spectrum is approximately 2.7 Hz (FWHM) and 1.0 Hz for the conventional NMR spectrum. Some concentration differences can be observed, this could be due to the differences in processing or the storage of the sample.
For a quantitative comparison of the sensitivity, the SNR of the lactate and glucose peak is calculated for both spectra. For lactate at 1.23 ppm, we find a SNR of 97 for the stripline spectrum and SNR is 250 for the conventional NMR spectrum, for glucose at 5.2 ppm, 23.5 and 14, respectively. In the conventional NMR spectrum the glucose peak is diminished due to suppression of the large water peak. In the conventional NMR sample, 100 μM TSP is used as an internal standard. From the TSP peak in the conventional NMR spectrum, the concentrations of lactate (approximately 69 μM, 23 nmol in the detection volume) and glucose (63 μM) were estimated. Since the stripline NMR sample is 194 times as concentrated as the conventional NMR sample, the lactate concentrations is estimated 13.4 mM and the amount of lactate in the sample volume is approximately 2 nmol.
The conventional NMR sample consists of about 10 times more material, but results in only 2.5 times higher SNR, consequently the stripline NMR chip gives a factor 4 sensitivity enhancement (compared to 3.4 in the previous results[22]).
The spectra of sample 2 - 4 are shown in Figures 2.6 and 2.7, were taken without any processing of the CSF, and measured in a stripline sample plug. It can be expected that the spectra vary due to individual differences for each mouse, but also chemical shift positions and line shapes can change due to differences in concentrations, pH, salt concentration[15]. These variations are indeed observed within these spectra.
The SNR of the lactate peak in the sample plugs measured in the stripline NMR was 97, 197, 34, 67 for samples 1-4, respectively. For glucose SNR of 24, 84, 26 and

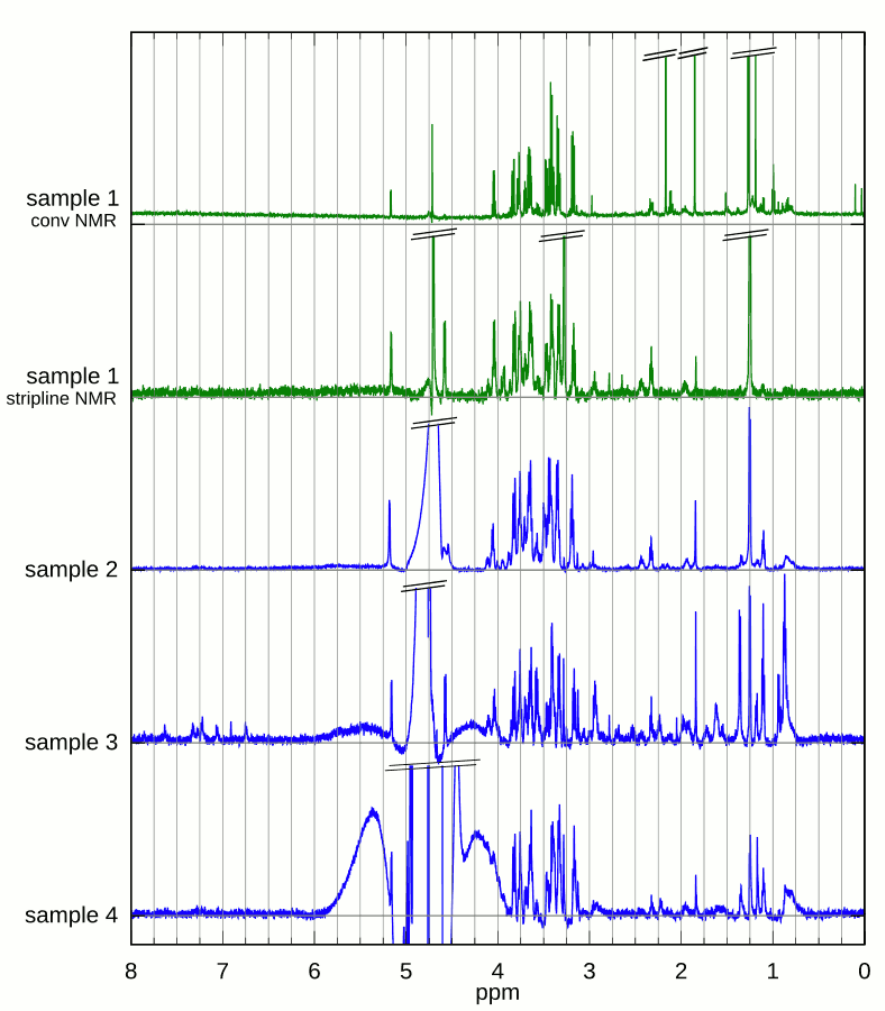

Figure 2.6: CSF samples measured in stripline NMR chip and conventional NMR, sample 1 is processed freezedried and dissolved in D2O, sample 2-4 are directly put into a capillary

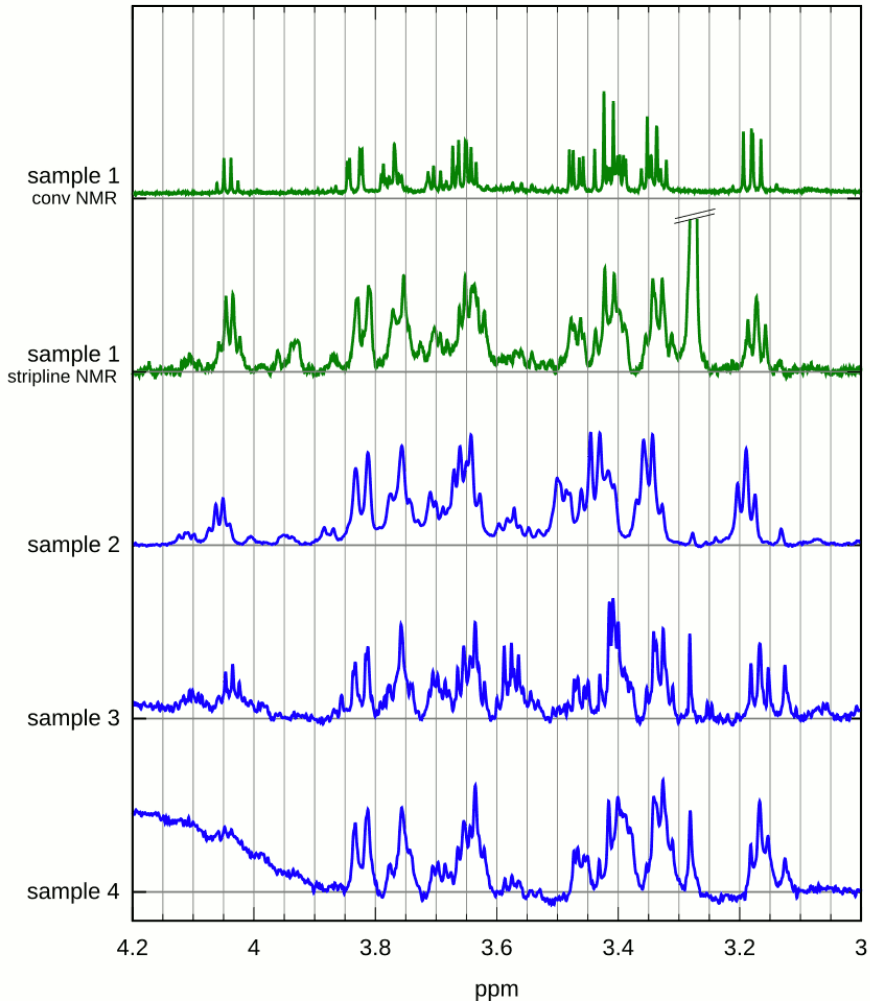

Figure 2.7: CSF samples measured in stripline NMR chip, zooming into the region 3.2-4 ppm

23 were found. Unfortunately, without reference to either an internal or an external standard the concentrations cannot be accurately determined.
Adding an internal standard is not straightforward for these small sample volume, because the volume of the standard should be as small as possible, which is rather impractical. Moreover, the concentration of the sample decreases relatively much if a volume of standard is added. Therefore, an external standard using the second stripline channel may be a better choice for this purpose, for exampe with $CDCl_3$ with TMS, as calibration. Stopped plug flow could be an option, in which a calibrated sample plug may aid in quantification and shimming.
The sample plugs were prepared after long storage in plastic containers, so evaporation and contamination is possible. It is imaginable that samples turn out more concentrated at the time of measurement. For a mouse study keeping the CSF samples frozen would be recommended in order to maintain original concentrations [15].
While it can be difficult to know the exact amount of sample volume for small volumes [21], in the stripline setup with FS capillary the sample volume is precisely known from measuring the length of the plug, if the detection volume is (more than) entirely filled it is constant, namely 150 nl.
We conclude that mouse CSF we used as a test case has a relatively large volume for the present stripline NMR chip, and is concentrated enough to be measured in conventional NMR as well. However, the setup is suitable for these type of measurements and might be especially of an advantage for serial sampling (individual mouse study), for precious or very small volume samples. Furthermore, it was possible to obtain good spectra from the CSF samples that were measured without applying any processing steps, although proteins could be present. Using Shim-on-Chip [13] would further increase resolution and therefore spectral sensitivity. However, calibration is necessary to be able to determine the concentration of metabolites. In the current stripline NMR chip it is feasible to adjust the setup to enable flow. Measuring the samples in continuous flow, or sample plugs in stopped flow, can be interesting for easier calibration and determination of the concentrations.

2.5 Strigolactones

Strigolactones are plant hormones, root exudates functioning as signaling molecules, released into the soil by host plants in very small amounts which rapidly decompose [26]. Parasitic weeds (*Striga*, *Orobanche* and *Phelipanche* spp.) use strigolactones as a signal

to germinate. The parasitic weeds deprive nutrients from their host plants, depending on strigolactones to germinate in synchronisation with the host plant. Because of the dramatic effect on the food crop, much research is focused on strigolactones in order to find an effective control for the parasitic weeds[26, 27, 28, 29].

Apart from their role as germination stimulants, it was recently discovered that strigolactones also function as host detection signals in arbuscular mycorrhizal (AM) fungi. Root colonization of AM fungi is a beneficial and important symbiosis for plants, since they receive photosynthates (sugars produced by photosynthesis) while supplying water and nutrients to the AM fungi. Strigolactones are essential signaling molecules for localisation of the AM fungi. Moreover, research is ongoing to explore the function of strigolactones in shoot branching[29]. Altogether, the role and mechanisms of the strigolactones is complex.

The general structure of naturally occurring strigolactones is a tricyclic lactene (ABC), which is attached via an enol ether bridge to a butenolide ring (D), similar to for example the synthetic compound GR-24 depicted in Figure 2.8b. Structural requirements such as the stereochemistry and/or the configuration of the C-D ring are essential for germination activity[30, 31, 32, 33].

Studying the activity of synthetic analogues of natural strigolactones provides understanding about the influence of the structure and more precisely the stereochemistry of the molecules in relation to their activity[34, 35, 36]. In order to unravel the molecular structure of strigolactones and gain full insight into the mechanisms involved, spectroscopy is an important tool. However, the available amount of sample often is very limited, which hinders a full analysis[26, 29]. A microfluidic spectroscopic device, such as the stripline NMR chip, therefore may assist in studying in more detail the mass-limited strigolactone samples, either synthetic or natural. Here, we aim to evaluate the stripline NMR setup for this purpose. In these experiments, we analyse 8 synthetic strigolactones, available in 0.7 to 5.4 mg, using both stripline and solid state NMR spectroscopy.

2.5.1 Experimental

Synthetic analogues of SL

The synthetic analogues of strigolactones that were analysed in the experiments: Nijmegen -1[37], GR24[38], fast and slow moving diastereoisomers of 6-methyl-GR24 (6-Me-GR24 *fast* and 6-Me-GR24 *slow*), 8-methyl-GR24 (8-Me-GR24 *fast* and 8-Me-GR24

slow)[35] and desmethylsorgolactone (DMSL *fast* and DMSL *slow*)[34]. The molecular structures are depicted in Figure 2.8.

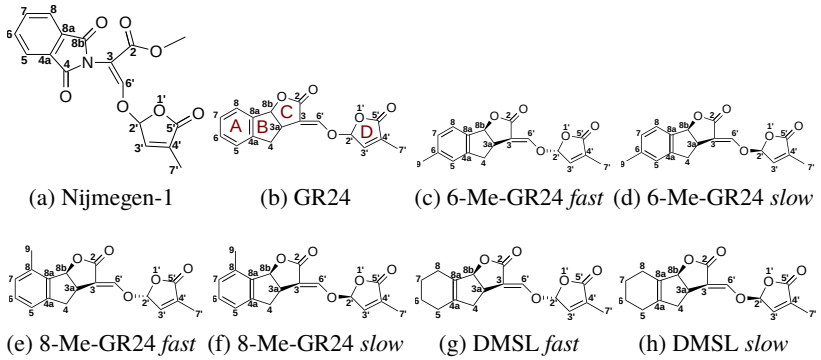

(a) Nijmegen-1 (b) GR24 (c) 6-Me-GR24 *fast* (d) 6-Me-GR24 *slow*

(e) 8-Me-GR24 *fast* (f) 8-Me-GR24 *slow* (g) DMSL *fast* (h) DMSL *slow*

Figure 2.8: Molecular structures of synthetic analogues of strigolactones

NMR measurements

For the stripline NMR measurements, strigolactone powders were dissolved in $CDCl_3$ and measured in the stripline NMR probe on a 600 MHz VNMRS Varian spectrometer. The amount of material used for the experiments was estimated to be around 0.3 mg for each sample, which was sufficient to obtain a highly concentrated plug in most cases.

The FS capillaries were prepared with a plug long enough to cover the detection area and the wings of the stripline chip were the rf field is highest. The plugs were not enclosed between fluorinert, so that the sample can in principle be recovered after the experiments. Depending on the concentration of the sample, the amount of scans was 16, 64 or 1024. Furthermore, total correlation (TOCSY) spectra were acquired with 60-80 μs mixing time. For the synthetic analogue 6-Me-GR24 *slow* a ^{1}H-^{13}C correlation spectrum (HMQC) was acquired with 128 increments of 16 scans.

For the solid state NMR experiments, a 1.2 mm HX MAS probe was used on an 850 MHz Varian VNMRS spectrometer. The magic angle spinning (MAS) speed was 55 kHz for all samples except Nijmegen-1 at 12 kHz and 8-Me-GR24 *slow* at 40 kHz. The ^{13}C spectra were obtained using tangent cross polarisation (Hartmann-Hahn[39]) CP/MAS pulse sequence[40, 41]. The number of scans varied between 6000 and 7500 scans, a relaxation delay of 5 seconds was used. The spectra were acquired with short (1 ms) and long (4 ms) cross-polarisation contact time.

A ^{1}H-^{13}C correlation spectrum of GR24 was acquired using a HETCOR sequence[42], with 128 increments and accumulating 500 scans. A relaxation delay of 4 seconds was taken into account, with a short cross-polarisation contact time (1 ms).
Both DMSL samples were available in less than 1 mg, which was not sufficient to fill the 1.2 mm rotor.

2.5.2 Results

Stripline NMR measurements

The strigolactone powders ($\sim$ 0.3 mg) were dissolved in $CDCl_3$, and sample capillaries were prepared as described above. Figure 2.9 shows the ^{1}H spectra measured in the stripline NMR, and some of the total correlation (TOCSY) spectra in Figure 2.10a and in Figure A.1 in Appendix A.1. In the TOCSY spectra peaks belonging to the ABC ring and the D ring can be distinguished, which enables assignment of the peaks in the crowded area. Using literature data[35, 43, 34, 44] and the TOCSY spectra, the peaks could be assigned and an overview is given in Table A.1 in Appendix A.2. Small chemical shift differences are found in the aromatic region of the slow and fast diastereoisomers. Structural differences between GR24, 6-Me-GR24, 8-Me-GR24 and DMSL are reflected in the A-ring in Figure 2.8. From GR24, the multiplet at 7.23 - 7.49 ppm is expected to split up and shift up to 0.2 ppm downwards for 6-Me-GR24 (7.06, 7.11 and 7.40) and 8-Me-GR24 (7.04, 7.04 and 7.22), and towards 2 ppm for DMSL. These shifts are indeed observed in the spectra measured in the stripline NMR, so the resolution is sufficient to obtain this type of structure information.
In the stripline NMR setup ^{13}C spectra could not be measured in a reasonable amount of time. However, a Heteronuclear Multiple-Quantum Correlation (HMQC) spectrum could be obtained. Figure 2.10b shows the HMQC ^{1}H-^{13}C correlation spectrum of 6-Me-GR24 *slow*. From this spectrum, some ^{13}C peaks can be assigned, as summarised in Table A.2 in Appendix A.3. The measurements are in agreement with the sample description and no impurities are observed.

Solid state NMR measurements

Since the amount of sample was not sufficient for ^{13}C NMR measurements in the current setup, more concentrated samples are needed. Obviously, the highest concentration that can be attained is simply analysing the samples in the solid state. Depending on

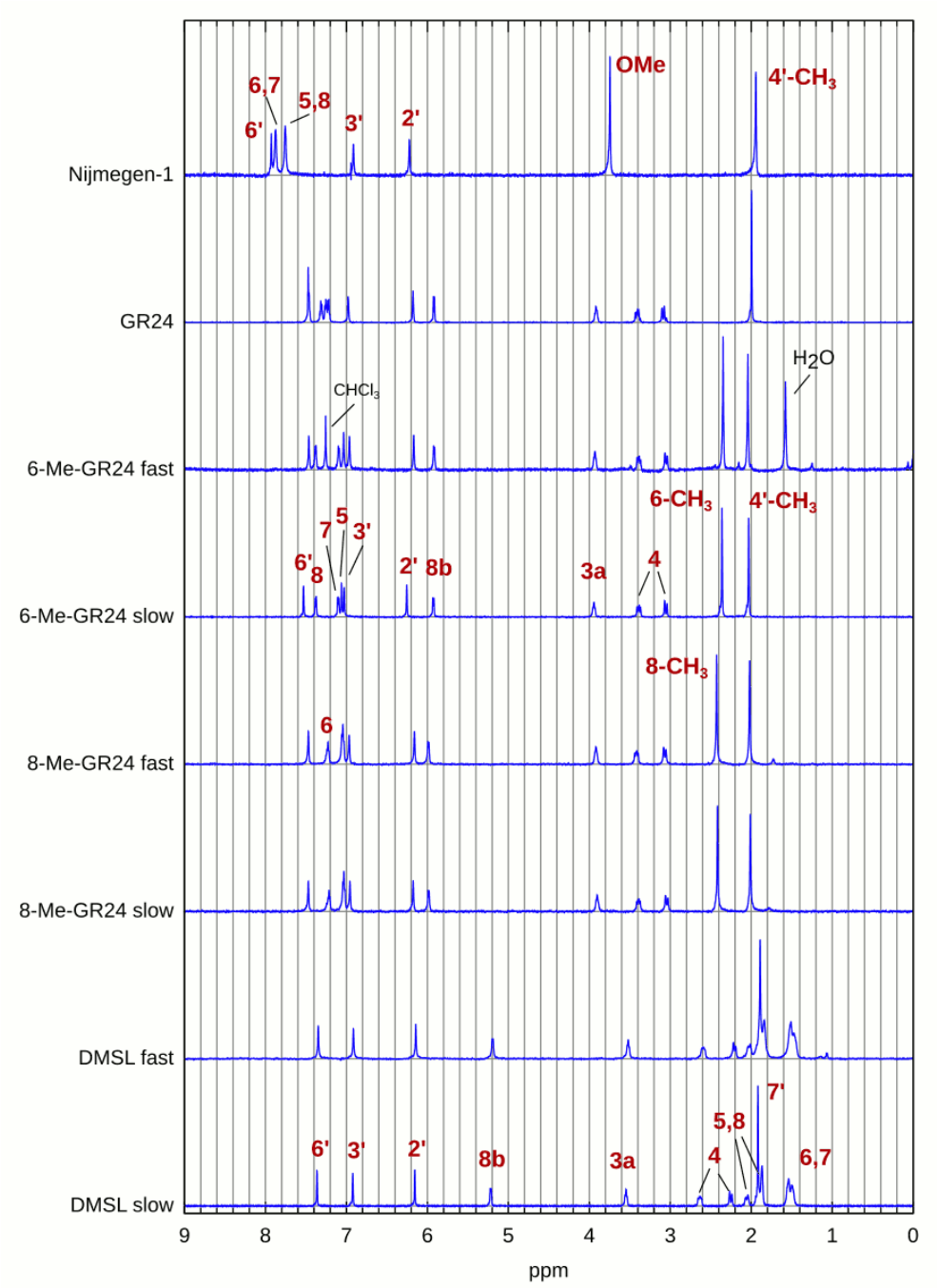

Figure 2.9: ^{1}*H NMR spectra of synthetic strigolactones, measured in the stripline NMR chip*

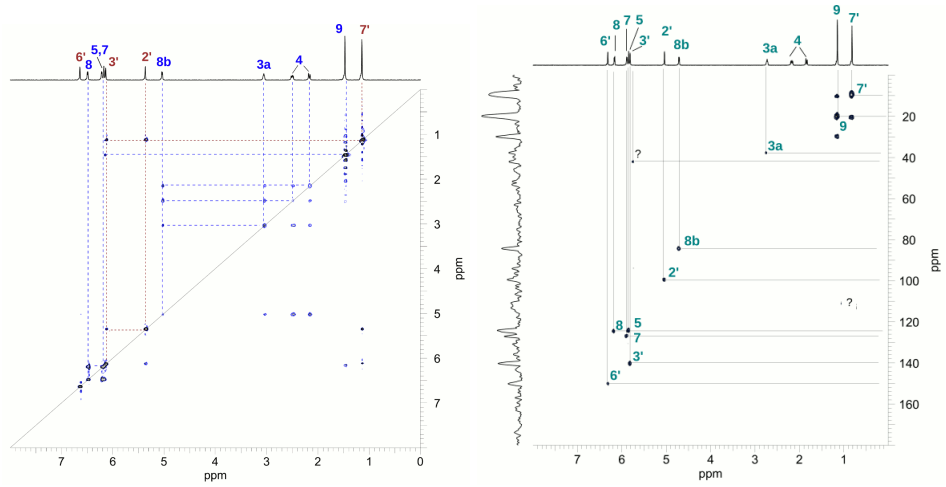

(a) TOCSY (red: D-ring, blue: ABC structure) (b) HMQC

Figure 2.10: TOCSY and HMQC ^{1}H-^{13}C correlation spectrum of strigolactone 6-Me-GR24 slow*, measured in the stripline NMR chip*

available sample quantities small diameter rotors have to be used. Here, we use a 1.2 mm HX MAS probe, in which the samples of more than approximately 1 mg could be fitted.

The CP MAS ^{13}C solid state spectra of Nijmegen-1 and GR24 derivatives are shown in Figures 2.11. Both short and long contact time spectra are shown, for short contact time (in blue) the quaternary carbon atoms give a less strong signal, which is useful information for assigning the peaks. Unfortunately, the spectra of 6-Me-GR24, which was available in only limited amount, and the rotor could not be packed properly, gave not enough SNR to be able distinguish the peaks. This also holds for Nijmegen-1 to a lesser extent, although some peaks can be detected in the spectrum at similar chemical shift position as the GR24 derivative peaks, except for the OMe peak at around 50 ppm, which is not present in the GR24 type molecules. Table A.2 in Appendix A.3 gives an overview of the chemical shifts of the peaks. Using this information in combination with literature[35, 43, 44] and chemical shift estimations made by ChemDraw (CambridgeSoft), the peaks could tentatively be assigned. The atom numbers from Figure 2.8 are indicated at the peaks in the spectra.

The spectra look very similar, as can be expected as the chemical structure of the strigolactones are not very different. Chemical shift differences are most pronounced in the aromatic region (i.e. for atoms 5, 6, 7, 8ab), since the methyl group of 6-Me-GR24

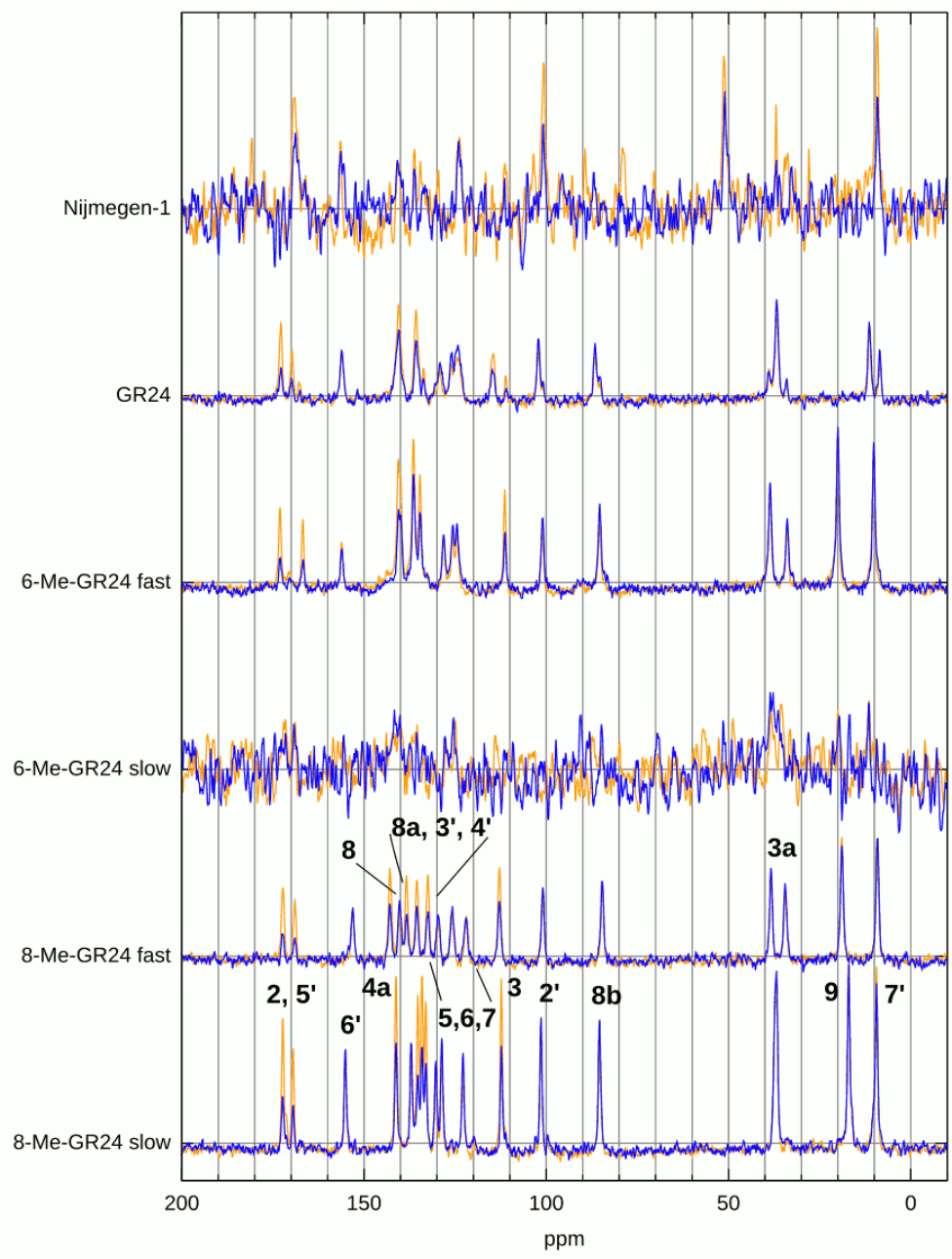

Figure 2.11: Solid state ^{13}C NMR spectra of strigolactones. Short contact time (blue) and long contact time (orange), reduced signal for short contact time indicates quaternary carbon atoms.

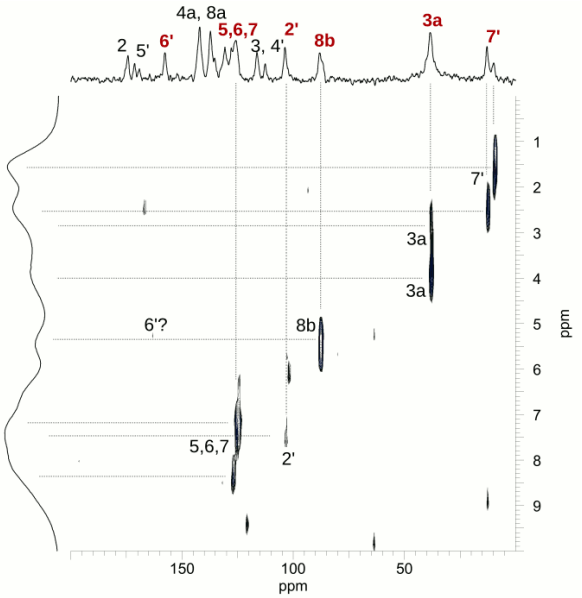

Figure 2.12: HETCOR ^{1}H-^{13}C spectrum of GR24. The carbon atom numbers are given on top, with the carbon nuclei with protons attached in red.

and 8-Me-GR24 is attached to the A-ring. A comparison of the spectra of the slow and fast moving diastereoisomer 8-Me-GR24 shows small chemical shift differences for most of the peaks, see Table A.2 (Appendix A.3), the peak of 3a is split for the fast diastereoisomers. GR24 is a mixture of fast and slow moving diastereoisomers, which is observed in the ^{13}C spectrum as double peaks from the two compounds, most clearly for nuclei from the C- ring and D-ring (7', 3a, 8b, 2' and 3), but possibly also for peaks in the region above 100 ppm, which is more difficult to observe because of crowding and lower peak intensities.

To give an indication of the sensitivity of the measurements, the SNR was calculated from the FID for two samples. For the spectrum of 6-Me-GR24 *fast*, the SNR is approximately 29 with 7000 scans, or corresponding to 0.35 for a single scan. For 8-Me-GR24 *fast*, the SNR is 21 with 7500 scans, or corresponding to 0.25 for a single scan.

For sample GR24 a ^{1}H-^{13}C correlation spectrum was measured, shown in Figure 2.12. The cross peaks from the protonated carbon nuclei could be clearly observed, except for carbon atom 6. Some crowding in the aromatic region is present, the resonances of atoms 5, 6, 7 and 8b overlap.

2.6 Discussion

In this Chapter, a set of small volume samples have been measured in the stripline NMR setup. The resolution of these spectra was 0.5 Hz for a plug of ethanol (70%, single scan) and a linewidth of around 3 Hz can reasonably be achieved for the low concentrated mouse CSF samples with the use of a lock function. Deviations from these linewidths occur, such as 6 Hz for estradiol (10mM), due to not being able to shim properly. The current experiments suffer from having broad linewidths at the bottom of the peaks, which can become a problem for overlapping peaks and low intensity peaks. However, with the recent developments of a Shim-on-Chip[13], higher resolutions can be expected which also improve the SNR, approaching the resolution of 1 Hz obtained in the conventional NMR setup. For the strigolactones, structural differences between GR24, 6-Me-GR24, 8-Me-GR24 and DMSL are reflected in the A ring in Figure 2.8. These shifts are indeed observed in the spectra in Figure 2.9 measured in the stripline NMR, so the resolution is sufficient to obtain this type of structure information.

The sensitivity of the stripline NMR chip is estimated for a 150 nl sample of 70% ethanol, from which an LOD of $8 \cdot 10^{13}$ spins/$\sqrt{Hz}$ is obtained. A ^{1}H NMR spectrum of 150 nl of 10mM 17α-estradiol was obtained accumulating 1024 scans, resulting in a SNR of 205 for the highest intensity peak in the spectrum and 23 for a peak in the aromatic region. Metabolites concentrations in mouse CSF vary between the samples. In sample 1 the lactate concentration is much higher than in the samples 2-4. Part of the other peaks in the spectrum are comparable to the lactate peak, although some are much lower. From sample 1 it was estimated that the lactate concentration is approximately 13.4 mM, with a SNR of 97. A quantitative result within 1% error can be given for a SNR of at least 150, which can be achieved in 2 hours experiment time. However, the glucose peak with a SNR of 24, would need 8 hours for the same accuracy. From the other (not pre-processed) samples, the same order of concentrations are observed from the spectra. Lactate concentrations naturally occurring in human CSF are in the range 0.5 mM to 4 mM[45]. Other metabolites, if detected and identified, can be present in much lower concentration, less than μM range. To be able to analyse these lowly concentrated metabolites, concentrating the sample will be necessary, for example by freezedrying and dissolving in a very small volume of D_2O just fitting the stripline NMR active region.

The amount of sample of strigolactones used for the stripline NMR measurements was

estimated to be 0.3 mg. If all the sample was collected in the solution the maximum concentration in the sample plug would be 1 M. The ^{1}H NMR spectra were acquired accumulating 16, 64 or 1024 scans, which demonstrates that because of the difficulty of working with these small amounts, not in all cases these concentrations were reached. The concentrations are such that ^{1}H NMR measurements are not a problem, a ^{13}C spectrum could not be measured, however. In the next Chapter, ^{13}C spectra were taken from 1.6 M and 2 M solutions in around 15 hours, so a 1 M strigolactone ^{13}C spectrum would take around 2 days to acquire. In this case it would be advantageous to use a larger detection volume, which can be accomplished by scaling up the design of the stripline NMR chip. Assuming that the strigolactone powder that was used in the solid state measurements (around 1 mg) could be dissolved in $CDCl_3$ to a total volume of 2 μl (a 1.5 M solution), this would fit into a scaled up version of the stripline chip, using a commercially available FS capillary of 700 μm inner diameter, and a strip length of 4 mm. The solid state ^{13}C NMR spectra of 6-Me-GR24 *fast* and 8-Me-GR24 *fast* were taken in 7250 scans (averaged), in approximately 10 hours, with a SNR value of 0.3 for a single scan. If the scaled-up stripline NMR chip has a similar performance as the stripline NMR chip in Chapter 3 (section3.3.2), which gave a 0.5 single scan SNR, then it can be estimated that a ^{13}C measurement would be possible in approximately 4 hours. Measuring in liquid state in the stripline NMR chip would have the advantage that linewidths decrease, comparing the spectra in Figure 3.2 in section 3.3.2 with Figure 2.11 a 8-fold increase in resolution is observed for the stripline NMR spectra.

Current developments in microfluidic NMR as well as solid state NMR can be expected to improve resolution and sensitivity so that these type of measurements will be possible in the future. Progress in solid state NMR, such as indirect detection and increasing spinning speed, e.g. with the novel 0.7 mm MAS systems spinning faster than 100 kHz, will boost resolution and sensitivity of the experiments. In addition to ^{13}C NMR measurements, a lot of structural information can be obtained if high resolution ^{1}H NMR spectra can be obtained. Also, miniaturisation is an advantage in the context of small volume samples, such as the high resolution μMAS spinning NMR detector for nanolitre volumes, developed recently[46].

2.7 Conclusion

Many biological samples are available only in limited amount, some sample quantities are typically extremely small by their nature, for example single insect studies, some samples are very expensive or laborious to produce. Miniaturised NMR coils that have an improved sensitivity per amount of sample, can be important tools to enable NMR measurements on these kinds of samples. Here we use a stripline NMR chip with replaceable FS sample capillaries to analyse some examples of mass-limited samples. Plugs of 150 nl enclosed by fluorinert cover the entire detection volume, and a high sensitivity with a good resolution can be obtained. The stripline NMR chip has a limit of detection of $8 \cdot 10^{13}$ spins/$\sqrt{Hz}$ with a resolution of 0.5 Hz for a 70% ethanol plug. Mouse CSF was measured in the stripline NMR setup and compared with conventional NMR results. The SNR and resolution are sufficient to distinguish the peaks in the stripline NMR spectrum. For an estimated lactate concentration of approximately 13.4 mM, an SNR of 97 was obtained in 1024 scans. The enhancement factor for the stripline NMR is 4, taking into account the amount of sample and the SNR in the spectra. Furthermore, three mouse CSF samples were measured without any pre-processing, which resulted in satisfactory spectra as well. During storage part of the samples may have condensed, therefore when measuring fresh mouse CSF without processing the concentrations may be lower and measurement time may be increased. To make optimal use of the enhancement factor of the stripline NMR chip, the sample needs to be concentrated in the detection volume ($f_{obs} = 1$), so the current setup is especially beneficial for samples of approximately the same volume (150 nl). This might be an advantage for living mouse studies, or analysis of other precious or very small volume samples with approximately the size of the detection volume. Since the unprocessed mouse CSF samples are much larger than the detection volume, better results in terms of sensitivity are obtainable in a stripline chip with a detection volume that matches the amount of sample ($\sim \mu$l).

Strigolactones are important plant hormones that play a key role in parasitic weed germination, which dramatically affects food crop. Structure determination of synthesized strigolactones is important for understanding structural requirements for functioning and finding efficient synthetic analogues. The amount of sample that can be synthesized is often very limited. Spectra of 8 synthetic strigolactones were measured using NMR spectroscopy. The samples were analysed in full capillaries in the stripline NMR chip, using a maximum of 0.3 mg of compound. ^{1}H and correlation (TOCSY and HMQC)

spectra could be obtained. Subsequently, solid state NMR ^{13}C spectra were measured of the 6 larger samples (up to about 3 mg) and in addition a HETCOR spectrum of one of the samples. Differences in molecular structure are reflected in the spectra, so these type of measurements can be of help in strigolactone research.
In conclusion, the stripline NMR chip was tested with good results using two examples. The samples consist of sample plugs, either enclosed between fluorinert or covering more than the entire strip length. Using sample plugs between fluorinert, sample volumes smaller than 150 nl can be analysed, which is very suitable for limited or precious samples or when samples can be concentrated. Using a plug larger than the strip length is beneficial when the samples need to be recovered after analysis. The biological samples in this study, as well as many other biological samples, consist of a larger volume than 150 nl, for which a stripline chip with a larger detection volume matching the sample size can further improve sensitivity.

Acknowledgement

The synthetic analogues of strigolactones were received from Dr. Tatsiana Charnikhova (Laboratory of Plant Physiology, Wageningen UR, Wageningen University, the Netherlands). The mouse CSF samples were received as a surplus material from a study 47 by Dr. Anita Dankers (Department of Pharmacology and Toxicology, Radboudumc, Nijmegen, the Netherlands). Hans Janssen (Radboud University Nijmegen, The Netherlands) is thanked for the stripline NMR probe and lock channel development. Dr. Ard Kolkman is acknowledged for measuring the mouse CSF ^{1}H NMR spectrum at the conventional Bruker 600 MHz spectrometer.

References

[1] T. D. W. Claridge, *High-resolution NMR techniques in organic chemistry*, vol. 27 of *Tetrahedron Organic Chemistry*. Elsevier, 2009.

[2] R. M. Fratila and A. H. Velders, "Small-volume nuclear magnetic resonance spectroscopy," *Annu. Rev. Anal. Chem.*, vol. 4, p. 227, 2011.

[3] C. J. Jones and C. K. Larive, "Could smaller really be better? Current and future trends in high-resolution microcoil NMR spectroscopy," *Anal. Bioanal. Chem.*, vol. 402, p. 61, 2012.

[4] D. Hoult and R. Richards, "The signal-to-noise ratio of the nuclear magnetic resonance experiment," *J. Magn. Reson.*, vol. 24, p. 71, 1976.

[5] A. Webb, "Radiofrequency coils in magnetic resonance," *Prog. Nucl. Magn. Reson. Spectrosc.*, vol. 31, p. 1, 1997.

[6] A. Webb, "Radiofrequency microcoils for magnetic resonance imaging and spectroscopy," *J. Magn. Reson.*, vol. 229, p. 55, 2013.

[7] P. J. M. van Bentum, J. W. G. Janssen, A. P. M. Kentgens, J. Bart, and J. G. E. Gardeniers, "Stripline probes for nuclear magnetic resonance," *J. Magn. Reson.*, vol. 189, p. 104, 2007.

[8] J. Bart, J. W. G. Janssen, P. J. M. van Bentum, A. P. M. Kentgens, and J. G. E. Gardeniers, "Optimization of stripline-based microfluidic chips for high-resolution NMR," *J. Magn. Reson.*, vol. 201, p. 175, 2009.

[9] D. L. Olson, J. A. Norcross, M. O'Neil-Johnson, P. F. Molitor, D. J. Detlefsen, A. G. Wilson, and T. L. Peck, "Microflow NMR: Concepts and capabilities," *Anal. Chem.*, vol. 76, p. 2966, 2004.

[10] B. Behnia and A. G. Webb, "Limited-sample NMR using solenoidal microcoils, perfluorocarbon plugs, and capillary spinning," *Anal. Chem.*, vol. 70, p. 5326, 1998.

[11] D. L. Olson, T. L. Peck, A. G. Webb, R. L. Magin, and J. V. Sweedler, "High resolution microcoil 1H-NMR for mass-limited, nanoliter-volume samples," *Science*, vol. 270, p. 1967, 1995.

[12] R. Subramanian, M. M. Lam, and A. G. Webb, "RF microcoil design for practical NMR of mass-limited samples," *J. Magn. Reson.*, vol. 133, p. 227, 1998.

[13] S. G. J. van Meerten, P. J. M. van Bentum, and A. P. M. Kentgens, "Shim-on-Chip design for microfluidic NMR detectors," *Anal. Chem.*, 2018.

[14] A.-H. M. Emwas, R. M. Salek, J. L. Griffin, and J. Merzaban, "NMR-based metabolomics in human disease diagnosis: applications, limitations, and recommendations," *Metabolomics*, vol. 9, p. 1048, 2013.

[15] D. Wishart, "Quantitative metabolomics using NMR," *Trends in Anal. Chem.*, vol. 27, no. 3, p. 228, 2008.

[16] A. Smolinska, L. Blanchet, L. Buydens, and S. Wijmenga, "NMR and pattern recognition methods in metabolomics: From data acquisition to biomarker discovery: A review," *Anal. Chim. Acta*, vol. 750, p. 82, 2012.

[17] E. Garcia, C. Andrews, J. Hua, H. L. Kim, D. K. Sukumaran, T. Szyperski, and K. Odunsi, "Diagnosis of early stage ovarian cancer by ^{1}H NMR metabonomics of serum explored by use of a microflow NMR probe," *J. Proteome Res.*, vol. 10, p. 1765, 2011.

[18] J. S. Smith, T. E. Angel, C. Chavkin, D. Orton, R. Moore, and R. Smith, "Characterization of individual mouse cerebrospinal fluid proteomes," *Proteomics*, vol. 14, p. 1102, 2014.

[19] A. Dossey, S. Walse, J. Rocca, and A. Edison, "Single-insect NMR: A new tool to probe chemical biodiversity," *ACS Chem. Biol.*, vol. 1, no. 8, p. 511, 2006.

[20] M. Gronquist, J. Meinwald, T. Eisner, and F. Schroeder, "Exploring uncharted terrain in nature's structure space using capillary NMR spectroscopy: 13 steroids from 50 fireflies," *J. Am. Chem. Soc.*, vol. 127, p. 10810, 2005.

[21] T. J. Ragan, A. P. Bailey, A. P. Gould, and P. C. Driscoll, "Volume determination with two standards allows absolute quantification and improved chemometric analysis of metabolites by NMR from submicroliter samples," *Anal. Chem.*, vol. 85, p. 12046, 2013.

[22] J. Bart, A. J. Kolkman, A. J. Oosthoek-de Vries, K. Koch, P. J. Nieuwland, J. W. G. Janssen, P. J. M. van Bentum, K. A. M. Ampt, F. P. J. T. Rutjes, S. S. Wijmenga, J. G. E. Gardeniers, and A. P. M. Kentgens, "A microfluidic high-resolution NMR flow probe," *J. Am. Chem. Soc.*, vol. 131, p. 5014, 2009.

[23] L. Liu and K. Duff, "A technique for serial collection of cerebrospinal fluid from the cisterna magna in mouse," *JoVE*, vol. 21, 2008.

[24] J. O. Fleming, J. Ting, S. Stohlman, and L. Weiner, "Improvements in obtaining and characterizing mouse cerebrospinal fluid," *J. Neuroimmunol.*, vol. 4, p. 129, 1983.

[25] P. Eilers, "A perfect smoother," *Anal. Chem.*, vol. 75, p. 3631, 2003.

[26] X. Xie, K. Yoneyama, and K. Yoneyama, "The strigolactone story," *Annu. Rev. Phytopathol.*, vol. 48, p. 93, 2010.

[27] J. A. López-Ráez, R. Matusova, C. Cardoso, M. Jamil, T. Charnikhova, W. Kohlen, C. Ruyter-Spira, F. Verstappen, and H. Bouwmeestera, "Strigolactones: ecological significance and use as a target for parasitic plant control," *Pest Manag. Sci.*, vol. 64, p. 471, 2008.

[28] B. Zwanenburg, S. K. Nayak, T. V. Charnikhova, and H. J. Bouwmeester, "New strigolactone mimics: Structure–activity relationship and mode of action as germinating stimulants for parasitic weeds," *Bioorg. Med. Chem. Lett.*, vol. 23, no. 1, p. 5182, 2013.

[29] B. Zwanenburg and T. Pospíšil, "Structure and activity of strigolactones: New plant hormones with a rich future," *Mol. Plant*, vol. 6, no. 1, p. 38, 2013.

[30] X. Xie, K. Yoneyama, T. Kisugi, K. Uchida, S. Ito, K. Akiyama, H. Hayashi, T. Yokota, T. Nomura, and K. Yoneyama, "Confirming stereochemical structures of strigolactones produced by rice and tobacco," *Mol. Plant*, vol. 6, no. 1, p. 153, 2013.

[31] K. Akiyama, S. Ogasawara, S. Ito, and H. Hayashi, "Structural requirements of strigolactones for hyphal branching in AM fungi," *Plant Cell Physiol.*, vol. 51, p. 1104, 2010.

[32] S. Nomura, H. Nakashima, M. Mizutani, H. Takikawa, and Y. Sugimoto, "Structural requirements of strigolactones for germination induction and inhibition of *Striga gesnerioides* seeds," *Plant Cell Rep.*, vol. 32, p. 829, 2013.

[33] B. Zwanenburg, A. S. Mwakaboko, A. Reizelman, G. Anilkumar, and D. Sethumadhavan, "Structure and function of natural and synthetic signalling molecules in parasitic weed germination," *Pest Manage. Sci.*, vol. 65, p. 478, 2009.

[34] J. W. J. F. Thuring, N. W. J. T. Heinsman, R. W. A. W. M. Jacobs, G. H. L. Nefkens, and B. Zwanenburg, "Asymmetric synthesis of all stereoisomers of demethylsorgolactone. dependence of the stimulatory activity of *Striga hermonthica* and *Orobanche crenata* seed germination on the absolute configuration," *J. Agric. Food Chem.*, vol. 45, p. 507, 1997.

[35] S. Wigchert and B. Zwanenburg, "An expeditious preparation of all enantiopure diastereoisomers of aromatic A-ring analogues of strigolactones, germination stimulants for seeds of the parasitic weeds *Striga* and *Orobanche*," *J. Chem. Soc., Perkin Trans. 1*, p. 2617, 1999.

[36] E. Artuso, E. Ghibaudi, B. Lace, D. Marabello, D. Vinciguerra, C. Lombardi, H. Koltai, Y. Kapulnik, M. Novero, E. G. Occhiato, D. Scarpi, S. Parisotto, A. Deagostino, P. Venturello, E. Mayzlish-Gati, A. Bier, and C. Prandi, "Stereochemical assignment of strigolactone analogues confirms their selective biological activity," *J. Nat. Prod.*, vol. 78, p. 2624, 2015.

[37] G. Nefkens, J. Thuring, M. Beenakkers, and B. Zwanenburg, "Synthesis of a phthaloylglycine-derived strigol analogue and its germination stimulatory activity toward seeds of the parasitic weeds *Striga hermonthica* and *Orobanche crenata*," *J. Agric. Food Chem.*, vol. 45, p. 2273, 1997.

[38] A. W. Johnson, G. Gowda, A. Hassanali, J. Knox, S. Monaco, Z. Razavi, and G. Rosebery, "The preparation of synthetic analogues of strigol," *J. Chem. Soc., Perkin Trans. 1*, p. 1734, 1981.

[39] S. R. Hartmann and E. L. Hahn, "Nuclear double resonance in the rotating frame," *Phys. Rev.*, vol. 128, p. 2042, 1962.

[40] S. Hediger, B. Meier, and R. Ernst, "Adiabatic passage Hartmann-Hahn cross polarization in NMR under magic angle sample spinning," *Chem. Phys. Lett.*, vol. 240, no. 5, p. 449, 1995.

[41] R. Taylor, "Setting up ^{13}c CP/MAS experiments," *Conc. Magn. Reson. Part A*, vol. 22A, p. 37, 2004.

[42] P. Caravatti, L. Braunschweiler, and R. R. Ernst, "HETCOR spectroscopy in rotating solids," *Chem. Phys. Lett.*, vol. 100, p. 305, 1983.

[43] E. M. Mangnus, F. J. Dommerholt, R. L. P. de Jong, and B. Zwanenburg, "Improved synthesis of strigol analogue GR24 and evaluation of the biological activity of its diastereomers," *J. Agric. Food Chem.*, vol. 40, p. 1230, 1992.

[44] J. W. J. F. Thuring, A. A. M. A. van Gaal, S. J. Hornes, M. M. de Kok, G. H. L. Nefkens, and B. Zwanenburg, "Synthesis and biological evaluation of strigol analogues modified in the enol ether part," *J. Chem. Soc., Perkin Trans. 1*, p. 767, 1997.

[45] D. Wishart, M. J. Lewis, and J. A. Morrissey, "The human cerebrospinal fluid metabolome," *J. Chromatogr. B Analyt. Technol. Biomed. Life Sci.*, vol. 871, no. 2, p. 164, 2008.

[46] J. O. Brauckmann, J. W. G. Janssen, and A. P. M. Kentgens, "High resolution triple resonance micro magic angle spinning NMR spectroscopy of nanoliter sample volumes," *Phys. Chem. Chem. Phys.*, vol. 18, p. 4902, 2016.

[47] A. C. A. Dankers, *New insights into the role of breast cancer resistance protein in endocrine and metabolic processes*. PhD thesis, Radboud Universiteit Nijmegen, the Netherlands, 2014.

Chapter 3

Continuous Flow ^{1}H and ^{13}C NMR Spectroscopy in Microfluidic Stripline NMR Chips

Anna Jo Oosthoek - de Vries, Jacob Bart, Roald M. Tiggelaar, Johannes W. G. Janssen, P. Jan M. van Bentum, Han J. G. E. Gardeniers and Arno P. M. Kentgens

This chapter has been published in Analytical Chemistry, **89** (4), pp 2296-2303 (2017)

Abstract

Microfluidic stripline NMR technology not only allows for NMR experiments to be performed on small sample volumes in the submicroliter range, but also experiments can easily be performed in continuous flow because of the stripline's favourable geometry. In this study we demonstrate the possibility of dual-channel operation of a microfluidic stripline NMR setup showing one- and two-dimensional ^{1}H, ^{13}C and heteronuclear NMR experiments under continuous flow. We performed experiments on ethyl crotonate and menthol, using three different types of NMR chips aiming for straightforward microfluidic connectivity. The detection volumes are approximately 150 and 250 nl, while flow rates ranging from 0.5 μl/min to 15 μl/min have been employed. We show that in continuous flow the pulse delay is determined by the replenishment time of the detector volume, if the sample trajectory in the magnet toward NMR detector is long enough to polarise the spin systems. This can considerably speed up quantitative measurement of samples needing signal averaging. So it can be beneficial to perform continuous flow measurements in this setup for analysis of e.g. reactive, unstable or mass-limited compounds.

3.1 Introduction

Nuclear Magnetic Resonance (NMR) spectroscopy is a powerful technique and an important tool for complex molecular structure determination and mixture analysis in biology and chemistry. However, because of the inherent low sensitivity of the technique[1], relatively large amounts of sample are needed in order to prevent very long signal averaging for obtaining meaningful spectra. Since the signal-to-noise ratio (SNR) of the measurement scales linearly with the number of spins contributing to the signal, but scales only with square root of the number of scans, for mass limited samples it can become a problem to achieve sufficient SNR in the time available. Moreover, if the sample volume does not match the coil volume (typically 500 μl for commercial NMR probes), substantial dilution of the sample is needed, and as a consequence the signal of the sample may be obscured by the signal of the solvent. Furthermore, the composition of the sample itself should be constant during the acquisition in order to measure a representative spectrum. In some cases, e.g. for fast reactions and/or long measurements, such as 2D or ^{13}C experiments on unstable compounds, changes in composition of the sample during the total measurement time result in spectra that reflect only an approximation of the average composition of the sample.

A possible solution to these problems is miniaturisation, as reducing the diameter of the NMR coil increases the sensitivity per amount of spins[1, 2]. Therefore, since the introduction of the first solenoidal microcoils[3, 4] and the first planar microcoils[5], microcoils are an extensively explored topic in NMR research[6, 7, 8, 9, 10]. In the past decade, several approaches to microscale NMR include: solenoid coils[11, 12, 13], planar coils[14, 15], Helmholtz coils[16] and striplines/microslots[17, 18, 19, 20, 21, 22].

Microcoils are not only more suited for measuring mass-limited samples, but depending on the design, also in situ measurements in a microfluidic setup are facilitated. In this contribution we investigate the use of stripline NMR microcoils coupled to a standard microfluidic setup for continuous flow NMR. Microfluidic continuous flow NMR can be of importance in chemistry[23], where in-line analysis can be advantageous especially in applications where samples are unstable or in quantitative high-throughput analysis. Another approach in microfluidic NMR is remote detection NMR[24, 25, 26], where separation of encoding and detection steps results in a higher sensitivity. Some applications of microfluidic NMR focus on in situ monitoring of reaction kinetics (including 2D structural analysis, e.g. in synthetic chemistry, metabolic studies, drug delivery), continuous flow quality control, and fast quantitative analysis (unbiased for samples with long relaxation times). Also, microfluidic NMR enables the hyphenation of NMR to chromatographic separation techniques[3, 27, 28, 29]. The monitoring of chemical reactions has successfully been performed in a microcoil NMR setup by several groups[13, 30, 31, 32, 33]. The small volumes permits an efficient use of solvents, which is less expensive, e.g. when deuterated solvents are used, and environmentally friendly because of the low solvent consumption. When a mass-limited sample can be completely dissolved in the small microcoil detection volume, one can work with higher analyte concentrations than when using the larger conventional NMR detection volume. When using higher analyte concentration, methods, such as solvent suppression, become easier. It should be noted that if sufficient sample with a fixed concentration is available, conventional NMR gives a higher sensitivity, but for a limited amount of sample the sensitivity is better for the smallest coil matching the sample volume[1, 34].

The stripline resonator is a straight flat wire that is used to generate and detect the radio frequency (rf) fields in the NMR experiments. The stripline NMR chip is manufactured using microfabrication techniques such as photolithography, electroplating and wet chemical etching.

The ground planes (”shields”) surrounding the stripline enclose the generated rf B_1 field. The boundary conditions imposed by the ground planes arrange the field lines

parallel to the stripline surface, as a result the B_1 field is homogeneous, which is crucial for complex pulse sequences. The sample volume is scaled down to 150 nl in the design used in the present study. Standard microfluidics can be connected to the stripline NMR chip, making it possible to continuously flow the sample during acquisition. Continuous-flow or recycled-flow NMR[35, 36] can be advantageous, for example for samples that have long relaxation times, mass-limited samples or unstable samples.

The stripline design is scalable, so one can use an optimal volume for each specific application. We have previously shown the application of this setup for real-time monitoring of fast chemical reactions, acquiring steady state ^{1}H signals during the first minutes of the reaction[37]. Furthermore, the upright geometry of the stripline is particularly convenient for realising a flow setup with straight capillaries running through the probehead.

Proton NMR spectra are very information-rich as such. However, more detailed information can be obtained from two-dimensional (2D) NMR, ^{13}C NMR and/or heteronuclear NMR experiments. Investigating the correlations within the molecules and the surrounding of the carbon nuclei is of considerable use in molecular structure determination. Particularly for the analysis of mass-limited complex molecules or mixtures, the addition of an X-channel is a very useful feature. Here, the possibility to add flow is particularly helpful to overcome SNR issues due to long T_1 relaxation times of X-nuclei compared to ^{1}H spins. Finally, for in situ monitoring of fast reactions the higher resolution of, e.g. ^{13}C spectra can be a valuable asset. In this paper we demonstrate, as a proof of principle, some common ^{1}H 2D, ^{13}C and heteronuclear NMR experiments, during flow of the model compounds ethyl crotonate and menthol in a microfluidic stripline probe.

3.2 Experimental

3.2.1 Chemicals

Ethyl crotonate (99%) and menthol (99%) were obtained from Sigma-Aldrich and used without further purification. Chloroform-d_3 + 0.05%v/v TMS (Cambridge Isotopes Laboratories, Inc.) was used as a solvent. A 20 vol% ethyl crotonate solution in chloroform-d_3 (1.6 M) and a 30 vol% menthol solution in chloroform-d_3 (2 M) were used for the stripline NMR flow experiments. For the ^{13}C channel, pulse length

and decoupling parameters were set up by using a 1 M D-glucose-1-^{13}C (CAMPRO Scientific, Veenendaal, The Netherlands) solution in D_2O.

3.2.2 Stripline rf-coil

The stripline rf-coil[17, 20] consists of a copper strip through which the radio frequency (rf) current runs (see the pictures in Figure 3.1). In the middle part of the chip, the width of the strip is constricted to 0.6 mm (for a section of 3 mm length) in order to enhance the rf field strength in this area and therefore localise detection to this area. The boundaries of the resonator are formed by flat copper shielding layers parallel to the strip, so the magnetic field lines are arranged parallel to the surface. In the region of homogeneous and high B_1 field, two microfluidic microchannels run along both sides of the strip. In the experiments described here, only one of the microchannels is used; however, the other microchannel can be used, e.g. for a reference sample or D_2O for the locking of the NMR spectrometer.

The stripline chips **a**, **b** and **c** used in the present work are displayed in Figure 3.1; the design differs from the design that was described in our previous work[20]. Technical details can be found in Appendix B.1. The design of chips **a** and **c** was motivated by aiming for straightforward connection of microfluidics and a higher filling factor. The substrates are borosilicate glass into which the microchannels are etched in such a way that optimal use is made of the space between stripline and shielding. The inlet and outlet are positioned on the top and bottom of the chips and flow is enabled by fused silica (FS) capillaries glued into the chip, which ensures a convenient microfluidic connection. Chip **c**, which has a detection volume of approximately 215 nl, was fabricated first, however, it did not give as good sensitivity results as expected. Chip **a** was made from thinner substrates in order to make a smaller detection volume of 165 nl. The sensitivity improved, but unfortunately the chip turned out to be fragile, so that leakages occurred in the substrate itself as well as in the connecting capillaries. For chip **b**, FS substrates are used, because this material has a better dielectric performance, so that dielectric losses from the substrate that affect the sensitivity can be avoided. Chip **b** was designed to be more robust, with a diced channel which contains a separate and replacable FS capillary with standard dimensions to make leak-proof and simple connection to a microfluidic setup or use of a sample plug in the capillary, so that a detection volume up to 145 nl results. The observe factor is the fraction of the sample volume from which the NMR signal is observed[34], which is high when sample plugs are

used, since up to 100% of the sample can be placed in the detection volume. However, the filling factor, defined as the part of the detection volume which is occupied by the observed part of the sample[34], is lower in chip **b** as the space between stripline and shielding is not as efficiently used as in chips **a** and **c**. The spectral resolution obtained with chip **b** is not as good as expected, which is attributed to irregularities in the microfluidic channel resulting from the dicing procedure. Nevertheless, considering the benefits of the design of chip **b**, it is worthwhile to explore the possibilities of this chip, e.g., the chip is directly accessible from the outside allowing not only flow experiments, but it is also possible to use a piece of capillary as a tiny NMR tube for mass-limited samples. Since having a high resolution is not as critical in ^{13}C NMR measurements as in ^{1}H NMR measurements, in this work we demonstrate chip **b** for the ^{13}C experiments. Descriptions of the fabrication of the chips **a** and **c** are given in Ref. 38 and of chip **b** in Appendix B.2.

The stripline chips can be placed in one of two homebuild probes; a single resonance probe with a ^{1}H channel and a double resonance probe with a ^{1}H channel and a variable frequency X-channel. In order to enable continuous flow, a syringe pump is attached to the inlet and outlet capillaries via standard microfluidic components. Information regarding the probeheads and microfluidics can be found in Appendix B.3 and B.4.

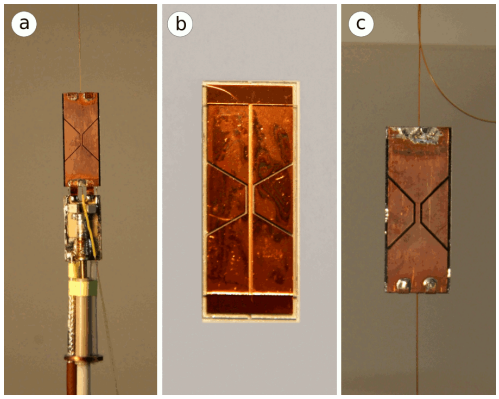

*Figure 3.1: NMR stripline chips used in this study: chip **a**, chip **b** and chip **c**.*

3.2.3 Acquisition and processing

The spectra were taken at room temperature on a VNMRS 600 MHz Varian NMR spectrometer with VNMRJ software. MatNMR[39] was used for data processing and

plotting, and ACD/NMR Processor (Advanced Chemistry Development, Inc.)[40] was used for plotting of the correlation spectra.

3.3 Results and Discussion

3.3.1 Practical Considerations

An important feature of in situ microfluidic NMR measurements is that by continuously flowing the sample through the detection volume during acquisition, the spins that have received an rf pulse are continuously replaced by spins with thermal equilibrium polarisation that have not yet received an rf pulse. The apparent relaxation delays of the experiment are affected, as both the observed spin-lattice relaxation time (T_1^{obs}) and the observed spin-spin relaxation time (T_2^{obs}) decrease[35, 41, 42]. The stationary value of T_1 reflects the time constant for the spins to return to thermal equilibrium after receiving an rf pulse, which poses limitations on the repetition rate. However, when the analyte flows through the detection area during acquisition, the spins can be refreshed faster than the stationary value of T_1, the recycle delay between scans can be shortened. In effect, measurement time can be decreased by using continuous flow during acquisition for samples with long T_1 relaxation times. At a moderate flow rate of 5 μl/minute, the detection volume of 150 nl is refreshed in almost 2 s, whereas for the 215 nl detection volume it takes 3 s to completely replenish the detection volume. At a flow rate of 15 μl/minute this retention time decreases to 0.6 and 1 s, respectively. The repetition rate of the scans can be increased, and thereby the signal-to-noise ratio per unit time. Here it is assumed that the sample flows linearly through the channel, but in reality a more complicated flow profile arises because of the laminar pressure-driven flow. The part of the sample close to the walls of the capillary has a lower flow rate because of the parabolic Poiseuille flow profile, while the center part has a higher flow rate. This might affect the accuracy of quantifiability of the experiments.

From the moment the analyte flows into the magnet until the detection scan in the stripline, polarisation build-up takes place. When the flow rate increases, the time in the magnet is shortened and it is important to verify that the time for polarisation build-up is long enough to reach the thermal equilibrium polarisation. In order to fully polarise the spins in the sample, a build-up time of 5*T_1 is needed. In our setup the sample flows through a 250 μm inner diameter capillary of approximately 60 cm long before arriving at the stripline. At the highest used flow rate of 15 μl/minute,

the build-up time is still 37.5 s, long enough for most spins in our samples to achieve thermal equilibrium polarisation. A longer build-up time can easily be established by increasing the volume of the analyte inside the magnet before reaching the stripline, e.g. by using a longer capillary trajectory inside the magnet toward the NMR detector. Flowing the sample out of the detection area during acquisition can result in line broadening, since the recorded free induction decay (FID) is shortened by nuclear spins flowing out of the detection area during acquisition. When the residence time of spins in the detection coil decreases, the effective decay time of the FID decreases, so that the observed relaxation time T_2^{obs} decreases as well[42]. The observed relaxation time depends on the residence time τ and the stationary value of the relaxation time T_2^{stat}: $\frac{1}{T_2^{obs}} = \frac{1}{T_2^{stat}} + \frac{1}{\tau}$. For the smallest detection volume (145 nl) and the highest flow rates (15 μl/minute) an estimated increase of $\sim$ 0.4 Hz can be expected for line widths of approximately 3 Hz (full-width at half-maximum). In the present setup and for the used flowrates, this broadening effect does not significantly affect the spectra. A broadening of 1 Hz, i.e. from 3 to 4 Hz, would be expected at flow rates of approximately 30 μl/minute.

3.3.2 One-dimensional ^{1}H and ^{13}C spectra

NMR measurements can be performed, while the solution is flowing at constant flow rate through the stripline microchannel. The proton spectra of ethyl crotonate and menthol during flow are shown in Figure B.5 in Appendix B.5. The spectra can be assigned in agreement with the literature[43, 44]. We find a resolution of 2.8 Hz for ethyl crotonate and 2.7 Hz for menthol (measured full-width half-maximum). No significant line broadening due to flow was observed for the employed flow rates.

We tested the ^{13}C channel of the HX dual channel probe with chip **b**. The experiments were first optimised using a 1 M ^{13}C-labelled D-glucose-1-^{13}C solution. The 90° pulse was found to be 3.5 μs using 240 W rf power. The decoupler is set to 2W WALTZ-16 proton-decoupling with NOE enhancement. To determine the sensitivity of the ^{13}C channel, a spectrum accumulating 1000 scans was acquired for this test sample, from which a signal-to-noise ratio of 0.5 for a single scan was deduced. This corresponds to a limit of detection (LOD) of approximately $1 \cdot 10^{15}$ spins/$\sqrt{Hz}$ for the ^{13}C nuclei, defined by the number of spins needed in 1 Hz bandwidth in order to obtain a signal to noise ratio of 1[17].

After finding the optimal pulse and decoupling settings, stopped flow ^{13}C measurements

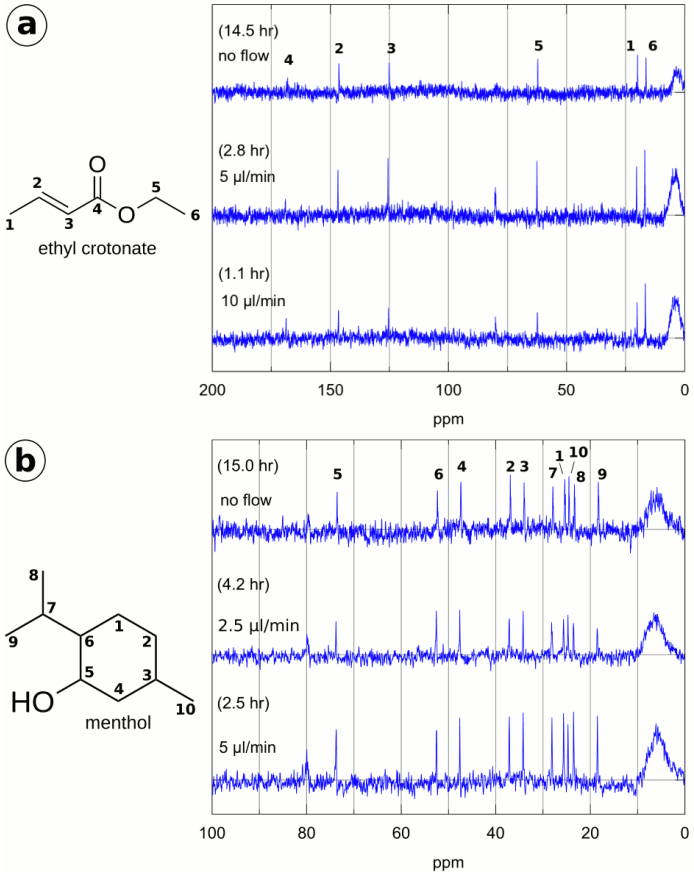

Figure 3.2: ^{13}C *measurements using stopped flow or continuous flow, with a) ethyl crotonate (20 vol%) and b) menthol (30%). The HX dual channel probe fitted with chip* ***b*** *was employed. Each spectrum was recorded by accumulating 4096 scans. For increasing flow rates, the repetition rate was increased using shorter recycle delays and acquisition times. Ethyl crotonate was measured with a recycle delay of 12 s without flow, which decreased to 1.5 and 0.5 s, for 5 µl/min and 10 µl/min flow rates, respectively. The acquisition time was 0.25 s for stopped flow and decreased to 0.1 s for the highest flow rate. Overall, this decreased the experiment time from 14.5 to 1.1 h. Menthol was measured with a recycle delay of 12.5 s without flow, and 3 and 1.8 s for 2.5 µl/min and 5 µl/min flow rates, respectively. The acquisition time was 0.25 s for the measurement without flow and 0.1 s for the two measurements in flow. Measurement time decreased from 15.0 to 2.5 h.*

of ethyl crotonate (20 vol%) and menthol (30%) were successfully performed, as displayed in Figure 3.2. Relaxation times T_1 can be very long for ^{13}C nuclei, for protonated carbon atoms the values lie typically in the range from 0.1 - 10 s, whereas quaternary carbon atoms have values ranging from 10 up to 300 s[45].

For ethyl crotonate, we found experimental T_1 relaxation times varying between 6 s and 18 s (quaternary carbon 4 in Figure 3.2a), i.e. the relaxation delay in the stopped-flow experiments was too short to ensure quantitative interpretation of the resonances. In continuous flow NMR, the sample in the detection volume is completely refreshed faster than the relaxation time T_1, so the recycle delay can be shortened and thus the overall measurement time significantly decreased for slow relaxing nuclei[41]. At a flow rate of 10 μl/min, the sample has been inside of the magnet for 56 s, which is equivalent to $9T_1$ for the fastest relaxing nuclei (T_1 is 6 s) and $3T_1$ for the quaternary carbons (T_1 is 18 s) of ethyl crotonate. We measured a spectrum acquiring 4096 scans in 14.5 h using a recycle delay of 12 s between scans in the case of stopped flow and could obtain a similar spectrum in 2.8 h at 5 μl/min flow rate and in 1.1 h at 10 μl/min flow rate using a recycle delay of 1.5 and 0.5 s respectively. During continuous flow, the line widths of the peaks increased from approximately 4 Hz in the stopped flow spectra to around 7-8 Hz under continuous flow conditions. The ^{13}C T_1 values for menthol varied from 2 to 6 s. The stationary (stopped flow) measurement of 4096 scans took 15.0 h with a recycle delay of 12.5 s, whereas this took only 4 h at a flow rate of 2.5 μl/min and 2.5 h at a flow rate of 5 μl/min, using a recycle delay of 1.8 s. As a measure of accuracy of the experiments, the peaks in the spectra have been integrated after peak deconvolution of the baseline corrected spectra. The standard deviations for the peaks are 8%, 9% and 10%, respectively, for the menthol spectra acquired at flow rates of 5 μl/min, 2.5 μl/min and stopped flow. The standard deviations for the peaks of ethyl crotonate are 36%, 10% and 12% for the experiments using flow rates of 10 μl/min, 5 μl/min and stopped flow.

In order to obtain quantitative results, all spins in the detection volume should be fully polarised, i.e. have been in the magnetic field for 3-5 T_1 before a pulse is applied, to fully contribute contribute to the signal. In these experiments, the repetition rate is somewhat higher than the time for completely refreshing the detection volume. Furthermore, the laminar Poiseuille flow profile causes a variation in the velocity of the flow that may cause a small decrease in the intensity for nuclei with a T_1 larger than the recycle delay. However, this is only observed for peak 4 of ethyl crotonate, the T_1 value of this quaternary carbon is 18 s, which is much larger than the repetition

rate. The other carbon atoms of ethyl crotonate have T_1 values of around 6 - 7 s, and no effect of decreasing intensity with changing flow rate is found. The T_1 values of menthol are around 6 s for three of the nuclei and around 3 s for the rest. In the stopped flow experiment, the peaks of carbon atoms with a shorter T_1 have a higher intensity (averaged 105%) than the peaks of carbon atoms with a longer T_1 (averaged 90%). For the measurements in continuous flow this difference is not present.

The average value of the SNR (defined by the peak height divided by the rms (root-mean-square) of the noise over a 200 Hz bandwidth) of all peaks in the spectrum except quaternary carbon peak 4 is 10.6 for the stopped flow experiment and increases to 15.2 and 13.5 for the spectra measured in 5 and 10 μl/min flow rates, respectively. The lowest intensity peaks have an SNR of 8.5, 12.1 and 10.0 for the stopped flow, 5 and 10 μl/min flow measurements, meaning that if we aimed for an SNR of at least 10 the spectra could have been obtained in 20 h, 2 h or 1 h under the given flow conditions. For menthol the average SNR measured in stopped flow was 9.3, which increased under continuous flow conditions to 13.1 and 16.0 for 2.5 and 5 μl/min flow, respectively. The lowest measured SNR was 8.0, 10,5 and 13.5 for stopped flow, 2.5 and 5 μl/min flow, so that a spectrum with a minimum SNR of 10 could have been measured in 23.5 h, 3.5 h and 1.4 h, respectively.

Applying continuous flow during the acquisition consumed 750 μl for experiments using 2.5 μl/min and 5 μl/min flow rate and 600 μl for the experiments using 10 μl/min flow rate. Clearly a setup flowing in fresh sample continuously, as in the current setup, is not feasible for mass-limited samples. In that case, flow NMR is still feasible but with a small storage volume close to the stripline. The size of the storage volume for optimal SNR is then a trade-off between sample availability and length of T_1^{stat}.

We did not further increase the flow rate to speed up the measurement, because it was experimentally observed that a delay between scans is needed to take into account the decoupling period before acquisition and the duty cycle of the decoupler to prevent heating of the detection area of the chip.

Finally, it has to be noted that the resolution obtained with chip **b** is suboptimal, probably because of susceptibility broadening, which is attributed to imperfections in the microchannel as a result from the dicing procedure disturbing the B_0 homogeneity. It is expected that a modification to the stripline NMR chip fabrication process which avoids the dicing procedure will result in a more homogeneous B_0 field, so that a higher spectral resolution can be achieved. This will further enhance the effective signal-to-noise ratio of the spectra, so that the experimental time to achieve the same

SNR at a given resolution can be further decreased.

3.3.3 Two-dimensional correlation spectroscopy

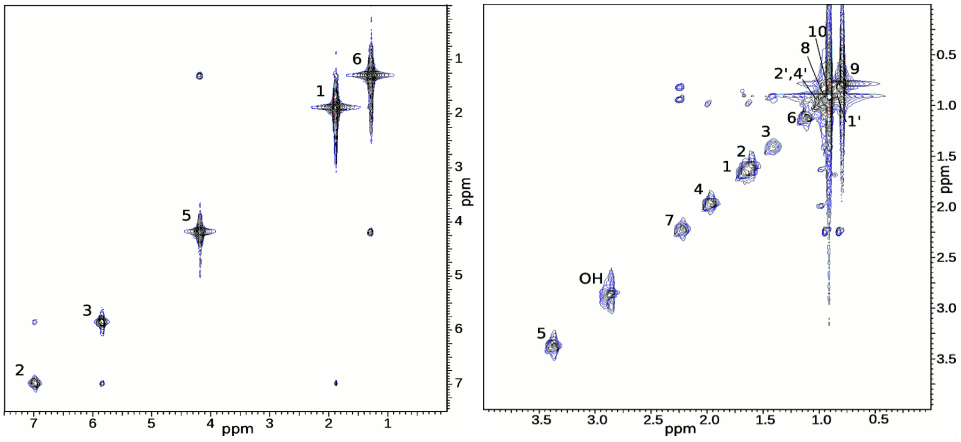

(a) Ethyl crotonate, 15 μl/min (b) Menthol, 1 μl/min

*Figure 3.3: Continuous flow COSY measurements at (a) 15 μl/min flow rate for ethyl crotonate (20 vol%) and (b) at 1 μl/min flow rate for menthol (30%), performed in the ^{1}H probe fitted with chip **a**. Both spectra were taken accumulating 4 scans for 256 t_1-increments. A relaxation delay of 1 s was taken into account for ethyl crotonate (20 vol%) using 15 μl/min flow and 2 s for menthol (30%) at a flow rate of 1 μl/min. The experiment time was 30 minutes for ethyl crotonate and 47 minutes for menthol. Zero filling up to 8192 x 4096 points and a line broadening of 3 Hz for the direct dimension and 5 Hz for the indirect dimension was applied for ethyl crotonate and 1 Hz broadening and a sine-function for menthol.*

For structural elucidation, two-dimensional NMR is a valuable addition to the one-dimensional NMR experiments. Common experiments are correlation spectroscopy (COSY[46]) and total correlation spectroscopy (TOCSY[47]). Both experiments show correlations of proton spins within the molecule. A COSY spectrum shows cross peaks for directly coupled spins over one or more bonds, whereas a TOCSY spectrum also can be used for studying longer range couplings depending on the mixing time.
COSY and TOCSY spectra have been acquired both at low and high flow rates as shown in Figures 3.3 and 3.4. Considering the small molecules, we used short mixing times (50 ms) with an MLEV17[48] spinlock for the TOCSY. The line widths are around 5 Hz in the F2 dimension and 10 Hz in the F1 dimension for the TOCSY spectra. For the COSY spectra, however, the cross peaks are around 30 Hz in the F1 dimension. In COSY experiments, the cross peaks have an antiphase absorption lineshape, while

the diagonal peaks have a broad, dispersion lineshapes. For larger line widths, the wide tail of the diagonal peak may obscure the cross peaks and the intensity of the cross peaks may be diminished due to the antiphase lineshapes. Cancellation of the cross peaks can arise from these lineshapes and is a known disadvantage of COSY experiments[43]. TOCSY experiments do not suffer from these cancelation effects for broad lines and are therefore more preferred. So it is interesting to perform TOCSY experiments in the stripline chip, especially in the case of unstable samples or reaction monitoring in continuous flow, if the sample is not stable during the acquisition time of two-dimensional NMR experiments in conventional NMR. Alternatively, mass-limited samples can be measured in a static plug in a FS capillary in chip **b**, as described before.

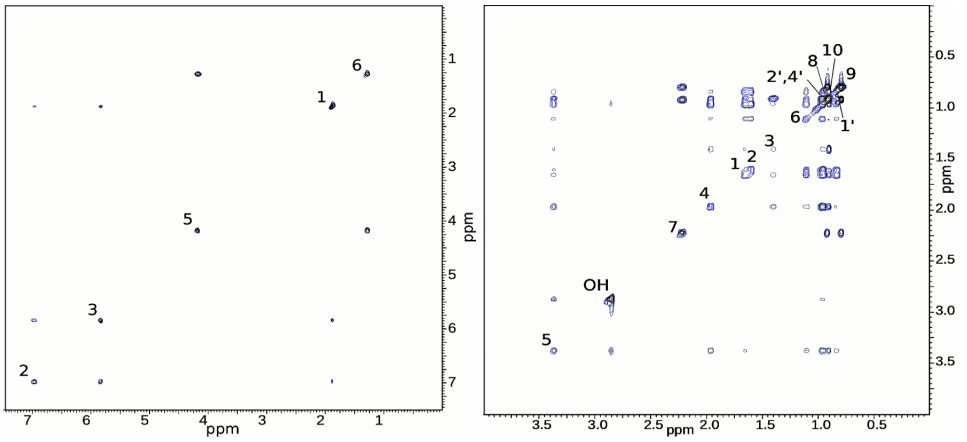

(a) Ethyl crotonate, 1 μl/minute

(b) Menthol, 15 μl/minute

*Figure 3.4: Continuous flow TOCSY measurements, at a flow rate of (a) 1 μl/min for ethyl crotonate and (b) 15 μl/min for menthol, performed in the ^{1}H probe fitted with chip **a**. (a) 4 scans for 512 t_1-increments were acquired for ethyl crotonate (20 vol%) and (b) 4 scans and 256 increments for menthol (30%). For ethyl crotonate a recycle delay of 3 s was taken into account. The experiment time was 4 h and 20 min. For menthol the recycle delay was 1 s and the experiment time was 1 h and 30 min. For both experiments, a mixing time of 50 ms using an MLEV17 spinlock and a trim pulse of 2 ms was used. Zero-filling up to 8192 x 2048 and a line broadening of 1 Hz was applied in both directions.*

Finally, double-resonance experiments can be performed in the dual-channel probe providing relevant structural information. Heteronuclear multiple-quantum correlation (HMQC)[49] spectroscopy correlates proton and carbon spins that are directly coupled. After establishing the optimal decoupling and pulse length parameters on D-glucose-1-^{13}C, HMQC experiments were performed for both model compounds using low (0.5 μl/min) and medium (7 μl/min) flow rates (Figure 3.5). The experimental time for the measurement of ethyl crotonate at a 7 μl/min flow rate, was 25 h with a consumption of 10 ml solution. The menthol spectrum was obtained in 69 h, consuming 2 ml of solution (at 0.5 μl/min).

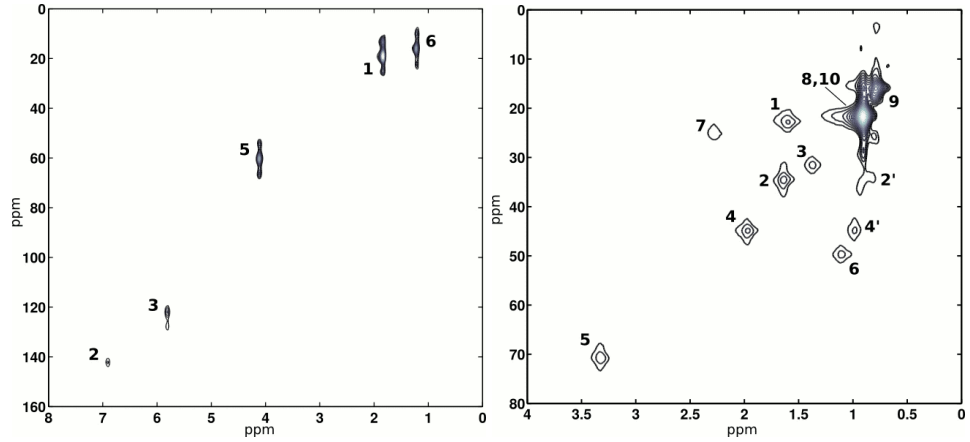

(a) Ethyl crotonate, 7 μl/min (b) Menthol, 0.5 μl/min

Figure 3.5: HMQC spectra of (a) ethyl crotonate (20 vol%) and (b) menthol (30%) with flowrates of 7 μl/min for ethyl crotonate and 0.5 μl/min for menthol, performed in the HX channel probe and chip ***c****. We acquired 400 scans for 64 increments for ethyl crotonate and 512 scans with 128 increments for menthol. The recycle delays were 1 and 1.2 s, respectively, and a BIRD delay of 0.6 and 0.5 s. The pulse sequence delays were adjusted to a one-bond ^{1}H-^{13}C coupling constant of 145 Hz.*

3.3.4 Comparison of the chips

Good resolution and sensitivity are crucial in obtaining informative NMR spectra. Since the copper stripline structure is defined with the same geometry (i.e. a 3mm long constriction) in each of the chips employed in this study, the results can be directly compared to give information about their performance.

The sensitivity of the stripline NMR chip has a substantial effect on the efficiency of the measurement, i.e. the signal-to-noise ratio in the spectrum obtained per unit time.

A good measure of sensitivity is the limit of detection (LOD), defined as the number of spins needed in 1 Hz bandwidth in order to obtain a signal to noise ratio of 1[17]. The LOD for protons (LOD_H) is measured from a single-scan ethanol free-induction-decay (FID). For proton detection in chips **a** and **b**, we found a similar LOD_H of $2.5-4\cdot10^{13}$ spins/$\sqrt{Hz}$ respectively, whereas for chip **c** a LOD_H of $2\cdot10^{14}$ spins/$\sqrt{Hz}$ was found. The significantly lower detection limit (LOD_H) of chips **a** and **b** indicates a higher sensitivity of these chips compared to the sensitivity of chip **c**. The theoretically expected LOD_H is around $2\cdot10^{13}$ spins/$\sqrt{Hz}$ for all chips but does not take into account dielectric losses due to the substrate (which can be rather large due to inclusion of, e.g. metal-oxide impurities); therefore the low sensitivity of chip **c** is attributed to the non-optimal substrate[38].

In terms of resolution, chip **a** in Figure 3.1 was found to perform best with a line width of less than 3 Hz for the ^{1}H spectra. In the single-scan spectra of ethyl crotonate and menthol, we find for ethyl crotonate the following line widths (full-width half-maximum): chip **a** 2.7 Hz, chip **b** 7 Hz, chip **c** 9 Hz (estimated via deconvolution of the multiplets). Similar results were estimated from the menthol spectra, where, due to overlapping peaks could not be as precisely defined. Another comparison of the spectral resolution can be made from a single-scan spectrum of ethanol (70%), having the advantage that since the concentration is high a large signal is obtained; therefore, the shimming procedure is uncomplicated. For single-scan ethanol (70%) spectra the best resolution of chip **a** is approximately 2 Hz, for chip **b** and chip **c** the line width is around 3 Hz. The peak shape of chip **b**, however, contains a broad foot structure and other irregularities.

The signal-to-noise ratio (SNR) in the spectrum obviously depends on the amount of sample (concentration per unit volume vs total volume) but is also affected by the LOD and resolution provided by each chip. For ethyl crotonate, the SNR is calculated from the single scan ^1H spectrum using the methyl group 6 in Figure 3.2a, Figure B.5a in Appendix B.5, resulting in 1080 for chip **a**, 168 for chip **b** and 446 for chip **c**. For menthol we find: chip **a** 3308, for chip **b** 238 and chip **c** 313, calculated using the resonances of the methyl groups 8) and 10) in Figure 3.2b, Figure B.5b in Appendix B.5. In conclusion, the SNR for chip **a** is significantly better than the SNR for chips **b** and **c**. Furthermore, we find that although the detection limit (LOD_H) of chip **b** is only slightly higher than for chip **a**, in the spectrum a relatively low SNR is found. The lower SNR in the spectrum is attributed to the loss of signal in the broad foot of the peaks and the relatively low spectral resolution, which decreases the intensity of the

signal in the spectrum.
Overall, chip **a** gives the best results, combining a high resolution with high sensitivity. Currently, work is in progress to improve the performance of chip **b**, as according to theoretical calculations it should be possible to increase the signal-to-noise ratio in the spectrum by an order of magnitude. The design of chip **b** would enable easier measurement of small volume samples, since a sample plug can be positioned offline in the exchangeable FS capillary.

3.3.5 Approach for mass-limited samples

For mass-limited samples it is necessary to decrease the total sample volume that is used, therefore we currently investigate the use of a recycled-flow[50] system using a micropump. For example, an HMQC experiment on menthol accumulating 512 scans and 128 t_1 increments, such as shown in Figure 3.5b, could be performed in recycled-flow at a flow rate of 15 μl/minute, taking into account a T_1 of 30 s. When the time between measurement on the same part of the sample is set to T_1, the loop would need to contain approximately 7.5 μl, which corresponds to an amount of 15 μmol of menthol in our experiment. Decreasing the flow rate can further reduce the required sample volume, but the recycle delay between scans has to be longer to account for T_1, which implies that the total experiment takes longer. In turn, a smaller recycle delay would decrease the amount of sample that is necessary, since measurement of the same sample can be repeated faster.
Alternatively, for very small amounts of sample, it can be advantageous to concentrate all of the sample in a single plug, i.e. a droplet of concentrated sample covering the detection area embedded in a nonmixable buffer solution. This can easily be accomplished using chip **b** (Figure 3.1). Since the single-scan signal-to-noise ratio increases by concentrating the sample, measurement time can be reduced. Depending on the limitations in amount and solubility of the sample, measurement time and T_1, one can optimise the setup using a recycled-flow sample loop with a micropump or concentrating the sample in a single plug.

3.4 Conclusions

In the work presented here, we successfully performed the most common experiments that are used to elucidate structures of small organic molecules, ^{1}H NMR and ^{13}C NMR

as well as homonuclear and heteronuclear correlation spectroscopy, in the stripline microfluidic NMR probe under continuous flow conditions.
Acquiring spectra in continuous flow made it possible to perform ^{13}C NMR experiments on two test compounds, ethyl crotonate and menthol, in a drastically decreased measurement time. The two-dimensional correlation spectra showed all expected peaks with no observed differences between low and high flow rates (1 and 15 μl/min, respectively). COSY and TOCSY spectra were successfully acquired for both compounds. The HMQC spectra that were obtained in continuous flow accurately showed the expected proton-carbon correlations.
The concentrations of stock solutions that were used are high (1.6 and 2.0 M), but still the plug the size of the 150 nl detection volume contains only 0.3 μmol of compound. This amount of compound, when dissolved in a 500 μl volume, corresponds to a 0.5 mM solution in a conventional NMR tube. Considering the good signal-to-noise ratios of the proton spectra, lower concentrated samples can easily be measured on the proton channel of our setup.
Possible ways to further shorten the experiment time and/or sample volume are increasing the sample concentration and using the sample very efficiently in a sample plug or a recycled-flow system. The design of chip **b** as displayed in Figure 3.1, features a removable FS capillary, in which the sample can be positioned by hand as an alternative to continuous flow conditions. This design would therefore be perfectly suited for the measurement of concentrated sample plugs or for measuring a very small sample without the need for dilution. Moreover, a microflow system could be attached to the sample capillary straightforwardly. However, more work is needed to optimise the resolution of this chip design.
In conclusion, the results show that various stripline setups are suitable for experiments on mass-limited samples as well as fast chemical reactions or otherwise unstable samples and can be advantageously performed in situ during flow. Attractive applications for continuous flow stripline NMR include monitoring of reaction kinetics, quality control and fast quantitative analysis. Measuring in continuous flow can also be beneficial for obtaining ^{13}C spectra of samples with very long ^{13}C relaxation times, since in that case the detection volume can be refreshed much faster than the relaxation time.

Acknowledgement

This research was financially supported by the ACTS - Process on a Chip Programme of the Netherlands Organization for Scientific Research (NWO). NWO is furthermore acknowledged for their support of the solid-state NMR facility for advanced materials science. Ruud Aspers is acknowledged for acquiring the T_1 relaxation time data.

References

[1] A. Webb, "Radiofrequency coils in magnetic resonance," *Prog. Nucl. Magn. Reson. Spectrosc.*, vol. 31, p. 1, 1997.

[2] D. Hoult and R. Richards, "The signal-to-noise ratio of the nuclear magnetic resonance experiment," *J. Magn. Reson.*, vol. 24, p. 71, 1976.

[3] N. Wu, T. L. Peck, A. G. Webb, R. L. Magin, and J. V. Sweedler, "^{1}H-NMR spectroscopy on the nanoliter scale for static and on-line measurements," *Anal. Chem.*, vol. 66, p. 3849, 1994.

[4] D. L. Olson, T. L. Peck, A. G. Webb, R. L. Magin, and J. V. Sweedler, "High resolution microcoil 1H-NMR for mass-limited, nanoliter-volume samples," *Science*, vol. 270, p. 1967, 1995.

[5] T. Peck, R. Magin, J. Kruse, and M. Feng, "NMR microspectroscopy using 100 μm planar RF coils fabricated on gallium arsenide substrates," *IEEE Trans. Biomed. Eng.*, vol. 41, no. 7, p. 706, 1994.

[6] A. P. M. Kentgens, J. Bart, P. J. M. van Bentum, A. Brinkmann, E. R. H. van Eck, J. G. E. Gardeniers, J. W. G. Janssen, P. Knijn, S. Vasa, and M. H. W. Verkuijlen, "High-resolution liquid- and solid-state nuclear magnetic resonance of nanoliter sample volumes using microcoil detectors," *J. Chem. Phys.*, vol. 128, p. 052202, 2008.

[7] R. M. Fratila and A. H. Velders, "Small-volume nuclear magnetic resonance spectroscopy," *Annu. Rev. Anal. Chem.*, vol. 4, p. 227, 2011.

[8] V. Badilita, R. C. Meier, N. Spengler, U. Wallrabe, M. Utz, and J. G. Korvink, "Microscale nuclear magnetic resonance: a tool for soft matter research," *Soft Matter*, vol. 8, p. 10583, 2012.

[9] C. J. Jones and C. K. Larive, "Could smaller really be better? Current and future trends in high-resolution microcoil NMR spectroscopy," *Anal. Bioanal. Chem.*, vol. 402, p. 61, 2012.

[10] S. S. Zalesskiy, E. Danieli, B. Blűmich, and V. P. Ananikov, "Miniaturization of NMR systems: Desktop spectrometers, microcoil spectroscopy, and *NMR on a Chip* for chemistry, biochemistry, and industry," *Chem. Rev.*, vol. 114, p. 5641, 2014.

[11] N. Sun, Y. Liu, L. Qin, H. Lee, R. Weissleder, and D. Ham, "Small NMR biomolecular sensors," *Solid-State Electron.*, vol. 84, p. 13, 2013.

[12] R. C. Meier, J. Höfflin, V. Badilita, U. Wallrabe, and J. G. Korvink, "Microfluidic integration of wirebonded microcoils for on-chip applications in nuclear magnetic resonance," *J. Micromech. Microeng.*, vol. 24, p. 045021, 2014.

[13] A. Brächer, S. Hoch, K. Albert, H. J. Kost, B. Werner, E. von Harbou, and H. Hasse, "Thermostatted micro-reactor NMR probe head for monitoring fast reactions," *J. Magn. Reson.*, vol. 242, p. 155, 2014.

[14] H. Ryan, S.-H. Song, A. Zaß, J. Korvink, and M. Utz, "Contactless NMR spectroscopy on a chip," *Anal. Chem.*, vol. 84, p. 3696, 2012.

[15] R. M. Fratila, V. Gomez, S. Sýkora, and A. H. Velders, "Multinuclear nanoliter one-dimensional and two-dimensional NMR spectroscopy with a single non-resonant microcoil," *Nat. Commun.*, vol. 5, p. 3025, 2014.

[16] N. Spengler, J. Höfflin, A. Moazenzadeh, D. Mager, N. MacKinnon, V. Badilita, U. Wallrabe, and J. G. Korvink, "Heteronuclear micro-helmholtz coil facilitates μm-range spatial and sub-Hz spectral resolution NMR of nL-volume samples on customisable microfluidic chips," *PLoS ONE*, vol. 11, no. 1, p. e0146384, 2016.

[17] P. J. M. van Bentum, J. W. G. Janssen, A. P. M. Kentgens, J. Bart, and J. G. E. Gardeniers, "Stripline probes for nuclear magnetic resonance," *J. Magn. Reson.*, vol. 189, p. 104, 2007.

[18] Y. Maguire, I. L. Chuang, S. Zhang, and N. Gershenfeld, "Ultra-small-sample molecular structure detection using microslot waveguide nuclear spin resonance," *Proc. Natl. Acad. Sci. U. S. A.*, vol. 104, no. 22, p. 9198, 2007.

[19] H. G. Krojanski, J. Lambert, Y. Gerikalan, D. Suter, and R. Hergenroder, "Microslot NMR probe for metabolomics studies," *Anal. Chem.*, vol. 80, p. 8668, 2008.

[20] J. Bart, J. W. G. Janssen, P. J. M. van Bentum, A. P. M. Kentgens, and J. G. E. Gardeniers, "Optimization of stripline-based microfluidic chips for high-resolution NMR," *J. Magn. Reson.*, vol. 201, p. 175, 2009.

[21] M. C. D. Tayler, S. G. J. van Meerten, A. P. M. Kentgens, and P. J. M. van Bentum, "Analysis of mass-limited mixtures using supercritical-fluid chromatography and microcoil NMR," *Analyst*, vol. 140, p. 6217, 2015.

[22] G. Finch, A. Yilmaz, and M. Utz, "An optimised detector for in-situ high-resolution NMR in microfluidic devices," *J. Magn. Reson.*, vol. 262, p. 73, 2016.

[23] V. Sans and L. Cronin, "Towards dial-a-molecule by integrating continuous flow, analytics and self-optimisation," *Chem. Soc. Rev.*, vol. 45, p. 2032, 2016.

[24] A. J. Moule, M. M. Spence, S. I. Hans, J. A. Seeley, K. L. Pierce, S. Saxena, and A. Pines, "Amplification of xenon NMR and MRI by remote detection," *Proc. Natl. Acad. Sci. USA*, vol. 100, p. 9122, 2003.

[25] J. Granwehr, E. Harel, S. Hans, S. Garcia, A. Pines, P. N. Sen, and Y. Q. Song, "Time-of-flight flow imaging using NMR remote detection," *Phys. Rev. Lett.*, vol. 95, p. 075503, 2005.

[26] E. E. McDonnell, S. Han, C. Hilty, K. L. Pierce, and A. Pines, "Nmr analysis on microfluidic devices by remote detection," *Anal. Chem.*, vol. 77, p. 8109, 2005.

[27] D. A. Laude, Jr. and C. L. Wilkins, "Direct-linked analytical scale high-performance liquid chromatography/nuclear magnetic resonance spectrometry," *Anal. Chem.*, vol. 56, p. 2471, 1984.

[28] K. Albert, "On-line use of NMR detection in separation chemistry," *J. Chromatogr. A*, vol. 703, p. 123, 1995.

[29] J. C. Lindon, J. K. Nicholson, and I. D. Wilson, "Direct coupling of chromatographic separations to NMR spectroscopy," *Prog. Nucl. Magn. Reson. Spectrosc.*, vol. 29, p. 1, 1996.

[30] L. Ciobanu, D. A. Jayawickrama, X. Zhang, A. G. Webb, and J. V. Sweedler, "Measuring reaction kinetics by using multiple microcoil NMR spectroscopy," *Angew. Chem., Int. Ed.*, vol. 42, p. 4669, 2003.

[31] M. Kakuta, D. A. Jayawickrama, A. M. Wolters, A. Manz, and J. V. Sweedler, "Micromixer-based time-resolved NMR: Applications to ubiquitin protein conformation," *Anal. Chem.*, vol. 75, p. 956, 2003.

[32] H. Wensink, F. Benito-Lopez, D. C. Hermes, W. Verboom, J. G. E. Gardeniers, D. N. Reinhoudt, and A. van den Berg, "Measuring reaction kinetics in a lab-on-a-chip by microcoil NMR," *Lab Chip*, vol. 5, p. 280, 2005.

[33] M. V. Gomez, A. M. Rodriguez, A. de la Hoz, F. Jimenez-Marquez, R. M. Fratila, P. A. Barneveld, and A. H. Velders, "Determination of kinetic parameters within a single nonisothermal on-flow experiment by nanoliter NMR spectroscopy," *Anal. Chem.*, vol. 87, p. 10547, 2015.

[34] D. L. Olson, J. A. Norcross, M. O'Neil-Johnson, P. F. Molitor, D. J. Detlefsen, A. G. Wilson, and T. L. Peck, "Microflow NMR: Concepts and capabilities," *Anal. Chem.*, vol. 76, p. 2966, 2004.

[35] J. L. Sudmeier, U. L. Günther, K. Albert, and W. W. Bachovchin, "Sensitivity optimization in continuous-flow FTNMR," *J. Magn. Reson., Ser. A*, vol. 118, p. 145, 1996.

[36] J. D. A. Laude and C. L. Wilkins, "Applications of a recycled-flow fourier transform nuclear magnetic resonance system: Molecular weight determination of siloxane polymers by ^{29}Si NMR," *Macromolecules*, vol. 19, p. 2295, 1986.

[37] J. Bart, A. J. Kolkman, A. J. Oosthoek-de Vries, K. Koch, P. J. Nieuwland, J. W. G. Janssen, P. J. M. van Bentum, K. A. M. Ampt, F. P. J. T. Rutjes, S. S. Wijmenga, J. G. E. Gardeniers, and A. P. M. Kentgens, "A microfluidic high-resolution NMR flow probe," *J. Am. Chem. Soc.*, vol. 131, p. 5014, 2009.

[38] J. Bart, *Stripline-based microfluidic devices for high-resolution NMR spectroscopy*. PhD thesis, University of Twente, Enschede, the Netherlands, 2009. ISBN 978-90-365-2898-6.

[39] J. D. van Beek, "matNMR: A flexible toolbox for processing, analyzing and visualizing magnetic resonance data in Matlab," *J. Magn. Reson.*, vol. 187, p. 19, 2007.

[40] "ACD/NMR Processor Academic Edition." Advanced Chemistry Development, Inc., Toronto, ON, Canada, 2010.

[41] J. D. A. Laude, R. W. K. Lee, and C. L. Wilkins, "Signal enhancement of long-relaxing ^{13}C nuclei by flow NMR," *J. Magn. Reson.*, vol. 60, p. 453, 1984.

[42] C. Fyfe, M. Cocivera, S. Damji, T. Hostetter, D. Sproat, and J. O'Brien, "Apparatus for the measurement of transient species and effects in flowing systems by high-resolution nuclear magnetic resonance spectroscopy," *J. Magn. Reson.*, vol. 23, p. 377, 1976.

[43] T. D. W. Claridge, *High-resolution NMR techniques in organic chemistry*, vol. 27 of *Tetrahedron Organic Chemistry*. Elsevier, 2009.

[44] S. Braun, H.-O. Kalinowski, and S. Berger, *100 and more basic NMR experiments : a practical course*. Weinheim: Wiley VCH, 1996.

[45] R. Abraham, J. Fischer, and P. Loftus, *Introduction to NMR spectroscopy*. Wiley, 1988.

[46] W. P. Aue, J. Karhan, and R. R. Ernst, "Homonuclear broad band decoupling and two dimensional J resolved NMR spectroscopy," *J. Chem. Phys.*, vol. 64, p. 4226, 1976.

[47] A. Bax and D. Davis, "MLEV-17-based two-dimensional homonuclear magnetization transfer spectroscopy," *J. Magn. Reson.*, vol. 65, p. 355, 1985.

[48] M. Levitt, R. Freeman, and T. Frenkiel, "Broadband heternuclear decoupling," *J. Magn. Reson.*, vol. 47, p. 328, 1982.

[49] A. Bax and S. Subramanian, "Sensitivity-enhanced two-dimensional heteronuclear shift correlation NMR spectroscopy," *J. Magn. Reson.*, vol. 67, p. 565, 1986.

[50] S. T. K. Ha, R. W. K. Lee, and C. L. Wilkins, "Sensitivity enhancement for ^{13}C-^{1}H 2D J-Resolved NMR using a recycled-flow method," *J. Magn. Reson.*, vol. 73, p. 467, 1987.

Chapter 4

Inline reaction monitoring of amine-catalysed acetylation of benzyl alcohol using a microfluidic stripline NMR setup

Anna Jo Oosthoek - de Vries, Pieter J. Nieuwland, Jacob Bart, Kaspar Koch, Johannes W. G. Janssen, P. Jan M. van Bentum, Floris P. J. T. Rutjes, Han J. G. E. Gardeniers and Arno P. M. Kentgens

This chapter has been published in J. Am. Chem. Soc., **141** (13), pp 5369–5380 (2019)

Abstract

We present an in-depth study of the acetylation of benzyl alcohol in the presence of *N,N*-diisopropylethylamine (DIPEA) by nuclear magnetic resonance (NMR) monitoring of the reaction from 1.5 s to several minutes. We have adapted the NMR setup to be compatible to microreactor technology, scaling down the typical sample volume of commercial NMR probes (500 μl) to a microfluidic stripline setup with 150 nl detection volume. *Inline* spectra are obtained to monitor the kinetics and unravel the reaction mechanism of this industrially relevant reaction. The experiments are combined with conventional 2D NMR measurements to identify the reaction products. In addition, we replace DIPEA with triethylamine and pyridine to validate the reaction mechanism for different amine catalysts. In all three acetylation reactions, we find that the acetyl ammonium ion is a key intermediate. The formation of ketene is observed during the first minutes of the reaction when tertiary amines were present. The pyridine-catalysed reaction proceeds via a different mechanism.

4.1 Introduction

Spectroscopic techniques are extensively used in organic chemistry for analysing molecular compounds and for monitoring chemical reactions because they provide quantitative chemical information at the molecular level. Gas/liquid chromatography-mass spectroscopy (GC/LC-MS), infrared (IR) spectroscopy and nuclear magnetic resonance (NMR) spectroscopy are methods that are frequently employed[1, 2, 3, 4]. Nuclear magnetic resonance (NMR) spectroscopy is a particularly versatile technique and is the method of choice for elucidation of molecular structure of organic compounds in a broad range of fields[5]. NMR has also proven to be very suitable for the study of organic reactions[6, 7, 8].

Microscale chemical reactions are attracting increasing attention in chemical research[9, 10, 11]. Compared to conventional batch reactors, microreactors have extremely high surface-to-volume ratios, which allows for better heat exchange and mass transfer[12, 13]. The small volumes, which are typically involved, enable potentially dangerous and/or fast reactions, such as exothermic reactions or reactions with flammable, explosive, toxic or hazardous chemicals, to be performed under relatively safe conditions. Some recent examples employ the controlled environment of the microreactor and the increased mass and heat transfer capabilities. The autoxidation of olefins was performed in a microreactor, which improved safety and yield due to increased mass

transfer and increased temperature[14]. Also, fluorine reactions, which are in batch difficult to control and unstable, involving hazardous compounds that are difficult to handle, were successfully performed using microreactor-based continuous flow chemistry, due to the fast mixing, high heat and mass transfer in a microreactor[15]. Cantillo[16] et al. developed a procedure for the synthesis of triaminophlorogluconol, an important compound for industrial and medical use, involving a very unstable and explosive intermediate, which could be safely performed in continuous flow in a microreactor using a thermostated ultrasound bath for controlling the temperature of this exothermic reaction.

Mixing of reactants in conventional reactions occurs by convection and turbulence. Microfluidic systems have low Reynold numbers and therefore operate in the laminar flow regime, where mixing takes place mainly by mass transfer through diffusion. The diffusion distance may be decreased by using split-and-recombine mixing elements in the microreactor: flows are split up, deformed and recombined, creating thin layers of laminar flows. Whereas turbulent mixing can give rise to large concentration gradients, microfluidic diffusion-limited mixing is more homogeneous and the reaction progress is more reproducible as a result. This enhances chemical selectivity and significantly suppresses side product formation[17]. The reproducibility is also a great advantage in efficient screening or optimisation of reactions, which is of considerable interest for a variety of pharmaceutical and industrial processes and for research and development in organic chemistry. High throughput optimisation in microfluidic setups is achieved at reduced costs, due to low material requirements and low waste generation[18], even for dangerous and explosive compounds[19].

With the developments in microreactor technology comes a growing interest in online spectroscopic analysis techniques[20, 21]. For accurate monitoring of fast reaction intermediates, it is required that the applied spectroscopic technique operates at the same volumetric scale as the microreactor[22], and in order to be able to follow the reaction *in situ*, this method should be integrated with the reaction element, which calls for the scaling down of the NMR volume. Miniaturisation of the NMR detection coil increases mass sensitivity[23], i.e. scaling down of the NMR coil increases the sensitivity per unit mass, but decreases the sensitivity per unit concentration[24]. For a sample with a certain, limited concentration, but sufficient volume available, the sensitivity of a measurement is decreased for smaller coil. For samples with limited mass, however, sensitivity increases when the coil is better fitted to the size of the sample. This is beneficial not only for mass-limited samples but also for the limited volumes that are present in the

microfluidic reactions. Considerable effort has been devoted to the development of microscale NMR techniques and several approaches for microcoil NMR have been explored[25, 26, 27, 28]. Different types of microcoils can be distinguished: microsolenoids wound around a capillary[29, 30, 31], planar spiral microcoils[32, 33, 34, 35] and transmission line type (stripline or microslot) NMR detector[36, 37, 38, 39, 40, 41, 42, 43]. Our stripline based NMR chip[38, 44] consists of a planar copper structure in which a central flat wire is defined that excites and detects the nuclear spins, having a constriction where a high and homogeneous radio frequency (rf) field is generated, with a fluidic channel running directly above the copper strip. Furthermore, microfluidic connections can be straightforwardly applied so that a straightforward microfluidic setup for the study of microscale reactions in flow is realised.

Several groups have investigated the applicability of microscale NMR devices for inline reaction monitoring[45]; Ciobanu et al.[46] studied the reaction of D-xylose and borate by multiple physically distinct solenoidal microcoils. Wensink et al.[47] presented a microfluidic chip with an integrated planar microcoil for the real-time monitoring of imine formation from benzaldehyde and aniline. Kakuta et al.[48] monitored ubiquitin protein conformation by coupling a micromixer to a solenoidal NMR microcoil. More recently, Brächer et al.[49] combined a microreactor with a capillary NMR flow cell, where the flow path and the solenoid NMR coil are thermostatted using FC-43 (perfluorotributylamine). In this setup, as a test system a catalytic esterification of methanol with acetic acid was studied under isothermal conditions. Hyphenation of a continuous flow microreactor and a microfluidic NMR chip to determine kinetic parameters of a reaction with a single on-flow experiment was employed by Gomez et al.[50]

In an earlier study, we showed that the stripline-based microfluidic NMR setup could be conveniently used for reaction monitoring and analysing mass-limited biological samples samples[44]. This setup is further optimised for monitoring the amine base-catalysed acetylation of benzyl alcohol *in situ*. Acetylation of hydroxyl groups is an important and fundamental process in organic chemistry. The acetylation is mostly used to protect alcohol groups from undesired side reactions but also to turn hydroxyl substituents into better leaving groups. It is frequently performed using an acid chloride in the presence of an amine to significantly speed up the reaction. We performed the acetylation with acetyl chloride in the presence of DIPEA, which gives a fast and exothermic reaction. The time scale of this reaction is several minutes, which can be perfectly monitored with our microfluidic NMR setup.

Despite the abundance of esterification examples with acetyl chloride, there is still

discussion about the exact mechanism. The reaction mechanism for a base catalysed acetylation in general can be thought to proceed via base-assisted nucleophilic attack of the alcohol with acetyl chloride[51]. However, it has also been suggested that the reaction proceeds via a tetrahedral intermediate (the quaternary acetyl ammonium ion)[52] or via a highly reactive ketene intermediate that is formed through base-assisted alpha-elimination of HCl from acetyl chloride[53]. Our setup enables the observation of unstable intermediates such as ketene. Complemented with conventional NMR measurements, this allows us to fully unravel the reaction mechanism. Furthermore, we applied different base catalysts to compare the mechanisms when different amines are involved.

4.2 Experimental section

4.2.1 Chemicals

All chemicals were used as received without further purification and consisted of acetyl chloride (Fluka Analytical from Sigma-Aldrich), acetyl-2-^{13}C chloride, 99 atom% ^{13}C (Aldrich), benzyl alchohol (reagent Plus, Sigma-Aldrich), *N,N*-diisopropylethylamine (DIPEA) (Biotech grade 99.5%, Sigma-Aldrich), triethylamine (Sigma-Aldrich), pyridine (Fluka analytical, puriss.p.a.), and chloroform-d_3 + 0.05% v/v TMS (Cambridge Isotope Laboratories, Inc.) as a solvent.

4.2.2 Microfluidic stripline NMR setup

The stripline NMR chip used in these experiments has been described before in Chapter 3. The stripline NMR chip is a microfabricated chip, where the rf coil consists of a copper stripline structure sputtered and electroplated onto the glass substrate. The analyte flows through the detection area via a microfluidic channel. The volume sensitive for detection is 150 nl. The chip is coupled to a standard microfluidic setup. Syringe pumps are used for providing a continuous flow of the reactants. Prior to entering the stripline NMR chip, the reactants are brought together using a Y-junction and subsequently flow into the chip using a fused silica (FS) capillary with 75 μm inner diameter (I.D.). A reaction volume of approximately 1 μl results.
From the point of the Y-junction, mixing takes place by laminar diffusion. By a rough approximation the mixing time from Fick's law can be calculated to be approximately 1.4 s. More accurately, the Damköhler number can be estimated, which compares

diffusion to reaction rate[54]. For our reaction process the Damköhler number is around 1, so the reaction rate is possibly limited by the mixing process.
In a pressure-driven laminar flow through the capillary, a parabolic Poiseuille flow profile arises, instead of plug flow with a linear profile. Radial diffusion takes place, which disrupts the parabolic profile. Bodenstein numbers can be estimated, which give an indication on the validity of assuming plug flow for the reaction[54]. We find that for our microfluidic system the Bodenstein number is below 1000 for reaction times up to 30 s. So, small deviations from plug flow can be present up to reaction times of 30 s, where the differences between center velocity and flow rate at the wall may cause a velocity distribution.
An effective reaction time can be calculated by dividing flow rate with the reaction volume, so that depending on the applied flow rates, detection can take place at effective reaction times ranging from 1.5 s and 5 min. Details regarding the chip, probe and microfluidics setup can be found in Appendix C.1. Pictures and schematics of the stripline NMR chip and probe are shown in Figure C.1.

4.2.3 In flow measurements

For the reaction monitoring, a continuous flow of the reaction mixture to the stripline was established. After having set a new flow rate, a stabilisation time depending on the flow rate was taken into account (varying from at least 1 min for high flow rates up to 15 min for low flow rates). Flow rates ranging from 20 μl/min down to 0.1 μl/min correspond to effective reaction times of 1.5 s to 5 min at the NMR measurement. A steady state spectrum is recorded and saved. The spectra were taken acquiring 4 or 16 scans, depending on the concentration of the analyte. The acquisition delay between scans varied between 5 s for the lower flow rates to 1 s for the higher flow rates, when the detection volume is refreshed faster. All spectra were recorded at room temperature on a VNMRS 600 MHz Varian NMR spectrometer operated with VNMRJ software. The flow of analyte through the NMR detection area continuously replaces depolarised spins with polarised spins that did not yet receive an rf pulse. As a result, it is not necessary to wait for 5 times the relaxation time T_1 for the spins to repolarise; therefore, the pulse repetition rate can be increased for an improved signal to noise ratio (SNR) per unit time[24, 55]. However, the residence time will increase signal linewidth for any spin not in the detection volume of the NMR probe for a period long enough to record a full free induction decay (FID), as determined by the transverse relaxation T_2[56]. The

resulting increase in linewidth due to flow is inversely proportional to the residence time. Although the expected decrease in resolution with increasing flow rate occurs, the effect is minor, so that the intrinsic high resolution of the stripline chip still permits a spectral resolution of approximately 2 Hz for flow rates up to 50 μl/min.
From the spectrum of 0.5 M acetyl chloride in flow, a single scan SNR of 683 is estimated for the methyl peak. For calculation of the concentration within 1% error, at least a SNR of 150 is needed[57], which is valid for a concentration of more than 0.11 M. When accumulating 4 or 16 scans, the minimum concentration becomes 55 and 27 mM, respectively. An SNR of 1:3 is necessary for detection of a peak, corresponding to a minimum concentration of 2 mM in a single scan. The first measurement is acquired at an effective reaction time of 2 s. Intermediate products that have a lifetime of less than 2 s will not be observed. The time between the effective reaction times at the measurements varies between a few seconds at the beginning of the reaction up to a minute at the end of the reaction (selected spectra are shown in the figures). Intermediates that are not present at a time of measurement will not be present in the spectra. Furthermore, the acquisition time is 1 s; intermediates appearing and/or disappearing during this period will give dispersive and/or broadened lines[58].
Temperature changes can be present as the reaction generates heat or in hot spots. According to guidelines provided by Westermann and Mleczko[59], we operate in a regime that does not have a high risk on hot spots. Due to the small diameter of the reaction channel (75 μm) temperature rise is expected to remain well below 1 K.

4.2.4 Conventional NMR experiments

The reaction mixtures were prepared in the fumehood, mixed in a tube and allowed to equilibrate. After 15 min the mixtures were relatively stable, and the conventional NMR measurements were performed typically after a reaction time of around 2 h. After the desired reaction time, a sample was taken and put into a 5 mm (500 μl) NMR tube and subsequently measured with a commercially available probe in a Bruker Avance III 600 MHz NMR spectrometer operated with Bruker TopSpin 3.0 software. For each sample, a ^{1}H spectrum, a ^{13}C spectrum, a heteronuclear single quantum coherence (HSQC)[60] spectrum and a heteronuclear multiple-bond correlation (HMBC)[61] spectrum was taken.

4.2.5 Data processing

The data were processed with VnmrJ and matNMR[62]. Advanced Chemistry Development, Inc. ACD/NMR Processor was used for plotting the conventional 2D experiments[63]. The concentration of the methyl products during the reaction were monitored from the spectra measured in the stripline probe by deconvolution fitting of the peaks with MatNMR[62].

4.3 Results and Discussion

4.3.1 The acetylation of benzyl alcohol with DIPEA

The acetylation of benzyl alcohol without a base catalyst is a slow reaction. The reaction proceeds via a tetrahedral intermediate and is completed in one day. In Appendix C.5, the reaction mechanism (Scheme C.1) and a series of NMR spectra (Figure C.3) that are taken during the conversion are shown. However, the presence of an amine significantly increases the reaction rate. Several mechanisms that can play a role have been suggested in the literature[52]. First of all, HCl is formed in the nucleophilic addition-elimination reaction, and a basic amine can absorb HCl to form the corresponding ammonium salt. This would shift the equilibrium of the reaction to accelerate it. Therefore, we would expect to see protonation of DIPEA, and possibly the tetrahedral intermediate. Second, the basic amine can deprotonate the alcohol in trace amounts. However, this process is not expected to be a significant factor since acetyl chloride and DIPEA react vigorously. Third, it has been suggested that an acetyl ammonium ion might be formed[52, 53]. Acetyl chloride and the amine then react to give ketene and the protonated amine. Ketene is very reactive and reacts with the alcohol into an ester (reaction k_5 in Scheme 4.1) [64] or with the protonated amine to give an acetyl ammonium ion **9** (reaction k_4 in Scheme 4.1)[65, 66]. These various insights have been brought together in Scheme 4.1, which we will validate by detailed NMR analyses as described below.

In situ NMR spectra

To get detailed insights in the reaction mechanism of this fast amine catalysed acetylation, we performed the reactions in a microfluidic setup (Figure C.1 in Appendix C.1). The syringes were loaded with A: 0.5 M benzyl alcohol with 0.5 M DIPEA and B:

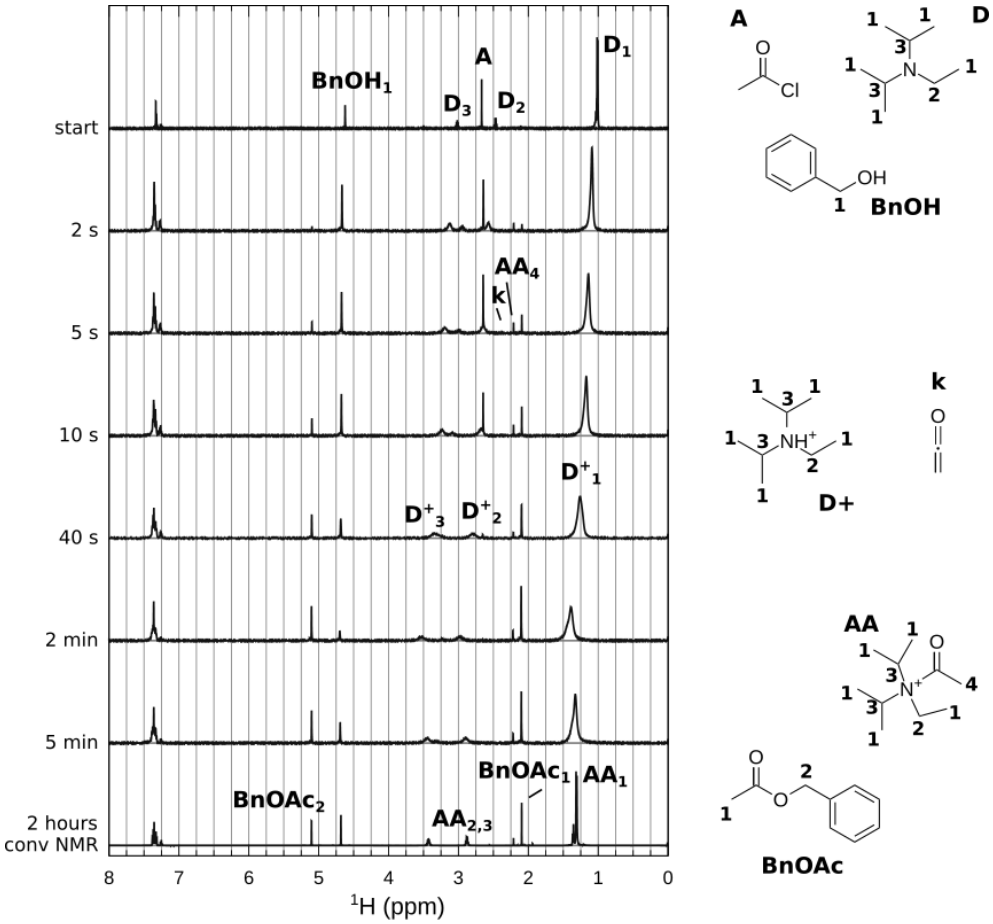

*Figure 4.1: Selected spectra for the reaction of benzyl alcohol **2** (0.5 M) with acetyl chloride **1** (0.5 M) in the presence of DIPEA **5** (0.5 M). Top: unreacted compounds: acetyl chloride (A), DIPEA (D), benzyl alcohol (BnOH). The series of in situ spectra show the broadening and shifting of DIPEA peaks, formation of product benzyl acetate **4** (BnOAc) and intermediate peaks marked 'k' (ketene **7**) and 'AA$_4$' (acetyl group of acetyl ammonium ion **9**). Bottom: conventional NMR spectrum after 2 h reaction time. The slightly broadened DIPEA peaks are shifted to a position of protonated DIPEA **8** and/or acetyl ammonium ion **9** ('AA').*

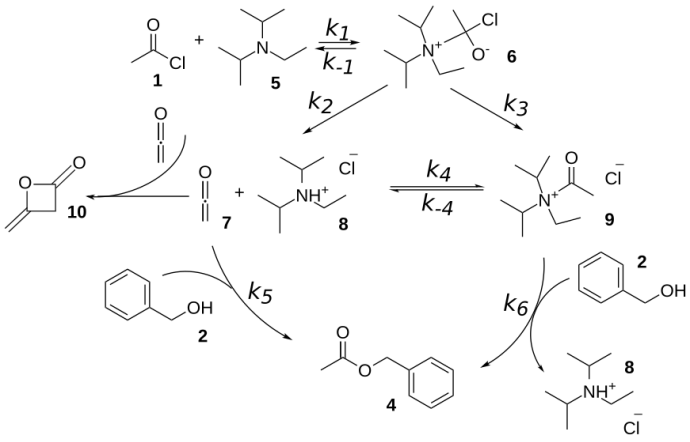

*Scheme 4.1: Proposed reaction mechanism of benzyl alcohol **2** with acetyl chloride **1** and DIPEA **5**. Acetyl chloride and DIPEA form an unstable tetrahedral intermediate **6**, which gives ketene **7**, protonated DIPEA **8** and acetyl-*N,N*-diisopropylethylammonium ion **9**. Benzyl alcohol **2** reacts with ketene **7** or acetyl ammonium ion **9** into benzyl acetate **4**. Diketene **10** is formed as a side product in trace amounts.*

0.5 M acetyl chloride. Comparing the spectra of DIPEA and DIPEA with benzyl alcohol, protonation of DIPEA from benzyl alcohol is not observed. By keeping the flow rates constant at a certain flow rate during the acquisition we obtained a steady state spectrum while the reaction is in progress. By adjustment of the flow rates A and B, a series of steady state spectra was obtained at effective reaction times ranging from 1.5 s up to 5 min. Selected spectra and a conventional NMR spectrum are shown in Figure 4.1. Table C.1 in Appendix C.8 gives an overview of the methyl peaks observed in the reactions discussed in this chapter.

In the "conventional" NMR spectrum (bottom of Figure 4.1), taken after 2 h reaction time, we observe the DIPEA peaks at a position (marked 'AA') shifted with respect to the original position (marked 'D' in the top spectrum of the unreacted compounds), which indicates the protonation of the amine. There are two main methyl resonances present; the benzyl acetate peak at 2.09 ppm ($BnOAc_1$) and a smaller peak at 2.23 ppm, which will be discussed in more detail in the next section.

More information can be obtained from the analysis of the stripline NMR spectra of the ongoing reaction shown in Figure 4.1. The conversion into benzyl acetate can be monitored nicely using the resonances of the alpha protons. The spectra show the shifting and broadening of the DIPEA peaks (from 'D' to 'D^+' and 'AA'), and

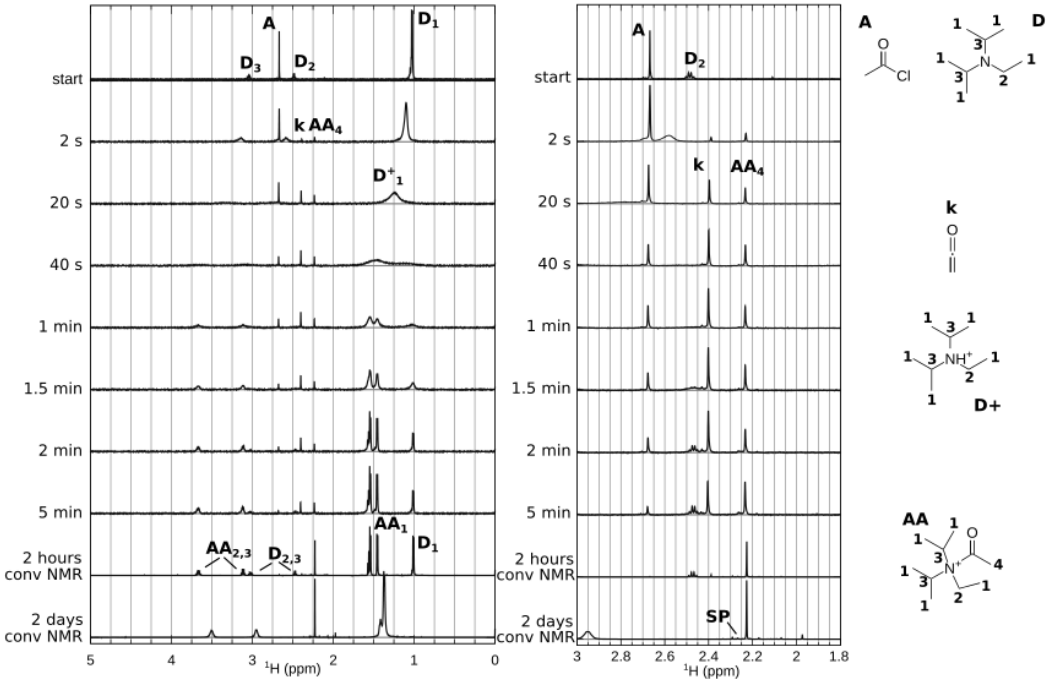

*Figure 4.2: Selected spectra for the reaction of acetyl chloride (0.5 M) with DIPEA (0.5 M). Top: unreacted compounds: acetyl chloride **1** (A) and DIPEA **5** (D). The series of in situ spectra shows the broadening and shifting of DIPEA peaks, intermediate peaks marked 'k' (ketene **7**) and 'AA$_4$' (acetyl group of acetyl ammonium ion **9**). Bottom: two conventional NMR spectra. After 2 h reaction time, the DIPEA peaks are found at the original position (D) and at the shifted position acetyl ammonium ion **9** ('AA$_{1,2,3}$'), the main methyl product is associated with the acetyl group of the acetyl ammonium ion **9** (AA$_4$). After 2 days reaction time, the DIPEA/acetyl ammonium ion peaks are broadened.*

four peaks in the methyl region can be observed: acetyl chloride (2.69 ppm, labelled 'A'), two intermediates at 2.4 ppm ('k') and 2.23 ppm ('AA$_4$') and benzyl acetate at 2.09 ppm ('BnOAc$_1$').

To simplify the identification of the different steps in the reaction, the interaction of DIPEA **5** and acetyl chloride **1** was studied separately. Experiments are performed in a similar way, with syringe A: acetyl chloride (0.5 M) and syringe B: DIPEA (0.5 M). Figure 4.2 shows selected spectra acquired in the stripline NMR chip, and two conventional NMR spectra acquired after 2 h and 2 days reaction time. Since all of these peaks are still present in the conventional NMR spectrum after 2 h reaction time, we were able to perform conventional 2D NMR experiments of these reaction products. In order to come to a reaction mechanism, we first need to assign the various

resonances in the stripline and conventional NMR spectra.

Protonation of DIPEA

The spectra in Figure 4.2 clearly show that the DIPEA peaks first broaden, then split. Three main resonances are present in the methyl region (2.69 ppm (AcCl), 2.4 ppm, 2.23 ppm), see also Table C.1 in Appendix C.8. A similar effect is seen in the spectra of the full reaction obtained with the stripline probe (Figure 4.1) showing that the DIPEA peaks broaden and shift as the reaction proceeds. This suggests (partial) protonation of DIPEA.

$$D + H^+ \underset{k_{-1}}{\overset{k_1}{\rightleftarrows}} DH^+ \tag{4.1}$$

If the resulting protonation/deprotonation process is a fast exchange process, the position of the resulting (narrow) peak in the NMR spectrum is the weighted average of the shift of the protonated and unprotonated resonances, whereas in the slow exchange limit these separate resonances would both be present in the spectrum[67]. Since we observe a broadened, averaged signal, we conclude that this is an intermediate exchange process, meaning that the proton is exchanged from one molecule to another on the NMR time scale. The observed chemical shift δ is the population averaged shift, where the populations γ_i are the relative concentrations:

$$\delta(t) = \sum_{i=1}^{n} \gamma_i(t)\delta_i \tag{4.2}$$

For intermediate exchange rates NMR peaks broaden as observed in the spectra, meaning the lifetime of the species is shorter than the transverse relaxation time T_2 and of similar magnitude of the frequency difference of the individual resonances.[67]. As the reaction progresses, the position of the broadened DIPEA peak moves from the original chemical shift of the unprotonated DIPEA to a position similar to the protonated DIPEA chemical shift. This shift reflects the gradually increasing protonation of DIPEA during the course of the reaction.

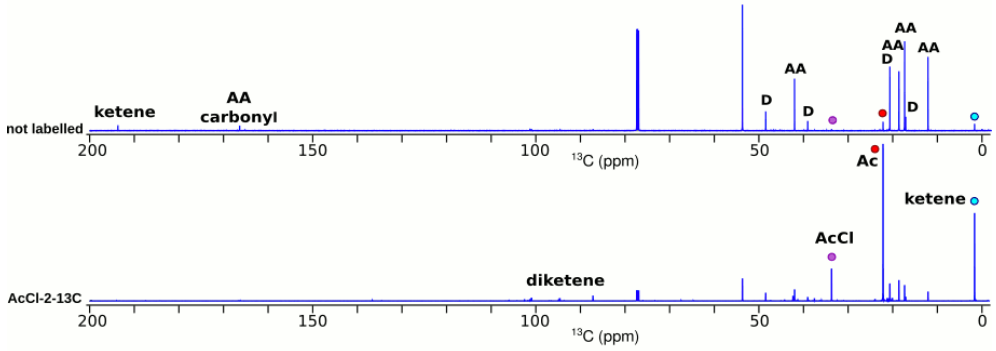

(a) ^{13}C spectra

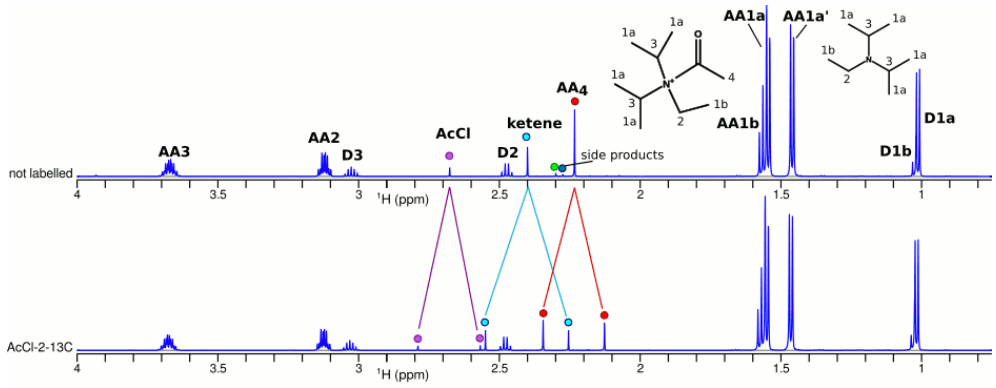

(b) ^{1}H spectra

*Figure 4.3: DIPEA (0.5 M) and AcCl (0.5 M) after two h reaction time, for natural abundance and ^{13}C-labelled AcCl, measured in a conventional 600 MHz NMR spectrometer. In the ^{13}C spectra (a), the peaks of labelled products in the bottom spectrum are enlarged; the bottom spectrum has been scaled down (1:6, relative to the $CDCl_3$ peaks), to accommodate for these intensity differences. The peaks of labelled products that are increased are mainly acetyl chloride **1**, the acetyl group of acetyl ammonium ion **9** (AA4) and ketene **7**, but also diketene **10** and some side products are found. In the natural abundance spectrum, we see also the carbons from the carbonyl groups for ketene **7** and acetyl ammonium ion **9** (AA). In the ^{1}H spectra (b), the peaks belonging to DIPEA **5** are indicated with D1a-1b, D2 and D3. The acetyl ammonium ion peaks are at a position shifted from the DIPEA, indicated with AA1a-1b (partly overlapping), AA2 and AA3. Due to ^{13}C-labelling of acetyl chloride, splitting due to J_{CH} coupling of the acetyl chloride **1** and product methyl peaks occurs: ketene **7** and acetyl ammonium ion **9** (AA4), marked with dots. Due to hindered rotation, the acetyl ammonium ion peaks (AA1-3) are split, which is visible in this spectrum.*

Reaction products of acetyl chloride

To unravel which resonances correspond to the reaction products of acetyl chloride, labelled acetyl chloride-2-^{13}C was used for the reaction with DIPEA. Figure 4.3 shows the conventional ^{13}C and ^{1}H NMR spectra after two h reaction time for reactions using either natural abundance or ^{13}C labelled acetyl chloride. Since we observed protonated DIPEA **8**, the formation of ketene **7** as an intermediate in the reaction is a possible consequence in this part of the reaction. The ^{13}C chemical shifts of ketene are known from literature to be 2.5 ppm and 194 ppm[68]. Both peaks are indeed observed in the ^{13}C spectrum (Figure 4.3a), confirming the presence of ketene **7** in the reaction mixture.

The peaks that belong to the reaction products of acetyl chloride can be identified by their increased peak intensity in the spectrum of the reaction performed with labelled acetyl chloride relative to the spectrum with natural abundance acetyl chloride. The methyl region (below 50 ppm) shows that three of the main resonances have much higher intensity (marked with dots in Figure 4.3a). Since ketene **7** is a reactive compound we assume that it will react with protonated DIPEA **8** and form acetyl *N,N*-diisopropylethylammonium ion **9**. With the peaks corresponding to the resonances of acetyl chloride and ketene already identified, we assign the third peak to the acetyl group of the acetyl ammonium ion (AA_4). Interestingly, we also observe diketene **10** as a side product of the reaction.

To verify that the peaks at 2.5 ppm and 194 ppm in the conventional ^{13}C NMR spectra in Figure 4.3a indeed belong to ketene **7**, and to determine which peak in the proton spectrum corresponds to ketene, a heteronuclear multiple-bond correlation (HMBC) spectrum is acquired (Figure 4.4b). It is clear from the connection between the 2.5 ppm and 194 ppm ^{13}C peaks to the 2.4 ppm ^{1}H peak, that the ketene protons resonate at 2.4 ppm peak in the proton spectrum.

Figure 4.3b shows the proton spectra for reactions of DIPEA with the natural abundance and the ^{13}C labelled acetyl chloride. For the ^{13}C labelled acetyl chloride, the peaks in the spectra that belong to the ^{13}C labelled compound are split due to the J_{CH} coupling. This splitting can be observed for the resonances at 2.69 ppm, 2.4 ppm and 2.23 ppm, in agreement with the previous findings. In addition, some low intensity peaks at 6 ppm, 2.30 ppm and 2.27 ppm (too small to be marked in the ^{13}C labelled spectrum) exhibiting J_{CH} couplings are observed. For acetyl chloride a J_{CH} coupling of 133 Hz is perceived, for ketene 177 Hz and for the acetyl ammonium ion 131 Hz.

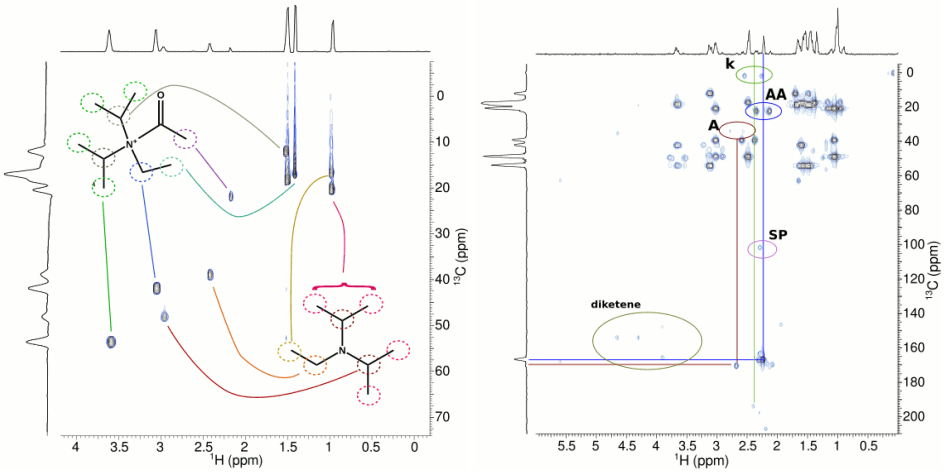

(a) HSQC (b) HMBC

*Figure 4.4: Acetyl chloride with DIPEA: conventional 2D spectra after 2 h reaction time, (a) HSQC, b) HMBC. The HSQC shows the separation of the DIPEA **5** and acetyl ammonium ion **9** peaks in the ^{13}C spectrum. In the HMBC, other than multiple peaks from DIPEA **5** and acetyl ammonium **9**, we observe ketene **7** (k) at 2.4 ppm in ^{1}H spectrum, and at 2.5 ppm and 194 ppm in the ^{13}C spectrum. Furthermore, acetyl chloride **1** (A), the acetyl group of the acetyl ammonium ion **9** (AA), side products (SP) and diketene **10** are found.*

The acetyl-*N,N*-diisopropylethylammonium ion **9** has a hindered rotation around the N-CO bond, therefore the protons 1a are inequivalent and show a split resonance[69, 70]. When the initial (fast) part of the reaction is completed, the acetyl ammonium ion peaks are split as can be seen in Figure 4.3. This is also observed in the series of spectra in Figure 4.2 (at 5 min reaction time and the first conventional NMR spectrum). The protons from the acetyl group of the acetyl ammonium ion, marked 1a and 1b in Figure 4.3, are found as two doublets with 51 Hz splitting with a 1:1 ratio (1a and 1a') and one triplet (1b) partly overlapping with the doublet. The other acetyl ammonium peaks (2 and 3) exhibit a 4.2 Hz splitting. The observed chemical shift difference between the cis-trans isomers, due to hindered rotation around the N-CO bond, confirms the presence of acetyl ammonium ion as an intermediate.

As can be observed in the bottom spectrum in Figure 4.2, the DIPEA peaks broaden again after 2 days. Since the acetyl ammonium ion **9** is not stable this is not unexpected. Upon dissociation of the acetyl moiety, it may form side products and protonated DIPEA **8** which, due to exchange with the acetyl ammonium ion **9**, will broaden the peaks.

Since both acetyl ammonium ion **9** and ketene **7** are unstable compounds, side products are formed during the reaction. Diketene **10** is identified by its resonances at 4.88, 4.53 and 3.93 ppm. Furthermore, a product with resonances at 2.27, 2.3 and 6 ppm is observed. This may be a product of (instable) ketene and/or diketene, since both disappeared while this product appears. Some minor products at 1.97 ppm and 2.05 ppm that are present in all of the reactions are observed as well. The peak at 2.05 ppm might be from acetic acid, which can be formed from acetyl chloride and has approximately this chemical shift. Table C.1 in Appendix C.8 gives an overview of the main peaks that were found in the spectra.
Considering the observed intermediates, acetyl ammonium ion and ketene, several reaction steps can be envisioned. Acetyl chloride **1** and DIPEA **5** were shown to react, forming either ketene **7** and protonated DIPEA **8** or acetyl ammonium **9**. An explanation for this could be that the reaction proceeds via an unstable tetrahedral intermediate **6**, which results from addition of the amine to the carbonyl group. The proposed reaction mechanism is shown in Scheme 4.2.

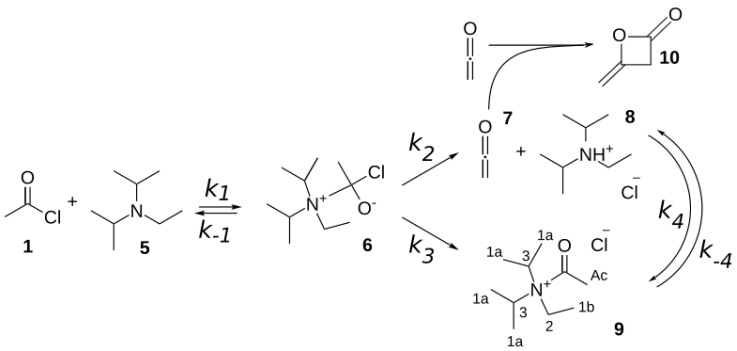

*Scheme 4.2: Proposed reaction mechanism of acetyl chloride **1** and DIPEA **5**. The reaction proceeds via tetrahedral intermediate **6**, which gives either ketene **7** and protonated DIPEA **8** or acetyl-*N,N-*diisopropylethylammonium ion **9**. Diketene **10** is a side product.*

Reaction mechanism

As ketene **7** and acetyl ammonium **9** are products in the reaction of acetyl chloride **1** with DIPEA **5**, it is very likely that they are also present in the first minutes of the DIPEA catalysed acetylation of benzyl alcohol. Small quantities of ketene **7** are indeed observed in the stripline NMR spectra shown in Figure 4.1. During the reaction, the

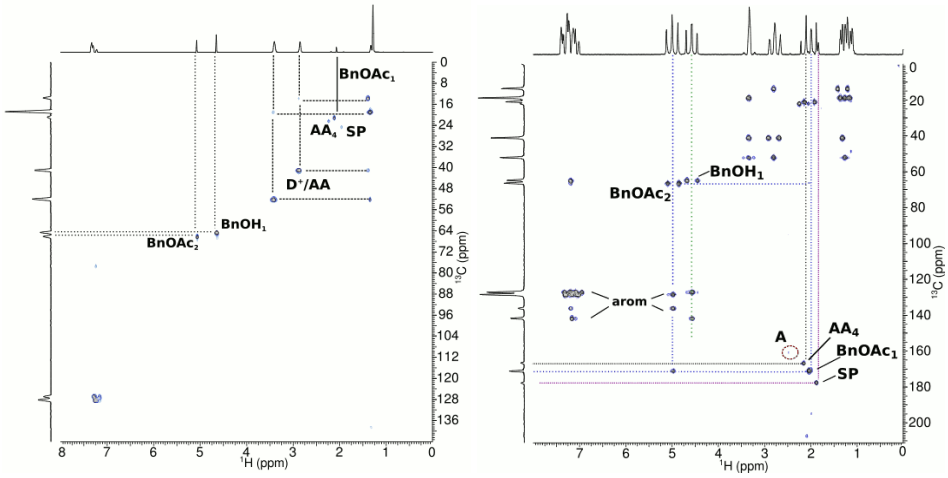

(a) HSQC (b) HMBC

*Figure 4.5: Acetyl chloride **1** and benzyl alcohol **2** with DIPEA **5**: conventional 2D spectra after 2 h reaction time, a) HSQC, b) HMBC. The HSQC shows the direct correlation between ^{1}H and ^{13}C peaks for benzyl acetate **4** (BnOAc), benzyl alcohol **2** (BnOH), protonated DIPEA **8** or acetyl ammonium ion **9** (D+/AA) and its acetyl group (AA_4). In the HMBC we find the correlated peaks of the benzyl acetate **4** (BnOAc), benzyl alcohol **2** (BnOH) and their peaks in the aromatic region, acetyl chloride **1** (A), and side products.*

DIPEA peaks are broadened and shifted to lower field. The acetyl group of the acetyl ammonium ion **9** appears at the start of the reaction and remains present throughout the progressing reaction. At the end of the reaction, acetyl ammonium is identified by the slightly broadened and shifted multiplets in the conventional NMR spectrum (bottom trace of Figure 4.1). As discussed before, the broadening indicates an exchange process, suggesting the presence of protonated DIPEA **8**. The 2D NMR spectra in Figure 4.5 show the correlations between the ^{1}H NMR and the ^{13}C chemical shifts. The peaks of the acetyl group of acetyl ammonium ion are found at the same chemical shift position as in the reaction with DIPEA (see Table C.1 in Appendix C.8) which confirms that the acetyl ammonium ion **9** is a reaction product.

The observed reaction products and the protonation of DIPEA suggests that the increased reaction rate of the acetylation in the presence of DIPEA is induced by the reaction of benzyl alcohol with ketene and acetyl ammonium. Since these products were found in the reaction of acetyl chloride and DIPEA as well, the proposed reaction mechanism for the acetylation of benzyl alcohol in the presence of DIPEA is an extension of Scheme 4.2. Benzyl alcohol may react with either ketene and/or the

acetyl ammonium ion, forming benzyl acetate. This gives credibility to the reaction mechanism as shown in Scheme 4.1.

4.3.2 Kinetics

The proposed reaction schemes are explored further using a fitting procedure to a kinetic model described in Appendix C.3. Considering the large number of reaction constants (seven for the full reaction) in relation to the limited number of experimental points we do not claim that we can fully characterise the kinetics with this approach. Nevertheless, the analysis is useful to determine the relative importance of the various steps in the reaction. Based on the integrated intensities of the resonances, the concentrations of the reaction products during the reaction progress are calculated, as shown in Figure 4.6. A set of differential equations representing the reaction scheme (Eq. (C.2) in Appendix C.3) is solved while varying the k values to minimise the difference between experimental and fitted values via an object function F[71], for the concentrations of acetyl chloride **1**, ketene **7** and the acetyl group of the acetyl ammonium ion **9**.
For the reaction of acetyl chloride and DIPEA, the reaction scheme shown in Scheme 4.2 gives the best fit to the data, compared to a similar reaction mechanism without an intermediate and/or different equilibria. Thus, we postulate that the tetrahedral intermediate **6** is formed in the first step of the reaction acetyl chloride and DIPEA. Comparing the backwards and forwards reactions, k_{-1} is much smaller than k_1, and so, the backwards reaction is assumed to be negligible. Since the concentration of the tetrahedral intermediate **6** is very small in the model, the backwards reaction can not be accurately fit and k_{-1} is set to zero. The tetrahedral intermediate **6** disintegrates forming ketene **7** with protonated DIPEA **8** (k_2) or the acetyl ammonium ion **9** (k_3). These are the fastest steps in the reaction mechanism; the values of k_2 and k_3 are much larger than all other reaction constants so the corresponding reactions can be considered instantaneous. For this reason, the relative ratio between k_2 and k_3 (2.4 ± 0.5) is more relevant than their absolute values. Likewise the ratio of the (much smaller) equilibrium constants of the reactions between ketene **7** and DIPEA **5** with acetyl ammonium ion **9** ($K = k_4/k_{-4} = 1.7 \pm 0.5$) can be determined more accurately than the absolute value of the individual rates.
After optimisation we find the k values: $k_1 = 0.16(\pm 0.03) M^{-1}s^{-1}$, $k_2 = 12 s^{-1}$, $k_3 = 5 s^{-1}$, $k_4 = 0.0035(\pm 0.002) M^{-1}s^{-1}$ and $k_{-4} = 0.0020(\pm 0.002) M^{-1}s^{-1}$. The error margin given for the reaction constants reflects the influence on the accuracy

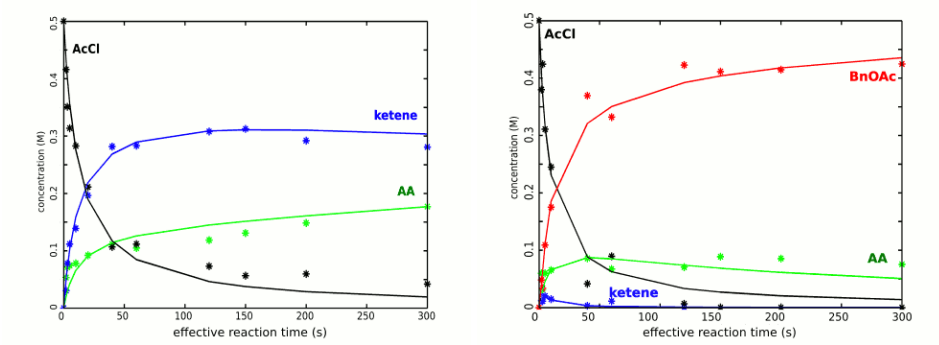

(a) (b)

*Figure 4.6: Modelling of the kinetics of the acetylation of benzyl alcohol, (a) reaction of acetyl chloride with DIPEA, (b) reaction of acetyl chloride with benzyl alcohol in the presence of DIPEA. Experimentally derived values of concentrations in the mixture during the reaction are marked with *, the solid line is the result of the fit. Starting product acetyl chloride **1** (AcCl), intermediates ketene **7** and acetyl ammonium ion **9** (AA), and end poduct benzyl acetate **4** (BnOAc). The concentrations have been estimated by the relative deconvoluted areas of the peaks.*

of the model. One of the reaction constants is changed, while the other k-values remain at their optimal value. The relative effect of such a change in k-values on the fit result is different for each reaction constant. The given amount of deviation of the k-value will decrease the object function[71] of the fit (summed squared residuals) with 5 %. The values of k_2 and k_3 can be set much larger, which slightly improves the fit, as long as the ratio remains 2.4; however, the calculation slows down when these k values are set too high. The resulting k values suggest that the tetrahedral intermediate **4** is indeed very unstable, and breaks down into ketene **7** and protonated DIPEA **8**, and acetyl ammonium ion **9**, with a preference for the ketene route. Some exchange between ketene and protonated DIPEA with acetyl ammonium ion is possible, favouring acetyl ammonium ion, which is the end product at the longest reaction times that we used in the microfluidic stripline setup. We conclude from the broadening for very long reaction times that the acetyl ammonium ion **9** partly dissociates, leaving protonated DIPEA **8** and some side products. This slower process has not been included in the reaction scheme modelling.

The proposed reaction mechanism of the complete acetylation of benzyl alcohol (Scheme 4.1) is modelled next. The reaction of DIPEA and acetyl chloride results in ketene **7** and protonated DIPEA **8** and acetyl ammonium ion **9**. Benzyl alcohol **2**

may react with ketene**7** or with acetyl ammonium ion **9**, forming benzyl acetate **4**. The direct reaction of benzyl alcohol and acetyl chloride is not taken into account because it is much slower (hours) relative to the reaction times we studied in-line (seconds to minutes).

Analogous to the reaction of acetyl chloride with DIPEA, the first reaction step is the formation of the tetrahedral intermediate **6**, in which the forward reaction rate is much higher than the backwards reaction rate; so, again k_{-1} was assumed to be negligible and set to zero. Also as before, the ratio of k_2 and k_3, in which the tetrahedral intermediate **6** breaks down into ketene **7** and protonated DIPEA **8** or acetyl ammonium ion **9**, can be determined more accurately than the actual values. For the ratio between k_2 and k_3, the best fit is found for the value $k_2/k_3 = 2.7(\pm 0.3)$, thus favouring ketene and protonated DIPEA formation. Since the concentration of ketene is very small, k_4 does not critically influence the outcome of the model, as long as it is very small and k_4 is therefore set to zero.

Seven k values as indicated in Scheme 4.1 are thus needed for representation of the reaction with a set of differential equations (Eq. (C.3) in Appendix C.3), which is optimised with respect to the concentrations of acetyl chloride **1**, ketene **7**, the acetyl group of acetyl ammonium ion **9** and benzyl acetate **4**. The optimised k values that were found are: $k_1 = 0.23(\pm 0.05)M^{-1}s^{-1}$, $k_2 = 3s^{-1}$, $k_3 = 1s^{-1}$, $k_4 = 0M^{-1}s^{-1}$, $k_{-4} = 0.04(\pm 0.2)s^{-1}$, $k_5 = 2.6(\pm 1.3)M^{-1}s^{-1}$ and $k_6 = 0.030(\pm 0.003)M^{-1}s^{-1}$. The given error margin, as before, decreases the variance of the fit with approximately 5 %, reflecting the influence of the fit parameter on the accuracy of the model.

Interestingly, k_5 is found to be much larger than k_6, which suggests that the formation of benzyl acetate **4** via the reaction of benzyl alcohol **2** with ketene **7** is the fastest. After 5 min reaction time the conversion of benzyl alcohol **2** into benzyl acetate **4** is approximately 56%. The fast part of the reaction is finished by then since there is no ketene **7** and acetyl chloride **1** left in the mixture. If left to stand for 2 days, the acetyl ammonium **9** peak diminishes and benzyl acetate **4** increases slightly, which indicates that the reaction proceeds slowly via the acetyl ammonium route (reaction k_6 in Scheme 4.1). The high reactivity/instability of both ketene **7** and acetyl ammonium **9** prevents the achievement of full conversion as witnessed by the formation of diketene **10** and protonated DIPEA **8** leading to various side products.

When the slower reaction steps are left out of the PDE model, it can be simplified into a two step and three step model, for the reaction of acetyl chloride with DIPEA and the acetylation of benzyl alcohol in the presence of DIPEA, respectively. The fit results

are shown in Appendix C.4 in Figure C.2. The variance of the fit decreases with only approximately 5% for acetyl chloride with DIPEA and with 10% for the acetylation.

4.3.3 Variation of amines as base catalyst

Having established the role of DIPEA in the acetylation of benzyl alcohol we set out to study different types of amines as catalysts to examine whether the reaction proceeds via a similar mechanism. DIPEA, triethylamine **11** (TEA) and pyridine **15** differ in reactivity; pyridine is a weakly aromatic base (acid dissociation constant $pK_a \approx 5.2$), TEA and DIPEA have, due to increasing steric hindrance, a reduced nucleophilicity and a higher base reactivity ($pK_a \approx 10.6$ and $pK_a \approx 11.4$, respectively)[72]. The proton affinity of DIPEA is highest (984 kJ/mol), that of TEA slightly lower (972 kJ/mol) and that of pyridine lowest (924 kJ/mol)[73]. With the high proton affinity, the DIPEA molecule was postulated to act as a proton scavenger while not taking part in the reaction, due to steric hindrance, contrary to the findings in the previous section. Pyridine, having lower proton affinity but little steric effects, would instead be acetylated rather than protonated.

Triethylamine

Figure 4.7 shows a series of stripline NMR spectra, and Figure C.4 in Appendix C.6 shows the conventional 2D NMR spectra for the reaction of acetyl chloride (0.5 M) and TEA (0.5 M). Peaks of intermediate products, ketene **7** and the acetyl group of acetyl ammonium ion **14** are found at the same positions as in the reaction with DIPEA. This suggests that similar products are involved with the proposed reaction mechanism shown in Scheme 4.3. However, the reaction kinetics are markedly different. The first step of acetyl chloride reacting with TEA is much faster as compared to DIPEA. Ketene **7** and deketene **10** form at a much higher rate, being already visible within 1.5 s in the spectra taken with the stripline probe. With the highly reactive ketene **7** and diketene **10** being formed at high rate, we observe the formation of more side products, which can be seen in the conventional 2D spectra in Figure C.4.
In Figure 4.8, a series of *in situ* spectra for the acetylation of benzyl alcohol in the presence of TEA is shown, and Figure C.5 in Appendix C.6 shows the conventional 2D NMR spectra at later stages in this reaction. In these spectra, benzyl acetate **4** and acetyl ammonium ion **14** are observed with a small amount of acetic acid as a side product. Much less side products are observed, compared to the spectra of acetyl

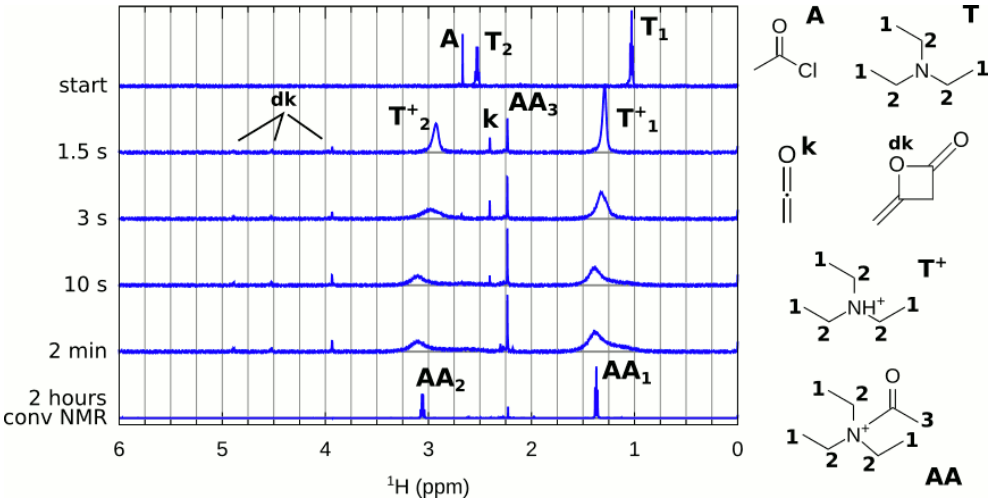

*Figure 4.7: Monitoring of the reaction of acetyl chloride (0.5 M) with triethylamine (0.5 M). Top: unreacted compounds: acetyl chloride **1** (A) and TEA **11** (T). The series of in situ spectra show the broadening and shifting of TEA peaks, peaks of the intermediates are marked 'k' (ketene **7**) and 'Ac' (acetyl group of acetyl ammonium ion **14**). Diketene **10** is formed as a side product, also other side products are present at 2 minutes reaction time. Bottom: conventional NMR spectrum after 2 hours reaction time, the TEA peaks are found at shifted positions, the main methyl peak is associated with the acetyl peak of the acetyl ammonium ion **14**.*

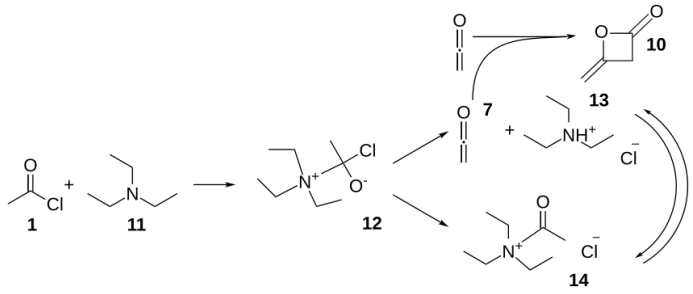

*Scheme 4.3: Proposed reaction mechanism of acetyl chloride **1** and triethylamine **11**. A tetrahedral intermediate **12** is formed, which breaks down into ketene **7** and protonated TEA **13** or acetyl ammonium ion **14**. Diketene **10** is a side product.*

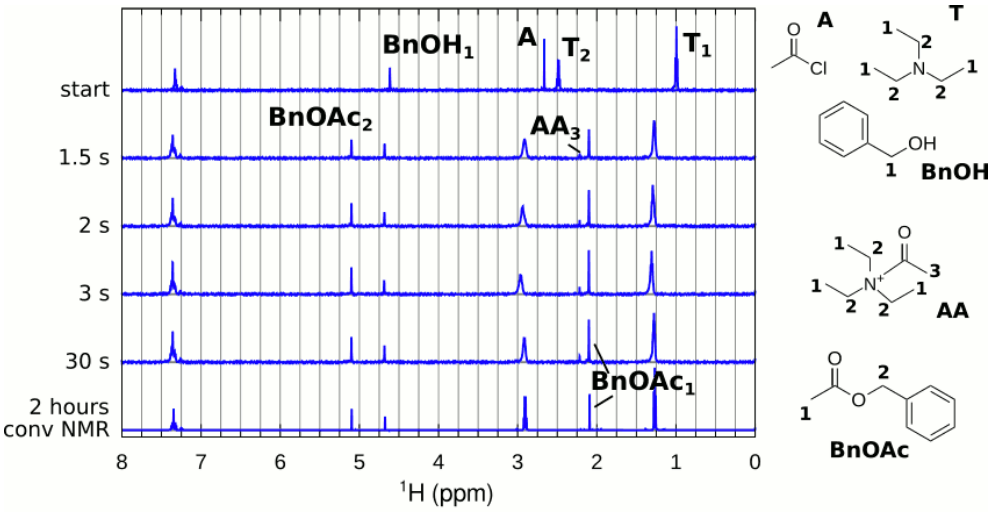

*Figure 4.8: Monitoring of the reaction of benzyl alchohol (0.5 M) with acetyl chloride (0.5 M) and triethylamine (0.5 M). Top: unreacted compounds: acetyl chloride **1** (A), TEA **11** (T) and benzyl alcohol **2** (BnOH). In the series of in situ spectra the TEA peaks are slightly broadened and shifted, a small amount of acetyl ammonium ion **14** is present (acetyl peak marked 'AA$_3$'), benzyl acetate **4** is formed (BnOAc). For longer reaction times the spectra remain similar. Bottom: conventional NMR spectrum after 2 hours reaction time, the TEA peaks are found at shifted position, benzyl acetate **4** is formed, also benzyl alcohol **2** remains present.*

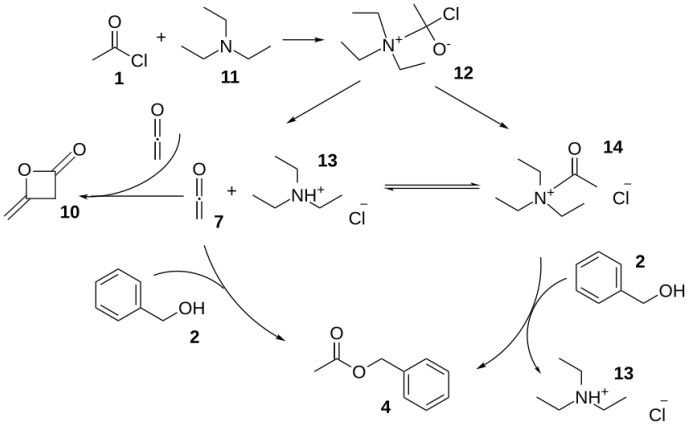

*Scheme 4.4: Proposed reaction mechanism of acetyl chloride **1** and triethylamine **11** with benzyl alchohol **2**. First acetyl chloride and TEA form a tetrahedral intermediate **12**, from which an equilibrium between acetyl ammonium ion **14** and ketene **7** with protonated TEA **13**. Benzyl alcohol **2** reacts with ketene **7** or acetyl ammonium ion **14** into benzyl acetate **4**.*

chloride and TEA. With the rapid formation of ketene that is available for reaction with benzyl alcohol to form benzyl acetate, the reaction is completed within 30 s, the overall conversion is 57% after 5 min reaction time.

From the NMR analyses, we conclude that the TEA-catalysed acetylation proceeds similarly to the acetylation in the presence of DIPEA, as summarised in Scheme 4.4. Despite TEA being a somewhat weaker base, the reaction rates are higher than in the reaction with DIPEA. This further corroborates that the amine is not merely a proton scavenger but takes part in the reaction, leading to the formation of ketene, where steric factors are more important than basicity.

Pyridine

Despite the fact that pyridine **15** is regularly used as base catalyst in similar reactions, it is a very different base. From the literature[74, 75], we expect an acetyl pyridinium ion **16** to play an important role in this reaction, similar to the acetyl ammonium ion that we observed in the preceding reactions.

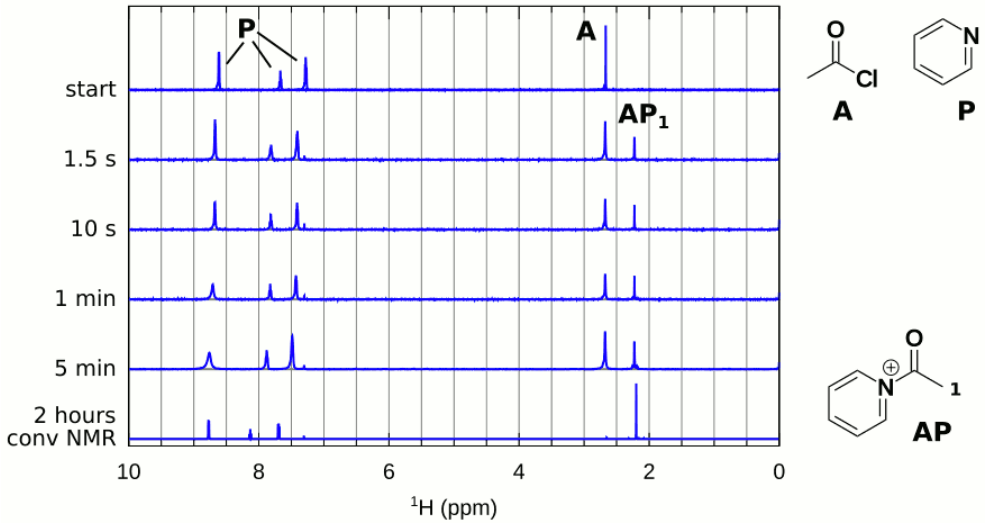

*Figure 4.9: Monitoring of the reaction of acetyl chloride (0.5 M) with pyridine (0.5 M). Top: unreacted compounds: acetyl chloride **1** (A) and pyridine **15** (P). In the series of spectra the pyridine peaks are found to shift and broaden and an acetate peak for acetyl pyridinium ion **16** is marked (AP_1). Bottom: In the conventional NMR spectrum after a few hours reaction time, the pyridine peaks are sharp and at a shifted position, the acetyl chloride **1** has fully reacted with pyridine **15** into acetyl pyridinium ion **16**.*

Figure 4.9 shows the results of the *in situ* experiments in the stripline probe using pyridine as a base catalyst. Figure C.6 in Appendix C.7 shows the conventional 2D NMR spectra. In these spectra, a methyl peak at 2.22 ppm is observed at a similar position as the acetyl ammonium ion **9**. Furthermore, during the reaction, the pyridine peaks are found to shift and broaden suggesting the formation of a complex. Based on this we conclude that the predicted acetyl pyridinium ion **16** is indeed formed, in agreement with literature[74, 75]. Ketene **7** is not observed at any point of this reaction. We conclude that acetyl chloride **1** and pyridine **15** directly react to give acetyl pyridinium ion **16** as shown in Scheme 4.5.

The spectra for the pyridine (0.5 M) catalysed reaction of benzyl alcohol (0.5 M) with acetyl chloride (0.5 M) are shown in Figur 4.10, with the conventional 2D NMR

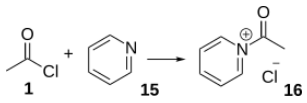

*Scheme 4.5: Proposed reaction mechanism of acetyl chloride **1** and pyridine **15**, giving acetyl pyridinium ion **16***

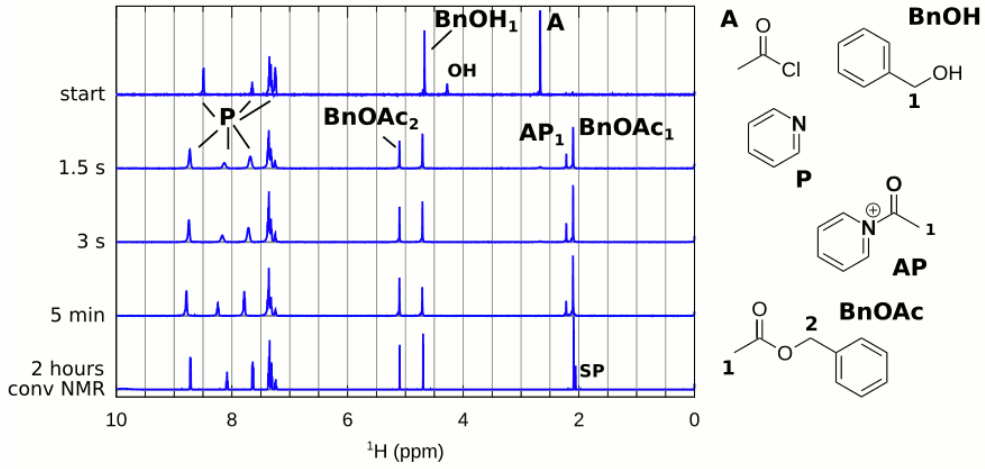

*Figure 4.10: Monitoring of the reaction of benzyl alchohol (0.5 M) with acetyl chloride (0.5 M) and pyridine (0.5 M). Top: unreacted compounds: acetyl chloride **1** (A), pyridine **15** (P) and benzyl alcohol **2** (BnOH). In the series of spectra the pyridine peaks are broadened and shifting, the acetyl peak for acetyl pyridinium ion **16** is found (AP_1), benzyl acetate **4** is formed already in the spectrum after 1.5 seconds (BnOAc). Bottom: In the conventional NMR spectrum after a few hours reaction time, the pyridine peaks are sharp and at a shifted position, benzyl acetate **4** (BnOAc) is present, benzyl alchohol **2** (BnOH) remains present and a side product (SP) is formed.*

spectra at a later stage of the reaction displayed in Figure C.7 in Appendix C.7. In these spectra, a methyl peak at 2.22 ppm and a broadening and shift of the pyridine peaks are observed as before, suggesting the presence of acetyl pyridinium **16**. Already after 1.5 s (top spectrum in Figure 4.10), acetyl chloride **1** has almost completely reacted into benzyl acetate **4** and acetyl pyridinium **16**. Furthermore, benzyl alchohol **2** and some side product formation, probably acetic acid, is observed. This corroborates that the acetylation takes place via the reaction of benzyl alcohol with the acetyl pyridinium **16** intermediate as depicted in Scheme 4.6. The reaction rates are much faster compared to the reaction performed with DIPEA. The overall conversion of benzyl alcohol to benzyl acetate is similar, however, being 55% after 5 min.

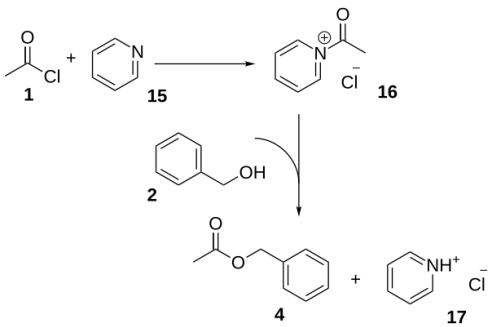

*Scheme 4.6: Proposed reaction mechanism of acetyl chloride **1** and pyridine **15** with benzyl alchohol **2**, via acetyl pyridinium **16**, forming benzyl acetate **4** and protonated pyridine **17***

Conclusion

In the work presented here we show that a microfluidic stripline NMR setup offers the possibility to study fast reactions *in situ*. Microreactor technology is advantageous for very fast and/or exothermic reactions. The acetylation of benzyl alcohol in the presence of DIPEA was studied in detail and intermediates of the reaction were identified as ketene and acetyl ammonium ion. The kinetics of this reaction were monitored and modelled by solving the rate equations for the proposed reaction scheme. Based on these results, a reaction mechanism via a tetrahedral intermediate was proposed. It was found that the product is formed most rapidly by the reaction of benzyl alcohol with ketene. Replacing DIPEA with TEA accelerates the reaction, but the mechanism remains similar, as suggested by the observation of the same intermediates, ketene and acetyl ammonium. Using pyridine as a base catalyst, no evidence is found that this

reaction also proceeds via ketene, but acetyl pyridinium ion **16** was observed.

Acknowledgements

Ruud Aspers is acknowledged for acquiring of the conventional NMR spectra. This work was financially supported by The Netherlands Organisation for Scientific Research (NWO), ACTS, Process on a Chip programme.

References

[1] R. Eisert and K. Levsen, "Solid-phase microextraction coupled to gas chromatography: a new method for the analysis of organics in water," *J. Chromatogr. A*, vol. 733, p. 143, 1996.

[2] L. L. Gur'eva, A. I. Tkachuk, E. A. Dzhavadyan, G. A. Estrin, N. F. Surkov, I. V. Sulimenkov, and B. A. Rozenberg, "Kinetics and mechanism of the anionic polymerization of acrylamide monomers," *Polym. Sci., Ser. A*, vol. 49, no. 9, p. 987, 2007.

[3] J. S. Moore and K. F. Jensen, "Automated multitrajectory method for reaction optimization in a microfluidic system using online IR analysis," *Org. Process Res. Dev.*, vol. 16, p. 1409, 2012.

[4] J. K. Puri, R. Singh, V. K. Chahal, R. P. Sharma, J. Wagler, and E. Kroke, "New silatranes possessing urea functionality: Synthesis, characterization and their structural aspects," *J. Organomet. Chem.*, vol. 696, p. 1341, 2011.

[5] J. S. McKenzie, J. A. Donarski, J. C. Wilson, and A. J. Charlton, "Analysis of complex mixtures using high-resolution nuclear magnetic resonance spectroscopy and chemometrics," *Prog. Nucl. Magn. Reson. Spectrosc.*, vol. 59, p. 336, 2011.

[6] J. Kang, G. Hilmersson, J. Santamaria, and J. Rebek, Jr., "Diels-Alder reactions through reversible encapsulation," *J. Am. Chem. Soc.*, vol. 120, p. 3650, 1998.

[7] S. P. Babailov, "NMR studies of photo-induced chemical exchange," *Prog. Nucl. Magn. Reson. Spectrosc.*, vol. 54, p. 183, 2009.

[8] M. D. Christianson, E. H. P. Tan, and C. R. Landis, "Stopped-flow NMR: Determining the kinetics of [rac-(C2H4(1-indenyl)2)ZrMe][MeB(C6F5)3]-catalyzed polymerization of 1-hexene by direct observation," *J. Am. Chem. Soc.*, vol. 132, no. 33, p. 11461, 2010.

[9] Y. Liu and X. Jiang, "Why microfluidics? merits and trends in chemical synthesis," *Lab Chip*, vol. 17, 2017.

[10] M. B. Plutschack, B. Pieber, K. Gilmore, and P. H. Seeberger, "The hitchhiker's guide to flow chemistry," *Chem. Rev.*, vol. 117, p. 11796, 2017.

[11] D. T. Chiu, A. J. deMello, D. D. Carlo, P. S. Doyle, C. Hansen, R. M. Maceiczyk, and R. C. Wootton, "Small but perfectly formed? successes, challenges, and opportunities for microfluidics in the chemical and biological sciences," *Chem.*, vol. 2, p. 201, 2017.

[12] K. Jähnisch, V. Hessel, H. Löwe, and M. Baerns, "Chemistry in microstructured reactors," *Angew. Chem., Int. Ed.*, vol. 43, p. 406, 2004.

[13] P. Watts and C. Wiles, "Recent advances in synthetic micro reaction technology," *Chem. Commun.*, p. 443, 2007.

[14] U. Neuenschwander and K. F. Jensen, "Olefin autoxidation in flow," *Ind. Eng. Chem. Res.*, vol. 53, p. 601, 2014.

[15] H. Amii, A. Nagaki, and J. Yoshida, "Flow microreactor synthesis in organo-fluorine chemistry," *Beilstein J. Org. Chem.*, vol. 9, p. 2793, 2013.

[16] D. Cantillo, M. Damm, D. Dallinger, M. Bauser, M. Berger, and C. O. Kappe, "Sequential nitration/hydrogenation protocol for the synthesis of triaminophloroglucinol: Safe generation and use of an explosive intermediate under continuous-flow conditions," *Org. Process Res. Dev.*, vol. 18, p. 1360, 2014.

[17] J. Yoshida, A. Nagaki, T. Iwasaki, and S. Suga, "Enhancement of chemical selectivity by microreactors," *Chem. Eng. Technol.*, vol. 28, no. 3, p. 259, 2005.

[18] D. M. Ratner, E. R. Murphy, M. Jhunjhunwala, D. A. Snyder, K. F. Jensen, and P. H. Seeberger, "Microreactor-based reaction optimization in organic chemistry - glycosylation as a challenge," *Chem. Commun.*, p. 578, 2005.

[19] M. M. E. Delville, P. J. Nieuwland, P. Janssen, K. Koch, J. C. M. van Hest, and F. P. J. T. Rutjes, "Continuous flow azide formation: Optimization and scale-up," *Chem. Eng. J.*, vol. 167, p. 556, 2011.

[20] J. Yue, J. C. Schouten, and T. A. Nijhuis, "Integration of microreactors with spectroscopic detection for online reaction monitoring and catalyst characterization," *Ind. Eng. Chem. Res.*, vol. 51, p. 14583, 2012.

[21] V. Sans and L. Cronin, "Towards dial-a-molecule by integrating continuous flow, analytics and self-optimisation," *Chem. Soc. Rev.*, vol. 45, p. 2032, 2016.

[22] D. Belder, "Integrating chemical synthesis and analysis on a chip," *Anal. Bioanal. Chem.*, vol. 385, p. 416, 2006.

[23] D. Hoult and R. Richards, "The signal-to-noise ratio of the nuclear magnetic resonance experiment," *J. Magn. Reson.*, vol. 24, p. 71, 1976.

[24] M. E. Lacey, R. Subramanian, D. L. Olson, A. G. Webb, and J. V. Sweedler, "High-Resolution NMR spectroscopy of sample volumes from 1 nl to 10 μL," *Chem. Rev.*, vol. 99, no. 10, p. 3133, 1999.

[25] A. P. M. Kentgens, J. Bart, P. J. M. van Bentum, A. Brinkmann, E. R. H. van Eck, J. G. E. Gardeniers, J. W. G. Janssen, P. Knijn, S. Vasa, and M. H. W. Verkuijlen, "High-resolution liquid- and solid-state nuclear magnetic resonance of nanoliter sample volumes using microcoil detectors," *J. Chem. Phys.*, vol. 128, p. 052202, 2008.

[26] R. M. Fratila and A. H. Velders, "Small-volume nuclear magnetic resonance spectroscopy," *Annu. Rev. Anal. Chem.*, vol. 4, p. 227, 2011.

[27] O. Gökay and K. Albert, "From single to multiple microcoil flow probe NMR and related capillary techniques: a review," *Anal. Bioanal. Chem.*, vol. 402, p. 647, 2012.

[28] S. S. Zalesskiy, E. Danieli, B. Blűmich, and V. P. Ananikov, "Miniaturization of NMR systems: Desktop spectrometers, microcoil spectroscopy, and *NMR on a Chip* for chemistry, biochemistry, and industry," *Chem. Rev.*, vol. 114, p. 5641, 2014.

[29] B. Behnia and A. G. Webb, "Limited-sample NMR using solenoidal microcoils, perfluorocarbon plugs, and capillary spinning," *Anal. Chem.*, vol. 70, p. 5326, 1998.

[30] D. L. Olson, T. L. Peck, A. G. Webb, R. L. Magin, and J. V. Sweedler, "High resolution microcoil 1H-NMR for mass-limited, nanoliter-volume samples," *Science*, vol. 270, p. 1967, 1995.

[31] R. C. Meier, J. Höfflin, V. Badilita, U. Wallrabe, and J. G. Korvink, "Microfluidic integration of wirebonded microcoils for on-chip applications in nuclear magnetic resonance," *J. Micromech. Microeng.*, vol. 24, p. 045021, 2014.

[32] S. Leidich, M. Braun, T. Gessner, and T. Riemer, "Silicon cylinder spiral coil for nuclear magnetic resonance spectroscopy of nanoliter samples," *Concepts Magn. Reson., Part B*, vol. 35B, no. 1, p. 11, 2009.

[33] H. Ryan, S.-H. Song, A. Zaß, J. Korvink, and M. Utz, "Contactless NMR spectroscopy on a chip," *Anal. Chem.*, vol. 84, p. 3696, 2012.

[34] R. M. Fratila, V. Gomez, S. Sýkora, and A. H. Velders, "Multinuclear nanoliter one-dimensional and two-dimensional NMR spectroscopy with a single non-resonant microcoil," *Nat. Commun.*, vol. 5, p. 3025, 2014.

[35] I. Swyer, R. Soong, M. D. M. Dryden, M. Fey, W. E. Maas, A. Simpson, and A. R. Wheeler, "Interfacing digital microfluidics with high-field nuclear magnetic resonance spectroscopy," *Lab Chip*, vol. 16, p. 4424, 2016.

[36] P. J. M. van Bentum, J. W. G. Janssen, and A. P. M. Kentgens, "Towards nuclear magnetic resonance m-spectroscopy and μ-imaging," *Analyst*, vol. 129, p. 793, 2004.

[37] P. J. M. van Bentum, J. W. G. Janssen, A. P. M. Kentgens, J. Bart, and J. G. E. Gardeniers, "Stripline probes for nuclear magnetic resonance," *J. Magn. Reson.*, vol. 189, p. 104, 2007.

[38] J. Bart, J. W. G. Janssen, P. J. M. van Bentum, A. P. M. Kentgens, and J. G. E. Gardeniers, "Optimization of stripline-based microfluidic chips for high-resolution NMR," *J. Magn. Reson.*, vol. 201, p. 175, 2009.

[39] H. G. Krojanski, J. Lambert, Y. Gerikalan, D. Suter, and R. Hergenroder, "Microslot NMR probe for metabolomics studies," *Anal. Chem.*, vol. 80, p. 8668, 2008.

[40] Y. Maguire, I. L. Chuang, S. Zhang, and N. Gershenfeld, "Ultra-small-sample molecular structure detection using microslot waveguide nuclear spin resonance," *Proc. Natl. Acad. Sci. U. S. A.*, vol. 104, no. 22, p. 9198, 2007.

[41] G. Finch, A. Yilmaz, and M. Utz, "An optimised detector for in-situ high-resolution NMR in microfluidic devices," *J. Magn. Reson.*, vol. 262, p. 73, 2016.

[42] Y. Chen, H. S. Mehta, M. C. Butler, E. D. Walter, P. N. Reardon, R. S. Renslow, K. T. Mueller, and N. M. Washton, "High-resolution microstrip NMR detectors for subnanoliter samples," *Phys. Chem. Chem. Phys.*, vol. 19, p. 28163, 2017.

[43] E. G. Sorte, N. A. Banek, M. J. Wagner, T. M. Alam, and Y. J. Tong, "In situ stripline electrochemical NMR for batteries," *ChemElectroChem*, vol. 5, p. 2336, 2018.

[44] J. Bart, A. J. Kolkman, A. J. Oosthoek-de Vries, K. Koch, P. J. Nieuwland, J. W. G. Janssen, P. J. M. van Bentum, K. A. M. Ampt, F. P. J. T. Rutjes, S. S. Wijmenga, J. G. E. Gardeniers, and A. P. M. Kentgens, "A microfluidic high-resolution NMR flow probe," *J. Am. Chem. Soc.*, vol. 131, p. 5014, 2009.

[45] M. V. Gomez and A. de la Hoz, "NMR reaction monitoring in flow synthesis," *Beilstein J. Org. Chem.*, vol. 13, p. 285, 2017.

[46] L. Ciobanu, D. A. Jayawickrama, X. Zhang, A. G. Webb, and J. V. Sweedler, "Measuring reaction kinetics by using multiple microcoil NMR spectroscopy," *Angew. Chem., Int. Ed.*, vol. 42, p. 4669, 2003.

[47] H. Wensink, F. Benito-Lopez, D. C. Hermes, W. Verboom, J. G. E. Gardeniers, D. N. Reinhoudt, and A. van den Berg, "Measuring reaction kinetics in a lab-on-a-chip by microcoil NMR," *Lab Chip*, vol. 5, p. 280, 2005.

[48] M. Kakuta, D. A. Jayawickrama, A. M. Wolters, A. Manz, and J. V. Sweedler, "Micromixer-based time-resolved NMR: Applications to ubiquitin protein conformation," *Anal. Chem.*, vol. 75, p. 956, 2003.

[49] A. Brächer, S. Hoch, K. Albert, H. J. Kost, B. Werner, E. von Harbou, and H. Hasse, "Thermostatted micro-reactor NMR probe head for monitoring fast reactions," *J. Magn. Reson.*, vol. 242, p. 155, 2014.

[50] M. V. Gomez, A. M. Rodriguez, A. de la Hoz, F. Jimenez-Marquez, R. M. Fratila, P. A. Barneveld, and A. H. Velders, "Determination of kinetic parameters within a single nonisothermal on-flow experiment by nanoliter NMR spectroscopy," *Anal. Chem.*, vol. 87, p. 10547, 2015.

[51] K. Ishihara, H. Kurihara, and H. Yamamoto, "An extremely simple, convenient, and selective method for acetylating primary alcohols in the presence of secondary alcohols," *J. Org. Chem.*, vol. 58, p. 3791, 1993.

[52] P. Hubbard and W. J. Brittain, "Mechanism of amine-catalyzed ester formation from an acid chloride and alcohol," *J. Org. Chem.*, vol. 63, p. 677, 1998.

[53] D. H. Paull, A. Weatherwax, and T. Lectka, "Catalytic, asymmetric reactions of ketenes and ketene enolates," *Tetrahedron*, vol. 65, p. 6771, 2009.

[54] K. D. Nagy, D. Shen, T. Jamison, and K. Jensen, "Mixing and dispersion in small-scale flow systems," *Org. Process Res. Dev.*, vol. 16, p. 976, 2012.

[55] D. A. Laude, Jr. and C. L. Wilkins, "Direct-linked analytical scale high-performance liquid chromatography/nuclear magnetic resonance spectrometry," *Anal. Chem.*, vol. 56, p. 2471, 1984.

[56] N. Wu, A. Webb, T. L. Peck, and J. V. Sweedler, "On-line NMR detection of amino acids and peptides in microbore LC," *Anal. Chem.*, vol. 67, no. 18, p. 3101, 1995.

[57] F. Malz and H. Jancke, "Validation of quantitative NMR," *J. Pharm. Biomed. Anal.*, vol. 38, no. 5, p. 813, 2005.

[58] R. O. Kühne, T. Schaffhauser, A. Wokaun, and R. R. Ernst, "Study of transient chemical reactions by NMR. Fast stopped-flow fourier transform experiments," *J. Magn. Reson.*, vol. 35, p. 39, 1979.

[59] T. Westermann and L. Mleczko, "Heat management in microreactors for fast exothermic organic syntheses - first design principles," *Org. Process Res. Dev.*, vol. 20, p. 487, 2016.

[60] G. Bodenhausen and D. Ruben, "Natural abundance nitrogen-15 NMR by enhanced heteronuclear spectroscopy," *Chem. Phys. Lett.*, vol. 69, p. 185, 1980.

[61] A. Bax and M. Summers, "^{1}H and ^{13}C assignments from selectivity-enhanced detection of heteronuclear multiple-bond connectivity by 2D multiple quantum NMR," *J. Am. Chem. Soc.*, vol. 108, p. 2093, 1986.

[62] J. D. van Beek, "matNMR: A flexible toolbox for processing, analyzing and visualizing magnetic resonance data in Matlab," *J. Magn. Reson.*, vol. 187, p. 19, 2007.

[63] "ACD/NMR Processor Academic Edition." Advanced Chemistry Development, Inc., Toronto, ON, Canada, 2010.

[64] D. P. N. Satchell and R. S. Satchell, "Acylation by ketens and isocyanates. a mechanistic approach," *Chem. Soc. Rev.*, vol. 4, p. 231, 1975.

[65] E. C. Aquino and W. J. Brittain, "Kinetics of acyl ammonium salt formation: mechanistic implications for carbonate macrocyclization," *Macromolecules*, vol. 25, p. 3827, 1992.

[66] A. E. Taggi, A. M. Hafez, H. Wack, B. Young, W. J. Drudy III, and T. Letcka, "Catalytic, asymmetric synthesis of β-lactams," *J. Am. Chem. Soc.*, vol. 122, p. 7831, 2000.

[67] J. Sandström, *Dynamic NMR Spectroscopy*. Academic Press, 1982.

[68] H. R. Seikaly and T. T. Tidwell, "Addition reactions of ketenes," *Tetrahedron*, vol. 42, no. 10, p. 2587, 1986.

[69] T. Drakenberg, K.-J. Dahlqvist, and S. Forsen, "The barrier to internal rotation in amides. IV. N,N-Dimethylamides; substituent and solvent effects," *J. Phys. Chem.*, vol. 76, no. 15, p. 2178, 1972.

[70] F. P. Gasparro and N. H. Kolodny, "NMR determination of the rotational barrier in N,N-dimethylacetamide," *J. Chem. Educ.*, vol. 54, no. 4, p. 258, 1977.

[71] A.-L. Seoud and L. A. M. Abdallah, "Two optimization methods to determine the rate constants of a complex chemical reaction using FORTRAN and MATLAB," *Am. J. Appl. Sci.*, vol. 7, no. 4, p. 509, 2010.

[72] P. A. Koutentis, M. Koyioni, and S. S. Michaelidou, "Synthesis of [(4-Chloro-5H-1,2,3-dithiazol-5-ylidene)amino]azines," *Molecules*, vol. 16, p. 8992, 2011.

[73] S. G. Lias, J. F. Liebman, and R. D. Levin, "Evaluated gas phase basicities and proton affinities of molecules; heats of formation of protonated molecules," *J. Phys. Chem. Ref. Data*, vol. 13, p. 695, 1984.

[74] A. R. Fersht and W. P. Jencks, "The acetylpyridinium ion intermediate in pyridine-catalyzed hydrolysis and acyl transfer reactions of acetic anhydride. observation, kinetics, structure-reactivity correlations, and effects of concentrated salt solutions," *J. Am. Chem. Soc.*, vol. 92, no. 12, p. 5432, 1970.

[75] P. Spanu, A. Mannu, and F. Ulgheri, "An unexpected reaction of pyridine with acetyl chloride to give dihydropyridine and piperidine derivatives," *Tetrahedron Lett.*, vol. 55, p. 1939, 2014.

Chapter 5

Paal-Knorr pyrrole synthesis: reaction and detection in a microfluidic NMR setup

Anna Jo Oosthoek - de Vries, S. A. M. W. van den Broek, Ruud L. E. G. Aspers and Arno P. M. Kentgens

This chapter is in preparation for publication.

Abstract

The Paal-Knorr pyrrole synthesis is of substantial use in synthetic chemistry, nevertheless the reaction mechanism is not completely understood and, moreover, it is a difficult reaction to perform on industrial scale due to its exothermic behaviour. However, the Paal-Knorr synthesis can be performed well in a microfluidic setup, that ensures optimal heat transfer. In this paper, the Paal-Knorr pyrrole synthesis is performed in a microreactor coupled to a stripline NMR microcoil, obtaining 1D and 2D ^{1}H NMR experiments under steady state conditions. First, the related reaction of ethanol amine with 2,5-hexanedione, which comes to an equillibrium, was examined from 1D and 2D ^{1}H NMR spectra. The reaction kinetics model suggested that the nucleophilic attack of cabonyl group is the rate determing step. However, the pyrrole synthesis completes in a few minutes. The intermediate products only present in these first minutes are assigned from a series of ^{1}H NMR and TOCSY spectra measured in stripline NMR under continuous flow conditions. The reaction mechanism was found to involve cyclisation of the hemiaminal. Optimisation of the kinetic model showed that the cyclisation is very fast, whereas the dehydration and addition are relatively slow steps.

5.1 Introduction

Pyrroles are not only important structural elements of many natural compounds, but also of significant use in synthetic chemistry [1], biology, pharmacy [2, 3, 4] and toxicology [5]. Therefore, synthetic pathways of compounds with a pyrrole ring are subject of much research [6, 7].

The Paal-Knorr cyclocondensation is a procedure in which complex pyrroles are formed from primary amines and γ-dicarbonyl compounds (diketones) [8, 9]. The reaction mechanism of the Paal-Knorr synthesis has been under some debate in literature, regarding the intermediates and sequence of the steps involved in the reaction. The details of the mechanism are relevant for designing synthetic pathways. The generally proposed mechanisms [5, 10, 11] are shown in Scheme 5.1. Two different pathways can be considered, route A involves cyclisation of the hemiaminal intermediate **3**, whereas route B involves cyclisation of the enamine intermediate **6**.

Previous work of Katritzky et al. [10] proposes route B, based on ^{1}H, ^{13}C and ^{15}N NMR analysis of intermediates. However, later studies by Amarnath et al. [5, 11] suggest that route A is the preferred route and that the cyclisation of the hemiaminal **3** is the rate-limiting step, as deduced from detailed analysis of stereoisomer reactivity, deuterium

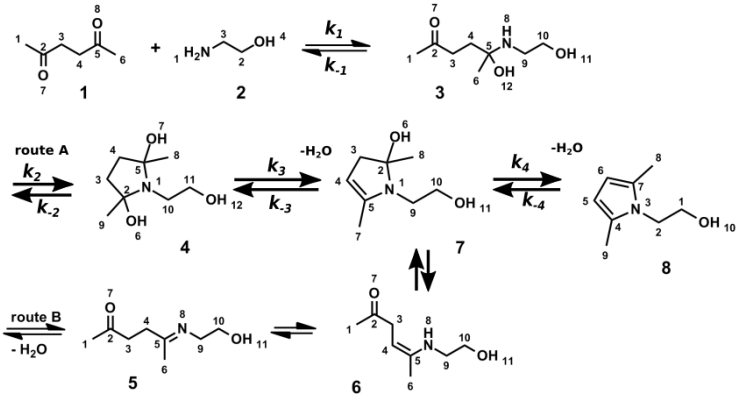

Scheme 5.1: Possible reaction mechanisms of Paal Knorr pyrrole synthesis

labelling and the isotope effect. Mothana and Boyd[12] carried out a density functional theory calculation and concluded that the hemiaminal cyclisation pathway, route A, is indeed preferred, agreeing with Amarnath et al. Observation of the imine intermediate **5** by Kratritzky et al. may have been explained by formation of imine in equilibrium, which however is unlikely to cyclise into pyrrole[11]. Since generally, amines and hemiaminals are formed in rapid equilibrium, it is suggested that the rate-limiting step is the cyclisation or the elimination of the diol[12]. More recently, Akbaşlar et al. reported that using boiling water as a solvent, not only qualifies as green chemistry, but also gives excellent yields[13]. A reaction mechanism was proposed similar to the enamine pathway (route A) with protonation from water. Cho et al.[14] developed a solvent and catalyst free method for generating pyrroles with a variety of amines. It is proposed that the reaction mechanism in acidic and non-acidic conditions differ. While the formation of enamine and imine is likely in acidic conditions, in non-acidic conditions it is proposed that the hemiaminal cyclises directly into diol **4**, thus following route A.

Abbat et al.[15] carried out quantum chemical calculations on possible mechanisms, also including mechanisms involving water or proton catalysis, concluding that water participation could play an important role in reducing energy barriers for cyclisation by conformational changes in intermediates that release strain involved in the cyclisation process. Water participation also lowers energy barriers for the following water elemination steps. The hemiaminal pathway (route A) with explicit water participation was calculated to be more favourable.

The Paal-Knorr reaction is a valuable procedure, but unfortunately it is a difficult reaction to perform at industrial scale, due to exothermic behaviour at high concentrations[2]. Microreactors can be an answer to this problem, since the high heat transfer and high mass transfer capabilities enable safe execution of exothermic reactions[16, 17]. Taghavi-Moghadam et al.[18] performed the Paal-Knorr synthesis under solvent-free conditions in a microreactor, as a way to optimise the use of resources (solvents). Nieuwland et al.[19] optimised the Paal-Knorr reaction in continuous flow in a microreactor, showing that the reaction could be well-controlled at high concentrations. The optimisation was performed on two amine substrates in microreactors with volumes of 0.13 μl and 7.02 μl and resulted in 100% conversion. The experiment was designed for scale-up, using microstructured reactors with 9.6 ml internal volume. Jensen et al.[4, 20] developed an automated multitrajectory platform with temperature control, using inline infrared (IR) monitoring of the Paal-Knorr synthesis performed in a 232 μl microreactor, for maximisation of the production rate and kinetic data collection. While this efficiently monitors the reaction and the one-step model kinetics, the reaction mechanism and the intermediates were not studied in these papers. Our microfluidic NMR setup directly coupled to a microreactor enables online monitoring of the reaction and studying the intermediate products. Using Nieuwland's optimised procedure for the reaction in a microreactor[19], the pyrrole synthesis proceeds within a few minutes with little or no side product. Experiments were performed during the first few minutes of the Paal-Knorr reaction. Using a series of ^{1}H NMR spectra, we can follow the concentrations of the reaction products and 2D correlation spectroscopy is used to obtain information about the molecular structure, in order to gain more insight into the reaction mechanism, and determine whether ring closure takes place at the hemiaminal **3** or the enamine **6**. First, we focus on the reaction kinetics of 2-hexanone with ethanol amine, which reacts only at one side of the molecule so that ring closure cannot take place. Then, we investigate the intermediates found in the Paal Knorr synthesis, and analyse the kinetic parameters of the full reaction. Knowledge of both kinetic and mechanistic parameters can be helpful in designing synthetic routes in chemistry of pyrroles.

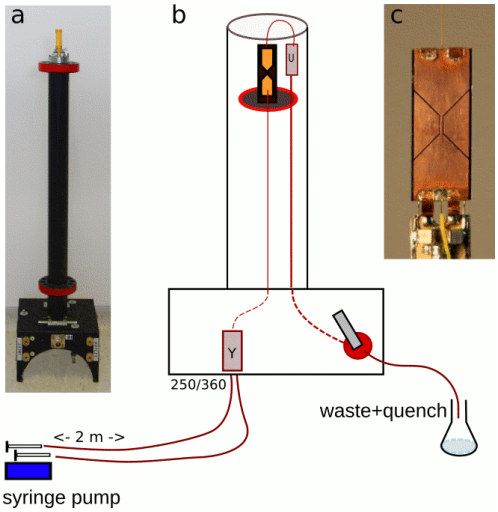

Figure 5.1: Microfluidic NMR setup: a) a picture of the probe. On the bottom of the probe the microfluidic connections are located. b) A schematic of the microfluidic setup: the solution flows from the syringe pump on the bottom, to the bottom of the probe, where two reactants mix in the Y-junction (Y), flowing upwards to the stripline NMR chip, then downwards to a waste container outside the magnet. c) a picture of the stripline NMR chip, electronic connections at the bottom and FS capillaries at the top and bottom glued into the chip.

5.2 Experimental section

5.2.1 Microfluidic setup

The microfluidic setup is shown in Figure 5.1. A syringe pump (Fusion 100, Chemyx Inc.) is placed approximately two metres from the magnet, the pump is loaded with two syringes (1 ml, gas tight, VWR) containing the reactants. Using a luer lock, the syringes are connected to two fused silica (FS) capillaries (250 μm I.D., 360 μm O.D., Polymicro technologies) running to the bottom of the probe. At that point a Y-junction (P-773, Upchurch Scientific) brings the two flows together. The solutions mix and continue through a 55 cm long (75 μm I.D., 150 μm O.D.) FS capillary upwards to the top of the probe, where the capillary is glued into the stripline chip. At the outlet of the chip, the FS capillary is connected to a wider capillary (250 μm I.D., 360 μm O.D.) to prevent buildup of pressure, and is led into the waste (a vessel with acetone quench) at the bottom of the magnet.

The reaction volume consists of the Y junction (17 nl void volume), 0.55 m of FS capillary (250 μm I.D.) and the 250 nl volume chip, which amounts up to approximately

2.6 μl. A steady-state flow is realised through the system, so that the effective reaction time at the point of measurent depends on the flow rate varying between 0.1 and 35 μl/minute. NMR detection is carried out at reaction times between 2.5 seconds and 10 minutes.

5.2.2 Microfluidic detection

NMR detection takes place in the stripline NMR chip[21, 22] that has been described before in studying the acetylation of benzyl alcohol in similar microfluidic conditions in Chapter 4. The stripline NMR chip is depicted in Figure 5.1c. The chip consists of a stack of fused silica substrates (D263T borosilicate, Schott). Two microfluidic channels are etched in the substrates. For continuous flow reaction monitoring only one of the microfluidic channels is used, with a detection volume of 150 nl. The radio frequency (rf) coil resonator and two ground planes are copper electroplated onto the fused silica substrates. The rf current runs through the rf coil resonator, detection takes place at the middle part of the stripline (3 mm length), where the width of the strip is constricted to 0.6 mm to locally increase the rf field at the point of detection. The two copper ground planes are applied at both sides of the chip parallel to the stripline in order to concentrate the rf field and to enhance the rf homogeneity[22].

5.2.3 Chemicals

All chemicals were used as received without further purification. The reactant solutions are ethanolamine (ReagentPlus 99% from Aldrich, 50%vol in methanol-d4, 16.5 M) with 2% 1-bromonaphtalene as an internal standard, 2-hexanone (reagent grade 98% from Sigma-Aldrich, 50%vol in methanol-d4, 8.1 M), and 2,5-hexanedione (98% from Sigma-Aldrich, 50%vol in methanol-d4 from Sigma-Aldrich, 8.5 M). Acetone was used as a quench.

5.2.4 Data aquisition

The 1D stripline NMR spectra are acquired in single-scan or by accumulating 64 scans. Between scans a relaxation delay of 2 seconds was taken into account for short reaction times, up to 5 seconds for long reaction times. For processing, zero filling up to 32000 points and an exponential broadening of 0.5 Hz was applied. A 17^{th} order polynomial fitting was used for baseline correction. The conventional NMR 1D spectra were

acquired in single-scan.

Two-dimensional correlation spectra were acquired both in continuous flow in the stripline NMR setup and using conventional NMR. Total correlation[23] (TOCSY) spectra were acquired while flowing at 0.145 μl/minute (accumulating 4 scans with 256 t_1 increments and using 2.5 seconds relaxation delay) and at 4.35 μl/minute (accumulating 8 scans with 256 t_1 increments and using 1 second relaxation delay). A correlation spectrum[24] (COSY) was taken while flowing at 1 μl/minute (accumulating 8 scans with 256 t_1 increments and 3 secons relaxation delay) In conventional NMR, TOCSY spectra were acquired accumulating 8 scans with 128 t_1 increments.

All stripline NMR measurements are performed at room temperature on a VNMRS 600MHz Varian NMR spectrometer controlled by VNMRJ software. Conventional NMR experiments were obtained with a 5 mm CryoProbe TCI on a Bruker Avance III 600 MHz NMR spectrometer controlled by Bruker TopSpin 3.0 software. The data was processed using matNMR[25], ChemBioDraw Ultra[26] was used for plotting molecular structures and as an aid in estimating chemical shifts of the compounds. MestReNova[27] (version 11.03-18688, released 2017-02-08) was used for processing the 2D spectra.

5.3 Results/Discussion

5.3.1 Ethanol amine and 2-hexanone

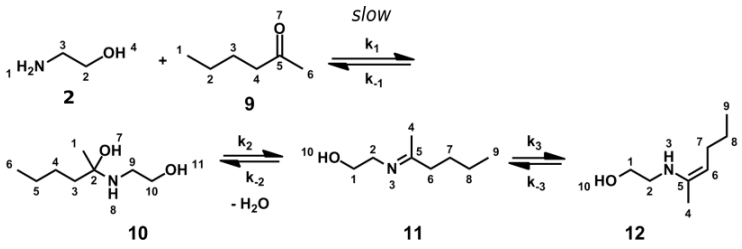

*Scheme 5.2: Proposed reaction mechanism of ethanol amine **2** and 2-hexanone **9**, resulting in an equilibrium between the products **10**, **11** and **12**.*

In the Paal-Knorr cyclocondensation (Scheme 5.1) 2,5-hexadione **1** and ethanol amine **2** react at both carbonyl groups of the diketone, forming pyrrole either via cyclisation (route A) or hydrolysis (route B) of the hemiaminal (compound **3**). The time required for conversion of the N,O-acetal (Scheme 5.2, compound **10**) is an important factor

for the mechanism of the Paal-Knorr synthesis. To break down the mechanism of the Paal-Knorr synthesis in steps, we perform the addition of ethanol amine **2** with 2-hexanone **9**, the reaction mechanism of which is depicted in Scheme 5.2. This reaction provides the N,O-acetal intermediate **10**, which converts to the corresponding enamine intermediates **11** and **12** by elimination of a H_2O molecule. Since the reaction can take place only at one carbonyl group, cyclisation cannot occur and an equilibrium between the three products is established.

In the stripline NMR detection setup, 1D ^{1}H NMR spectra are acquired under steady state reaction conditions for reaction times ranging from 5 seconds up to 13 minutes. In addition, a conventional NMR ^{1}H spectrum (up to 1 day reaction time) and a TOCSY spectrum (after 10 minutes reaction time) are acquired to aid in assigning the peaks. For reference, a stripline NMR COSY spectrum is acquired as well, in continuous flow at 3 minutes reaction time. A selection of the 1D spectra is shown in Figure 5.2. In the spectra, the four methyl peaks of 2-hexanone and the reaction products can be observed. The peak of the 2-hexanone methyl group $\mathbf{H}_6$ is present at the beginning of the reaction, but steadily decreases with increasing reaction time. The other 2-hexanone peaks can be assigned as well from the top spectrum in Figure 5.2. The methyl peak (1) of product **10** is expected to resonate at lower ppm values relative to $\mathbf{H}_6$, due to the neighbouring OH and NH group instead of a double bond, as confirmed by ChemBioDraw chemical shift predictions[26]. Similarly, the triplet $\mathbf{10}_3$ can be observed at a lower ppm value relative to $\mathbf{H}_4$. Atoms 4, 5 and 6 of compound **10** overlap with atoms 7, 8 and 9 of compounds **11** and **12** and some of the 2-hexanone peaks, therefore these peaks could not be clearly resolved in these spectra.

The conventional NMR TOCSY spectrum in Figure 5.3a is acquired after the reaction is completed (2 hours). By analysing the cross peaks and the peak pattern, the peaks of compound **11** and compound **12** can be assigned. Cross peaks of triplet $\mathbf{11}_6$ to the peaks of atoms $\mathbf{11}_7$, $\mathbf{11}_8$ and $\mathbf{11}_9$ can be observed, and a weaker coupling with atoms $\mathbf{11}_2$ and $\mathbf{11}_1$ of the amine moiety. The methyl group $\mathbf{11}_4$ is also coupled to the atoms $\mathbf{11}_2$ and $\mathbf{11}_1$. For compound **12**, the methyl peak $\mathbf{12}_4$ can be assigned from the coupling to atom **6**, which is very characteristic for this compound. Several more peaks can be tentatively assigned from the TOCSY spectrum as is indicated in Figure 5.3a, but overlap of other peaks obscures their exact positions. The stripline NMR COSY in Figure 5.3b is acquired to determine if we can observe the same cross peaks in the spectra measured under continuous flow at 1 μl/minute while the reaction is taking place. When comparing Figures 5.3a and 5.3b, it should be taken into account that

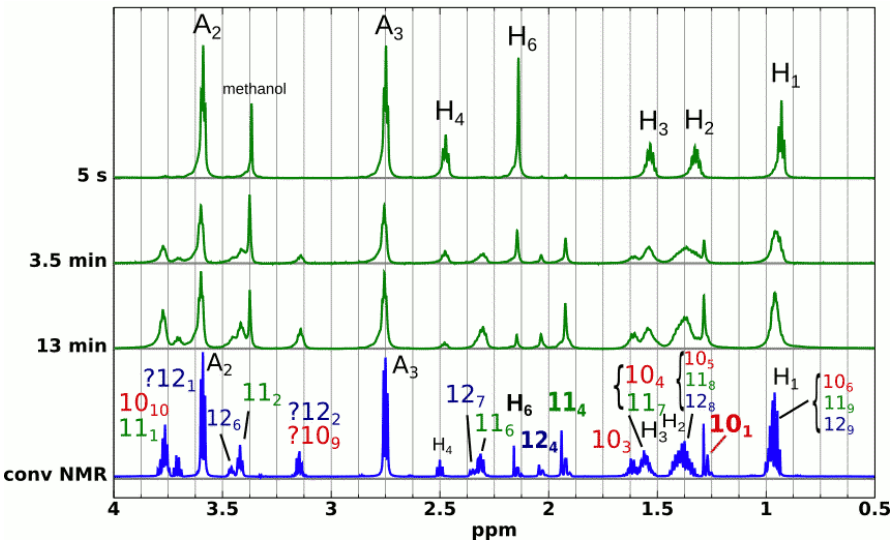

*Figure 5.2: Stripline NMR spectra (in green) and conventional NMR spectrum (in blue) of the addition of ethanol amine ('A') to 2-hexanone ('H'), resulting in an equilibrium between products **10**, **11** and **12**. The assigned peaks are denoted with subscripts giving the associated carbon atom numbers according to Scheme 5.2.*

a COSY spectrum gives only correlations of coupled spins over up to four bonds, whereas the TOCSY spectrum shows also multiple bond correlations. The expected cross peaks are indeed observed as indicated in Figure 5.3b.

Monitoring the kinetics of the reaction between ethanol amine and 2-hexanone

The methyl peaks of 2-hexanone $\mathbf{H}_6$ and the three products ($\mathbf{10}_1$, $\mathbf{11}_4$ and $\mathbf{12}_4$), as assigned in the series of spectra in Figure 5.2, are used for monitoring the reaction progress by integrating the peaks in the spectra at different reaction times. The set of partial differential equations (PDE) in Eq. (5.1) is used to describe the reaction shown in Scheme 5.2, where c_H represents the concentration of 2-hexanone, c_{10}, c_{11} and c_{12}

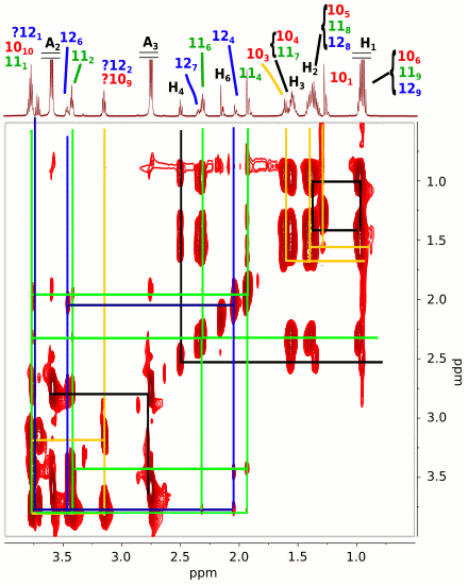

(a) TOCSY spectrum measured in conventional NMR after 2 hours reaction time.

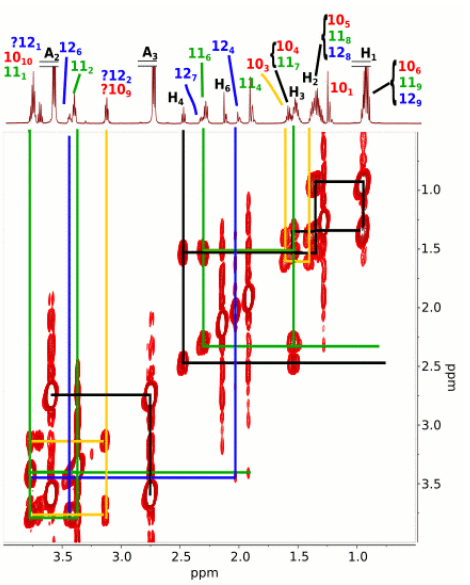

(b) COSY spectrum measured in stripline NMR, with a continuous flowrate of 1 μl/minute, corresponding to a effective reaction time of approximately 3 minutes.

Figure 5.3: 2D spectra of the reaction of ethanolamine with 2-hexanone. Cross correlation are indicated with lines, 2-hexanone is indicated in black, ***10*** *in red/yellow,* ***11*** *in green and* ***12*** *in blue, the conventional NMR 1D spectrum on top gives the atom numbers of the assigned peaks. For clarity, the top spectrum with assigned peaks in b) is the same as in a).*

the concentrations of products **10**, **11** and **12**, respectively:

$$\frac{dc_H}{dt} = -k_1 c_H^2 + k_{-1} c_{10} \tag{5.1a}$$

$$\frac{dc_{10}}{dt} = k_1 c_H^2 + k_{-2} c_{11} - (k_{-1} + k_2) c_{10} \tag{5.1b}$$

$$\frac{dc_{11}}{dt} = k_2 c_{10} + k_{-3} c_{12} - (k_{-2} + k_3) c_{11} \tag{5.1c}$$

$$\frac{dc_{12}}{dt} = k_3 c_{11} - k_{-3} c_{12} \tag{5.1d}$$

Using Matlab, the solution of the PDE set is numerically optimised to give the best fit to the experimental data by minimising the object function[28] F, while varying the k values k_1, k_2 and k_3, and the ratios between forward and backward reactions:

$$F = \sum (experimental - fitted)^2 \tag{5.2}$$

Figure 5.4 shows the experimental and modelled results.

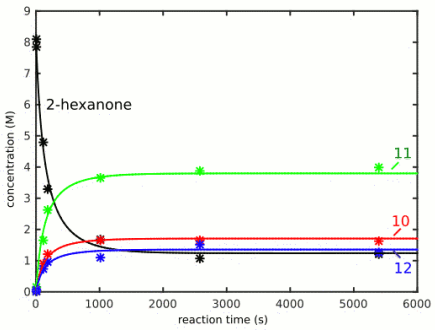

*Figure 5.4: Optimisation of the kinetic model of the reaction of 2-hexanone with ethanol amine (Scheme 5.2), for concentrations measured from methyl peaks in stripline NMR and conventional NMR spectra during the reaction: 2-hexanone (black), product **10** (red), product **11** (green), product **12** (blue). Experimental data points are marked with stars, the fit is shown as a solid line.*

The results of the fitting procedure indicate that the first step is rate-determining, and the optimal rate constant to fit the experimental data is $k_1 = 8.4 * 10^{-4} M^{-1} s^{-1}$. The ratio between forward and backward reactions critically define the fit result, giving a fast equilibrium between the three products. The fitted optimum ratios are k_{-1}/k_1 = 0.9, k_{-2}/k_2 = 0.45 and k_{-3}/k_3 = 2.8. The ratio between products **10**, **11** and **12** are

constant within 10 - 13% from 3 minutes reaction time onwards. Since the amounts are determined by the ratio between forward and backward reaction, the value of k_2 and k_3 influence primarily the first instances of the reaction, which are less accurately defined because of the smaller amount of product. The fit results suggest that the second and third step are much faster than the first one ($k_2 \gg k_1$, $k_3 \gg k_1$). It is determined that k_2 and k_3 need to be at least 100 times as large as k_1 to give a good fit. As long as this condition applies, k_2 and k_3 can be any value, the object function does not deviate more than 3 percent. For very large rate constants ($> 10^{11}$), the differential equations cannot be solved, however.
The fit results suggest that the dehydration (k_2) and rearrangement (k_3) processes are very fast with respect to the first step and the equillibrium of the reaction favoures compound **11**.
The optimised k values that were found are: $k_1 = 8.4 * 10^{-4} M^{-1} s^{-1}$, $k_{-1} = 7.6 * 10^{-4} s^{-1}$, $k_2 = 52.7 s^{-1}$, $k_{-2} = 23.7 s^{-1}$, $k_3 = 8.4 s^{-1}$ and $k_{-3} = 23.5 s^{-1}$. Figure 5.4 shows the experimental and modelled results.

5.3.2 Paal-Knorr cyclocondensation

In the complete Paal-Knorr cyclocondensation, diketone (2,5-hexanedione) and ethanolamine react into pyrrole. Literature[5, 11, 12, 14, 15] suggests that the reaction proceeds via route A in Scheme 5.1, where the intermediate **3**, first cyclises into a diol **4**, then twice eliminates H_2O into intermediate **7** and pyrrole **8**.
The reaction is allowed to occur in continuous flow in the microfluidic stripline NMR setup described above, ^{1}H NMR spectra are acquired with reaction times ranging from 2 seconds up to 10 minutes. The reaction proceeds very rapidly as can be observed in the series of spectra shown in Figure 5.5. After 1 minute reaction time, the reaction is almost finished. Small amounts of intermediate products are present, the highest amounts of intermediate products are found around approximately 20 seconds reaction time. Figure 5.6 zooms in on the resonances of these intermediate products. In the first instances of the reaction, the peaks that are visible already after 2.5 seconds reaction time, correspond to the peak pattern that is expected for the first intermediate product, the hemiaminal **3**. These peaks, labelled **3**, diminish during the reaction.
To be able to assign more peaks to intermediate products, in addition to the 1D spectra, TOCSY spectra were taken in continuous flow. A steady-state spectrum obtained at 1 minute effective reaction time is shown in Figure 5.7a. Starting materials and the

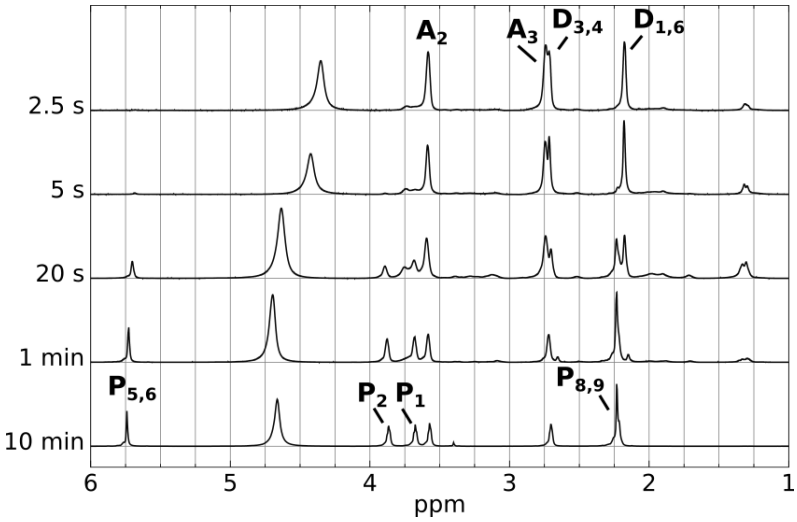

Figure 5.5: Paal Knorr cyclocondensation, a selected series of stripline NMR spectra taken in continuous flow at given effective reaction times. Indicated are starting materials (D is diketone, A is ethanol amine) and the end product (P is pyrrole)

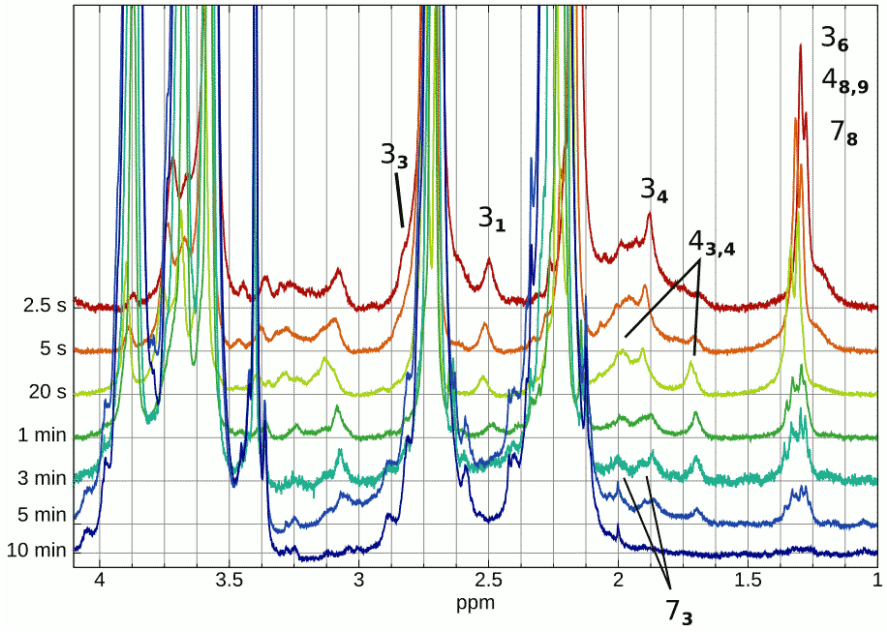

*Figure 5.6: Paal Knorr, series of spectra acquired in continuous flow in the stripline NMR, from 2.5 seconds effective reaction time up to 10 minutes. The assigned peaks from the intermediate hemiaminal (compound **3**) is shown, as well as some peaks of the diol **4** and the final intermediate **7***

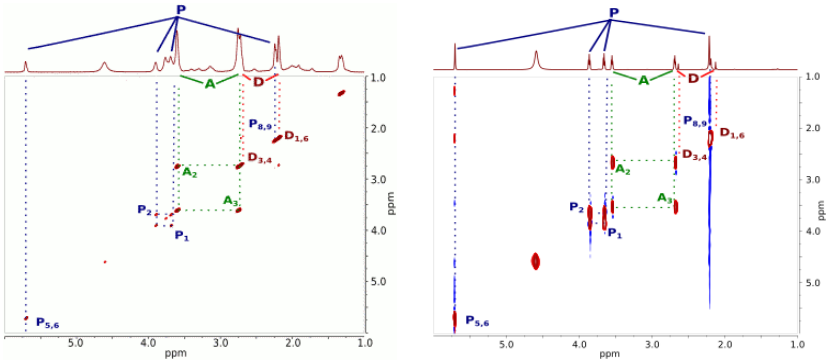

(a) Measured in in stripline NMR chip at continuous flow, 20 seconds effective reaction time

(b) Measured in conventional NMR, starting time of the experiment is 5-10 minutes after mixing.

Figure 5.7: Paal Knorr reaction, TOCSY measured a) in continuous flow, at 20 seconds effective reaction time, and b) in conventional NMR 5-10 minutes after mixing. Starting materials (D is diketone, A is amine) and pyrrole (P) are indicated.

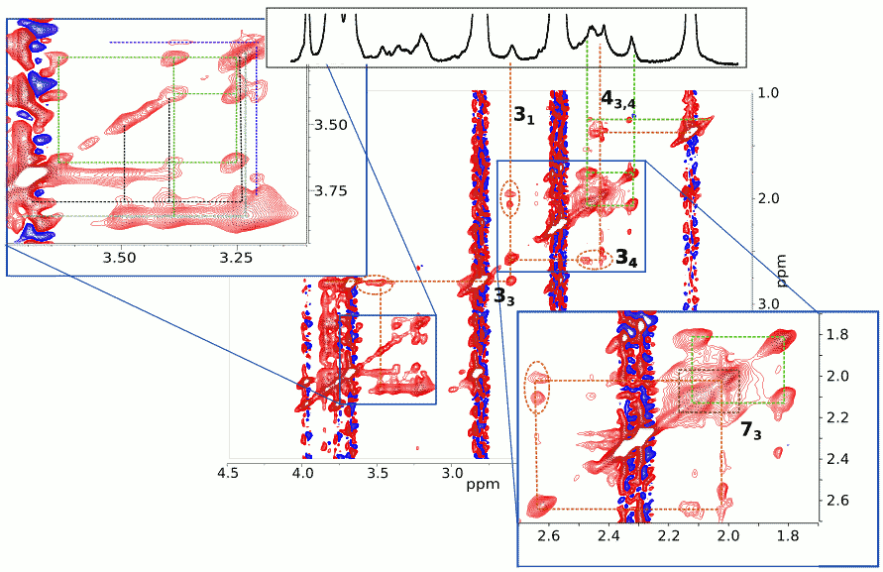

*Figure 5.8: Paal Knorr TOCSY measured in continuous flow at 20 seconds effective reaction time. Assigned peaks are of intermediates **3**, **4** and **7**. The insets show parts of the spectrum at different contour depth. The 1D spectrum on top was obtained under the same continuous flow conditions, before the TOCSY was acquired.*

end product can be distinguished. The TOCSY spectrum in Figure 5.8, acquired in continuous flow at 20 seconds reaction time, zoom in into the details. The correlation of the hemiaminal intermediate **3** can be observed through the molecule: $\mathbf{3}_4$, $\mathbf{3}_1$ and $\mathbf{3}_3$ are indicated, but also connections can be observed between $\mathbf{3}_4$ and the methyl moiety as well as $\mathbf{3}_3$ and the amine tail ($\mathbf{3}_{9,10}$).

In both the 1D spectra in Figure 5.6 and the TOCSY spectrum in Figure 5.8, small amounts of intermediate product peaks are present in the region below 2 ppm. Since the products **5** and **6** in Route B do probably not contain methyl resonances in the region below 2 ppm (from ChemBioDraw chemical shift predictions[26]), these peaks ($\mathbf{4}_{3,4}$ and $\mathbf{7}_3$) confirm the presence of products from route A.

In the TOCSY spectrum in Figure 5.8, in the region just below 2 ppm, we can distinguish two double multiplets. The double multiplets with highest intensity increase first in Figure 5.6 show cross peaks to the methyl moiety around 1.3 ppm, corresponding to the expected peak pattern for the diol **4** and assigned $\mathbf{4}_{3,4}$. These multiplets show cross peaks to the methyl moiety around 1.3 ppm, corresponding to the expected peak pattern. Therefore, the lower amount of product, which does not show other couplings, is assigned to the final intermediate $\mathbf{7}_3$. Furthermore, at around 1.3 ppm multiple overlapping peaks increase at different rate, therefore probably belong to different compounds. The resonances of the methyl moieties in the proximity of the OH-group are expected to be found in this region: $\mathbf{3}_6$, $\mathbf{4}_{8,9}$ and $\mathbf{7}_8$, and cross peaks with neighbouring nuclei are observed for compounds **3** and **4**.

In the region above 3 ppm, overlap of the intermediate peaks with the relatively large peaks of the amine and pyrrole, complicates the interpretation. Furthermore, the amine tails ($\mathbf{3}_{9,10}$, $\mathbf{4}_{10,11}$ and $\mathbf{7}_{9,10}$) are not expected to couple strongly to the peaks from the ring, as is also the case for pyrrole, due to the presene of the nitrogen atom in between. Although a cross peak with $\mathbf{3}_3$ and $\mathbf{3}_9$ seems to be present. The inset in Figure 5.8 shows that the intermediate product peaks at around 3.75 ppm consists of several overlapping peaks, since the cross peaks are found at slightly different position indicated in black, blue and green. The three sets of peaks probably belong to the three amine tails of the intermediates **3**, **4** and **7**, but cannot be resolved.

In Figure 5.9, a TOCSY spectrum is shown which is acquired in continuous flow at 1 minute effective reaction time. It can be observed that the intermediate products have been diminished.

For reference, a conventional NMR TOCSY spectrum is included in Figure 5.7b. Acquisition started as soon as possible after mixing the reactants, i.e. 5-10 minutes

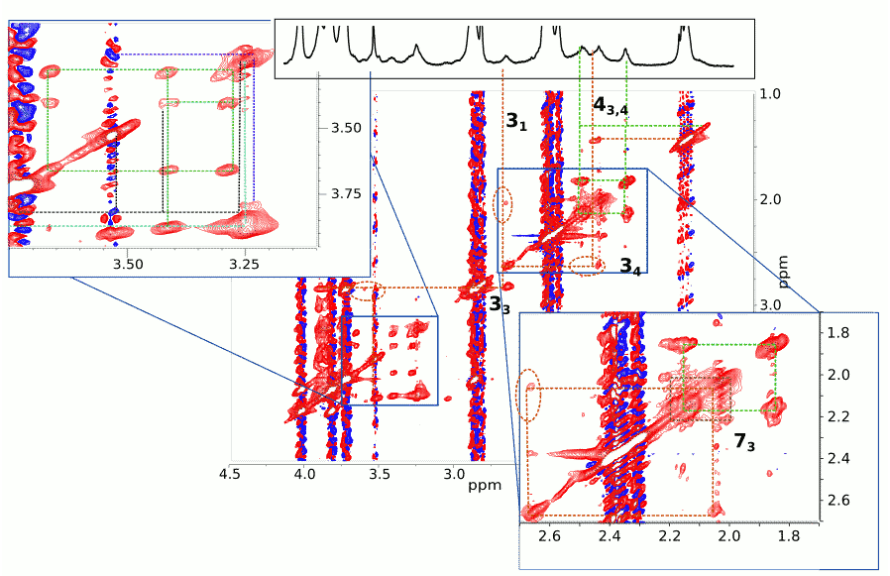

*Figure 5.9: Paal Knorr TOCSY measured in continuous flow at 1 minute effective reaction time. Assigned peaks are of intermediates **3**, **4** and **7**. The insets show the same lines as Figure 5.8, showing that some of the intermediate product peaks have diminished. The 1D spectrum on top was obtained just before the TOCSY experiment under the same conditions.*

reaction time, the spectrum is acquired in approximately 30 minutes experiment time. After 5-10 minutes, when the mixture is loaded into the spectrometer and acquisition can be started, the reaction is approximately completed as can be observed from Figure 5.5. Over the 30 minutes measurement time, any present intermediates will be further diminished. It is however possible that small amounts of intermediate products are still present and can be detected by the conventional NMR experiment. This is not the case for this experiment, as no useful information can be obtained regarding cross peaks of the fast intermediates from this spectrum. This demonstrates the benefit of being able to measure a 2D spectrum with a relatively long acquisition time in continuous flow at a steady state condition at a constant short effective reaction time.

Monitoring the kinetics of the pyrrole synthesis

Since the kinetic parameters are of interest for synthetic chemistry of pyrroles, we fit our data to a kinetic model of the reaction. In Figure 5.6, a series of 1D NMR spectra shows the conversion from ethanolamine and diketone into pyrrole. For each of the steady state spectra, the concentrations of the reactants and intermediate products (hemiaminal $\mathbf{3}_9$**,** $\mathbf{3}_1$**,** $\mathbf{3}_4$, diol $\mathbf{4}_{3,4}$ and final intermediate $\mathbf{7}_3$) were obtained by peak deconvolution, so that the reaction progress can be monitored. Although our data does not consist of sufficient data points to formally solve this model, it gives an impression of the results that are obtainable and we can qualitatively distinguish the influence of rate limiting steps in the reaction models.

Route A in Scheme 5.1 was found in literature[5, 11, 12, 14, 15] and as was confirmed in our experiments to be the most probable pathway for cyclocondensation, and can be represented by the set of partial differential equations (PDEs) in Eq. (5.3). The concentrations of the reactants are c_A for ethanolamine, c_D for the concentration of diketone, c_P for the concentration of pyrrole, and c_3, c_4 and c_7 the concentrations of

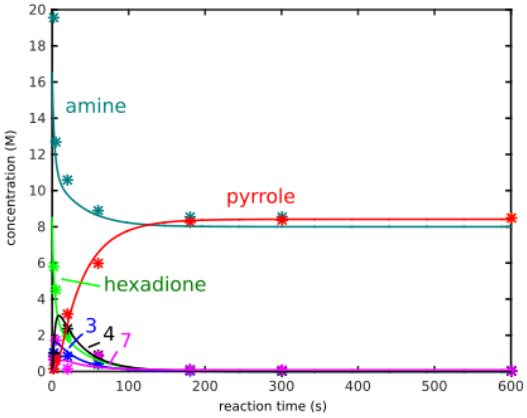

*Figure 5.10: Optimisation of the kinetic model of the pyrrole synthesis, according to route A in Scheme 5.1. Experimental data marked with *, fit results in a solid line. Starting products ethanol amine in teal, and diketone in green. The intermediate products in blue ('3'), black ('4') and magenta ('7'), and end product pyrrole in red.*

compounds **3**, **4** and **7**, respectively.

$$\frac{dc_A}{dt} = \frac{dc_D}{dt} = -k_1 c_A c_D + k_{-1} c_3 \tag{5.3a}$$

$$\frac{dc_3}{dt} = k_1 c_A c_D - (k_{-1} + k_2) c_3 + k_{-2} c_4 \tag{5.3b}$$

$$\frac{dc_4}{dt} = k_2 c_3 - (k_{-2} + k_3) c_4 + k_{-3} c_7 \tag{5.3c}$$

$$\frac{dc_7}{dt} = k_3 c_4 - (k_{-3} + k_4) c_7 + k_{-4} c_P \tag{5.3d}$$

$$\frac{dc_P}{dt} = k_3 c_7 - k_{-4} c_P \tag{5.3e}$$

The best fit of the PDE set to the experimental data is found by minimising the object function F[28] in Eq. (5.2), while varying the k values k_1, k_2, k_3 and k_4, as well as the ratios between forward and backward reactions.

The results indicate that for this reaction model, the nucleophilic attack is relatively slow and is a rate limiting step ($k_1 = 1.8 * 10^{-2} M^{-1} s^{-1}$). The ratio between k_1 and k_{-1}, and k_2 and k_{-2}, must stay the same for a good fit, 0.053 and 2.5 respectively. However, the ratios k_3/k_{-3} and k_4/k_{-4} are very large, as the backwards reactions are negligible.

We evaluate the effect of varying the k-values on the goodness of the fit. Increasing k_1

a factor 10, gives a 20% larger value for the resulting object function F. When k_3 is factor 10 times as large, the resulting object function F increases with 44%. However, k_{-3} can be decreased to 0, or increased without affecting the fit result significantly. Since $k_3 << k_{-2}$ and $k_{-3} << k_4$, the third reaction step, the dehydration step, is also relatively slow. The second and fourth step can be increased without affecting the fit much, for example increasing k_2 and k_4 10^6 times, gives deviations of the object function F within only 1.5% and 0.5%. At the same time, k_{-4} cannot be larger than the given value for a good fit, but it can be decreased to 0. From this we can conclude that the reaction rate is determined by the first step (nucleophilic attack) and the third step (dehydration), whereas cyclisation is a relatively rapid step.
For the reaction of ethanol amine with 2-hexanone, we found the dehydration to be a very fast process. The k-value that was found for the dehydration was at least $0.08s^{-1}$ (100 times the first step), with values possibly ranging up to $52.7s^{-1}$. For this reaction the dehydration (steps 3 and 4) is a similar process, so similar reaction rates may be expected. The dehydration rates of the cyclocondensation lie close to the minimum value of the range of k-values found for the reaction of ethanol amine with 2-hexanone, with values of 0.1 and $0.5s^{-1}$ for k_3 and k_4.
The optimised k values that were found are: $k_1 = 1.8*10^{-2}M^{-1}s^{-1}$, $k_{-1} = 0.34s^{-1}$, $k_2 = 1.15s^{-1}$, $k_{-2} = 0.46s^{-1}$, $k_3 = 1.1 * 10^{-1}s^{-1}$, $k_{-3} = 0.22s^{-1}$, $k_4 = 0.5s^{-1}$ and $k_{-4} = 5 * 10^{-2}s^{-1}$. Figure 5.10 shows the experimental and modelled results. It can be observed that the fit results match the data well, except for the final intermediate product **7**. It has to be taken into account that the low concentrations of the intermediate products were difficult to determine accurately, because of the overlap with larger peaks. Especially the data set of product **7** shows large deviations, so a good fit for this product cannot be expected.

Variations of fit model

Since the fit results suggest that the reaction is determined by two steps (k_1 and k_3), while the other two steps (k_2 and k_4) are in effect instantaneous, it is interesting to fit the data to a variation of the previous model, a two step reaction model, summing all intermediate products in one.

$$A + D \underset{k'_{-1}}{\overset{k'_1}{\rightleftharpoons}} Intm \underset{k'_{-2}}{\overset{k'_2}{\rightleftharpoons}} P \tag{5.4}$$

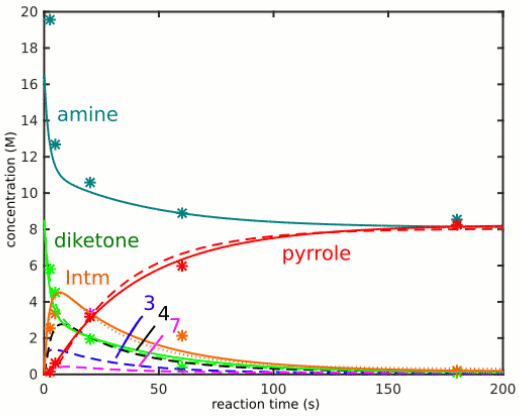

*Figure 5.11: Optimisation of the kinetic model of the pyrrole synthesis to a two step model. Starting products ethanol amine in teal, diketone in green, and end product pyrrole in red. The intermediate product in orange, marked 'Intm'. Experimental data is marked with *, fit results in a solid line. The results can be compared to the fit result in Figure 5.10 given in dashed lines, where the intermediate products are summed in an orange dotted line.*

The result is shown in Figure 5.11, with the obtained k-values k'$_1 = 0.02M^{-1}s^{-1}$, k'$_{-1} = 0.11s^{-1}$, k'$_2 = 0.04s^{-1}$ and k'$_2 = 7 * 10^{-4}s^{-1}$, this gives indeed a good approximation.

The optimised parameters found for the PDE's in Eq. (5.3) are not a unique solution for the reaction, therefore some variations in the reaction model are explored. In order to observe if the rate limiting steps are necessarily at the steps k_1 and k_3 as was found, or can be placed differently as well, we simulate a reaction model with the rate limiting steps at different places in the reaction. The rate limiting step can be placed at steps k_2, k_3 and k_4, by increasing the values of k_3 and k_4, k_2 and k_4, and k_2 and k_3, respectively, to 10 s^{-1}. The value of k_1 was not varied this way because it directly influences the rate of the reaction, instead the value of k_1 was optimised as before for each of the scenarios. The values of the rate limiting steps and the ratios between forward and backward reaction are optimised by minimising the object function. We observe that for all scenarios the overall reaction rate remains similar, however the concentrations of intermediate products show large differences. Figure 5.12a shows the fit results when placing the rate limiting step at the second step of the reaction model. Here only one intermediate product **3** is observed, because the next steps are so fast that the products **4** and **7** react very quickly into pyrrole. This is not in agreement with

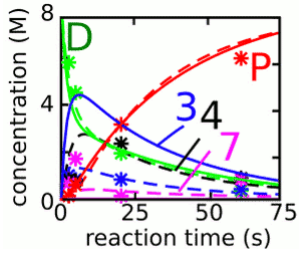

(a) Rate limiting step at second step k_2

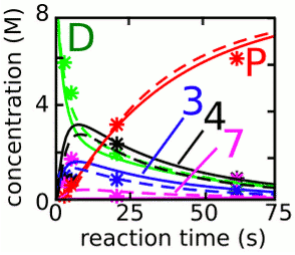

(b) Rate limiting step at third step k_3

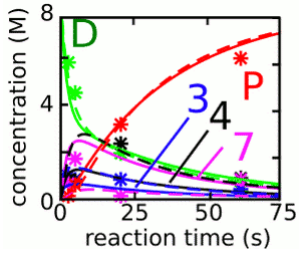

(c) Rate limiting step at fourth step k_4

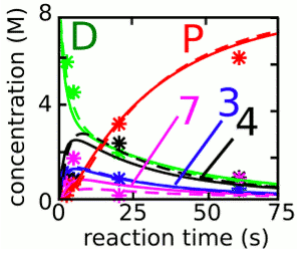

(d) Rate limiting step at third and fourth step, the values k_3 and k_4 are equal

Figure 5.12: Optimisation of the kinetic model of the pyrrole synthesis, according to route A in Scheme 5.1, with rate limiting steps placed at the given point in the reaction model. As in Figure 5.10, the experimentally observed (*) starting products are ethanol amine in teal, and diketone in green, intermediate products are given in blue ('3'), black ('4') and magenta ('7'), and the end product pyrrole in red. The solid lines are the fit results for the rate limiting steps artificially placed at the given place in the reaction, as described in the text. The fit results obtained according to route A in Scheme 5.1, without an artifical rate determining step, as shown before in Figure 5.10 are given as a comparison in dashed lines. Only for c) and d) the three intermediate products are correctly produced by the applicable model. In d) the two dehydration steps (step 3 and 4) are equal, which gives the best fit.

the experimental data. Similarly, when the rate limiting step is placed at the third step, only two intermediate products are observed, shown in Figure 5.12b. When placing the rate limiting step at the last step (Figure 5.12c), we find three intermediate products, which is in agreement with the experimental data. However, comparing the fit results for this model with the experimental data, there is a difference in the amount of intermediate product, less of product **4** and more of product **7** can be observed. For further adjustment of the model, we might assume that the two dehydration steps (step 3 and 4) have more or less the same value, as the type of reaction is equivalent. Abbat et al[15] find similar values for the theoretical calculations of the activation energy for both steps, whereas the values calculated by Mothana et al[12] are twice as high for the second dehydration step. In Figure 5.12d, the results can be found when the values for k_3 and k_4 are forced to be equal and only the reaction rate of the cyclisation step (k_2) is increased. The values are k_1 = 0.02 $M^{-1}s^{-1}$ (optimised), k_2 = 10 s^{-1} (constant), $k_3 = k_4$ = 0.25 s^{-1} (optimised). The fit results match the experimental data very well, which suggests that the assumptions that the nucleophilic attack (first step) is slow and the cyclisation (second step) is very fast, while the dehydration steps are equal gives a good desciption of the reaction. It is interesting to note the k_1 values that were found by optimisation are the same for every model.
According to literature the reaction rate is determined by either the cyclisation step (k_2)[5, 11, 12] or elimination of diol (k_3 and k_4)[15]. Also, water participation, solvent and acidity was found to be influencing the activation barriers of both processes, in particular facilitating the cyclisation step[15]. Our results indicate that after the first reaction step, the dehydration process determines the rate of the reaction, although it is a very fast process. We find that the cyclisation step is the fastest step of the reaction. In literature[12], a rapid equilibrium between amine and hemiaminal is suggested, which is the first step of our reaction model. However, we find that in comparison with the other steps, the first step determines the overall rate of the reaction. The finding that the cyclisation step is very fast is in agreement with route A, since this is faster than the dehydration in the alternative way via route B.

5.4 Conclusions

We performed the Paal-Knorr pyrrole synthesis in continuous flow in a microfluidic reaction setup coupled to a stripline NMR detection microcoil. The Paal-Knorr synthesis is a very fast and exothermic reaction that completes in a few minutes, and is

therefore difficult to monitor with NMR spectroscopy in a conventional lab setup. Our microfluidic setup enabled us to follow the reaction in detail during the progress of the reaction.

We examined two reactions, first the addition of ethanol amine and 2-hexanone and second the Paal-Knorr cyclocondensation in which ethanol amine and 2,5-hexanedione react. The first reaction involves similar compounds as the Paal-Knorr cyclocondensation, but the ring closure step cannot take place and the reaction comes to an equilibrium. The products in this reaction could be assigned from a TOCSY spectrum, acquired in a conventional NMR setup after the reaction was stable. The kinetic parameters of the reaction were approximated by fitting the data to a kinetic model. It was found that the nucleophilic attack of the carbonyl is a rate determining step, whereas the dehydration steps are very fast.

In the Paal-Knorr cyclocondensation, ethanol amine and 2,5-hexanedione react into pyrrole in a few minutes reaction time. In the stripline NMR setup, we performed a series of 1D measurements and TOCSY measurements in continuous flow during the progress of the reaction. This enabled us to assign some key intermediate peaks, that were not observable in the conventional NMR spectra. These findings confirm the reaction mechanics via route A in agreement with what is proposed in literature[5, 11, 12, 14, 15]. From the series of 1D spectra in the first minutes of the reaction, the reaction kinetics could be monitored and fitted to a kinetic model. The results indicate that the nucleophilic attack and the dehydration process are the relatively slow, rate determining steps, whereas the cyclisation process is very fast.

Acknowledgement

This research was financially supported by the ACTS - Process on a Chip programme, Netherlands Organisation for Scientific Research (NWO). The authors gratefully acknowledge Pieter Nieuwland and Kaspar Koch (FutureChemistry Holding B.V., Nijmegen, the Netherlands) for their input and feedback with regard to the microfluidic reaction setup and reaction. Jacob Bart, Roald Tiggelaar and Han Gardeniers (Mesoscale Chemical Systems, University of Twente, the Netherlands) are thanked for their support in the stripline NMR chip fabrication process. Hans Janssen and Jan van Os (Radboud University Nijmegen, the Netherlands) are acknowledged for technical support.

References

[1] C.-S. Li, Y.-H. Tsai, W.-C. Lee, and W.-J. Kuo, "Synthesis and photophysical properties of pyrrole/polycyclic aromatic units hybrid fluorophores," *J. Org. Chem*, vol. 75, p. 4004, 2010.

[2] N. P. Buu-Hoï, N. D. Xuong, and J. M. Gazave, "Hydroxy and thiol derivatives of 2,5-dialkylpyrroles," *J. Org. Chem.*, vol. 20, p. 639, 1955.

[3] G. Balme, "Pyrrole syntheses by multicomponent coupling reactions," *Angew. Chem., Int. Ed.*, vol. 43, p. 6238, 2004.

[4] J. S. Moore and K. F. Jensen, "Automated multitrajectory method for reaction optimization in a microfluidic system using online IR analysis," *Org. Process Res. Dev.*, vol. 16, p. 1409, 2012.

[5] V. Amarnath, K. Amarnath, W. M. Valentine, M. A. Eng, and D. G. Graham, "Intermediates in the paal-knorr synthesis of pyrroles. 4-oxoaldehydes," *Chem. Res. Toxicol.*, vol. 8, p. 234, 1995.

[6] S. Thirumalairajan, B. M. Pearce, and A. Thompson, "Chiral molecules containing the pyrrole framework," *Chem. Commun.*, vol. 46, p. 1797, 2010.

[7] I. O. Ryzhkov, I. A. Andreev, G. M. Belov, A. V. Kurkin, and M. A. Yurovskaya, "Preparation of chiral pyrrole derivatives by the Paal-Knorr reaction," *Chem. Heterocycl. Compd.*, vol. 47, p. 182, 2011.

[8] C. Paal, "Synthese von thiophen- und pyrrolderivaten," *Ber. Dtsch. Chem. Ges.*, vol. 18, p. 367, 1885.

[9] L. Knorr, "Einwirkung des diacetbernsteinsäureesters auf ammoniak und primäre aminbasen," *Ber. Dtsch. Chem. Ges.*, vol. 18, p. 299, 1885.

[10] A. R. Katritzky, D. L. Ostercamp, and T. I. Yousaf, "The mechanisms of heterocyclic ring closures," *Tetrahedron*, vol. 43, p. 5171, 1987.

[11] V. Amarnath, D. C. Anthony, K. Amarnath, W. M. Valentine, L. A. Wetterau, and D. G. Graham, "Intermediates in the paal-knorr synthesis of pyrroles," *J. Org. Chem.*, vol. 56, p. 6924, 1991.

[12] B. Mothana and R. J. Boyd, "A density functional theory study of the mechanism of the Paal–Knorr pyrrole synthesis," *J. Mol. Struct.: THEOCHEM*, vol. 811, p. 97, 2007.

[13] D. Akbaşlar, O. Demirkol, and S. Giray, "Paal–Knorr pyrrole synthesis in water," *Synth. Commun.*, vol. 44, p. 1323, 2014.

[14] H. Cho, R. Madden, B. Nisanci, and B. Török, "The Paal–Knorr reaction revisited. a catalyst and solvent-free synthesis of underivatized and N-substituted pyrroles," *Green Chem.*, vol. 17, p. 1088, 2015.

[15] S. Abbat, D. Dhaked, M. Arfeenb, and P. V. Bharatam, "Mechanism of the Paal–Knorr reaction: the importance of water mediated hemialcohol pathway," *RSC Adv.*, vol. 5, p. 88353, 2015.

[16] K. S. Elvira, X. Casadevall i Solvas, R. C. R. Wootton, and A. J. deMello, "The past, present and potential for microfluidic reactor technology in chemical synthesis," *Nat. Chem.*, vol. 5, p. 905, 2013.

[17] P. Watts and C. Wiles, "Micro reactors, flow reactors and continuous flow synthesis," *J. Chem. Res.*, vol. 36, p. 181, 2012.

[18] S. Taghavi-Moghadam, A. Kleemann, and K. G. Golbig, "Microreaction technology as a novel approach to drug design, process development and reliability," *Org. Process Res. Dev.*, vol. 5, p. 652, 2001.

[19] P. J. Nieuwland, R. Segers, K. Koch, J. C. M. van Hest, and F. P. J. T. Rutjes, "Fast scale-up using microreactors: Pyrrole synthesis from micro to production scale," *Org. Process Res. Dev.*, vol. 15, p. 783, 2011.

[20] K. C. Aroh and K. F. Jensen, "Efficient kinetic experiments in continuous flow microreactors," *React. Chem. Eng.*, vol. 3, p. 94, 2018.

[21] J. Bart, J. W. G. Janssen, P. J. M. van Bentum, A. P. M. Kentgens, and J. G. E. Gardeniers, "Optimization of stripline-based microfluidic chips for high-resolution NMR," *J. Magn. Reson.*, vol. 201, p. 175, 2009.

[22] P. J. M. van Bentum, J. W. G. Janssen, A. P. M. Kentgens, J. Bart, and J. G. E. Gardeniers, "Stripline probes for nuclear magnetic resonance," *J. Magn. Reson.*, vol. 189, p. 104, 2007.

[23] A. Bax and D. Davis, "MLEV-17-based two-dimensional homonuclear magnetization transfer spectroscopy," *J. Magn. Reson.*, vol. 65, p. 355, 1985.

[24] W. P. Aue, J. Karhan, and R. R. Ernst, "Homonuclear broad band decoupling and two dimensional J resolved NMR spectroscopy," *J. Chem. Phys.*, vol. 64, p. 4226, 1976.

[25] J. D. van Beek, "matNMR: A flexible toolbox for processing, analyzing and visualizing magnetic resonance data in Matlab," *J. Magn. Reson.*, vol. 187, p. 19, 2007.

[26] "ChemBioDraw Ultra." Cambridge Soft Corporation, Cambridge, Massachusetts, USA.

[27] "MestReNova, version 11.03." Mestrelab Research, S.L., Santiago de Compostela, Spain.

[28] A.-L. Seoud and L. A. M. Abdallah, "Two optimization methods to determine the rate constants of a complex chemical reaction using FORTRAN and MATLAB," *Am. J. Appl. Sci.*, vol. 7, no. 4, p. 509, 2010.

Chapter 6

EC–SPE–stripline-NMR analysis of reactive products: a feasibility study

David Falck, Anna Jo Oosthoek - de Vries, Ard Kolkman, Henk Lingeman, Maarten Honing, Sybren S. Wijmenga, Arno P. M. Kentgens and Wilfried M. A. Niessen

This chapter has been published in Analytical and Bioanalytical Chemistry, **405**, (21), pp. 6711-6720 (2013)

Abstract

Flow-through electrochemical conversion (EC) of drug-like molecules was hyphenated to miniaturised nuclear magnetic resonance spectroscopy (NMR) via online solid-phase extraction (SPE). After EC of the prominent p38α mitogen-activated protein kinase inhibitor BIRB796 into its reactive products, the SPE step provided preconcentration of the EC products and solvent exchange for NMR analysis. The acquisition of NMR spectra of the mass-limited samples was achieved in a stripline probe with a detection volume of 150 nl offering superior mass sensitivity. This hyphenated EC-SPE-stripline-NMR setup enabled the detection of the reactive products using only minute amounts of substrate. Furthermore, the integration of conversion and detection into one flow setup counteracts incorrect assessments caused by the degradation of reactive products. However, apparent interferences of the NMR magnetic field with the EC, leading to a low product yield, so far demanded relatively long signal averaging. A critical assessment of what is and what is not (yet) possible with this approach is presented, for example in terms of structure elucidation and the estimation of concentrations. Additionally, promising routes for further improvement of EC-SPE-stripline-NMR are discussed.

6.1 Introduction

Whereas hyphenation of electrochemical conversion (EC) and mass spectrometry (MS) has become an established technology, e.g. for studying drug metabolism to simulate cytochrome P450 biotransformation [1], this is not true for hyphenation of EC and nuclear magnetic resonance spectroscopy (NMR). Although EC-NMR is not an entirely new idea [2, 3], it has not been extensively studied. To some extent, this may be due to the mutual influence EC and NMR conditions may have, that is disturbance of the magnetic field homogeneity in NMR and/or of the EC processes by induction of additional currents [4]. Despite this, EC-NMR has been applied frequently and successfully to the study of processes at electrode surfaces by solid-state NMR techniques [5]. However, in the context of pharmaceutical applications, such as studying of redox pairs in vitamins [6] or structure elucidation of electrochemical products of drug-like compounds, the liquid state and bulk view is more desirable. Since the 1970s, a few groups have designed in situ EC-NMR probes where EC is carried out directly in the field region of the NMR, either in static [4] or continuous-flow approaches [2]. This allows a direct look at the EC reaction, its products and intermediates without delay. This approach has several disadvantages and limitations, such as the need for a dedicated NMR probe, the need

to use the same (inert deuterated) solvent in NMR and EC, and the possible overlap of analyte peaks with signals from additives like buffers and electrolytes. Recently, EC-NMR was reported for the analysis of EC products of acetaminophen, using a conventional 60 μl NMR flow cell under steady state conditions[7]. Though high-quality spectra were achieved with commercially available equipment, the other disadvantages remain in effect. As demonstrated in hyphenation of liquid chromatography (LC) and NMR[8, 9], some of these problems can be solved by the application of an on-line solid-phase extraction (SPE) step to decouple EC and NMR.

With respect to the application of EC-NMR in the drug discovery process, where initially only a few milligrams of a compound is available, a number of different setups are available[10]. Given the small sample amounts, an amperometric setup with a thin-layer cell is to be preferred over a coulometric setup. In addition, a flow-through approach is advantageous for the detection of unstable/reactive products[10, 11]. Obviously, limiting the amount of sample used results in high demands on the NMR sensitivity, which is a weak spot of NMR. To enhance NMR sensitivity, there is a strong trend towards capillary or chip-based NMR techniques. While higher sample concentrations are required in capillary NMR to achieve comparable performance in terms of spectrum quality, the total amount of sample necessary can be reduced up to 100-fold[8]. In microfluidic NMR, the sensitivity is improved by decreasing the detection volume in order to achieve high concentrations for mass-limited samples, because the same number of molecules is more effectively measured in a smaller volume[12]. As EC-NMR is somewhat underdeveloped, the implementation of miniaturisation and cryo technology in EC-NMR probes has not yet been reported. A relatively new trend in chip-based NMR is the stripline geometry featuring a planar resonator, which is optimised on radio frequency (rf) homogeneity, sensitivity and spectral resolution[13]. Previously, the stripline-NMR chip has been successfully used to analyse low concentrations of metabolites in human cerebrospinal fluid[14]. Moreover, the microfluidic stripline chip is perfectly suited for in situ measurements, for instance in a flow of analyte directed from the SPE to the NMR. Therefore, we chose a stripline-NMR setup for the detection of the relatively low sample amount produced by our EC setup.

Though requiring low absolute amounts of sample, the stripline-NMR setup demands high analyte concentrations. To this end, the intermediate SPE step enables significant sample preconcentration next to providing a favorable solvent exchange. The complete integration into one flow system in the EC-SPE-stripline-NMR platform greatly contributes to limiting the time elapsing between generation and analysis, thus preventing

degradation.

In order to achieve a more realistic assessment of the current state of this EC-SPE-stripline-NMR technology, we studied EC reactions of the p38α mitogen-activated protein kinase (p38α) inhibitors BIRB796 and SB203580, which are highly relevant in contemporary drug discovery [15, 16]. BIRB796 is currently studied in clinical phase III for the treatment of rheumatoid arthritis and Crohn's disease [15]. The EC production of reactive or unstable conversion products of BIRB796 has been reported [11].

6.2 Materials and Methods

6.2.1 Chemicals

Acetonitrile (ACN, LC-MS grade) and formic acid (ULC-MS grade) were delivered by Biosolve (Valkenswaard, The Netherlands). Water was purified by a Milli-Q academic from Millipore (Amsterdam, The Netherlands). BIRB796 (*N*-[3-(tert-butyl)-1-(4-methylphenyl)-1*H*-pyrazol-5-yl]-*N*'-[4-[2-(4-morpholinyl)ethoxy]-1-naphthalenyl]-urea) (structure in Figure 6.1) and SB203580 (4-[4-(4-fluorophenyl)-2-(4-methylsulfinylphenyl)-1*H*-imidazol-5-yl]pyridine) were obtained from various sources. All other chemicals were obtained from Sigma-Aldrich (Schnelldorf, Germany).

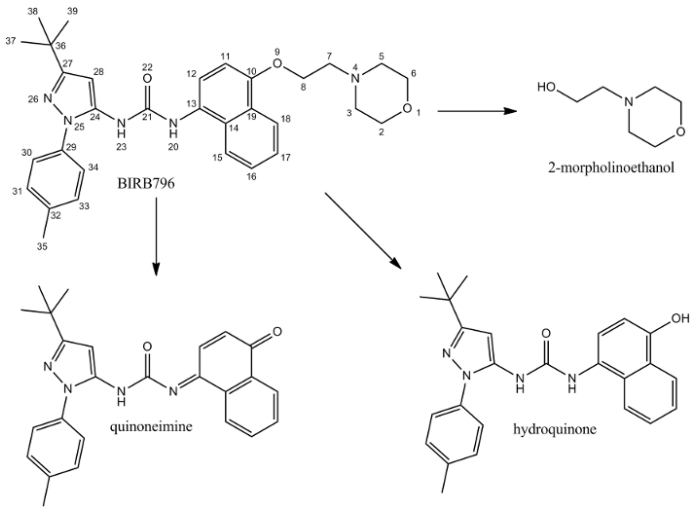

Figure 6.1: BIRB796 and its initial EC products. Electrochemical O-dealkylation at oxygen 9 results in the three major products shown. If not measured directly (on-line), these products undergo degradation reactions [11]

6.2.2 Electrochemical conversion

EC was achieved in a ROXY EC system (Antec, Zoeterwoude, The Netherlands) consisting of a μ-PrepCell and a ROXY potentiostat. The μ-PrepCell consists of a three electrode setup with a glassy carbon working electrode, a titanium counter electrode and a HyREF^{TM} (Pd/H_2) reference electrode. A spacer thickness of 150 μm was employed resulting in a volume of 12 μl in the cell. The EC reaction mixture was supplied by a syringe pump at a flow of 5 μl/min, converted at the working electrode at a direct current voltage of 0.7 V, and directed to the SPE. The mixture consisted of 10% aqueous ACN containing 370 μM ammonium formate/630 μM formic acid (pH 3.5) and 200 μM BIRB796.
The EC of BIRB796 was monitored at 254 nm at four different flow rates of 5, 10, 20 and 40 μl/min by LC - UV (LC-20 system, Shimadzu, 's-Hertogenbosch, the Netherlands) and analysed using a calibration curve of the standard (0 - 400 μM). The gradient, solvents and stationary phase used were the same as published earlier[11].

6.2.3 On-line solid-phase extraction

A SecurityGuard 4 $\times$ 2.0 mm C_{18} cartridge (Phenomenex, Utrecht, The Netherlands) was used. All steps were executed at room temperature at a flow rate of 5 μl/min. The trapping of the standards from the EC reaction mixture was done for 30 min, but the product mixture of BIRB796 was trapped for 60 min in order to achieve comparable concentrations for the competing quinoneimine and hydroquinone (see Figure 6.1). After a wash step with 99% D_2O and 1% ACN-d_3 for 10 min, the analytes were eluted with DMSO-d_6 for 11 min. Finally, the wash step was repeated for re-equilibration. Additionally, a 200 μM 10% aqueous ACN solution of SB203580 containing 2% DMSO (due to solubility issues with SB203580) and 1 mM ammonium bicarbonate (titrated to pH 10 with sodium hydroxide) was trapped and eluted, but not converted, using the same protocol.

6.2.4 Stripline chip, probe, and microfluidics

The stripline-structured rf coil consists of a stack of glass or fused silica substrates with etched microfluidic channels (see Figure D.1a in Appendix D.2)[14]. The copper structures, two ground planes and the rf coil resonator, are sputtered and electroplated. A constriction in the middle of the rf detector locally enhances the current density,

which results in a high rf field at the position of detection. The rf field is concentrated and rf homogeneity is enhanced by the two copper ground planes above and below the stripline. The layers are assembled and merged together with a bounding process so that they are leakage-free and stable. In the fused silica substrates, two microfluidic channels are etched, with a volume of 150 nl each, which may contain the sample; only one channels is used here. Fused silica capillaries (75 μm ID, 150 μm OD, approx. 15 cm long, Polymicro Technologies, Phoenix, AZ, USA) are glued into the top and bottom of the chip into the microfluidic channels to function as inlet and outlet. Via nanotight PEEK unions (P-779, Upchurch Scientific, Oak Harbor, WA, USA), both fused silica capillaries were connected to larger capillaries (150 μm ID, 360 μm OD at the inlet side and 250 μm ID, 360 μm OD at the outlet side) at the base of the magnet in order to protect the μ-PrepCell by avoiding a pressure buildup in the system higher than 10 bar. The inlet capillary was connected to the six-port switching valve (made in house) following the SPE unit. At the end of the outlet capillary, a shut-off valve (P-732, Upchurch Scientific) was used to prevent the sample from leaking out of the measurement area during measurements lasting longer than one hour. The homebuilt probe consists of an aluminum cylinder, the top of which is divided into halves in which the chip and the electronics circuit are placed [14].

6.2.5 Acquisition and processing

The stripline-NMR measurements were performed at room temperature in a VNMRS 600 MHz Varian NMR spectrometer, operated with VNMRJ software (Agilent, St. Clara, CA, USA). The 90° pulse length was 1.95 μs at 10 W power. At the start of the experiments, the shimming of the stripline-NMR probe was once performed on a 70% ethanol solution. Then, the chip was thoroughly flushed with solvent. With the sample solution in the probe, the shims were only slightly adjusted. Tuning and matching was performed on the sample in the probe.

The elution monitoring experiments by SPE-stripline-NMR (see Figure 6.3) were carried out by averaging 4 scans for one data point every 15 s. All other NMR experiments were performed in stopped-flow mode. The 3 mM BIRB796 standard spectrum (Figure 6.4b) was measured in 256 scans with a relaxation delay of 1 s; the acquisition took 9 min. The SPE-stripline-NMR spectrum (Figure 6.4c) was measured by accumulating 1,024 scans, taking 51 min. The EC-SPE-stripline-NMR sample (Figure 6.4d) was measured in an array of 25 times 256 scans with a relaxation delay

of 2 s. The scans were summed afterwards. The complete experiment took 12 h and 25 min. A total correlated spectroscopy (TOCSY) spectrum (Figure 6.5) was measured acquiring 128 t_1 increments of 16 scans with a relaxation time of 2 s. A mixing time of 50 ms with MLEV-17 spinlock was used[17]. The experiment took approximately 2 h and 45 min. A correlation spectroscopy (COSY) spectrum (Figure D.1b in Appendix D.2) was measured using 256 t_1 increments of 256 scans on the SPE-trapped sample[18]. The experiment took 45 h.

The 1 mM standard of BIRB796 depicted in Figure 6.4a was measured accumulating 618 scans with a relaxation delay of 1 s. The product mixture shown in Figure 6.6b and c, before and after storage at room temperature, was measured with a relaxation delay of 2.3 s using 130 and 160 scans, respectively. The COSY of the product mixture (data not shown) is measured obtaining 256 t_1 increments of 8 scans with a relaxation delay of 2 s. More details on the off-line EC experiments measured by conventional NMR can be found in Appendix D.1.

Data processing was done with MatNMR[19]. A zero filling up to 32,000 points and a line broadening of 1 Hz were used for noise reduction. An asymmetric least squares function was employed for baseline correction[20]. For peak-picking, a Lorentzian to Gaussian resolution enhancement (exp -0.7, Gauss -1.5 Hz) was applied. The 2D spectra were plotted using MatNMR and ACD/NMR Processor[21].

6.2.6 EC-SPE-stripline-NMR setup

A schematic diagram of the setup is given in Figure 6.2. The three syringe pumps (Model 11 Plus Advanced, Harvard Apparatus, Holliston, MA, US), which were placed at ca. 1 m distance to the magnet, were linked to a four-way connector (VICI, Schenkon, Switzerland) and delivered in turn the EC reaction mixture, the wash solution and DMSO-d_6. The EC reaction mixture passed the μ-PrepCell before arriving at the connector. The liquid from the four-way connector was guided to the SPE cartridge, which was connected to a six-port switching valve. During the trapping and half of the wash step, the SPE effluent was directed to waste in order to prevent contamination of the NMR probe with buffer salts and protonated solvents. When the wash step was halfway finished, the valve was switched and the wash solvent cleared the probe of analyte from the previous measurement. Afterwards, the new sample was eluted from the SPE cartridge with DMSO-d_6 into the stripline-NMR probe. When the elution was complete, the valve was switched again and both the re-equilibration and the trapping

step could be performed during sample measurement. Because the correct timing of the elution is essential and the void volume negatively correlates with repeatability, all connection volumes have been optimised (see Figure 6.2), within the limits of the above mentioned pressure restrictions. The comparably large void volumes V1 and V2 are necessary for bubble-free filling of the μ-PrepCell.

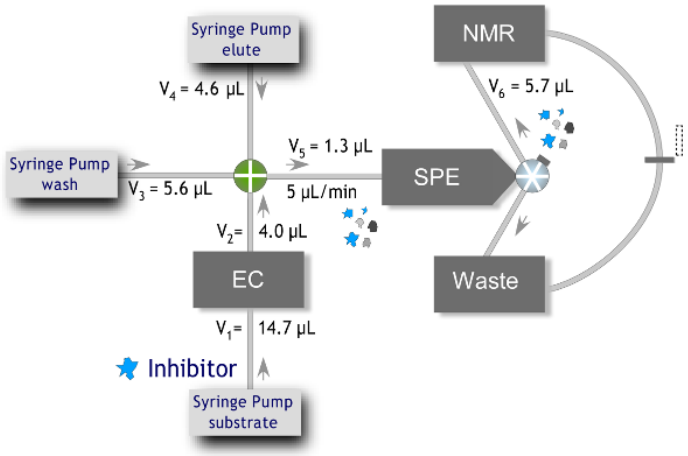

Figure 6.2: EC-SPE-stripline-NMR setup. The void volume of all connecting capillaries is specified

6.3 Results and discussion

The initial step in the EC-SPE-stripline-NMR setup was the EC of the substrate at a thin-layer electrode in the flow-through setup. Simultaneously, the products and residual substrate were trapped on the on-line SPE cartridge. After conversion/trapping, buffer salts and protonated solvents were washed away. Finally, substrate and products were eluted with DMSO-d_6 into the stripline-NMR probe. There, ^{1}H NMR as well as COSY and TOCSY spectra were recorded with excellent mass sensitivity.

6.3.1 Optimisation of EC and SPE steps

The EC conditions were transferred from a method published earlier[11], which used the same EC setup but with a ReactorCell^{TM} instead of the μ-PrepCell. It was expected that a higher concentration of substrate could be converted with the μ-PrepCell. Indeed, instead of the low to medium conversion at 10 μM with the ReactorCell^{TM} [11], $\sim$90%

consumption of BIRB796 was observed at 200 μM and 5 μl/min with the μ-PrepCell as assessed by LC-UV. The manufacturer indicates the optimal flow rate of the μ-PrepCell to be between 20 and 50 μl/min. As a decrease in product consumption to ca. 50, 30 and 5% was observed for 10, 20 and 40 μl/min, respectively, the original flow rate of 5 μl/min used in the ReactorCell^{TM} was considered optimal.
Trapping of the 200 μM standard of BIRB796 was possible for ca. 60 min. If trapping was continued after this period, breakthrough was observed. That indeed breakthrough was the cause of the detected analyte signal and not overloading of the stationary phase can be rationalised by comparing the trapped analyte weight of 32 μg with the estimated cartridge loading capacity of $\sim$1 mg.

6.3.2 SPE-stripline-NMR

This paragraph deals with the optimisation of the flow system and especially the hyphenation of the SPE and the stripline-NMR step. Although the experiments were carried out in the complete EC-SPE-stripline-NMR setup, EC was not yet applied. Contrary to off-line SPE, where the sample is obtained as a homogeneous solution in a predefined volume, the elution of the analytes in on-line SPE is comparable to an LC experiment without retention. Therefore, the determination of the void time equivalent to the elution time of the analytes is critical to the success of the stopped-flow stripline-NMR measurements. With the void time known, the flow can be stopped when the top of the elution peak is in the stripline-NMR channel. Obviously, an accurate and repeatable elution is one major determinant of the sensitivity of the system. The ^{1}H signals of the $tert$-butyl group of BIRB796 and of the methyl group of SB203580 allowed us to follow the elution of both compounds by stripline-NMR in the final EC-SPE-stripline-NMR setup, albeit with the voltage switched off. The reconstructed SPE-stripline-NMR chromatograms and their Gaussian fits are shown in Figure 6.3. The effective elution time, including the time to reach the stripline chip, was around 11 min for both compounds, its difference of 0.7 min being lower than the accuracy of the Gaussian fits ($\leq$0.9 min). The elution time is expected to be the same for all compounds not showing significant retention under these strong eluting conditions. This makes the SPE step widely applicable to compounds with medium to low polarity. The full width at half maximum (FWHM) for BIRB796 and SB203580 is 2.2 min or 11 μl and 1.4 min or 7 μl, respectively. The resulting concentration factor at half height should therefore be around 15- to 20-fold. On the one hand, this results in a rather

inefficient use of the sample, considering that the detection volume is only 150 nl. To some extent, this is due to the low flow rate applied, in combination with the large void volume which results from the use of a 2 mm I.D. SPE cartridge, a conventional six-way switching valve, and the long transfer tubing allowing the necessary distance between the SPE setup and the stripline-NMR probe. On the other hand, it reduces the strain on the repeatability of the elution, because even a deviation of $\sim$1 min leads to only 50% signal reduction, and on the sensitivity of the NMR experiment used to follow it, because multiple NMR spectra can be added to create one data point while following the elution. Both advantages are not to be underestimated when using such a highly experimental setup. However, the experimental data suggests that the signal would be strong enough to follow the elution using single scans instead of the four scans used per data point in these experiments. This would allow increasing the data point frequency from 0.07 to 0.33 Hz, thus enabling the detection of peaks with FWHM $\geq$12 s (7 data points above 10% signal). Thus, the elution volume at half height could in principle be reduced to 1 μl which would result in a ca. 10-fold gain in analyte concentration or equal reduction in substrate consumption through improvement of the SPE dimensions. At the moment, the substrate consumption of the EC-SPE-stripline-NMR is six times less than in the conventional NMR. When considering that only 1 or 2% of the sample was actually measured in the EC-SPE-stripline-NMR, this difference theoretically rises to approximately 300-fold.

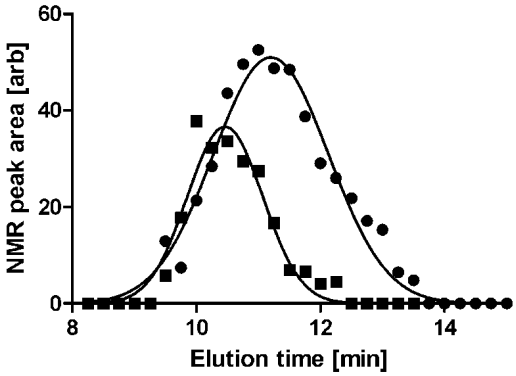

*Figure 6.3: Reconstructed SPE-stripline-NMR chromatograms. Elution of BIRB796 (*dots*) and SB203580 (*boxes*) from the SPE was monitored in real time by stripline-NMR using ^1H signals from a tert-butyl and a methyl group, respectively. The calculated elution time served as basis for the alignment of analyte peak and measurement area*

In order to assess whether the SPE step has an influence on the stripline-NMR, we first measured a 3 mM standard of BIRB796 by direct infusion into the stripline-NMR probe. The results were compared to a 30-min trapping and elution of a 200 μM standard. The aromatic region of the BIRB796 spectra obtained under different experimental conditions is presented in Figure 6.4 whereas the corresponding chemical shifts and J-couplings are summarised in Table D.1 in Appendix D.3. All C-H signals are found at the same chemical shifts in both measurements; the maximum deviation is about 0.05 ppm for proton 35. Similar differences are observed between conventional spectra in either DMSO-d_6 or ACN-d_3 which indicate that most likely small differences in residual ACN concentration cause these effects. Additionally, the chemical shifts of BIRB796 measured by conventional NMR in DMSO-d_6 do not deviate by more than 0.05 ppm from the stripline-NMR measurements in the same solvent (see Figure 6.4 and Table D.1 in Appendix D.3), except for protons 12, 16 and 17 whose peaks change positions in the spectra between Figure 6.4a and d. This allows comparison to off-line EC samples measured with conventional NMR. The exchangeable protons attached to the urea nitrogen atoms (N20 and N23) are no longer observed in the sample measured by SPE-stripline-NMR which indicates a very efficient exchange with deuterons. By comparing the average signal-to-noise ratios (SNR) of several peaks in the stripline-NMR and in the SPE-stripline-NMR spectrum, a concentration of 2.4 mM (12-fold) could be estimated for the SPE-stripline-NMR experiment which fits well to the previously calculated 15-20-fold concentration at half height.
Furthermore, we recorded a COSY spectrum of BIRB796 by SPE-stripline-NMR. All expected coupling peaks were observed (see Figure D.1b in Appendix D.2) in effectively measuring as little as 360 pmol of sample. Unfortunately, an extensive measurement time (45 h) proved necessary, as an attempt at recording a shorter COSY spectrum on the 3 mM standard was not successful. In the stripline-NMR experiment, relatively broad lines are found to which the long measurement time without lock might contribute. For a COSY, the diagonal peaks are in-phase whereas the cross-peaks have an anti-phase character, which may lead to vanishing signals in the case of broad peaks. This is in contrast to a TOCSY experiment, in which all peaks show in-phase absorptive lineshapes. It makes the TOCSY a more suitable experiment in our case. Therefore, we tried a TOCSY experiment on the standard, which took only 2 h and 45 min and provided a much clearer correlation. As can be seen in Figure 6.5 and Figure D.1b (see Appendix D.2), the same ^{3}J-couplings between protons 11 and 12, 15 and 16, and 17 and 18 are observed in the COSY and in the TOCSY spectrum.

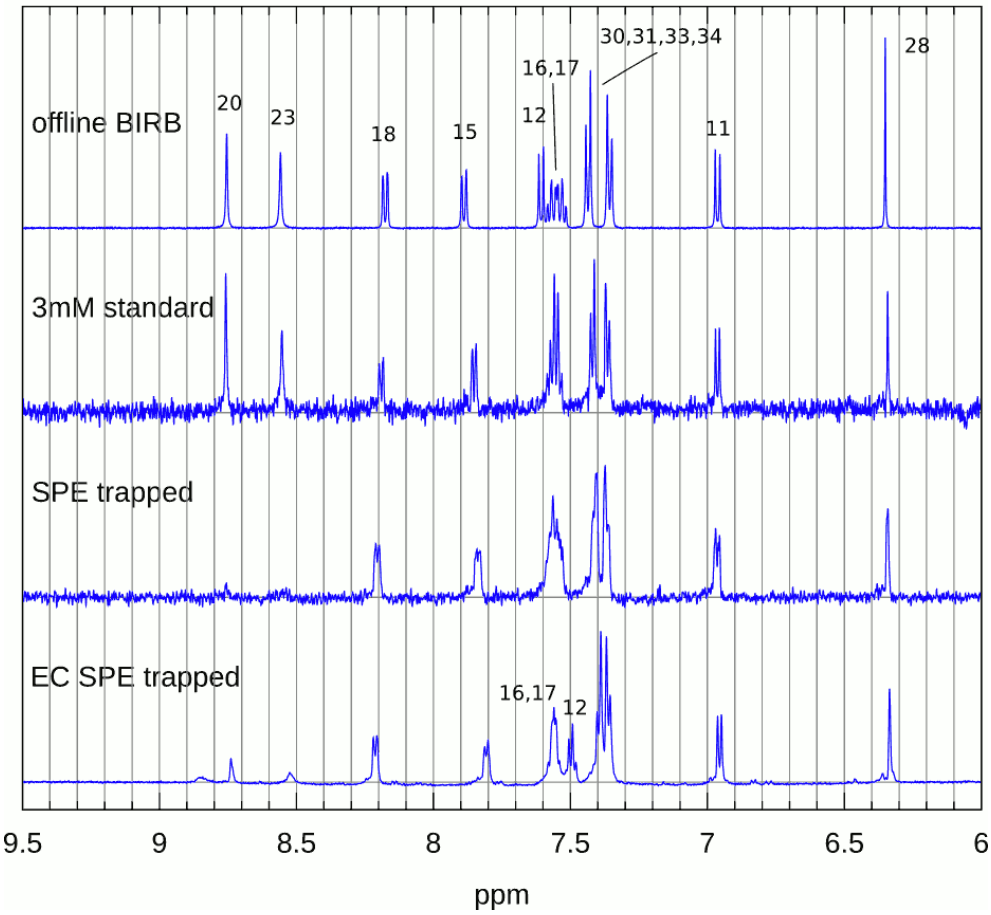

Figure 6.4: NMR spectra of the aromatic region of BIRB796. For the numbering, please refer to Figure 6.1. Spectra measured (a) in conventional NMR (1 mM, 618 scans), (b) in the stripline-NMR setup (3 mM, 256 scans), (c) in the SPE-stripline-NMR setup (200 μM, 1024 scans), and (d) in the full EC-SPE-stripline-NMR setup (product mixture generated from 200 μM, 25x256 scans). The spectra displayed are limited to the aromatic region for better visibility. The chemical shifts and J-couplings are described in Table D.1 in Appendix D.3. The product mixture in (d) is further described in the next section and Table D.2 in Appendix D.3

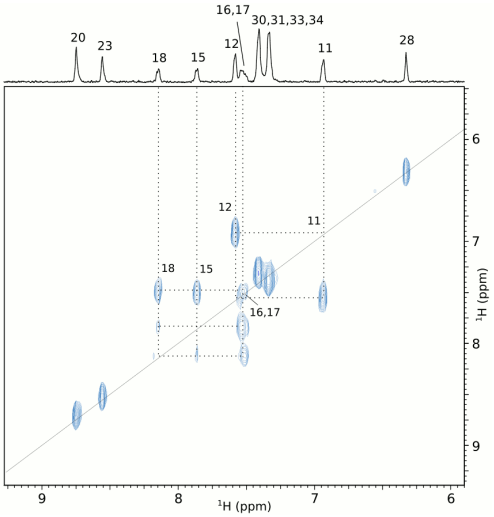

Figure 6.5: TOCSY spectrum of BIRB796 standard in the stripline-NMR

6.3.3 EC-SPE-stripline-NMR

After an initial validation of the SPE-stripline-NMR part of the integrated platform, the next step was the measurement and structural analysis of the EC products of BIRB796. For assessment of the possibilities and limitations of the platform as well as for validation of the structural analysis, the on-line spectra are compared to reference spectra obtained off-line by collection, evaporation and reconstitution with a conventional NMR probe. There is a significant difference in the overall time consumption of the experiments which stresses the advantage of the EC-SPE-stripline-NMR over the conventional approach for the detection of reactive products and is shared by the larger scale flow approach[7]. The preparation for the conventional NMR measurements often took more than a regular working day (see Appendix D.1), meaning that for between 8 and 24 h the sample was subjected to degradation and for at least 7 h at room temperature. In the EC-SPE-stripline-NMR, the time delay between generation and analysis was ca. 80 min. Though the NMR measurement itself was significantly longer, the products are far less likely to degrade in the elution solvent, than in the reaction solvent, for example by acid-catalysis hydrolysis or dehydration[11]. Figure 6.6a shows that degradation is not observed in the EC-SPE-stripline-NMR setup.

For BIRB796, three main products are expected from EC-MS experiments[11]. The EC reaction is an oxidative *O*-dealkylation at the ether function. It produces 2-

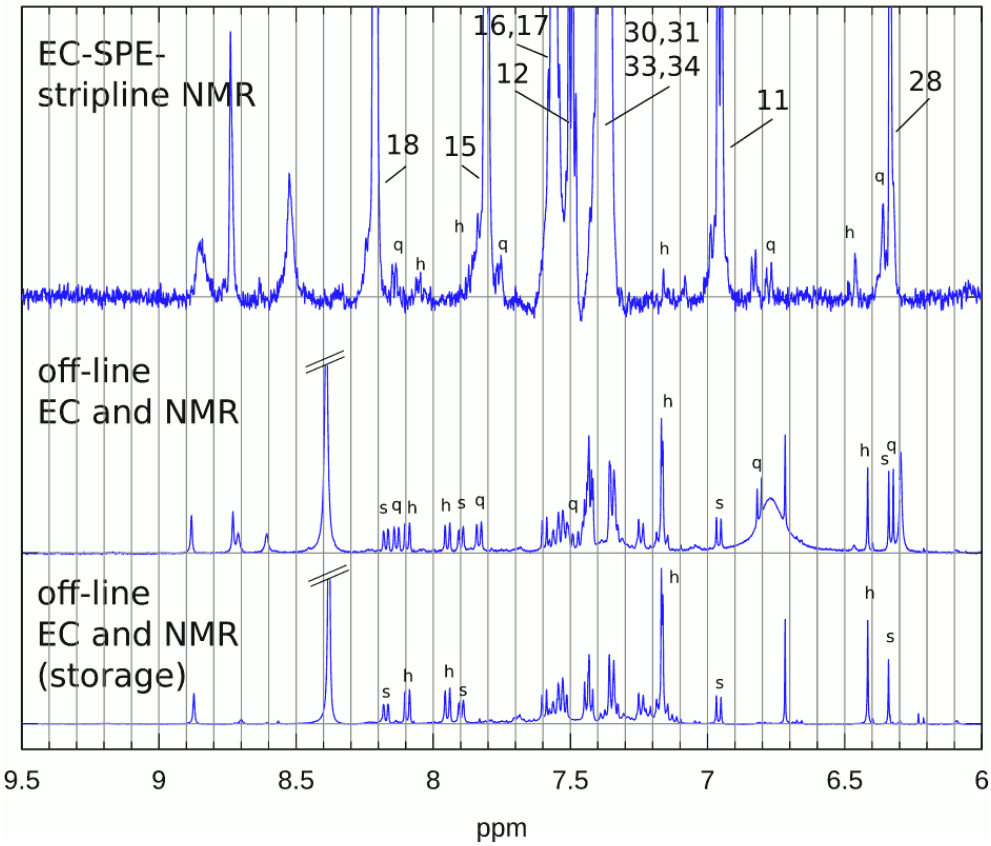

Figure 6.6: Aromatic region of the product mixture. (a) The sample measured by EC-SPE-stripline-NMR is magnified to reveal small product peaks. (b) The sample is measure off-line by conventional NMR directly after re-dissolving and (c) again the next day after storage at room temperature to show the stability of the different products. The substrate peaks are marked with s*, the hydroquinone marked with* h *and the quinoneimine with* q*. The quinoneimine is less stable than the hydroquinone[11]. After storage, the quinoneimine is not detected any more. This can be used additionally to distinguish the two products. An overview of the NMR signals of the two products in a numerical format can be found in Table D.2 in Appendix D.3*

morpholinoethanol, a quinoneimine and a hydroquinone structure (Figure 6.1). 2-morpholinoethanol was not observed in the EC-SPE-stripline-NMR spectrum, probably because it is too polar to be trapped by reversed-phase SPE. In the EC-SPE-stripline-NMR measurement, mainly the substrate and weak signals of the two other products are found, indicating low conversion efficiency in the EC-SPE-stripline-NMR, which conflicts with the high conversion rate measured by LC-UV. This might be due to interference of the magnetic field with the electrical currents of the EC. Unfortunately, the low conversion significantly hinders the routine application of the current setup for the structure elucidation of the products. Some improvement in the product SNR, either by increased EC conversion, by an improved SPE method or by improved stripline-NMR sensitivity, is still needed before the EC-SPE-stripline-NMR can be used for product structure elucidation independently.
However, if the structure of the products is elucidated with the off-line EC experiments measured by conventional NMR, the fingerprint can be used to identify the products present in the EC-SPE-stripline-NMR spectrum (see Table D.2 in Appendix D.3). Figure 6.6b shows the peak assignments in the aromatic region after off-line EC. These assignments were supported by a COSY spectrum (data not shown) and analysis of the J-couplings of these samples. Some peaks overlap with peaks from solvent constituents in the EC reaction mixture which complicates a clear assignment. Next to the substrate, BIRB796, the hydroquinone and quinoneimine conversion products are observed. The peaks for 2-morpholinoethanol cannot be assigned with confidence, because the aliphatic region shows a lot of interferences and only minor differences with the parent chemical shifts are expected. Having the fingerprint of the hydroquinone and the quinoneimine from the off-line experiment enables us to identify some of their peaks in the EC-SPE-stripline-NMR spectrum and thereby confirm their presence. This is shown in Figure 6.6a which is a zoom of Figure 6.4d. Comparison of the data in Figure 6.6b and c shows that the peaks of the reactive/instable quinoneimine disappear after storage as is expected from earlier studies[11].

6.4 Conclusions and perspectives

This study revealed the potential of the hyphenation of EC and miniaturised NMR in the proposed way. The EC-SPE-stripline-NMR platform allowed the acquisition of ^{1}H NMR and COSY as well as TOCSY proton-proton correlation spectra at substrate concentrations compatible with a high conversion rate in EC. The spectral resolution

and SNR is not as high as in the off-line experiments, but the differences are subtle considering that for the EC-SPE-stripline-NMR experiments six times less substrate was consumed. Employing a test compound which shows simpler NMR spectra, more pronounced spectral differences between substrate and product, and a higher conversion rate in EC might have lead to even higher quality NMR data, but consequently might have overestimated the usefulness of this technology at its current state of development in a drug discovery/development setting. The fact that every step of this hyphenated technology as well as the hyphenation itself can be improved significantly, either with existing technology or with easily imaginable technological improvements, promises this technology a future place in the analytical toolbox. Even despite these possibilities, the integration and miniaturisation already allows the use of 10-fold lower substrate concentrations at comparable sample volumes than recently published combinations of EC with conventional flow probe NMR[7]. Additionally, both flow-based approaches limit the time delay between product generation and analysis, thus counteracting interferences by degradation.

Possible improvements of the EC-SPE-stripline-NMR platform can be readily indicated. The relatively new stripline-NMR technology still awaits integration of recent improvements in NMR systems. For example, the addition of a deuterium lock channel would allow longer measurement times without compromising the resolution, thus improving sensitivity. However, interestingly, the maximum measurement time of 12.5 h (12,800 scans) for a ^{1}H NMR spectrum, applied in this study, did not result in increased line width for the 9H peak compared with the 512 scan or even the single scan spectrum of the same EC-SPE-stripline-NMR sample. Measurements of a 3 mM BIRB796 standard gave a line broadening of 0.2 Hz from single scan up to 256 scans. At longer measurement times, double lines are observed in some rare cases which may be prevented by use of a lock channel. A further advancement could be achieved by integration of cryotechnology, which has led to an up to sixfold increase in sensitivity in other miniaturised probes[22]. This might fill an existing gap in quantitative integration which requires an SNR of 150 in order to achieve less than 1% error[23]. In the EC-SPE-stripline-NMR (12,800 scans), the conversion mixture gave an SNR of 75 for the doublet of proton 18 of the substrate and of only 5 for the hydroquinone. Thus, the SPE-stripline-NMR combination is only a factor of two short of achieving sufficient quality 1D spectra from 300 μl sample material at 200 μM concentration. An additional way to improve sensitivity is found in the stripline-NMR chip. The limit of detection (LOD), which is given by the number of spins in 1 Hz bandwidth that need to

resonate to achieve an SNR of 1 in a single scan[13], is with $4 \cdot 10^{13}$ spins/$\sqrt{Hz}$ a factor of three higher than the theoretical value. This discrepancy is mainly attributed to losses due to the use of glass as a chip substrate. Therefore, other chip substrates might improve the sensitivity significantly. A fused silica chip is currently under development, and the first tests indicate that lower LOD, thus higher sensitivity, can be expected. Another contribution to higher sensitivity may come from an improved resolution of the chip, since the line width negatively correlates with SNR. We found an FWHM of around 3 Hz, although in a previous stripline-NMR chip we have found an FWHM of less than 1 Hz[24]. Thus, improvements in line width are also anticipated for the newly designed chip. Together with the change in chip substrate, this is expected to improve SNR by at least a factor of five. The main challenge in this study was the unexpectedly low conversion rate. If the conversion rate of 60% (long collection, estimated) to 90% (short conversion, measured) of the off-line experiments would have been achieved in the EC-SPE-stripline-NMR setup, the resulting four to sixfold sensitivity increase would be sufficient for acceptable product spectra.

Furthermore, improved tuning of the elution volume of the on-line SPE step to the stripline-NMR probe, bridging the 50-fold gap between measurement and elution volume, would allow increased sensitivity or decreased substrate consumption and trapping time as well. Although a second alternative would be the use of commercially available 5 μl NMR probes, these do not promise additional mass sensitivity as reported concentrations and measurement times are comparable to those reported for the stripline-NMR herein[25]. Therefore, it is likely more beneficial to bridge this gap by miniaturisation of the on-line SPE step.

In conclusion, the proposed improvements provide ample opportunity to close the small sensitivity gap to achieve a productive hyphenation of EC to miniaturised NMR, provided the conversion rate in EC can be brought to the off-line level.

Acknowledgements

This work was performed partly within the framework of the Dutch Top Institute Pharma project D2-102 (Metabolic stability assessment as new tool in the Hit-to-Lead selection process and the generation of new lead compound libraries) and partly within the research program ACTS - Process on a Chip (PoaC), financed by the Netherlands Organisation for Scientific Research (NWO). Agnieszka Kraj, Hendrik-Jan Brouwer and Jean-Pierre Chervet (Antec, Zoeterwoude, The Netherlands) are acknowledged for

their support of the electrochemistry part of the project. Hans Janssen, Jan van Os and Jan van Bentum (Radboud University Nijmegen, The Netherlands) are credited for technical and organisational support with regard to setup and ongoing development of the stripline probe. Additionally, Roald Tiggelaar, Jacob Bart and Han Gardeniers (Twente University/Mesoscale Chemical Systems, Enschede, The Netherlands) are acknowledged for their support of the stripline-NMR chip fabrication. Frans J.J. de Kanter and Andreas W. Ehlers are thanked for their input concerning the conventional NMR measurements.

References

[1] S. Jahn and U. Karst, "Electrochemistry coupled to (liquid chromatography/) mass spectrometry—current state and future perspectives," *J. Chromatogr. A*, vol. 1259, p. 16, 2012.

[2] J. A. Richards and D. Evans, "Flow cell for electrolysis within probe of a nuclear magnetic-resonance spectrometer," *Anal. Chem.*, vol. 47, no. 6, p. 964, 1975.

[3] K. Albert, E. Dreher, H. Straub, and A. Rieker, "Monitoring electrochemical reactions by C-13 NMR spectroscopy," *Magn. Reson. Chem.*, vol. 25, p. 919, 1987.

[4] X. C. Zhang and J. W. Zwanziger, "Design and applications of an in situ electrochemical NMR cell," *J. Magn. Reson.*, vol. 208, no. 1, p. 136, 2011.

[5] J. Wu, J. Day, K. Franaszczuk, B. Montez, E. Oldfield, A. Wieckowski, P. Vuissoz, and J. P. Ansermet, "Recent progress in surface NMR-electrochemistry," *J. Chem. Soc. Faraday Trans.*, vol. 93, no. 6, p. 1017, 1997.

[6] V. Mairanovsky, L. Yusefovich, and T. Filippova, "NMR electrolysis combined method (NMREL)—basic principles and some applications," *J. Magn. Reson.*, vol. 54, p. 19, 1983.

[7] H. Simon, D. M. ans S. Jacquoilleot P. Sanderson, and R. Z. U. Karst, "Combination of electrochemistry and nuclear magnetic resonance spectroscopy for metabolism studies," *Anal. Chem.*, vol. 84, p. 8777, 2012.

[8] O. Gökay and K. Albert, "From single to multiple microcoil flow probe NMR and related capillary techniques: a review," *Anal. Bioanal. Chem.*, vol. 402, p. 647, 2012.

[9] O. Corcoran and M. Spraul, "LC-NMR-MS in drug discovery," *Drug Discov. Today*, vol. 8, p. 624, 2003.

[10] A. Baumann and U. Karst, "Online electrochemistry/mass spectrometry in drug metabolism studies: principles and applications," *Expert Opin. Drug Metab. Toxicol.*, vol. 6, p. 715, 2010.

[11] D. Falck, J. de Vlieger, M. Giera, M. H. M, H. Irth, W. Niessen, and J. Kool, "On-line electrochemistry-bioaffinity screening with parallel HR-LC-MS for the generation and characterization of modified p38alpha kinase inhibitors," *Anal. Bioanal. Chem.*, vol. 403, p. 367, 2012.

[12] P. J. M. van Bentum, J. W. G. Janssen, A. P. M. Kentgens, J. Bart, and J. G. E. Gardeniers, "Stripline probes for nuclear magnetic resonance," *J. Magn. Reson.*, vol. 189, p. 104, 2007.

[13] J. Bart, J. W. G. Janssen, P. J. M. van Bentum, A. P. M. Kentgens, and J. G. E. Gardeniers, "Optimization of stripline-based microfluidic chips for high-resolution NMR," *J. Magn. Reson.*, vol. 201, p. 175, 2009.

[14] J. Bart, A. J. Kolkman, A. J. Oosthoek-de Vries, K. Koch, P. J. Nieuwland, J. W. G. Janssen, P. J. M. van Bentum, K. A. M. Ampt, F. P. J. T. Rutjes, S. S. Wijmenga, J. G. E. Gardeniers, and A. P. M. Kentgens, "A microfluidic high-resolution NMR flow probe," *J. Am. Chem. Soc.*, vol. 131, p. 5014, 2009.

[15] R. Eglen and T. Reisine, "The current status of drug discovery against the human kinome," *Assay Drug Dev. Technol.*, vol. 7, p. 22, 2009.

[16] S. Kumar, J. Boehm, and J. Lee, "p38 MAP kinases: key signalling molecules as therapeutic targets for inflammatory diseases," *Nat. Rev. Drug Discov.*, vol. 2, no. 9, p. 717, 2003.

[17] A. Bax and D. Davis, "MLEV-17-based two-dimensional homonuclear magnetization transfer spectroscopy," *J. Magn. Reson.*, vol. 65, p. 355, 1985.

[18] W. P. Aue, J. Karhan, and R. R. Ernst, "Homonuclear broad band decoupling and two dimensional J resolved NMR spectroscopy," *J. Chem. Phys.*, vol. 64, p. 4226, 1976.

[19] J. D. van Beek, "matNMR: A flexible toolbox for processing, analyzing and visualizing magnetic resonance data in Matlab," *J. Magn. Reson.*, vol. 187, p. 19, 2007.

[20] P. Eilers, "A perfect smoother," *Anal. Chem.*, vol. 75, p. 3631, 2003.

[21] "ACD/NMR Processor Academic Edition." Advanced Chemistry Development, Inc., Toronto, ON, Canada, 2010.

[22] Bruker, "Triple Resonance MicroCryoProbe for small volume applications." www.bruker.com/products/mr/nmr/probes/cryoprobes/microcryoprobe/overview.html, Accessed 11.03.2013.

[23] F. Malz and H. Jancke, "Validation of quantitative NMR," *J. Pharm. Biomed. Anal.*, vol. 38, no. 5, p. 813, 2005.

[24] A. P. M. Kentgens, J. Bart, P. J. M. van Bentum, A. Brinkmann, E. R. H. van Eck, J. G. E. Gardeniers, J. W. G. Janssen, P. Knijn, S. Vasa, and M. H. W. Verkuijlen, "High-resolution liquid- and solid-state nuclear magnetic resonance of nanoliter sample volumes using microcoil detectors," *J. Chem. Phys.*, vol. 128, p. 052202, 2008.

[25] A. Jansma, T. Chuan, R. W. Albrecht, D. L. Olson, T. L. Peck, and B. Geierstanger, "Automated microflow NMR: routine analysis of five-microliter samples," *Anal. Chem.*, vol. 77, no. 19, p. 6509, 2005.

Appendix A

Supplemental Information for Chapter 2: Stripline NMR experiments of subμL volume samples

A.1 TOCSY spectra of strigolactons Nijmegen-1 and DMSL *slow*

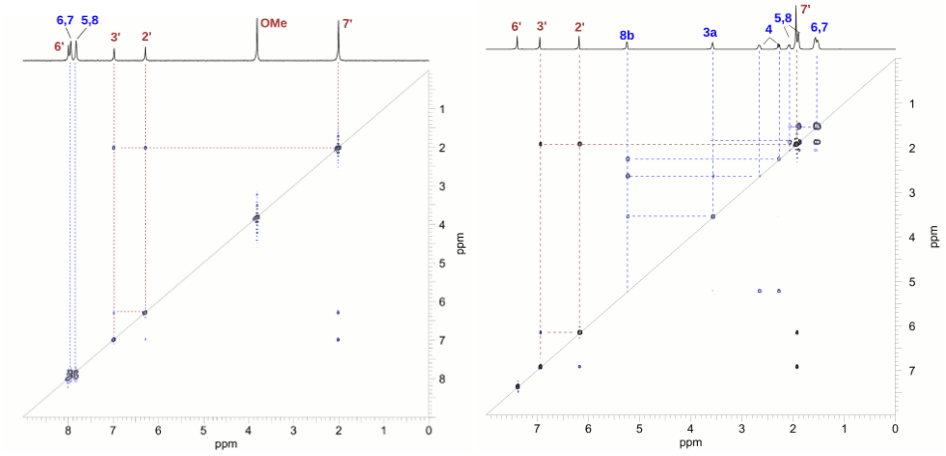

(a) Nijmegen-1 (b) DMSL *slow*

Figure A.1: TOCSY spectra of strigolactones Nijmegen-1 and DMSL slow. *In red the D-ring and in blue the ABC structure, measured in the stripline NMR chip*

A.2 ^{1}H NMR chemical shifts of synthetic strigolactones, measured in stripline NMR

Table A.1: Overview of chemical shifts of peaks in the ^{1}H NMR spectra measured in the stripline NMR chip, shown in Figure 2.9

	N1	GR24	6Me-GR24 f	6Me-GR24 s	8Me-GR24 f	8Me-GR24 s	DMSL f	DMSL s
H3a	-	3.93	3.94	3.94	3.91	3.92	3.52	3.55
H4	-	3.9, 3.42	3.06, 3.41	3.08, 3.38	3.05, 3.40	3.06, 3.41	2.21, 2.58	2.25, 2.65
H5	7.75	7.23 - 7.49	7.05	7.06	7.04	7.05	1.84 2.01	1.87 2.05
H6	7.87	7.23 - 7.49	7.40	7.39	7.22	7.23	1.51 1.47	1.50 1.54
H7	7.87	7.23 - 7.49	7.11	7.11	7.04	7.05	1.51 1.47	1.50 1.54
H8	-	7.23 - 7.49	-	-	-	-	-	-
H8b	7.75	5.93	5.94	5.92	5.98	6.01	5.20	5.23
H9	3.74 (OMe)	-	2.36	2.36	2.42	2.44	1.84, 2.01	1.87, 2.05
H2'	6.22	6.197.23-7.49	6.18	6.25	6.15	6.20	6.14	6.16
H3'	6.91	6.99	6.97	7.02	6.96	6.97	6.91	6.93
H6'	7.92	7.23-7.49	7.48	7.53	7.46	7.49	7.35	7.37
H7'	1.94	2.01	2.05	2.03	2.01	2.03	1.89	1.92

A.3 ^{13}C NMR chemical shifts of synthetic strigolactones, measured in solid state NMR and stripline NMR

Table A.2: Chemical shifts of the peaks in solid state ^{13}C NMR spectra, shown in Figure 2.11, and the stripline HMQC spectrum shown in Figure 2.10b, chemical shift differences (Δ (ppm)) for 8-Me-GR24 fast *and* slow

	N1	GR24	6Me-GR24 f	8Me-GR24 f	8Me-GR24 s	Δ (ppm)	6Me-GR24 s stripline
C2	-	174.0	174.4	173.6	173.8	0.2	-
C3	102.1	112.4	112.7	114.2	113.8	0.4	-
C3a	-	12.6?	32.3	39.8,35.8	38.3	1.5, 2.5	38
C4	171.1?	38.3	40.0	?	?	-	-
C4a	-	137.0	141.1	144.3	142.7	1.6	?
C5	-	127.0	129.6	131.0	131.8	0.8	124
C6	-	127.0	137.8	127.2	130.1	2.9	?
C7	-	127.0	125.9	123.3	124.3	1.0	126
C8	-	127.0	125.9	139.8	136.7	3.1	124
C8a	-	141.9	141.1	137.0	135.6	1.4	?
C8b	171.1?	88.1	86.8	86.1	86.9	0.8	84
C9	-	-	21.4	20.3	18.5	1.8	20
C2'	-	103.5	102.3	102.3	102.9	0.6	100
C3'	-	-	137.8	141.5	138.6	2.9	141
C4'	-	137.0	136.0	133.9	134.5	0.6	-
C5'	-	171.1	169.2	170.4	170.9	0.5	-
C6'	-	157.6	157.5	154.5	159.6	5.1	150
C7'	10.6	9.6	11.6	10.9	10.9	0.6	9
OMe	52.5	-	-	-	-	-	-

Appendix B

Supplemental Information for Chapter 3: Continuous Flow ^{1}H and ^{13}C Microfluidic Stripline NMR

B.1 Technical details NMR stripline chips

In general, the chips are composed of substrates of glass or fused silica (outer dimensions 25 mm x 10 mm). The stripline structure is copper electroplated (15 μm thick) onto the substrate using a 200 nm/15 nm thick copper/chromium seed/adhesion layer. The ground planes are applied on both sides of the stripline structure as electroplated Cu on substrates or as copper foil. At each side of the stripline, fluidic microchannels were etched or diced.

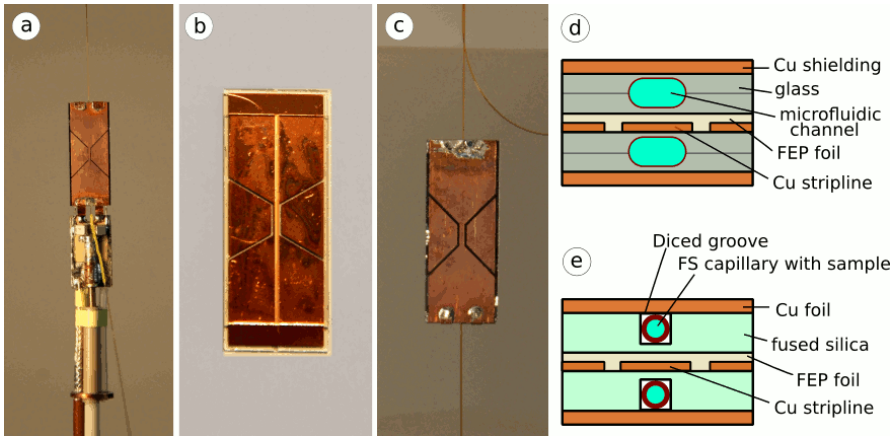

Figure B.1: NMR stripline chips used in this study: chip (A), chip (B), chip (C), d) shows the schematic cross section of chip (A) and (C). e) shows the schematic cross section of chip (B).

Design A: The stripline chip has two microfluidic channels into which the inlet and outlet capillaries are fastened by ceramic glue. The chip is made of 4 substrates of 100 μm thickness (D263T borosilicate, Schott) on which the copper stripline structure and shieldings are deposited, and microfluidic microchannels are isotropically etched. After mounting in the probe, the two halves of the probe hold the stripline together and make the ground connection. Fused silica capillaries (Polymicro Technologies, 75 μm ID, 150 μm OD) are glued into the inlet and outlet (Ormocer ceramic glue). The stadium-shaped detection volume is approximately 400 μm wide and 150 μm deep. Microchannel detection volume of a single microchannel: 165 nl (3 mm strip) (note that the stripline design makes use of two microchannels, on either side of the chip, possible). The thickness of the chips is 460 μm.
b) Design B: The stripline chip has one microchannel diced into the substrate into which a FS capillary containing the sample can be placed. The chip is made out of two fused silica substrates (500 μm thick). On one side the copper stripline structure is deposited. The two parts are bonded using FEP foil (fluorinated ethylene propylene; type 100C20, thickness 25 μm, DuPont) at 250 °C and a pressure of ca 70 bar. Both parts contain a diced groove of 400 x 400 μm, through which a FS capillary (250 μm ID, 360 μm OD) is loaded which is used as the microfluidic microchannel. Copper foil is used as shielding on both sides without bonding, short circuit is separately soldered onto the chip. Single microchannel sample volume: 150 nl, Thickness of the chip: 1100 μm, excl. shielding foils.
c) Design C: Similar design as chip (A), but made in thicker glass substrates (150 μm). Therefore, the fluidic microchannel is also wider and the connecting FS capillaries have a larger diameter (100 μm ID, 200 μm OD). Single microchannel detection volume: 245 nl (channel width: 400 μm, channel depth: 200 μm, 3mm length strip) Thickness of the chip is 630 μm.

B.2 Fabrication details of fused silica stripline NMR chips

The base material of the NMR-chips is fused silica. Figure B.2 shows an overview of the fabrication process of high-sensitivity stripline chips. Prior to sputter-deposition of a metallic copper-chromium thin-film on the frontside of fused silica substrates (100 mm diameter, thickness 525 μm, double-side polished; universitywafer.com), the substrates are cleaned using immersion in fuming 100% nitric acid for 10 min (Selectipur 100453, BASF) and boiling 69% nitric acid (VLSI 116445, BASF) for 15

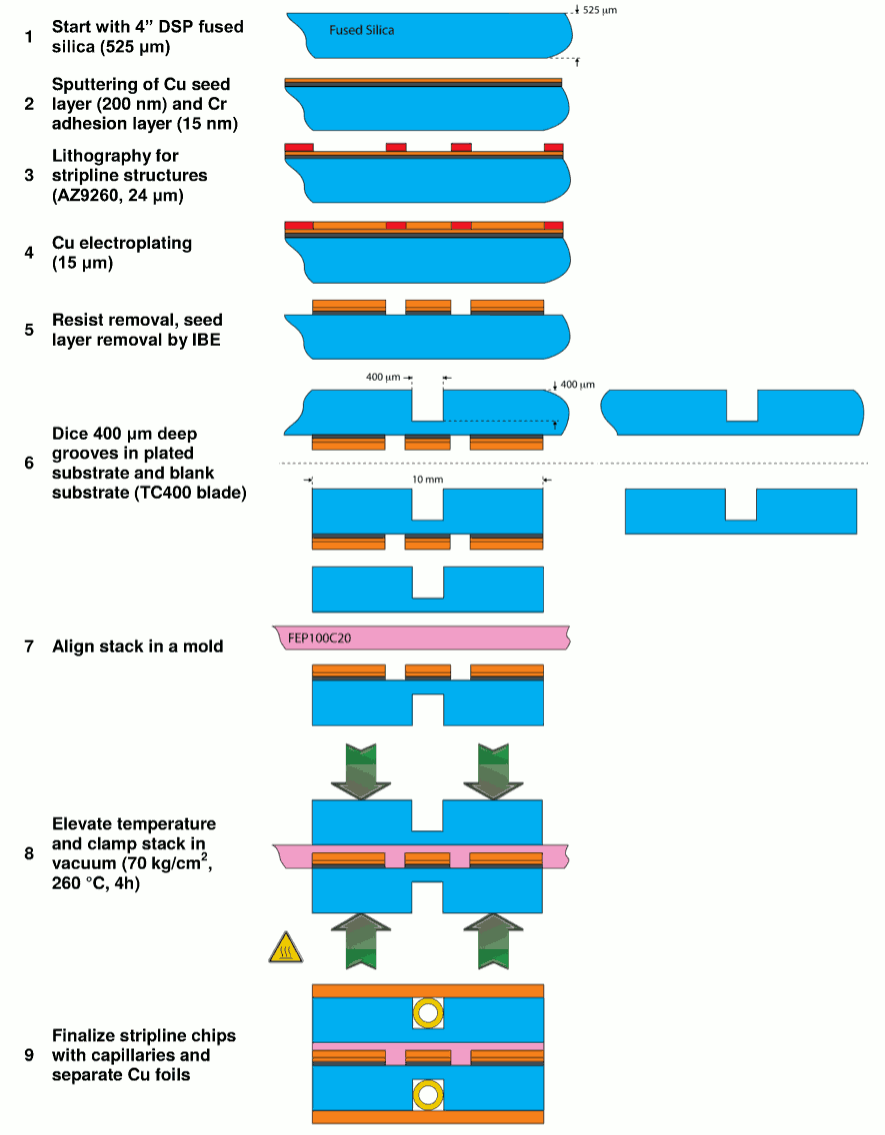

Figure B.2: Overview fabrication steps for high-sensitivity stripline NMR-chips in fused silica (DSP: double side polished; IBE: ion beam etching)

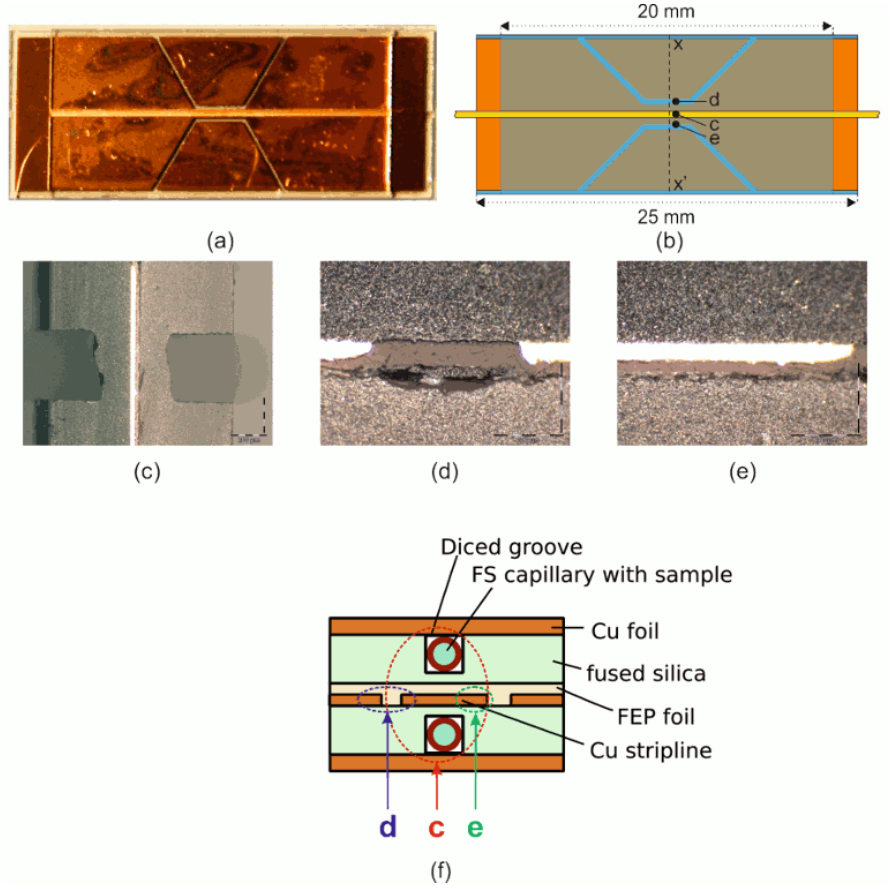

Figure B.3: Schematic representation (a), topview image (b) and cross-sectional images (c-e) of high-sensitivity stripline-based NMR-chips in fused silica. In b) the cross-sectional view-line x-x' is indicated of which c)-e) are images. In f) a schematic cross-section indicates where images c)-e) are taken.

min, followed by quick dump rinsing in de-mineralized water and spin-drying. Sputter-deposition at room temperature (argon pressure 0.67 Pa; Ar purity 99.999%) is done on a home-built DC-magnetron sputtering system. A 15 nm layer of chromium (target purity 99.95%; Kurt J. Lesker) is used as adhesion material for the 200 nm thick copper seed layer (target purity 99.999%; Kurt H. Lesker). Deposition from 2 inch targets is done without breaking the vacuum. Onto this metallic film a 24 μm thick layer of high-aspect ratio photoresist (AZ9260, AZ Electronic Materials; MicroChemicals GmbH) is spin-coated, which is patterned by means of standard UV-lithography. The pattern defined in the photoresist resembles the stripline structure, onto which a 15 μm thick copper layer is electroplated. Amongst other parts, the home-built electroplate set-up comprises a glass container with the electrolyte solution and a power supply (Dynatronix, model DuPR10-1-3) to accomplish plating of copper on the seed layer. The applied DC current density is 0.75 A per square decimeter of seed layer surface area. In order to obtain a uniform copper layer, during electroplating at room temperature, the electrolyte solution near the surface to be plated is continuously refreshed by means of vertical movement of a sprayhead (fully immersed in the electrolyte) at 30 mm distance of the surface and recirculation of the electrolyte with a pump (Masterflex). A volume of 10 liter electrolyte contains 1 kg copper salt (copper(II)-sulfate-pentahydrate, Schlötter Galvanotechnik GmbH), 1.1 liter 96% sulphuric acid (VLSI UN1830, BASF), 1.5 ml 50% hydrochloric acid (VLSI UN1790, BASF), 100 ml HL11 starter and 2.5 ml HL13 grain refiner (Schlötter Galvanotechnik GmbH), and de-mineralized water added to reach the given volume. After reaching the targeted Cu thickness (after $\sim$ 36 min), the substrate is thoroughly rinsed with de-mineralized water to prevent oxidation of the electroplated metal. Subsequently, the photoresist is removed with acetone (VLSI 100038, BASF), followed by removal of the Cu/Cr-seed layer by means of ion beam etching (Oxford i300 with in-situ SIMS end point detection system; Argon pressure 0.3 mTorr, temperature 25 °C, current $\sim$ 122 mA). In the backside of this substrate a 400 μm wide and deep groove/slit is diced, which is aligned with respect to the electroplate copper structure (Disco DAD-321 dicing machine; thermo-carbon TC-400 dicing blade, 25 krpm rotational speed, 6 mm/s feed speed), followed by dicing into samples of 25 mm $\times$ 10 mm. In a blank fused silica substrate a groove/slit chamber with similar dimensions is diced, followed by division into samples of 20 mm $\times$ 10 mm. The difference in length of the samples is required to be able to electronically contact the copper structure after assembly of the NMR-chip.

A stack of a sample with copper and a blank sample is realized in a home-built mold,

which is used to ensure that both sample chambers are well-aligned with respect to the stripline as well as to each other. In-between the two samples, a sheet of fluorinated ethylene propylene (FEP) is placed (FEP type 100C20, thickness 25 μm, DuPont). After clamping of this stack configuration in a home-built clamping tool, this tool is loaded into a vacuum furnace (modified Heraeus system, with Edwards pressure controller). The temperature of this system is increased to 260 °C, at which it was maintained for 4h. This temperature in combination with the load on the stack (ca. 70 kg/cm^2) ensures that the FEP bonds onto the copper/glass of the samples above/below the sheet, and that the FEP sheet is squeezed between the copper structures, which is a requirement to minimize distortions in the magnetic field (i.e. susceptibility match). Last step in the fabrication process of these stripline NMR-chips is finalization of the stripline geometry by means of assembly of separate copper foils on both sides of the FEP-bonded glass-stack. Prior to mounting of configured stripline chips in the probe of the NMR measurement set-up, fused silica capillaries (PolyMicro Technologies; outer diameter 360 μm, inner diameter 250 μm) are inserted in the grooves/slits, which serve as fluidic chambers. Figure B.3 shows a series of images of high-sensitivity stripline-based NMR chips. In Figure B.3a a fully assembled chip is shown. In Figure B.3b a schematic topview is given with outer dimensions. Figures B.3c-e are cross-sectional images along the line x-x' shown in Figure B.3b: both diced grooves/slits are well-aligned with respect to each other and the stripline (Figure B.3c), and this FEP-sheet indeed fills the gaps in the Cu-structure near the stripline (Figures B.3d and B.3e). The small gap underneath the FEP foil visible in Figure B.3d is an artifact caused by the cross-sectional cutting procedure.

Of the above-mentioned process, the steps 'substrate cleaning', 'sputtering of Cu/Cr', 'lithography on AZ9260 photoresist' and 'stack-alignment' should be done in a clean-room environment, to avoid problems with dust-particles. In our case 'clamping at elevated temperatures' and 'dicing' was also done in a cleanroom, but this is not a necessity. All other process steps, i.e. electroplating and finalization of the chips with copper sheets, are done in non-conditioned laboratory environments.

Acknowledgements

The starter and grain refiner additives to the electrolyte solution, i.e. Slotocoup HL11 and Slotocoup HL13 respectively, were a kind gift of Dr.-Ing. Max Schlötter GmbH & Co. KG, Galvanotechnik, Geislingen/Steige, Germany.

B.3 Homebuilt probeheads

Two homebuilt probes were used in this work; a single resonance probe with a ^{1}H channel and a double resonance probe with a ^{1}H channel and a variable frequency X-channel. In the probe design symmetry and simplicity of the probehead are of great importance. The single resonance (^{1}H) probe consists of a long aluminium cylinder, divided in two halves. The chip and circuit board exactly fit into trenches at the top of the probehead. The stripline structure is connected to tuning capacitors on one side and to ground on the other side by soldering. The return line connection is given by direct contact between the copper planes and the aluminium cylinder. This parallel rf circuit is capacitively coupled and matched to the 50Ω rf-connection. The tuning- and match capacitors (small Voltronics non-magnetic quartz trimmers and DLI non-magnetic ceramic chip capacitors) are mounted on a printed circuit board (PCB) and placed in one of the two halves of the aluminium cylinder. The rf circuit of the single resonance (^{1}H) probe is shown in Figure B.4a.

In the double resonance (HX) probe, the stripline chip is placed in a gold-plated copper cylinder, divided in two halves, both with milled trenches fitting the chip. The stripline is inserted as a short circuit at one side and soldered to a two channel tuning- and matching circuit on the other side. Both channels have capacitors connected to ground for tuning and series capacitors for matching end coupling with the NMR transmit/receiver channels. The X-channel is equipped with a parallel LC-filter circuit to block the ^{1}H frequency entering the X-channel. The tune- and match capacitors are mounted on a platform just below the chipholder and connected with a handformable coaxial cable to the rf-connectors. The chipholder is mounted in the center of this platform. The tune/match platform is mounted on top of an aluminium tube which is part of the probe housing. The rf circuit and pictures of the double resonance (HX) probe are shown in Figures B.4b to B.4d.

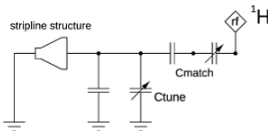

(a) Rf circuit of single resonance ^{1}H probe

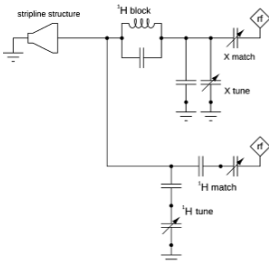

(b) Rf circuit of double resonance HX probe

(c) Picture of double resonance HX probe

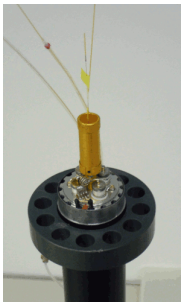

(d) Picture of opened top of double resonance HX probe

Figure B.4: Schematics of the rf circuits of single resonance ^{1}H probe (a) and double resonance HX probe (b), pictures of the double resonance HX probe showing (c) the stripline chip on top and the electronic and microfluidic connections on the bottom, and (d) the opened top of the probe with the microfluidic FS capillaries connected.

B.4 Microfluidics

For pumping the solution through the stripline NMR chip, one or two syringe pumps (NE-1000, New Era Pump Systems Inc.) were used, with syringes (1 to 5 ml, luer lock gas tight, SGE Analytical Science and VWR), connected by approx. 3 m long fused silica capillaries (360 μm O.D., 250 μm I.D., Polymicro Technologies) to the top of the probe. For chip (A) and (C) (B.1), a union (Upchurch Scientific, P-779) was used to make the connections to smaller diameter fused silica capillaries (chip (A): 150 μm O.D., 75 μm I.D., chip (C): 200 μm O.D.,100 μm I.D., Polymicro Technologies), which were glued into the inlet and outlet of the chip. At the outlet another union (Upchurch Scientific, P-779) was used to connect to a wider capillary (360 μm O.D., 250 μm I.D.) that led to a waste glass container at the bottom of the magnet. The connections to larger diameter FS capillaries at the inlet and waste lines were used to prevent buildup of pressure in the system. For chip (B) a fused silica capillary (360 μm O.D., 250 μm I.D.) runs through the chip, which was only fixed at the top to prevent motion, by leading it through a hole in a TEFLON disc. The FS capillary is connected to syringe pump and waste in the same way as with chips (A) and (C).

B.5 One-dimensional ^{1}H spectra

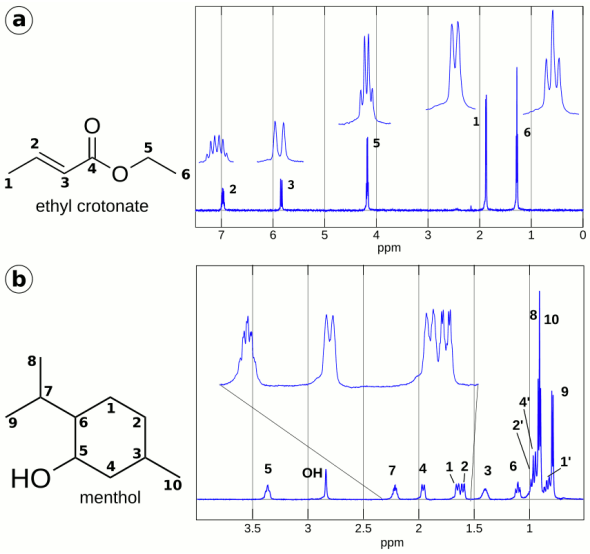

Figure B.5: ^{1}H NMR measurement in continuous flow, acquired in the single channel ^{1}H probe equipped with chip (A). A) Ethyl crotonate (20 vol% in $CDCl_3$), at a constant flow rate of 1 µl/min, single scan. B) Menthol (30% in $CDCl_3$), with a constant flow rate of 15 µl/min, single scan. Zero filling up to 32000 points and 3 Hz line broadening was applied for both spectra.

Appendix C

Supplemental Information for Chapter 4: Inline reaction monitoring of amine-catalyzed acetylation of benzyl alcohol

C.1 Probe design

The basic element in the design of our NMR probehead is the stripline rf resonator chip. The microfluidic stripline detector is an assembly of glass substrates with etched microfluidic channels and merged together with a bonding process such that the chip becomes leaktight and mechanically stable. On one side of the two merged substrates, copper ground planes are deposited by sputtering and electroplating. The copper stripline structure is sputtered and electroplated on one of the merged substrates. Due to a constriction in this structure, the current density will be enhanced resulting in a high rf-field at that position of the sample. The two parts, forming the microfluidic chip, are positioned in such a way that the stripline structure is embedded between the two substrates with the copper planes to the external sides. One side of the stripline chip is connected to one of the copper ground planes. Some pictures and a schematic of the stripline chip are shown in Figure C.1.

Special attention was given to the symmetry and simplicity of the probehead. The top part of a long aluminum cylinder was divided in two halves. Small trenches of half of the depth of the chip and circuit-board thickness were milled in both halves in which the chip and the circuit-board could be placed. The stripline structure was connected to the rf-circuit by soldering. The return line connection is established by the direct contact between the copper planes and the aluminum cylinder.

The stripline is inserted as a short at one side and soldered to tuning capacitors connected to ground on the other side. This parallel circuit is capacitively coupled and matched to the 50 Ω rf-connection. The tuning and matching capacitors are mounted on a printed circuit board (PCB) and placed in one of the two halves of the aluminum cylinder as described above. The tuning- and matching capacitors are small Voltronics non-magnetic quartz trimmers and DLI non-magnetic ceramic chip capacitors. The circuit is shown in Figure C.1b.

C.2 Microfluidic Setup

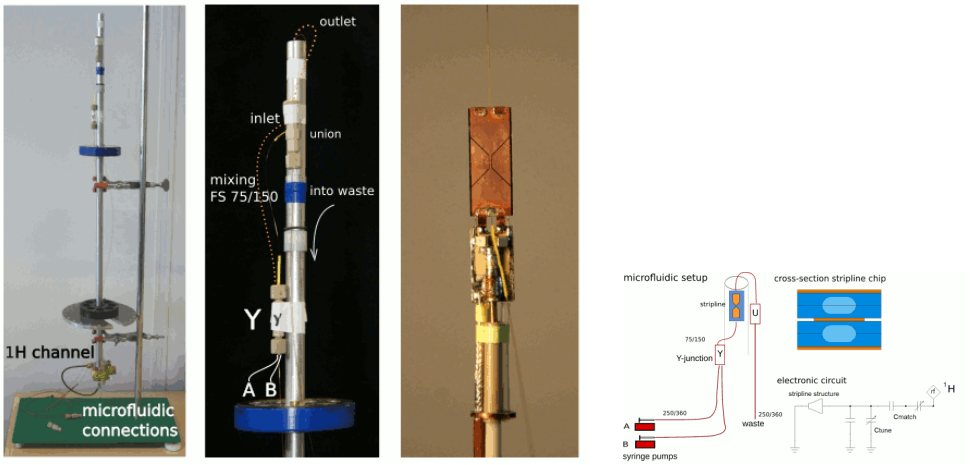

(a) a (b) b

Figure C.1: The microfluidic setup used for the series of ^1H spectra during the reaction. a) Pictures of the probe, microfluidics and the cap removed showing the stripline chip b) Schematic representation of the setup, cross section of the stripline chip and rf circuit

Two syringe pumps (NE-1000, New Era Pump Systems Inc.) were used, each loaded with a syringe (1 mL, gas tight, SGE Analytical Science and VWR) with luer lock connections to fused silica (FS) capillaries (360 μm O.D., 250 μm I.D., Polymicro technologies) that were led into the magnet to the probe. The microfluidic setup is shown in Figure C.1. At the top of the probe a Y connector (Upchurch Scientific, P-773, 17 nL void volume) is used to bring together the two reactant flows. The mixture then flows into an FS capillary (150 μm O.D., 75 μm I.D.) of 850 nL volume, that is glued into the stripline chip. An FS capillary (150 μm O.D., 75 μ I.D.) is glued into the outlet of the chip, which is connected via a nanotight PEEK union (Upchurch Scientific,

P-779) into a wider FS capillary that goes into the waste container. The NMR sensitive detection volume is 150 nL, the reaction volume before measurement (consisting of the volumes of the stripline entrance channel, the FS capillary and the Y connector) can be defined by choosing the length of the capillary and is in this case 850 nL, so that the total reaction volume is approximately 1 μL. The delay time between the start of the reaction in the Y connector and the measurement arises from this 1 μL reaction volume, and varied between 1.5 seconds ansd 5 minutes, depending on the applied flowrates.

C.3 Fitting procedure

For fitting of the kinetics, the rate constants k are optimised in Matlab by minimising an object function F that gives a value for the difference between experimental and fitted values at each measured point[1]:

$$F = \sum (experimental - fitted)^2 \tag{C.1}$$

The set of differental equations for the reaction of acetyl chloride with DIPEA (Scheme 2) is given in Eq. (C.2), in which the concentrations of AcCl (c_{AcCl}), DIPEA (c_{DIPEA}), a tetrahedral intermediate (c_{TI}), protonated DIPEA (c_{D^+}), ketene (ethenone) (c_K) and acetyl ammonium ion (c_{AA}) are utilised.

$$\frac{dc_{AcCl}}{dt} = \frac{dc_{DIPEA}}{dt} = -k_1 c_{AcCl} c_{DIPEA} + k_{-1} c_{TI} \tag{C.2a}$$

$$\frac{dc_{TI}}{dt} = k_1 c_{AcCl} c_{DIPEA} - (k_{-1} + k_2 + k_3) c_{TI} \tag{C.2b}$$

$$\frac{dc_{D+}}{dt} = \frac{dc_K}{dt} = k_2 c_{TI} - (k_4 - k_{-4}) c_{D+} c_K \tag{C.2c}$$

$$\frac{dc_{AA}}{dt} = k_3 c_{TI} + (k_4 - k_{-4}) c_{D+} c_K \tag{C.2d}$$

The acetylation of benzyl alcohol with DIPEA (Scheme 1) can be described by the set of differental equations in Eq. (C.3), extending Eq. (C.2) with the concentrations of benzyl alcohol (c_{BnOH}) and benzyl acetate (c_{BnOAc}).

$$\frac{dc_{AcCl}}{dt} = \frac{dc_{DIPEA}}{dt} = -k_1 c_{AcCl} c_{DIPEA} + k_{-1} c_{TI} \tag{C.3a}$$

$$\frac{dc_{TI}}{dt} = k_1 c_{AcCl} c_{DIPEA} - (k_{-1} + k_2 + k_3) c_{TI} \tag{C.3b}$$

$$\frac{dc_{D+}}{dt} = k_2 c_{TI} - (k_4 - k_{-4}) c_{D+} c_K + k_5 c_{BnOH} c_{AA} \tag{C.3c}$$

$$\frac{dc_K}{dt} = k_2 c_{TI} - (k_4 - k_{-4}) c_{D+} c_K - k_6 c_{BnOH} c_K \tag{C.3d}$$

$$\frac{dc_{AA}}{dt} = k_3 c_{TI} + (k_4 - k_{-4}) c_{D+} c_K - k_5 c_{BnOH} c_{AA} \tag{C.3e}$$

$$\frac{dc_{BnOH}}{dt} = -k_5 c_{BnOH} c_{AA} - k_6 c_{BnOH} c_K \tag{C.3f}$$

$$\frac{dc_{BnOAc}}{dt} = k_5 c_{BnOH} c_{AA} + k_6 c_{BnOH} c_K \tag{C.3g}$$

C.4 Kinetics for a reaction model with two and three steps

A simplified kinetic model for the reaction of acetyl chloride with DIPEA consists of two steps: AcCl + DIPEA $\xrightarrow{k_1}$ K + D^+ and AcCl + DIPEA $\xrightarrow{k_2}$ AA, resulting in the values $k_1 = 7M^{-1}s^{-1}$ and $k_2 = 3M^{-1}s^{-1}$. The acetylation of benzyl alcohol is represented by a three step model: AcCl + DIPEA $\xrightarrow{k_1}$ D^+ + K, side reaction AcCl + DIPEA $\xrightarrow{k_2}$ AA, and BnOH + K $\xrightarrow{k_3}$ BnOAc. This results in $k_1 = 0.2M^{-1}s^{-1}$, $k_2 = 4 * 10^{-2}M^{-1}s^{-1}$ and $k_3 = 4M^{-1}s^{-1}$.

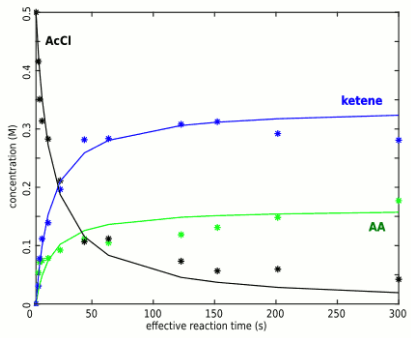

(a) Acetyl chloride with DIPEA

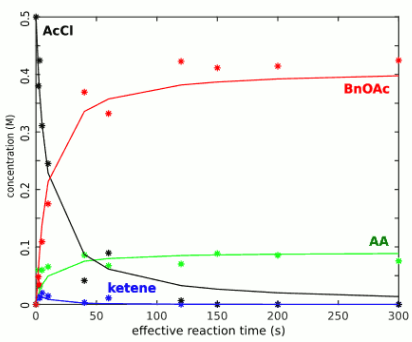

(b) Acetyl chloride with benzyl alcohol and DIPEA

*Figure C.2: Modelling of the kinetics with a simplified model of a) reaction of acetyl chloride with DIPEA, b) reaction of acetyl chloride with benzyl alcohol in the presence of DIPEA. Similar to Figure 4.6, experimentally derived values of concentrations are marked with *, fit results are in solid lines. Starting product acetyl chloride **1** (AcCl), intermediates ketene **7**, acetyl ammonium ion **9** (AA), and end poduct benzyl acetate **4** (BnOAc).*

C.5 The acetylation of benzyl alcohol without DIPEA

The acetylation of benzyl alcohol **2** without a base catalyst is thought to proceed via the tetrahedral intermediate **3**, producing HCl as a side product (Scheme C.1). The conversion of this reaction is slow, the reaction is completed in one day and can be followed by conventional NMR experiments in a standard NMR sample tube. Some spectra taken during the reaction progress are shown in Figure C.3.

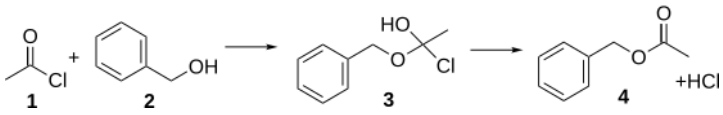

*Scheme C.1: The proposed reaction mechanism of acetyl chloride **1** with benzyl alcohol **2** giving benzyl acetate **4**, involving the tetrahedral intermediate **3**.*

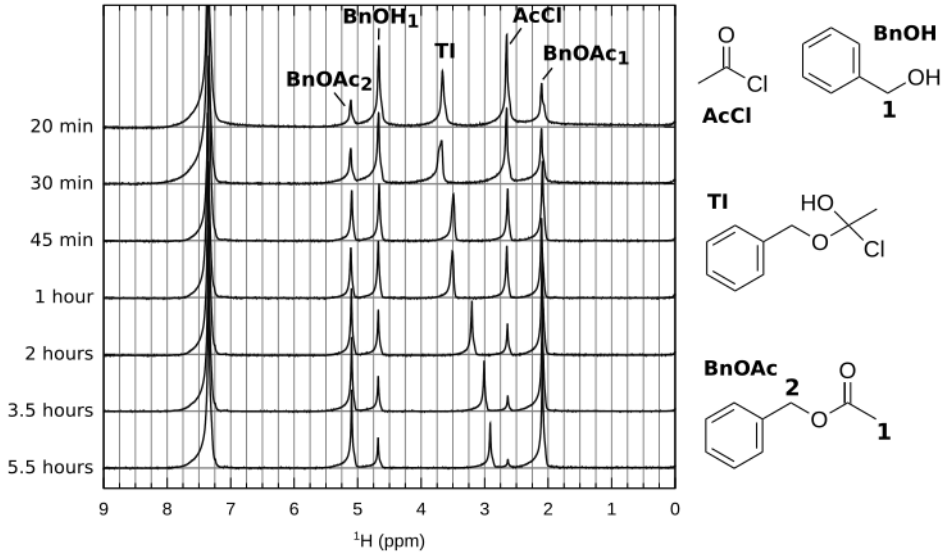

*Figure C.3: The reaction of acetyl chloride (0.5 M) with benzyl alcohol (0.5 M) as measured in a conventional 300 MHz NMR spectrometer for increasing reaction times. Indicated are benzyl alcohol (BnOH), benzyl acetate (BnOAc), both alpha proton (at 5.1 ppm) and acetyl group (at 2.1 ppm), acetyl chloride (AcCl) and the shifting tetrahedral intermediate **3** (TI).*

C.6 Triethylamine as base catalyst: conventional 2D spectra

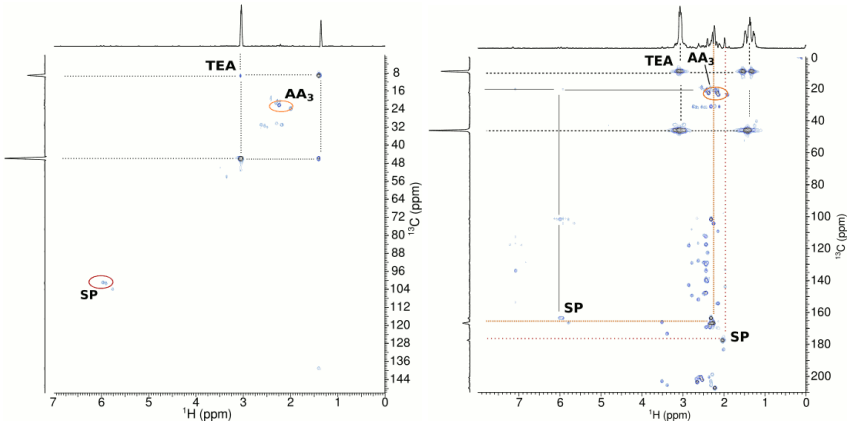

(a) HSQC (b) HMBC

Figure C.4: Acetyl chloride with TEA: conventional 2D spectra after a few hours reaction time

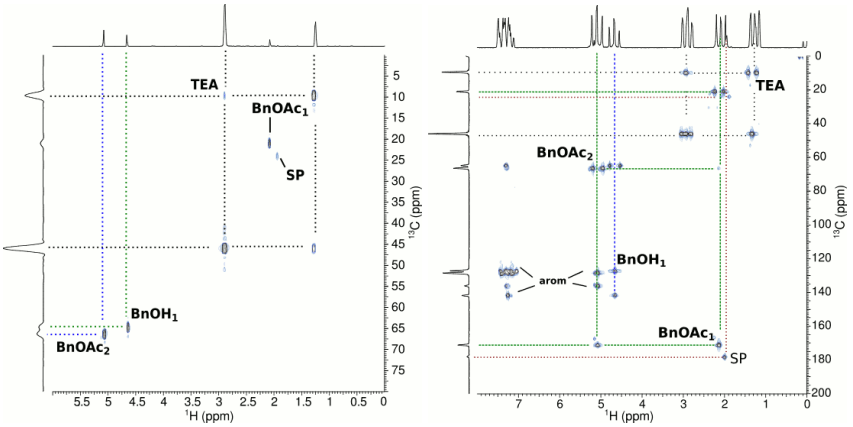

(a) HSQC (b) HMBC

Figure C.5: Acetyl chloride and benzyl alcohol with TEA: conventional 2D spectra after a few hours reaction time

C.7 Pyridine as base catalyst: conventional 2D spectra

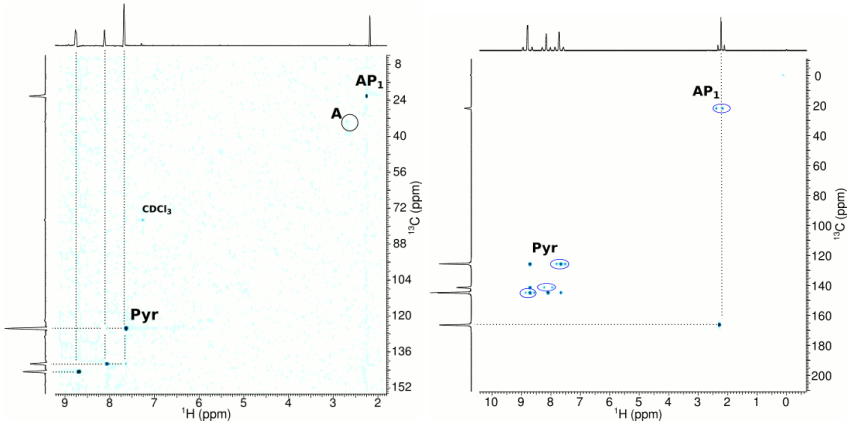

(a) HSQC (b) HMBC

Figure C.6: Acetyl chloride with pyridine: conventional 2D spectra after 2 hours reaction time

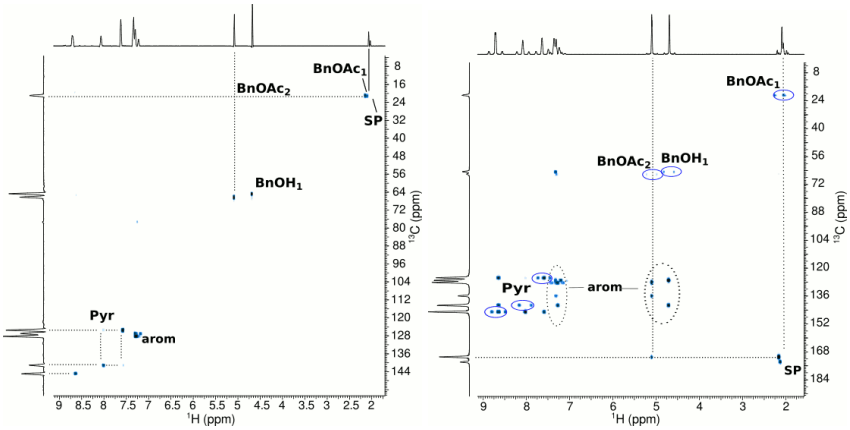

(a) HSQC (b) HMBC

Figure C.7: Acetyl chloride and benzyl alcohol with pyridine: conventional 2D spectra after a few hours reaction time

C.8 Overview of observed peaks

Table C.1: Observed peaks in the stripline and conventional NMR data, for all experiments discussed in this research. The amine or pyridine peaks are not mentioned here, from the proton spectra only the methyl peaks are taken. The reactions that are studied are acetyl chloride (A), with DIPEA (D), triethyl amine (T) or pyridine (P), either with or without benzyl alcohol (BnOH). The acetyl peaks of the acetyl ammonium ion or acetyl pyridinium ion peaks are found in the column 'Ac', side products are given as 'SP'.

	AcCl	Ac	ketene	BnOAc	diketene	end SP	other SP
A+D							
Stripline	2.68	2.23	2.4				
^{1}H ConvNMR	2.69	2.23	2.4			2.27, 2.3, 6	
^{13}C ConvNMR	33.6, 170.4	22.18, 166.4	2.5, 193.7			100	
BnOH+A+D							
Stripline	2.65	2.21	2.38	2.09			
^{1}H ConvNMR		2.2	2.39	2.09			
^{13}C ConvNMR		22.14, 166.42		66.3	170.9		
A+T							
Stripline	2.69	2.23	2.4		4.88, 4.5, 3.9	2.27,2.3,6	
^{1}H ConvNMR		2.23			4.9 ,4.5, 3.9	2.27, 2.3, 6	1.98, 2-2.5
^{13}C ConvNMR		22.21, 166.41		88, 94, 101	20.2, 101, 163.07	23.63, 177.12	
BnOH+A+T							
Stripline	2.65	2.22	2.39	2.1			1.99
^{1}H ConvNMR		2.23				2.27, 2.3, 6	1.95, 2-2.5
^{13}C ConvNMR		22.19, 166.41				20.12, 20.39, 101, 163.07	23.94,177.88
A+P							
Stripline	2.69	2.22					
^{1}H ConvNMR	2.69	2.22					
^{13}C Conv NMR		22.2, 166.43					
BnOH+A+P							
Stripline	2.67	2.22		2.10			
^{1}H ConvNMR				2.09			2.07
^{13}C ConvNMR				20.99, 170.91			173.83

References

[1] A.-L. Seoud and L. A. M. Abdallah, "Two optimization methods to determine the rate constants of a complex chemical reaction using FORTRAN and MATLAB," *Am. J. Appl. Sci.*, vol. 7, no. 4, p. 509, 2010.

Appendix D

Supplemental Information for Chapter 6: EC–SPE–stripline-NMR analysis of reactive products

D.1 Off-line EC and conventional NMR experiments

BIRB796 was converted to the product mixture in 6 hr under the conditions described in 'Electrochemical conversion'. After 2 and 4 hr, the EC cell was cleaned and refilled as operation for longer than two hours resulted in significant decrease of conversion efficiency. The product mixture was dried at 30°C under a nitrogen stream. The dried sample was then stored at –20°C overnight and reconstituted in DMSO-d_6 directly prior to the NMR measurements. These measurements were executed on an Advance 500 NMR spectrometer using a 5 mm CryoProbe^{TM} (Bruker, Fallanden, Switzerland) at 500.23 MHz.

D.2 Picture of stripline NMR chip and COSY spectrum

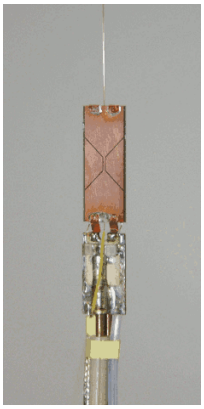

(a) 400 μm stripline, showing the stripline structure (with cap and ground planes removed) on top of the probe

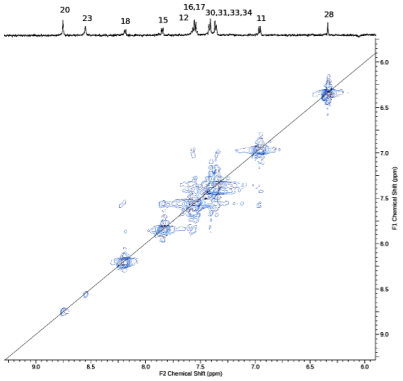

(b) COSY Spectrum of BIRB796 measured in the SPE–stripline-NMR setup

Figure D.1: 400 μm stripline NMR chip used for the measurements in Chapter 6 and COSY spectrum of BIRB796

D.3 NMR data on BIRB796 and EC products

Table D.1: NMR data on BIRB796. Chemical shifts and J-couplings are compared between the different NMR setups. The corresponding spectra are found in Figure 6.4. (overlap with dmso, ** overlap of peaks 12,16,17, for the multiplets averaged values are taken)*

Proton number	2,6	3,5	7	8	11	12	15	16,17	18	20	23	28	30,34	31,33	35	37,38,39
Stripline-NMR																
Chem. shift (ppm)	3.60	*	2.86	4.27	6.96	**	7.85	7.55	8.19	8.76	8.55	6.34	7.42	7.36	2.45	1.27
multiplet	t		t	br	d		d	m	d	s	s	s	dd	dd	s	s
J-coupling	4.1		5.4		8.6		7.8	8.0	8.1				8.0, 32.7	8.5, 33.2		
SPE-stripline-NMR																
chem. shift (ppm)	3.61	2.57	2.88	4.28	6.96	**	7.84	7.56	8.20	-	-	6.34	7.41	7.37	2.40	1.27
multiplet	br	br	br	br	d		d	m	d			s	dd	dd	br s	s
J-coupling					8.3		7.1	8.9, 4.0	7.1				8.3, 25.7	7.1, 24.7		
EC-SPE-stripline-NMR																
chem. shift (ppm)	3.62	2.55	2.89	4.28	6.96	7.50	7.81	7.56	8.21	8.74	8.53	6.33	7.40	7.36	2.39	1.27
multiplet	t	s	t	t	d	d	d	m	d	s	br s	s	dd	dd	s	s
J-coupling	4.1		5.4	4.5	8.2	7.9	7.0	7.4, 4.5, 0.4	7.6				8.1, 20.4	8.1, 20.4		
Conventional NMR																
chem. shift (ppm)	3.59	2.55	2.85	4.26	6.96	7.61	7.89	7.57	8.18	8.76	8.56	6.35	7.44	7.36	2.39	1.27
multiplet	t	br t	t	t	d	d	d	dt	d	s	s	s	dd	dd	s	s
J-coupling	4.6	4.5	5.6	5.6	8.4	8.3	8.3	8.2, 6.8	8.2				8.3, 39.1	8.2, 39.0		

Table D.2: NMR data on the two EC products of BIRB796. The chemical shift, coupling pattern and J-coupling strength are compared between the EC–SPE–stripline-NMR setup and the experiments using the conventional NMR. (overlap of peaks 12,16,17, ** multiple broad peaks in this region, *** overlap with parent compound solvent, x product does not contain these hydrogen atoms. For the multiplets averaged values are taken)*

	Proton number	2,6	3,5	7	8	11	12	15	16,17	18	20	23	28	30,34	31,33	35	37,38,39
hydroquinone																	
EC-SPE-stripline NMR	chem. shift (ppm)	x	x	x	x	6.78	*	7.84	*	8.06	**	**	6.46	***	***	***	1.37
	multiplet					d		***		d			s				s
	J-coupling					10.6				8.3							
offline, fresh	chem. shift (ppm)	x	x	x	x	7.24	*	7.95	7.54	8.09	**	**	6.42	7.35	7.42	2.35	1.37
	multiplet					d		d	t	d			s	dd	dd	s	s
	J-coupling					8.3		8.6	8.1	8.4				6.4, 36.6	7.2, 37.5		
offline, aged	chem. shift (ppm)	x	x	x	x	7.24	*	7.95	7.53	8.09	**	**	6.42	7.43	7.35	2.35	1.37
	multiplet					d		d	dt	d			s	dd	dd	s	s
	J-coupling					8.2		8.4	1.3, 6.0	8.4				6.7, 36.8	6.7, 36.8		
quinoneimine																	
EC-SPE-stripline NMR	chem. shift (ppm)	x	x	x	x	6.83	*	7.76	*	8.14	**	**	6.36	***	***	***	***
	multiplet					d		d		d			s				
	J-coupling					8.0		8.6		8.3							
Offline, fresh	chem. shift (ppm)	x	x	x	x	6.81	*	7.83	7.49	8.13	**	**	6.31	7.35	7.44	***	1.27
	multiplet					d		d	dt	d			s	dd	dd		s
	J-coupling					8.1		8.4	8.3, 17.8 , 1.3	8.0			13.5	8.1, 45.7	8.2, 45.4		

Summary

Nuclear magnetic resonance (NMR) spectroscopy is commonly used as an analytical technique in a wide range of fields, such as chemistry, physics, biology and medicine. The NMR measurement determines the resonance frequencies of the nuclear spins of a sample in a magnetic field. These resonance peaks in the NMR spectrum display small chemical shift differences, reflecting influences of their molecular structure and electromagnetic environment of the nuclei. However, NMR spectroscopy has relatively low sensitivity compared to other spectroscopic techniques. In cases where the amount of sample is limited, which may be due to availability, sustainability or safety reasons, the low sensitivity can become a barrier for using NMR spectroscopy. This is the motivation for the ongoing research on how to increase the sensitivity of the NMR experiment. In this thesis, the feasibility of using the stripline NMR chip is investigated for mass-limited volumes and microfluidic samples, and several chemical applications are explored.

From the expression of the signal-to-noise ratio of the NMR experiment it can be derived that miniaturisation of the NMR coil is one of the strategies for improving mass sensitivity (when only small amounts of samples are used), as reviewed in **Chapter 1**. The stripline NMR microcoil is one of the several possible designs of an NMR microcoil. The stripline is a planar transmission line type structure, which is constricted at the detection area to locally increase the current density and as a result focus on the radio frequency (rf) signal from nuclei in the detection volume. Furthermore, sandwiching the stripline structure between ground planes ensures a good rf homogeneity, resulting in high resolution. The stripline chips used in this thesis have a 150 nl sample volume, microfluidically connected to a pumping system via fused-silica capillaries. It is shown that the stripline rf coil design displays good resolution and high sensitivity.

However, some practical aspects were encountered that can diminish the performance. When substrates suffered from dielectric losses the sensitivity is reduced, while other substrates were difficult to process resulting in irregularities that affected the resolution. Also, leakages can occur when the substrates become too thin and analyte is in contact with the chip material. As a solution for these issues, the latest stripline design has FS substrates and a replaceable capillary that can be used to contain the sample or connected to a microfluidic system.

Some biological samples are only available in small amounts or very expensive to obtain/synthesise. Two examples are explored in **Chapter 2**. Single mouse CSF (cerebro spinal fluid) is typically present in only small amounts of 5 to 7 μl (ante mortem). Being able to measure metabolites in single mouse CSF minimises the use of lab animals, and also individual mouse study can give more information than pooling of material of several mice. A second example is the structural analysis of synthetic analogues of root exudates (strigolactones). These plant hormones are difficult to synthesise, and therefore only available in small amounts. The stripline NMR chip used for studying these samples in a replaceable capillary with sample plugs which have a volume of 150 nl, when covering the whole detection area. A field frequency lock channel was installed with a separate D_2O sample used to correct for any frequency drift during long measurements, which improved the resolution of the spectra. For both mass-limited examples, spectra were obtained in this setup. Stripline spectra of the single mouse CSF was compared with conventional NMR spectra. The spectra displayed sufficient resolution and the signal-to-noise ratio per amount of sample was 4 times higher in the stripline. For the strigolactone analogues, ^{1}H and 2D correlation spectra were measured. In addition, ^{13}C and HETCOR solid state NMR measurements were performed on the samples. The spectra of both of these examples could be measured well in stripline NMR (except for very long ^{13}C NMR spectra). Sufficient volume of sample was available so that analysis in conventional NMR was also possible. So, for these type of samples, it could be an option to scale up the stripline's detection volume to about microliter volumes to obtain the optimal sensitivity.

Another advantage of a miniaturised NMR coil emerges when it is scaled to match microfluidic applications. Microfluidic continuous flow chemistry is a very useful technique to which microfluidic NMR can be coupled to provide in-line analysis. Furthermore, continuous or recycled flow NMR spectroscopy can decrease the mea-

surement time of nuclei with very long relaxation times that are difficult to measure in conventional NMR. Moreover, microfluidic NMR enables in-line detection of unstable compounds. This motivates the investigation of stripline NMR chips in a continuous flow environment in **Chapter 3**. Three stripline NMR chips of different design are connected to a standard microfluidics setup and test pulse sequences are employed that are commonly used for structural research (^{1}H and ^{13}C 1D spectra and ^{1}H-^{1}H and ^{1}H- ^{13}C 2D correlation experiments). The experiments can be performed succesfully using both high and low flowrates. The study suggests that the use of stripline NMR can be valuable for experiments dealing with unstable or mass-limited samples and for online monitoring in continuous flow.

In chemistry, the ongoing trend towards microreactor technology has many advantages, especially when dealing with dangerous, toxic or explosive reactions. In a microreactor, chemical reactions take place in a microfluidic closed system with a very large surface-to-volume ratio, therefore the microreactor provides excellent control over the reaction in terms of thermodynamic and mixing properties. Moreover, as often higher concentrations can be used, less solvents are needed. Due to the smaller reaction volumes microreactor technology is safer and often more efficient than batch reactions. Microreactor technology can be characterised as green chemistry by these advantages for humans and the environment. In order to extend the benefits of microreactor technology into the analysis domain, it is interesting to develop in-line analysis techniques on the same microfluidic scale. For this purpose, the stripline NMR chip is coupled to a microfluidic pumping system to enable the reaction to be performed in a microreactor in continuous flow with *in situ* NMR analysis. In **Chapter 4 and 5**, two examples of chemical reactions analysed with this approach are explored; the acetylation of benzyl alcohol and the Paal-Knorr cyclocondensation.

The acetylation of benzyl alcohol is studied in **Chapter 4**. The presence of an amine (DIPEA) increases the reaction rate so that the reaction is finished in around 10 minutes, which makes it a suitable reaction to monitor in a microreactor-stripline NMR setup. In a conventional NMR setup, some time between mixing in the fumehood and acquisition in the spectrometer is needed, so that the first part of the reaction is excluded from measurement. Furthermore, within the time before completion of the reaction it is difficult to establish stable conditions, which are needed for accurate measurements. Although the product mixture of a very fast reaction may be measured

in conventional NMR after finishing or quenching of the reaction, for monitoring fast reaction kinetics and detection of fast intermediate products, a microfluidic NMR setup has many advantages. Using a microreactor coupled to the stripline NMR chip enables steady state measurements from a few seconds reaction time onwards, when maintaining constant flowrates. For studying the acetylation of benzyl alcohol, a series of 1D ^{1}H NMR spectra was acquired, from which kinetic information could be deduced from the first minutes of the reaction. Using a combination of stripline NMR and conventional ^{13}C NMR measurements, reaction intermediates could be determined. In addition, the amine DIPEA that is used in the reaction was replaced by two alternative amines to observe the role of the amine in the reaction. From these experiments we concluded that the reaction proceeds via a tetrahedral intermediate product and the key intermediates in these reactions are ketene and acetyl ammonium ion. These examples show that detailed structural and kinetic information can be explored within a continuous flow microreactor in combination with stripline NMR spectroscopy.

A second example of a reaction suitable for microreactor technology is the Paal-Knorr cyclocondensation, described in **Chapter 5**. This reaction, used in synthetic chemistry for the production of pyrroles, is very fast and exothermic and therefore difficult to monitor in a conventional lab setup. The mechanistic pathway of the reaction, however, is not clear since it is not known which intermediate products are present. The microfluidic stripline NMR setup offers the convenience of a controlled reaction environment as well as continuous flow detection, so that steady state measurements can be performed at any moment during the reaction. In order to explore if the stripline NMR setup can contribute to the understanding of such a very fast reaction, 1D and 2D ^{1}H NMR spectra were acquired in continuous flow during the reaction. The acquisition time of the 2D spectra is longer then the reaction itself takes to complete, but while maintaining a steady flow the measurement can be performed at a fixed point of time in the reaction progress. From these measurements, intermediate product peaks could be assigned, which enabled fitting the 1D ^{1}H NMR series data to a kinetic model. Compared to conventional NMR spectra taken as soon as a stable mixture is formed, it was shown that the stripline spectra are much clearer and information regarding intermediate products and reaction kinetics can be obtained with our setup, although the product mixture contains several intermediates in low concentrations, which resulted in complex spectra and obscured some intermediate product peaks because of large concentration differences. As a conlusion, a microreactor coupled to the stripline

NMR setup can be very helpful in deriving critical information for a very fast reaction.

Hyphenation refers to in-line coupling of analytical techniques, so that operations (separation, concentration, extraction) and *in situ* spectroscopic measurements can be done, thereby increasing the efficiency and reproducibility of experiments while decreasing contamination and degradation of the sample. **Chapter 6** explores the hyphenation of the stripline NMR chip to electro-chemical (EC) conversion and SPE (solid phase extraction) for pre-concentration and solvent exchange. After *in situ* EC conversion of protein kinase inhibitors, important molecules for drug research, the mass-limited mixture of reactive compounds which degradate over time was collected with SPE (solid phase extraction). The resulting mixture of parent compound, product and side products was measured in the stripline NMR chip setup. ^{1}H spectra and correlation spectra (COSY and TOCSY) were acquired of the unstable compounds and a reference compound. The quality of the NMR spectra obtained with this procedure was sufficient to distinguish and assign the peaks of the product mixture. However, the results indicate that improvements are needed regarding sensitivity of the NMR measurement and efficiency of the EC conversion to make the hyphenated platform a competitive alternative to conventional off-line analysis. Possible strategies to enhance sensitivity and resolution and improve the experimental setup are discussed, indicating that many opportunities are available to accomplish the measurement of quantitative spectra in the hyphenated EC-SPE-stripline NMR setup.

Samenvatting

Kernspinresonantie (NMR) spectroscopie is een analytische techniek die vaak wordt gebruikt in een breed scala van gebieden, zoals chemie, fysica, biologie en geneeskunde. De NMR-meting bepaalt de resonantiefrequenties van de spin van de atoomkernen in een magnetisch veld, weergegeven in een NMR spectrum. De resonantiefrequenties tonen kleine verschillen (chemische verschuivingen), die informatie bevatten over de moleculaire structuur en van de elektromagnetische omgeving van de atoomkernen. NMR-spectroscopie is echter relatief ongevoelig in vergelijking met andere spectroscopische technieken. Wanneer de hoeveelheid monster beperkt is, vanwege de beschikbaarheid of vanwege duurzaamheids- of veiligheidsredenen, kan deze ongevoeligheid een barrière vormen voor het gebruik van NMR-spectroscopie. Om deze reden wordt er veel onderzoek verricht met als doel het verhogen van de gevoeligheid van het NMR-experiment. In dit proefschrift wordt de bruikbaarheid onderzocht van de stripline NMR-chip met verhoogde gevoeligheid bij kleine detectievolumes, waarbij massa-gelimiteerde en microfluïdische monsters, alsmede een aantal chemische vraagstukken worden onderzocht.

Uit de expressie van de signaal-ruisverhouding van het NMR-experiment kan worden afgeleid dat miniaturisatie van de NMR-detectiespoel een van de strategieën is voor het verbeteren van de gevoeligheid bij massa-gelimiteerde monsters, zoals besproken in **Hoofdstuk 1**. De stripline NMR-chip is een mogelijk ontwerp van een NMR-microspoel. De stripline is een vlakke transmissielijnachtige structuur, die ter plaatse van het detectievolume is vernauwd om lokaal de stroomdichtheid te verhogen, zodat het radiofrequent (rf) signaal bijna uitsluitend van de kernen in het detectievolume komt. Bovendien resulteert de plaatsing van de stripline tussen twee grondvlakken in een goede rf-homogeniteit en dus in een hoge spectrale resolutie. De striplinechips ge-

bruikt in dit proefschrift hebben een detectievolume van 150 nl, dat via fused-silica (FS) capillairen microfluïdisch gekoppeld kan worden aan een pompsysteem. De stripline rf-spoel geeft een goede resolutie, hoge gevoeligheid en is eenvoudig microfluïdisch te koppelen. Er zijn echter enkele praktische aspecten gevonden die de prestaties kunnen verminderen. De gevoeligheid vermindert wanneer diëlektrische verliezen optreden in de substraten. Andere substraten bleken moeilijk te verwerken, hetgeen resulteerde in onregelmatigheden aan het oppervlak die de resolutie negatief beïnvloedden. Ook kunnen lekkages optreden bij hele dunne substraten, vooral wanneer het monster in contact komt met het chipmateriaal. Als oplossing voor deze problemen is het nieuwste stripline-ontwerp van FS-substraten en heeft een verwisselbaar capillair dat gebruikt kan worden om het monster te bevatten of gekoppels kan worden aan een microfluïdisch systeem.

Materialen van biologische oorsprong zijn soms alleen beschikbaar in kleine hoeveelheden of erg duur om te synthetiseren. Twee voorbeelden worden onderzocht in **Hoofdstuk 2**. Het CSF (hersenvocht) van een individuele muis bestaat slechts uit kleine hoeveelheden van 5 tot 7 μl (ante mortem). Het kunnen meten van metabolieten in CSF van een enkele muis minimaliseert het gebruik van proefdieren en tevens kan het onderzoek van een individuele muis meer informatie geven dan wanneer materiaal van meerdere muizen wordt samengevoegd (poolen). Een tweede voorbeeld is de structuur-analyse van synthetische analogen van wortelexsudaten (strigolactonen). Deze planthormonen zijn moeilijk te synthetiseren en daarom alleen in kleine hoeveelheden beschikbaar. De stripline-NMR-chip die wordt gebruikt voor het bestuderen van deze monsters in een verwisselbaar capillair met vloeistofpluggen die, wanneer ze het detectiegebeid volledig bedekken, een volume van 150 nl hebben. Er werd een zogeheten lock-kanaal geïnstalleerd met een afzonderlijke microspoel die een D_2O-volume meet om te corrigeren voor frequentiedrift tijdens lange metingen, waardoor de resolutie van de spectra verbeterd. Met deze opstelling werden NMR spectra gemeten voor beide massa-gelimiteerde voorbeelden. De stripline NMR spectra van muizen-CSF werden vergeleken met conventionele NMR-metingen. De resolutie van de stripline spectra was voldoende en een de signaal-ruis-verhouding per hoeveelheid materiaal was een factor 4 hoger bij de stripline NMR spectra. Voor de strigolacton-analogen werden ^{1}H en 2D-correlatiespectra gemeten. Daarnaast werden ^{13}C en HETCOR vaste stof NMR-metingen uitgevoerd. De spectra van deze twee voorbeelden konden goed worden gemeten in stripline-NMR (behalve zeer lange ^{13}C NMR-spectra). Er was

voldoende materiaal beschikbaar zodat analyse in conventionele NMR ook mogelijk was. Voor dit type monsters zou het detectievolume van de stripline kunnen worden opgeschaald tot ongeveer microlitervolume om de optimale gevoeligheid te verkrijgen.

Een ander voordeel van een geminiaturiseerde NMR-spoel wordt duidelijk wanneer deze wordt geschaald zodat de meetvolumes aansluiten op microfluïdische flowchemie. Continue flowchemie is een zeer bruikbare techniek waaraan microfluïdische NMR detectie kan worden gekoppeld om op die manier in-line analyse te verrichten. Verder kan continue of gerecyclede flow NMR-spectroscopie de meettijd verminderen van monsters die, als gevolg van zeer lange relaxatietijden, moeilijk te meten zijn met conventionele NMR. Bovendien maakt microfluïdische NMR in-line detectie van onstabiele chemische verbindingen mogelijk. In **Hoofdstuk 3** worden stripline NMR-chips in een continue flow opstelling getest. Drie verschillende stripline NMR-chips worden gekoppeld aan een reguliere microfluïdische opstelling. Terwijl de vloeistof met constante snelheid door het detectievolume stroomt, worden standaard testpuls-sequenties gebruikt (^{1}H en ^{13}C 1D NMR en ^{1}H - ^{1}H en ^{1}H- ^{13}C 2D correlatie NMR metingen). Deze metingen zijn met succes uitgevoerd voor zowel hoge als lage stroomsnelheden. De studie laat zien dat het gebruik van een stripline-NMR interessant kan zijn voor experimenten met onstabiele of massa gelimiteerde monsters en voor online monitoring in een continue flow opstelling.

In de chemie heeft de ontwikkeling van microreactortechnologie veel voordelen, vooral als het gaat om gevaarlijke, giftige of explosieve reacties. In een microreactor vinden chemische reacties plaats in een microfluïdisch gesloten systeem op microschaal met een zeer grote oppervlakte/volume-verhouding. De microreactor biedt thermodynamisch gunstige omstandigheden en een uitstekende controle bij het mengen van de reactants in een exotherme reactie. Bovendien kunnen reacties vaak in hogere concentraties worden gedaan, zodat minder oplosmiddelen nodig zijn. Vanwege de kleinere reactievolumes is de microreactor-technologie veiliger en vaak efficiënter dan batch-reacties. Door deze voordelen voor mens en milieu kan microreactor-technologie worden gekenmerkt als groene chemie. Om de voordelen van de microreactor-technologie uit te breiden naar het analysedomein, is het van belang om in-line analysetechnieken te ontwikkelen op dezelfde microfluïdische schaal. Vanuit dit oogpunt is de microfluïdische stripline-NMR-chip gekoppeld aan een microreactor en een microfluïdisch systeem om de reactie in continue flow op microschaal te kunnen uitvoeren en *in situ* te

analyseren. In **Hoofdstuk 4 en 5** worden twee voorbeelden van chemische reacties met deze benadering geanalyseerd: de acetylering van benzylalcohol en de Paal-Knorr-cyclocondensatie.

De acetylering van benzylalcohol wordt bestudeerd in **Hoofdstuk 4**. De aanwezigheid van een amine (DIPEA) verhoogt de reactiesnelheid zodat de reactie binnen ongeveer 10 minuten is voltooid, waardoor het een geschikte reactie is om te monitoren in de stripline NMR-chip. Bij een conventionele NMR meting is enige tijd tussen het mengen van de reactieproducten in de zuurkast en acquisitie in de spectrometer onvermijdelijk, zodat het eerste deel van de reactie niet kan worden gemeten. Bovendien is het, binnen de tijd vóór voltooiing van de reactie, moeilijk om stabiele omstandigheden te creëren, die nodig zijn voor nauwkeurige metingen. Hoewel het productmengsel van een zeer snelle reactie kan worden gemeten in conventionele NMR na beëindigen of quenchen van de reactie, heeft een microfluïdische NMR-opstelling vele voordelen bij het monitoren van snelle reactiekinetiek en detectie van kortlevende tussenproducten van een reactie. De combinatie van een microreactor en stripline NMR spectroscopie maakt het mogelijk bij constante stroomsnelheid steady-state metingen te doen vanaf een reactietijd van enkele seconden. Voor het bestuderen van de acetylering van benzylalcohol werd een reeks van 1D ^{1}H NMR-spectra gemeten, waaruit kinetische informatie vanaf de eerste minuten van de reactie kan worden opgemaakt. Gebruikmakend van een combinatie van stripline NMR en conventionele ^{13}C NMR-metingen, konden tussenproducten van de reactie worden bepaald. Bovendien werd de amine DIPEA die in de reactie wordt gebruikt vervangen door twee andere aminen om de rol van het amine in de reactie te observeren. Uit deze experimenten werd geconcludeerd dat de reactie verloopt via een tetraëdrisch tussenproduct en de belangrijkste tussenproducten bij deze reactie zijn keteen en acetyl-ammoniumion. Uit deze voorbeelden blijkt dat gedetailleerde informatie met betrekking tot de moleculaire structuur en reactiekinetiek kan worden verkregen door middel van een continue flow opstelling met een microreactor en stripline NMR-spectroscopie.

Een tweede voorbeeld van een reactie die zeer geschikt is voor microreactortechnologie is de Paal-Knorr cyclocondensatie, die wordt gebruikt in de synthetische chemie voor de productie van pyrrolen, uitgevoerd in **Hoofdstuk 5**. Deze reactie is erg snel en exotherm en daarom moeilijk gecontroleerbaard uitvoerbaar en meetbaar in een conventionele labopstelling. Doordat niet bekend is welke tussenproducten aanwezig

zijn, is het reactiemechanisme niet duidelijk. De microfluïdische NMR stripline biedt een gecontroleerde reactieomgeving en *in situ* NMR detectie. Om te onderzoeken of de stripline NMR kan bijdragen aan het begrip van het mechanisme en de kinetiek van een zeer snelle reactie zoals de Paal-Knorr cyclocondensatie, werden steady-state 1D- en 2D ^{1}H NMR-spectra gemeten tijdens de reactie. Interessant is dat de acquisitietijd van de 2D-spectra langer is dan de reactie duurt, maar door een constante stroomsnelheid kan de meting op een vast moment in de reactie worden uitgevoerd. Uit deze metingen konden enkele tussenproductpieken worden toegewezen in de spectra, waardoor een kinetisch model kon worden gefit aan de gegevens van de 1D ^{1}H NMR-serie, hetgeen inzicht geeft in het reactiemechanisme. Het productmengsel bevat verschillende tussenproducten in lage concentraties, waardoor de spectra erg complex zijn en sommige tussenproductpieken vanwege grote concentratieverschillen niet goed te onderscheiden zijn. Desondanks kon bruikbare informatie worden afgeleid met betrekking tot het reactiemechanisme. Vergeleken met conventionele NMR-spectra die werden genomen zodra een stabiel mengsel was gevormd, werden er met de stripline NMR duidelijkere spectra gemeten en kon informatie over tussenproducten en reactiekinetiek worden bepaald die niet uit de conventionele NMR metingen naar voren kwam. Concluderend kan een microfluïdische reactor gekoppeld aan de stripline-NMR-opstelling zeer bruikbaar zijn bij het analyseren van een zeer snelle reactie.

Hyphenation verwijst naar in-line koppeling van analytische technieken, zodat operaties (scheiding, concentratie, extractie) en spectroscopische metingen *in situ* kunnen worden uitgevoerd, waardoor de efficiëntie en reproduceerbaarheid van de experimenten worden verhoogd, terwijl contaminatie en degradatie van het monster worden verminderd. **Hoofdstuk 6** beschrijft de koppeling van de stripline NMR-chip met elektrochemische (EC) conversie en SPE (vaste fase-extractie) voor pre-concentratie en oplosmiddeluitwisseling. Na *in situ* EC-omzetting van proteïnekinaseremmers, belangrijke moleculen voor geneesmiddelenonderzoek, werd het massa-gelimiteerde mengsel van reactieve verbindingen dat na verloop van tijd degradeerde, verzameld en geconcentreerd door middel van SPE (vastefase-extractie), voordat het resulterende mengsel van beginproduct, product en bijproducten werd gemeten in de stripline NMR-chipopstelling. ^{1}H-spectra en correlatiespectra (COSY en TOCSY) werden gemeten van het onstabiele product en een referentie. De kwaliteit van de NMR-spectra verkregen met deze procedure was voldoende om de pieken van het productmengsel te onderscheiden en toe te wijzen. De resultaten geven echter aan dat er verbeteringen

nodig zijn met betrekking tot de gevoeligheid van de NMR-meting en de efficiëntie van de EC-conversie om van de gebruikte hyphenated setup een concurrerend alternatief voor conventionele off-line analyse te maken. Mogelijke strategieën om gevoeligheid, de resolutie en de experimentele opstelling te verbeteren, worden besproken, wat aangeeft dat er verschillende mogelijkheden zijn om kwantitatieve spectra te meten in de gekoppelde EC-SPE-stripline NMR-opstelling.

List of publications

- 'A Microfluidic High-Resolution NMR Flow Probe', J. Bart, A. J. Kolkman, A. J. Oosthoek - de Vries, K. Koch, P. J. Nieuwland, J. W. G. Janssen, P. J. M. van Bentum, K. A. M. Ampt, F. P. J. T. Rutjes, S. S. Wijmenga, J. G. E. Gardeniers and A. P. M. Kentgens, J. Am. Chem. Soc., **131**, pp. 5014 (2009)

- 'EC–SPE–stripline-NMR analysis of reactive products: a feasibility study', David Falck, Anna Jo Oosthoek - de Vries, Ard Kolkman, Henk Lingeman, Maarten Honing, Sybren S. Wijmenga, Arno P. M. Kentgens and Wilfried M. A. Niessen, Analytical and Bioanalytical Chemistry, **405**, (21), pp. 6711-6720 (2013)

- 'Continuous Flow ^{1}H and ^{13}C NMR Spectroscopy in Microfluidic Stripline NMR Chips', Anna Jo Oosthoek - de Vries, Jacob Bart, Roald M. Tiggelaar, Johannes W. G. Janssen, P. Jan M. van Bentum, Han J. G. E. Gardeniers and Arno P. M. Kentgens, Analytical Chemistry, **89** (4), pp 2296-2303 (2017)

- 'Inline reaction monitoring of amine-catalyzed acetylation of benzyl alcohol using a microfluidic stripline NMR setup', Anna Jo Oosthoek - de Vries, Pieter J. Nieuwland, Jacob Bart, Kaspar Koch, Johannes W. G. Janssen, P. Jan M. van Bentum, Floris P.J.T. Rutjes, Han J.G.E. Gardeniers and Arno P. M. Kentgens, J. Am. Chem. Soc., **141** (13), pp 5369–5380 (2019)

- 'Paal-Knorr pyrrole synthesis: reaction and detection in a microfluidic NMR setup', Anna Jo Oosthoek - de Vries, S.A.M.W van den Broek, Ruud Aspers and Arno P. M. Kentgens, in preparation.

Curriculum Vitæ

1992-1998	VWO, Dollard College in Winschoten, the Netherlands
1998-2005	Applied Physics, University of Twente, Enschede, the Netherlands
Minor:	Geo-data processing and Spatial Information, ITC, Enschede
Internship:	Computational Modelling Group, Tyndall Institute, Cork, Ireland
Major:	Solid state physics
MSc thesis:	”Ellipsometric and electrical characterisation of percolating electrolessly deposited silver layers”, 09-11-2005
2007-2014	PhD research, Physical Chemistry (solid-state NMR group) IMM (Institute for Molecules and Materials), Radboud University Nijmegen, the Netherlands